ACTIVE FORM ERROR CONTROL DURING ROBOTIC ASSISTED MILLING

Author:
Patrick Ludwig FENOU KENGNE

Supervisors:
Dr. Erdem OZTURK
Dr. Simon POPE

A thesis submitted in fulfilment of the requirements for the degree of Doctor of Philosophy in the

Advanced Manufacturing Research Centre
The University of Sheffield

February 2025

Abstract

Robotic milling is becoming increasingly popular, as an alternative to the use of conventional CNC (Computer Numerical Control) machines, due to the added dexterity, expansive working envelope and multi-station capability of robotic arms. However, one of the main issues that arises is the positional error that comes with using them and their low stiffness, compared to conventional industrial machines. There is therefore a great need to compensate these errors. Various methods have been investigated in the past in order to improve robotic milling errors, among which: robot command modification [1], [2], [3], manipulator model modification [4], [5], optimisation of the existing robotic machining cell [5] and the augmentation of the robotic machining cell [3], [6], [7], [8], [9], [10]. The concept of robotic assisted machining which was first proposed by Ozturk et al [11] in conventional CNC milling is now gaining popularity as a viable solution to reduce form errors in robotic milling.

This study focusses on the use of a collaborative robot to mitigate form errors in both conventional CNC and robotic milling. The first setup is similar to the one proposed by Ozturk et al [11] in peripheral milling, and the second setup is comprised of a milling robot and a colinear collaborative robot supporting the backface of the workpiece while the milling robot performs face milling.

The study begins with an in-depth analysis of cutting conditions, workpiece materials, and the various factors contributing to form errors in robotic milling. Simulations were conducted to model the performance of the proposed control methods under varying conditions, including robotic support forces, static stiffness, and position errors. Results from the simulations show that both force minimisation and thickness control significantly reduce form errors compared to traditional robotic milling approaches, with thickness control being particularly effective in mitigating errors across a range of scenarios. Under load ratings from the robot's ball caster, the thickness control method achieved a 62% reduction in form error across rectangular paths when compared to unsupported milling trials, while the force minimisation method achieved a 9% decrease.

Experimental validation was conducted using a collaborative robot system equipped with a force sensor to measure form errors during milling trials. The experimental setup was carefully designed to benchmark the force control method against conventional robotic milling without error compensation. There was a decrease of 69% and 50% in form error in peripheral and pocket milling operations. The findings from both the simulation and experimental work demonstrate that integrating active form error control enhances machining precision, especially in challenging robotic milling tasks involving complex geometries and varying material properties.

Acknowledgments

I would like first to thank God for the opportunities that He has availed in my life, for guiding me, strengthening me and always being my friend in time of trouble.

I also would like to express my deepest appreciation to everyone who has been a helping hand throughout the course of my research. First of all, I would like to thank my first supervisor Dr. Erdem Ozturk for taking a chance in giving me this opportunity and fighting for me every step of the way. Erdem's experience, knowledge, relentless patience and kindness has made all this research possible, and I am extremely grateful for his life, and I would not have hoped for a better supervisor. I would also like to thank my second supervisor Dr. Simon Pope for all the weekly meetings where crucial discussion steered the direction of the research. With this supervisory team, despite my lack of knowledge in the field, I slowly but surely caught up with the necessary tools to make the investigation fruitful. I would also like to thank Dr Chao Sun for his involvement in the primary stages of this research and for being instrumental in this opportunity being given to me.

Furthermore, I would like to thank AMRC Sheffield and the Industrial Doctoral Centre (IDC) for enabling this research to go forward, especially Professor David Curtis and Professor Pete Osborne, for their cooperation and always being there to help with advice and resources. Additionally, I would like to thank every staff member at the AMRC and at the University of Sheffield for their help and expert advice at every point of the service.

Last but not least, I would like to thank my family in Cameroon, especially my parents, for financially and emotionally supporting me through what seems like a very long academic journey. Your love and backing have greatly helped me in low times.

To everyone mentioned here and to many more, I could not have done it without you. Thank you so much for your help and support.

Statement of contribution

The work presented in this thesis would not have been possible without the contributions of many brilliant people, to whom I am very grateful. Due to the collaborative and interdisciplinary nature of this project, some of the data presented was acquired with the help of Dr. Chao Sun and Dr. Peace Onawumi. All experiments in this thesis were conceived and designed by myself, with additional input from my PhD supervisors, Dr. Erdem Ozturk, Dr. Simon Pope.

In the following I state the contribution of other people to the data presented by chapter:

Chapter 4: The position errors used to assess the robustness of the form error controls were obtained from milling trials conducted by Dr. Peace Onawumi.

Chapter 5: The experimental setup for the machining trials was done with the help of Dr. Chao Sun. Moreover, due to the multiples sources of data acquisition during the machining trials, he assisted in the acquisition of cutting force data while I was acquiring the support robot force data. He also proposed the three form error prediction models this work is compared with, when looking at the accuracy of the simulation results compared to experimental results.

Table of contents

List of figures

List of tables

Dedicated to my family and to God, whose I am and whom I serve…

Chapter 1

Introduction

1.1 Background

Over the past two decades, advances in automation have significantly impacted manufacturing, particularly in industrial sectors such as automotive and aerospace [12], [13]. The shift towards lightweight structures has increased the challenge of maintaining dimensional accuracy in thin-walled machining due to low structural stiffness and tighter tolerance requirements..

The motivation behind the increased adoption of industrial robots in machining, as opposed to conventional CNC machines, stems from the quest for heightened versatility, adaptability, and efficiency in manufacturing processes [14].

One key motivation is the superior flexibility of use of industrial robots. Unlike CNC machines, which are often specialised for specific tasks, robots can be reprogrammed and repurposed for a diverse range of machining operations. This flexibility enhances the overall agility of manufacturing processes, allowing for quick adaptation to changing production requirements.

Another motivation lies in the potential for enhanced automation and collaboration. Industrial robots can collaborate with human operators and other robots, enhancing manufacturing flexibility and responsiveness. While CNC machines have long been the standard in machining, it could be argued that industrial robots offer distinct advantages, particularly in terms of flexibility and collaboration. CNC machines, though highly specialised for certain tasks, are often limited in their ability to quickly adapt to changing production needs. In contrast, industrial robots can be easily used to perform a wide variety of machining operations, enhancing the versatility of manufacturing systems. However, it is important to note that CNC machines, like industrial robots, can also be integrated into automated systems and may be used in environments where human interaction is limited, often due to safety concerns. Collaborative robots (cobots) take this a step further by working alongside human operators, designed with built-in safety features such as sensors and force limitations, which reduce the risks of accidents and allow for more dynamic human-robot interaction. This collaboration improves safety and efficiency, allowing robots to assist in complex tasks and enhance manufacturing agility. This collaborative nature facilitates increased efficiency and resource utilisation.

However, the field of robotic machining has some limitations compared to CNC machine tools due to poor pose accuracy and dynamic characteristics. Such handicaps prevent industrial robots from achieving the same high tolerance requirements that CNC machines can provide. For this very reason, there has been a rising interest in researching methods to improve robotic machining accuracy, mainly through the optimisation [1], [2], [3], [5] by modifying the robot trajectory and the augmentation [3], [6], [7], [8] of the robotic cell with the introduction of the new elements in the robotic cell. Such elements can be other robots, giving rise to the concept of robotic co-operation [10], [15] or robotic assisted milling, which is the area of interest of this research.

1.2 Aim and objectives

This research investigates the implementation of active form error control on a collaborative robot while supporting the backface of a workpiece during CNC and robotic milling, thereby enhancing machining accuracy. This contribution stands as a unique and valuable addition to existing literature on machining. To achieve this aim, the following objectives were defined.

1. Define cutting conditions to establish the simulation framework, particularly focusing on workpiece material and properties.
2. Develop form error control methods and justify their relevance using cutting force models and error computation.
3. Implement and compare these control methods in simulations for various milling operations, including peripheral and face milling. Furthermore test their robustness across various cutting conditions such as position errors predominant in robotic milling, wide spectrum in static stiffness across the part, force limits and the radial engagement of the tool during milling trials. This is to have a thorough and more realistic appreciation of the simulation trials.
4. Benchmark control method performance against experimental results through detailed investigation.
5. Design an appropriate dual robot configuration to implement the control approaches on.

1.3 Thesis outline

This thesis provides a structured exploration of robotic-assisted milling and form error control to enhance machining accuracy in industrial applications.

Chapter 2 reviews the current state of robotic machining research, focusing on robotic-assisted milling. This chapter starts by examining the evolution of robotic machining, focusing on the advantages that industrial robots offer over traditional CNC systems, such as their flexibility, expansive working envelopes, and multi-station capabilities. Although robots offer advantages, this chapter highlights their limitations, including lower positional accuracy and weaker dynamic characteristics compared to CNC machines. The chapter goes on to categorise the sources of errors in robotic milling, such as environment-dependent errors, robot-related errors, and milling process-related errors, and critically evaluates methods that have been proposed to mitigate these challenges, including optimisation techniques (e.g., robot trajectory modification) and augmentation strategies (e.g., the addition of sensors and actuators). A key focus is placed on robotic-assisted milling, where additional robots or external support systems are integrated to compensate for errors, with robotic cooperation emerging as a particularly promising area of research. Finally, the chapter concludes with a gap analysis, identifying areas where further investigation is needed, especially in active form error control using collaborative robots.

Chapter 3 outlines the fundamental theories underpinning the research, focusing on the mechanics of milling operations and the prediction and control of form errors in robotic-assisted milling. It starts with a discussion of the cutting forces in milling, introducing the models used to predict these forces during peripheral and face milling operations. The chapter also delves into the role of workpiece material properties and static stiffness in influencing machining accuracy. Form errors are modelled, while considering only the static characteristics of the workpiece. The theoretical foundation for two novel form error control strategies—force minimisation and thickness control—is also presented. Force minimisation aims to reduce the total force acting on the workpiece, while thickness control focuses on real-time adjustments based on measurements of remaining workpiece thickness. The chapter concludes by framing these approaches within the broader context of control theory, providing a foundation for the simulation and experimental work that follows.

Chapter 4 presents the simulation studies used to evaluate the proposed control methods. This chapter first introduces the simulation environment, and the specific scenarios investigated, including peripheral and face milling with both supported and unsupported workpieces. The impact of robotic support forces on form errors is examined for the previously proposed force control method, and simulations are run to assess the performance of the force minimisation and thickness control methods. The chapter also explores the effects of machining robot position errors and varying workpiece stiffness on milling accuracy. Simulations are conducted to investigate how these factors influence the performance of the control strategies. A comprehensive comparison of the control methods with the conventional unsupported robotic milling case provides insights into their relative effectiveness. The results demonstrate the potential of both methods to reduce form errors, with thickness control outperforming force minimisation in most scenarios. The chapter concludes by discussing the implications of the simulation results and identifying key areas for further refinement in both simulation and experimental setups.

Chapter 5 describes the experimental setup and validation tests conducted to evaluate the performance of the control strategies on the mitigation of form errors. Although the experimental setup was not fully completed in time to test the novel control methods (force minimisation and thickness control), the chapter presents an overview of the machine-robot collaboration setup, including the use of the STAUBLI TX-90 robotic arm, force sensors, and laser displacement sensors. The focus of the chapter is on benchmarking the performance of machine-robot collaboration in peripheral milling, with a comparison of experimental results to simulation data from Chapter 4. Although dual-robot collaborative trials for face milling were planned, the experimental setup for this was not fully implemented by the time of writing, and no results are presented for this scenario. The chapter discusses the challenges faced in completing the experimental setup and outlines the plans for future validation of the proposed control strategies once the setup is fully operational.

Chapter 6 provides a synthesis of the research findings and discusses the contributions made to the field of robotic-assisted milling. The chapter begins with a summary of the key results from both the simulation and experimental work, highlighting the strengths and limitations of the control methods. A detailed discussion is provided on the implications of these findings for improving machining accuracy in industrial robotic applications, particularly in thin-walled and high-precision milling operations. This chapter discusses study limitations, particularly the incomplete experimental validation, and proposes directions for future research. Future investigations are suggested, including completing the experimental validation of the control methods, improving the robustness of the models, and extending the application of the methods to other milling operations, such as face milling. The chapter concludes by summarising the novel contributions of the thesis and suggesting potential industrial applications for the findings, particularly in the areas of collaborative robotics and precision machining.

Chapter 2

Literature review

2.1 Introduction

This chapter presents an overview of current research in robotic machining, with a focus on robotic-assisted milling. It begins by exploring the evolution of industrial robotic machining, emphasising its increasing role in manufacturing due to its flexibility, large working envelopes, and multi-station capabilities. Although industrial robots offer significant advantages over conventional CNC machines—such as cost-effectiveness and adaptability—they face challenges related to positional accuracy and structural stiffness, which affect machining precision [16], [17].

Next, the chapter categorises sources of error in robotic milling into three groups: environment-dependent, robot-related, and milling process-related errors [18]. Each category is examined in detail, with a focus on understanding how these errors affect machining outcomes. This is followed by a review of existing methods for improving robotic milling accuracy, which are broadly classified into optimisation techniques—such as robot trajectory modification—and augmentation techniques, including the addition of sensors, actuators, and secondary robotic systems [5], [6], [8].

A key focus is robotic-assisted milling, which integrates additional robotic support to enhance workpiece stability and reduce form errors. This section reviews notable studies in the field, including machine-robot collaborations [11], [19] and dual-robot mirror milling systems [15], [20]. While these approaches show promise in reducing form errors, the absence of active control methods remains a major limitation.

The chapter concludes with a gap analysis, highlighting research limitations and justifying further investigation into active form error control with collaborative robots. The novel contributions of this thesis are outlined, particularly the implementation of force-based control methods and the development of new form error compensation strategies designed to improve machining accuracy in both machine-robot and dual-robot collaborative setups.

2.2 An overview of industrial robotic machining

2.2.1 State-of-the-art of industrial robotic machining

Robotic machining, introduced by Appleton and Williams in 1987 [21], [22], has evolved to cover processes like grinding, deburring, drilling, milling, and polishing [17]. These processes require precise trajectory tracking and force application [23], with specific requirements depending on the material removal rate (MRR) [22]. Low-MRR processes, traditionally human-handled, require robots to mimic human motions and exhibit tool-workpiece compliance [22], emphasising programming challenges over physical robot properties.

In contrast, high-MRR processes, akin to CNC machining, demand robotic stiffness, speed, and accuracy [22], especially crucial for cutting forces in these operations. Despite CNC machines being the preferred choice for accuracy and stability [24], robots excel in tasks with small loads or on soft materials, achieving superior polishing quality [25].

The stiffness gap between CNC machines and robots (50N/μm vs. <1N/μm) minimises compliance issues in CNC machines, particularly for hard materials [17], preventing dynamic or static deflections [26]. Despite being used in industrial settings, robots constitute only 1.4% of total sales, with CNC machines dominating machining tasks [16].

Robotic machining also includes mobile robots, often featuring an arm or parallel kinematic mechanism on a mobile platform, which increases working volume [27]. A 2017 paper by Grau et al. anticipates the fourth industrial revolution's impact on industrial robotics, emphasising innovation through enhanced communication networks [28]. This suggests potential applications for data science and decision-making software in reducing compliance errors in robotic machining. Grau et al. [28] identify a gap between smart robotic applications in academia and industry requirements, advocating collaboration to address this divide, aligning with the goals of the current project.

2.2.2 Pros of robotic machining

This section outlines the perceived advantages of robotic machining compared to its technological counterparts. These advantages, both potential and realised, will be further discussed in the subsequent analysis. According to a key white paper from the Robotic Industries Association in 2008, robotic machining's intrinsic ability to operate in a 5+ axis configuration, coupled with flexibility, expansive working envelopes, and multi-station capabilities, provides a versatile solution. This versatility enables end-users to diversify machining applications while remaining competitive with traditional CNC machines in terms of cost [14].

A typical serial manipulator has six degrees of freedom, providing one degree of redundancy that can be optimised for 5-axis machining tasks. In some cases, this optimisation improves stiffness during milling operations [29].

The importance of an expanded working envelope is particularly evident in aerospace applications, where workpiece dimensions often exceed the conventional capacities of CNC machines. Despite this, the demand for precision machining of intricate geometries remains high [30].

Ji and Wang describe industrial robots as "multi-function and low-cost machines," suggesting their potential as alternatives to CNC machines. However, they acknowledge CNC machines' superiority in machining accuracy and stability [22]. This aligns with the common understanding that industrial robots face challenges integrating into the domain of industrial machining.

2.2.3 Limitations in the application of robotic machining

Despite their advantages over CNC machining, robots face significant limitations, especially when working with rigid materials like metals and composites [17]. A comprehensive overview in 2015 highlights the industrial robot's accuracy shortcomings compared to conventional machine tools but notes its relative competitiveness with rapid prototyping machines [17]. Challenges include deviations from intended toolpaths, resulting in geometric inaccuracies and compromised surface quality due to machining vibrations [23].

Effective robotic machining demands precise trajectory tracking, reliability, durability, configurability, programming simplicity, versatility, and sensory input capabilities [31]. In a critical review, Ji and Wang [22] highlight that low-MRR operations demand extensive programming due to robotic system flexibility, making them less competitive with human operators. This suggests a need to prioritise high MRR processes for exploration.

Quality standards for parts are assessed based on criteria like path straightness, surface flatness, and circularity [32]. Klimchik et al.'s study with various KUKA robot arms reveals a linear correlation between circularity (and accuracy) and cutting forces, making it a suitable metric for accuracy evaluation [32]. Currently, robotic machining falls short in milling processes with high force requirements compared to machine tools.

2.3 Errors in robotic milling

2.3.1 Introduction

Recent advancements in milling technology include improved computer control and increased use of sensors. These innovations have provided opportunities to increase machining productivity and accuracy. ‘Accuracy’ refers to how closely a finished part conforms to required dimensional and geometric specifications [33]. ‘Error’ is defined as any deviation in the cutting edge’s position from its theoretical value, affecting the workpiece’s tolerance; the extent of error in a conventional CNC machine gives a measure of its accuracy [34]. Machining errors fall into two categories: quasi-static and dynamic errors.

On one hand, quasi-static errors consist of positional errors between workpiece and machining tools that vary very slowly with time, as well as the structure of the machine tool itself. They include form errors, kinematic/geometric errors, errors due to dead weight of the machine's components and errors due to continuous thermally induced strains on the machine with time [34]. On the other hand, dynamic errors are due to spindle error motion, machine structure vibrations, and other machining conditions.

Machining errors can also be categorised as follows: geometric and kinematic [34], [35], thermally induced [34], [36], [37], cutting force induced errors [38], [39], [40], [41] as well as controller dynamics related errors [42], [43].

In robotic machining, the end effectors used as machine tools equally suffer from similar sources of error as well as those coming from the machine tool internal architecture. Specifically in robotic machining, all errors are categorised in the following: environment-dependent errors, process-dependent errors, and robot-dependent errors [18]. These errors are presented in the following sections.

2.3.2 Environment dependent errors

These errors originate from environmental influences on the robot’s behaviour. Key factors include temperature variations [44], robotic cell calibration [45], nearby machine vibrations, and floor material properties affecting the robot’s base. These errors are difficult to model and calibrate since they do not depend on quantifiable factors [4]. Thus, they are excluded from this investigation.

2.3.3 Robot-related errors

Robot-related errors fall into two categories: geometrical and non-geometrical [46], both stemming from structural imperfections affecting kinematic accuracy. Geometrical errors—including tolerance issues, assembly misalignment, gear backlash [47], bearing run-out, and transmission clearance—can accumulate along the kinematic chain, causing inaccuracies in the Tool Centre Point (TCP) pose. Kinematic calibration techniques offer effective compensation [48], [49], [50].

Non-geometrical errors arise from structural deformation, wear, friction, hysteresis [51], and non-linear effects at servo motors [52]. Factors like control issues during rapid TCP movements, joint wear, and thermal effects [53], [54] contribute to these time and configuration-dependent errors. While static compliance errors can be identified, modelled, and calibrated [5], [55], [56], addressing TCP path deviations during abrupt motion changes remains challenging.

In robotic machining applications, the majority of quantifiable errors result from manipulator geometrical structure and process loading. Approximately 90% of TCP position errors under small external loading are attributed to geometrical errors [46], yielding industrial manipulators with an accuracy range of about 1 mm [57], [58]. Kinematic compensation techniques can enhance pose accuracy to 0.1-0.3 mm [59]. Despite lower pose accuracy, industrial manipulators exhibit better repeatability (0.01-0.03 mm) [60], [61] due to their design for repetitive tasks [62], varying with manipulator size [63].

2.3.4 Milling process related errors

These errors depend on tool type, workpiece properties, and cutting conditions [38], [39], [40], [41]. However, in low-stiffness thin-walled parts, force-induced deflections are considerably contributing to the total surface error and therefore should not be overlooked, especially in operations like milling [64].

In milling, poor surface quality results from harmful vibrations, classified as self-excited or forced vibrations [12]. Self-excited vibrations are due to mode coupling and stability loss related to regenerative chatter [12], [13], [65], [66], [67], [68], [69]. Forced vibrations are often of large amplitudes occurring at resonant spindle speeds. These vibrations lead to surface location error (SLE) [70], which is the largest deviation between machined and intended surfaces [71]. Figure 2.1 illustrates the surface location error where a_e is the intended radial depth of cut.

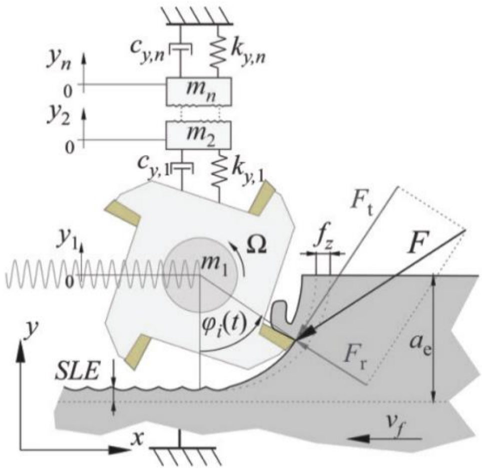

Figure 2.1 Surface location error [72]

The positional accuracy of robotic systems is highly dependent on loading conditions, often leading to structural deviations; the magnitude and direction of such deviations are directly influenced by the type and direction of the loading. Under static loads, it is comparatively straightforward to calibrate and account for errors when handling a payload [73]. However, in machining conditions, the errors generated by cutting forces at the TCP (Tool Centre Point) are a lot more complex to take into account. These errors significantly amplify error magnitudes, reaching up to 1.5mm due to the inherent limitations in manipulator structural dynamics [74]. As a result, the use of robots in machining parts with high dimensional tolerance is restricted [16].

Given that surface location errors are the most predominant errors in machining processes, the focus of the investigation will be on mitigating these errors.

2.4 Existing methods of improving robotic milling

Numerous methods have been employed in order to improve the positional accuracy in robotic milling. They can be separated in two subsets: optimisation and augmentation.

2.4.1 Optimisation techniques

This category focuses on modifying the robotic cell—particularly its control software—to improve trajectory accuracy. The correction of compliance errors can be accomplished by manipulation model modification and robot control program modification [5].

- Compliance errors can be reduced by refining the manipulator model through accurate geometric, static stiffness, structural, and dynamic modeling [4], [5].
- An improvement in compliance errors in robotic machining can be achieved by providing a modified milling trajectory that makes provision and compensates errors, thereby allowing the robot to follow a closer path to the intended one [5]. This can be done by either offline [3] or online [1], [2]. The offline compensation provides a pre-optimised cutting trajectory solution, which is often time-consuming. The online compensation however generally makes use of sensors mounted within the robotic cell and a control program is written to react to errors as they occur during the milling operations [75].

2.4.2 Augmentation techniques

Unlike optimisation methods, positional accuracy can be improved by augmenting the robotic machining cell with sensors and actuators. This enhancement is often done in three ways: general stiffness increase, active vibration control and robotic co-operation.

- The general stiffness increase approach involves upgrading to a manipulator with a higher stiffness rating. This upgrade aims to enhance the coverage of stability lobes within the operating space, thereby improving the overall performance.

- Active vibration control focuses on improving the robot's resistance to dynamic effects during machining. It is essential to note that static compliance errors may not be improved by this method. Moreover, this approach necessitates signal processing based on either measured vibrations or predictive modelling [3], [6], [7], [8].
- The enhancement of the robotic cell can involve the installation of other robots to support or assist the machining robot. This technique is often generally referred to as robotic assisted machining [9], [11], [76], or dual robot machining in robotic machining applications [10], [15].

The concept of robotic assisted milling is further investigated in the rest of this thesis, in collaborations with a CNC machine (it is referred to in later sections as "machine-robot collaboration") and with another robot (referred to as "dual robot collaboration").

2.5 The concept of robotic assisted milling

This section highlights some notable investigations in the field of robotic assisted milling.

2.5.1 Traditional milling

One of the pioneering works in the field of robotic assisted milling was the investigation carried out by Ozturk et al. [11] at the Advanced Manufacturing Research Centre in Rotherham. The team developed a novel concept that employs a robotic arm that applies a supporting force at the back face of an aluminium workpiece during peripheral milling operations. Solutions were already developed for fixed and mobile supports, such as the use of discrete masses attached to thin-walled casings via a viscoelastic tape by Kolluru et al [77] and a mobile support with a damper overhung to the spindle housing of a milling machine by Fei et al [78], [79]. Both demonstrated a considerable effect on the increase in stiffness and damping on the workpiece;

however, these approaches are limited to certain applications. The use of a robotic arm to provide a localised and moving support on the workpiece is therefore advantageous due to its reconfigurability.

In the proposed solution, contact between the workpiece and the robot is ensured through a rubber roller, as shown in Figure 2.2. In this application, the rubber roller moves along the workpiece, with the cutting tool; furthermore, the supporting force was monitored, not controlled.

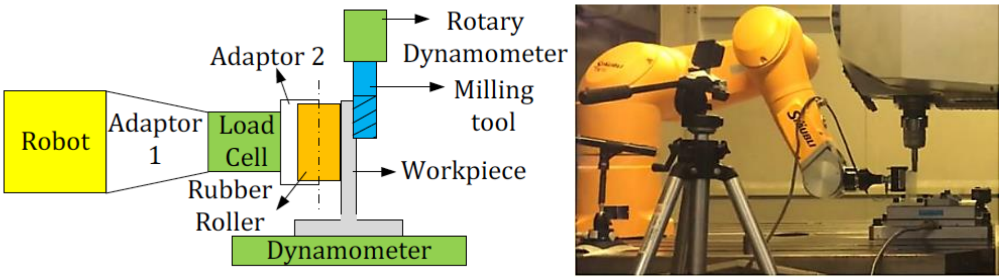

Figure 2.2 Solution developed in robotic assisted milling [11].

Nonetheless, experimental results, illustrated below, show a 68% improvement in form error with the help of the robotic support.

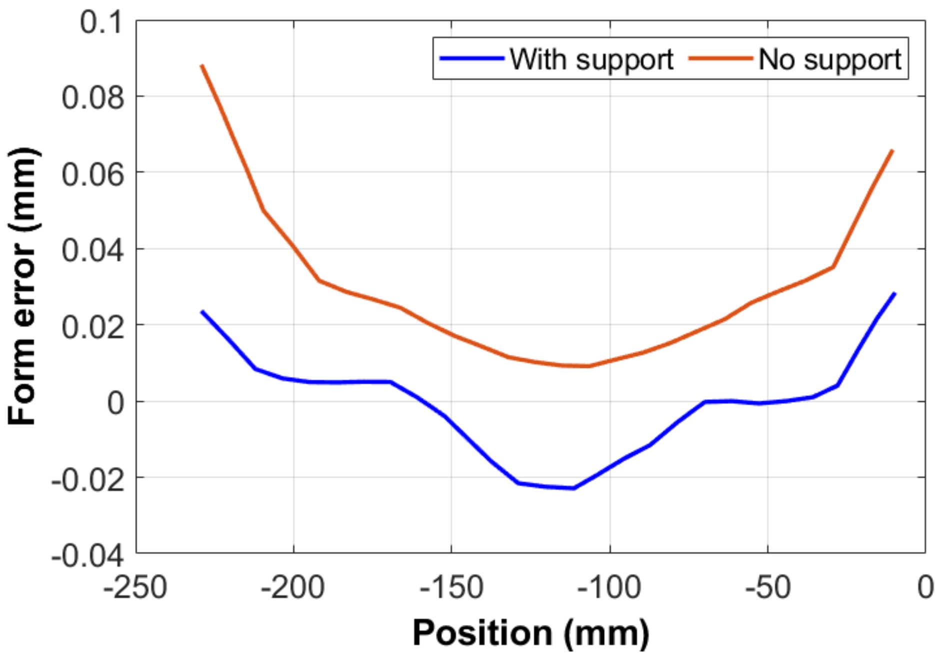

Figure 2.3 Form error results [11].

The author [19] carried out further work on Ozturk's robotic assisted milling setup by developing and implementing a novel, force-based, PID (Proportional-Integral-Derivative) control that will keep the supporting force exerted by the collaborative robot (in Figure 2.2) at the back of the workpiece.

Moreover, two types of rubber rollers (with different hardness) were attached at the end of the robotic arm to investigate the effect of added stiffness on the system. Depending on the type of rubber roller used, labelled as "soft rubber" and "hard rubber" in the research, there was a change in workpiece dynamics, based on tap test results shown in Figure 2.4.

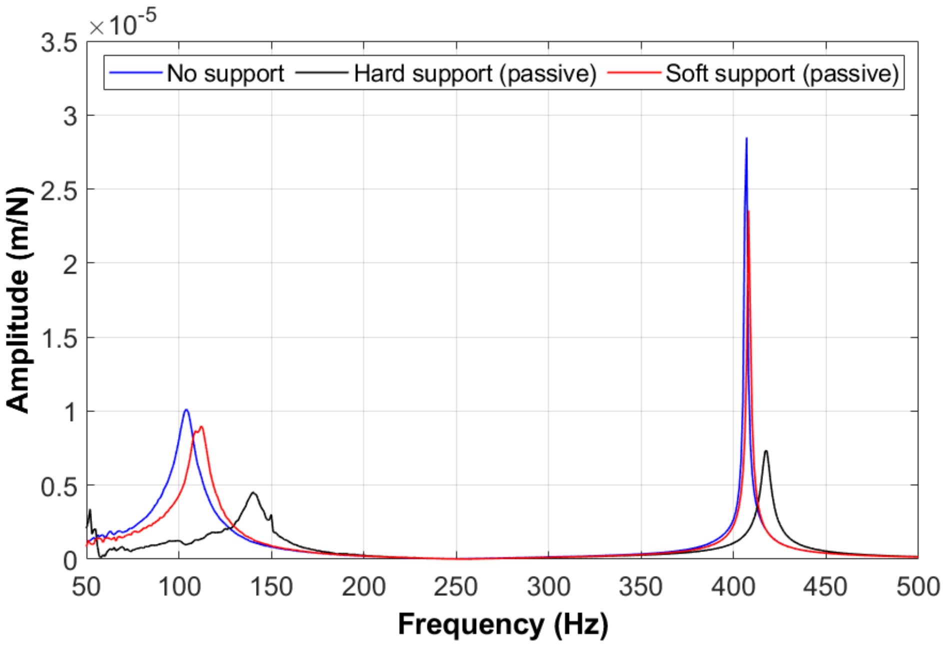

Figure 2.4 Tap test results [19]**.**

Frequency response functions (FRFs) were obtained for both robotic supports and compared with the unsupported workpiece. Robotic support showed a decrease of 17% and 74% in flexibility of the workpiece respectively with the soft and hard rubber rollers; this is because the hard roller (used in "hard support" case) had a higher static stiffness than the soft rubber.

However, the use of such end effectors caused force irregularities on the workpiece as the rollers travelled across the workpiece (see Figure 2.5). The blue and red force profiles show the support force applied at the backface of the workpiece without force control. After implementation of the PID control, the irregularities perceived with the soft rubber roller were minimised. Moreover, according to the same figure, the force values increased along the workpiece, highlighting a potential misalignment of the workpiece. This misalignment was also compensated through the force control (as it is shown with the soft rubber on the brown line in the figure).

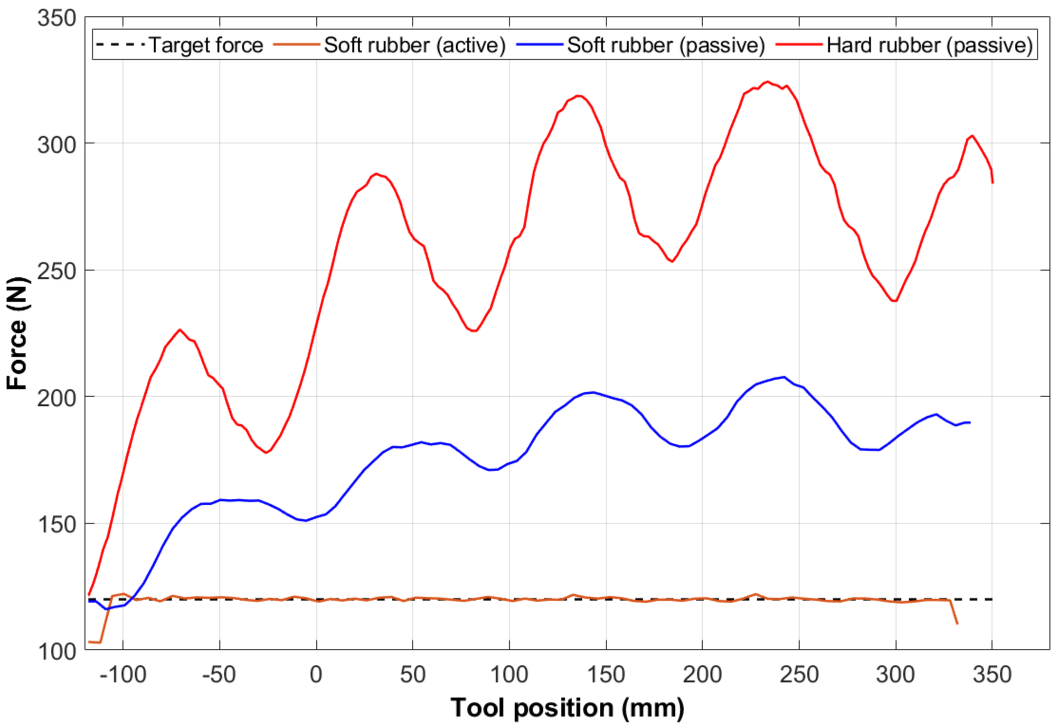

Figure 2.5 Force analysis summary [19]**.**

Furthermore, the reason why the force measured increased as the roller moved against the workpiece is illustrated in Figure 2.6. Unlike what was assumed – that the workpiece is parallel to the motion path of the roller, because of human errors during the fixturing of the part, the workpiece was slightly slanted; this slant therefore increased the force exerted by the roller along its nominal path (from point 1 to point 3). Moreover, due to the plastic deformation of the rubber rollers, there was a sinusoidal pattern observed on the force as well as the increasing trend due to the misalignment.

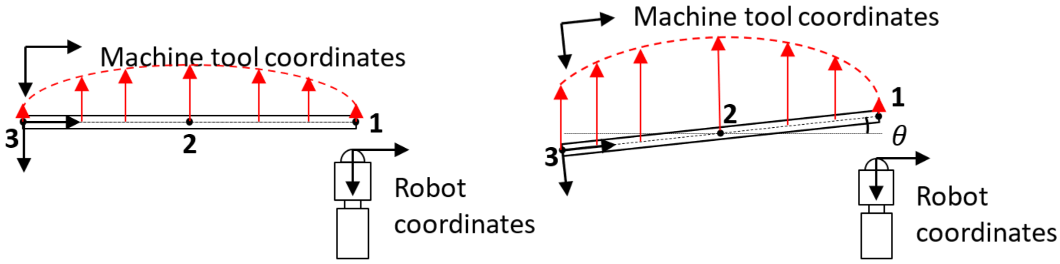

Figure 2.6 Workpiece-roller misalignments [19]**.**

As shown in Figure 2.5, the force control algorithm used enabled the cobot to compensate force errors from the abovementioned irregularities. For a given target force of 120N, the controller decreased the percentage error from 75% (when the force control is not used with the hard rubber) to 14% (when it is being used), as illustrated in Figure 2.5.

However, this investigation was just an early development and implementation of a force-based control in robotic assisted milling applications; no investigation was made on its impact on form errors prior to the research presented in this thesis. From the work presented above [11], [19], the use of a collaborative robot in conventional CNC machining leads to chatter mitigation through the local damping and stiffness contributed by the robotic arm (Figure 2.4), and form error reduction through the exertion of static force on the backface of the workpiece (Figure 2.3). It is therefore important to investigate form error control methods implemented on the cobot and their impact of form error values in machining conditions. It is also important to state that the above-mentioned investigation pre-dates the findings presented in the rest of this thesis.

2.5.2 Robotic milling

Inspired by Ozturk's pioneering work [11], Torres et al. [10] used a collaborative robot, KUKA LBR iiwa, which was used to provide mobile support at the back of a thin-walled workpiece during robotic milling, more specifically face milling. The robot end effector was very similar to the one used in Figure 2.2 (see Figure 2.7).

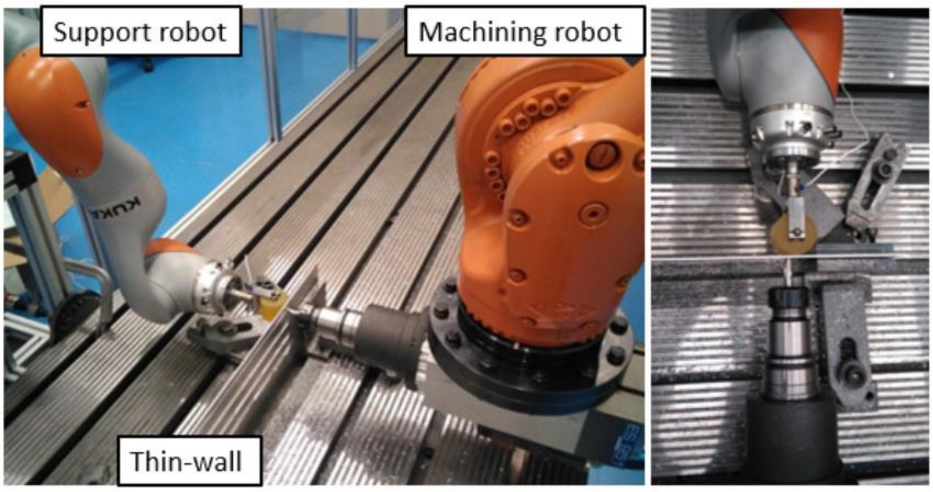

Figure 2.7 Robotic milling with a collaborative robot [10]

After running machining trials of 1mm depth of cut on 2mm and 3mm thick workpieces, the maximum form error values are plotted in the figure below. The team observed that, due to the static deflection of the workpiece contributed by the support robotic force, the axial depth of cut is increased, therefore leading to a decrease in form error of 40% (with the 2mm thick workpiece) and 50% (with the 3mm thick workpiece). However, no control method was implemented on either robot to decrease the form error values.

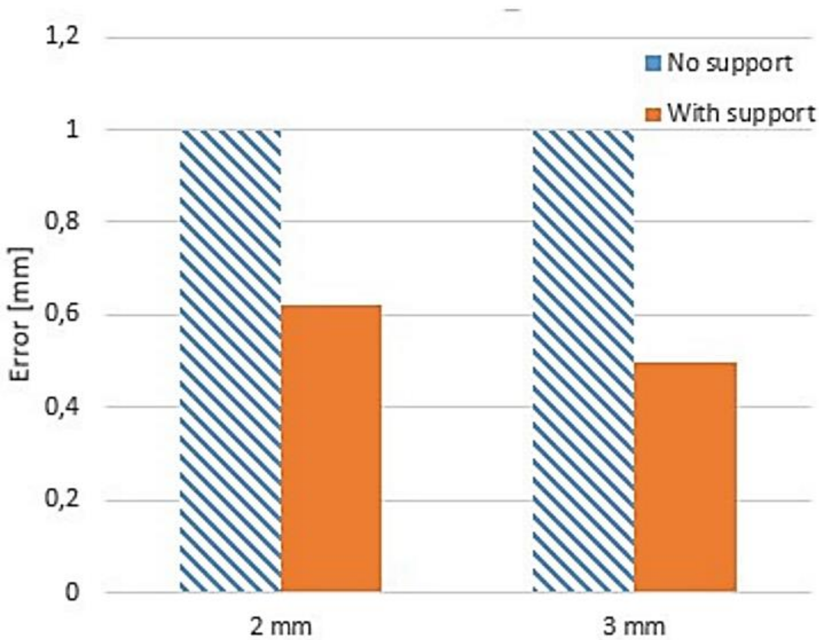

Figure 2.8 Maximum form error values [10].

Moreover, Xu et al. [80] explored an innovative dual-robot machining system designed to minimise deformation errors in the machining of thin-walled parts, which are prone to such errors due to their low rigidity. This system employs two industrial robots working in tandem (see Figure 2.9), with each robot supporting one side of the part to reduce deformation during the machining process. This setup eliminates the need for flipping or re-clamping parts, significantly improving machining efficiency and precision. A key feature of the system is the concept of *dual-robot stiffness matching*, where both robots are optimised to ensure equal rigidity, preventing mismatched forces that could introduce additional deformation. The research introduces a dual-robot posture optimisation model that not only ensures stiffness matching but also maximises the robots' normal stiffness, further minimising deformation errors. The optimisation process is achieved through a novel sequential algorithm based on directed node graphs (via Dijkstra searching method), which is shown to be effective in improving the accuracy of machining.

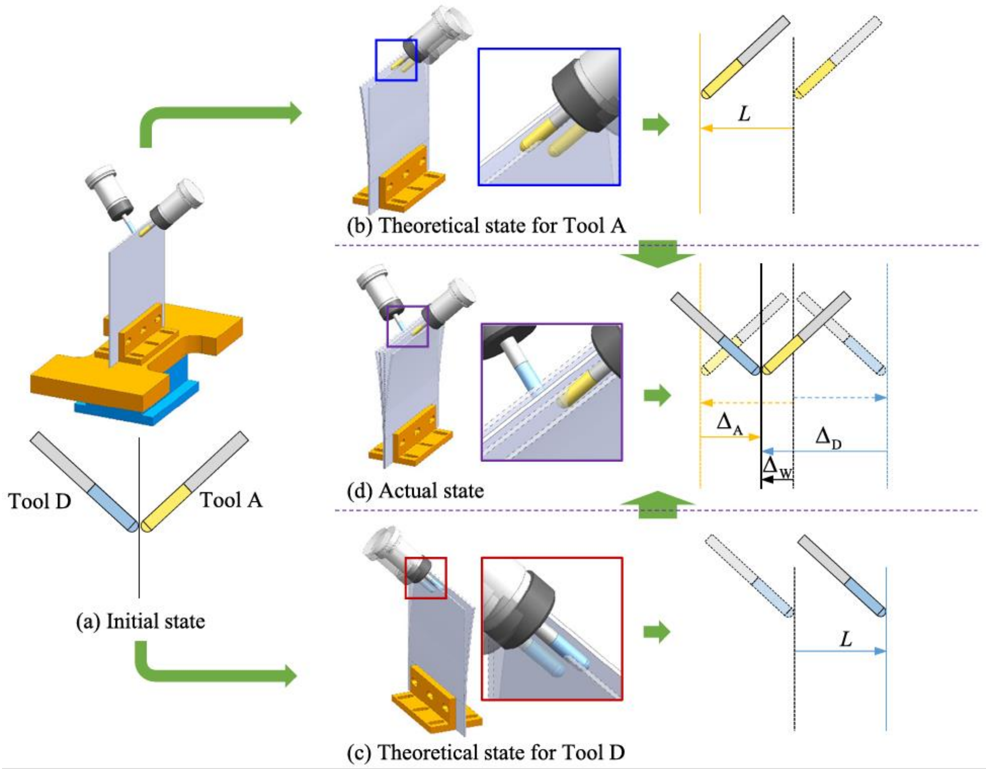

Figure 2.9 Displacement changed of tools a and D under external force during dual-robot machining [80].

The results demonstrate that dual-robot machining with stiffness matching significantly outperforms traditional single-robot machining. The system's dual-robot setup reduces workpiece deformation by approximately 40% compared to single-robot machining. Furthermore, when stiffness matching is implemented, the deformation is reduced by over 60%, illustrating the substantial benefits of the dual-robot stiffness matching strategy in controlling machining errors. However, the study has several limitations. First, while stiffness mismatching is identified as a major contributor to deformation, other factors such as dynamic cutting forces and vibrations, which also affect the machining process, are not fully explored. This opens a research gap for further studies to investigate how to balance cutting forces and suppress vibrations during dual-robot machining to improve overall accuracy. Second, while the dual-robot system is shown to reduce deformation, its performance depends on the precise calibration of the robots, and any errors in positioning may still affect the results. These limitations suggest an opportunity for research that extends the system's capabilities to a wider range of machining conditions (including robotic position errors), providing a clear gap for this research.

2.5.3 Hybrid robots in mirror milling

The concept of robotically assisted milling has also been investigated with hybrid robots; it is referred to as "dual-robot mirror milling system", named after its counterpart in conventional milling. A conventional mirror milling system is equipped with two mirror-symmetrically arranged heads, where the first one carries the milling tool, while the second one provides support at the back face of the workpiece. Hybrid robots featuring parallel mechanisms are gaining popularity in machining due to their superior flexibility, stiffness, and precision [81]. However, it's essential to note that their stiffness and positioning accuracy are relatively lower compared to conventional milling methods [15].

Xiao et al. [15] investigated a novel dual-robot mirror milling where a cutter and a flexible supporting head were mounted on two identical robots (see Figure 2.10). They both consisted of TriMule, a five-DOF hybrid mechanism [82]. The milling robot's cutter trajectory was computed in real-time based on the end trajectory of the supporting robot's motion path and pre-established machining parameters [15]. The remaining wall thickness was determined via contact-type online measurement through dual-robot endmost geometrical pose and wall thickness error compensated by the machining hybrid robot.

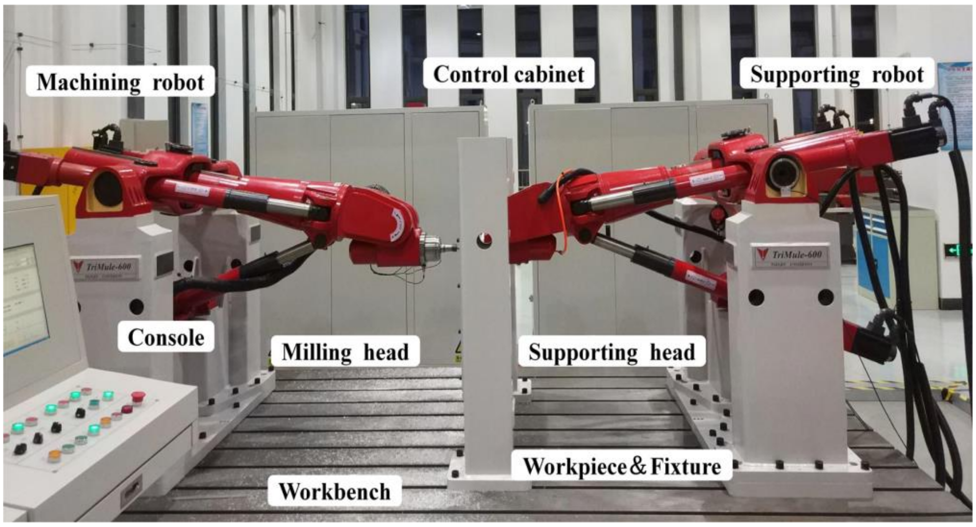

Figure 2.10 Dual robot mirror milling system [15]**.**

Results revealed however a disparity between wall thickness errors measured in-situ by the online measurement and the post-machining errors measured by ultrasonic thickness gauge; the former ones were less than ±0.05mm while the latter were less than ±0.2mm. More accurate measurement strategies are needed in this application.

Another notable investigation is that of the team led by Zhang [20]. The team developed a conventional mirror milling system that provides both wall thickness measurement and compensation in real-time through alteration of the axial depth of cut by the milling head as shown in Figure 2.11. An online measurement system is built to measure the geometric pose of the machine tool and local deformation of the workpiece, in order to estimate the wall thickness and compensate any error. Two types of measurement sensors were used; a high-frequency standard immersed transducer with a thickness gauge was used to measure the wall thickness, while four electric eddy transducers were used to approximate the wall thickness. Despite the high accuracy of the immersed transducer (ultrasonic), it had a very large lag in data acquisition, whereas the eddy transducer with lower accuracy and small delay was the method of choice for the method of choice when implementing the control approach. Nonetheless, both were used.

In order to reject the deformation errors measured during milling, a disturbance observer (DOB) was designed, and combined with a Modified Smith predictor (MSP), which provided stability to the closed control loop. After the implementation of the MSP-DOB controller, the form error was improved by 35%. An important takeaway from this investigation is the use of sensors to measure wall thickness error and directly compensate that error through the modification of the displacement of the milling robot in the W_1 axis, unlike the former use of force-based control proposed by the author [19].

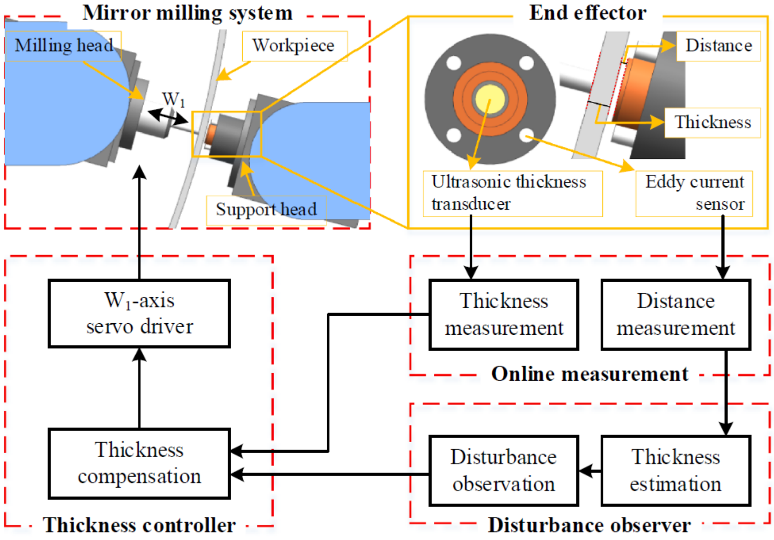

Figure 2.11 Overview of online measurement and compensation system [20].

Additionally, double sided machining is increasingly investigated [83], [84]. Fu et al. [85] presented a novel approach to double-sided milling of thin-walled parts with complex double-sided features using dual collaborative parallel kinematic machines (PKMs). This method addresses the challenges of traditional single-sided machining, such as the need for re-clamping, re-calibration, and multiple machining operations, by allowing synchronised and asynchronous cutting with support from both sides of the workpiece. The study compares three milling strategies: synchronised double-sided milling (S-1), alternative single-sided milling (S-2), and sequential single-sided milling (S-3). The results show that the synchronised double-sided milling strategy (S-1) outperforms the other two strategies in terms of dimensional accuracy, with an improvement of approximately ~78.2% at the bottom section and ~58.1% at the top section compared to alternative single-sided milling (S-2), as shown in Figure 2.12. Furthermore, productivity is significantly enhanced, with the dual PKM setup doubling the material removal rate, reducing machining time, and eliminating the need for re-clamping or re-calibration, thus improving overall efficiency.

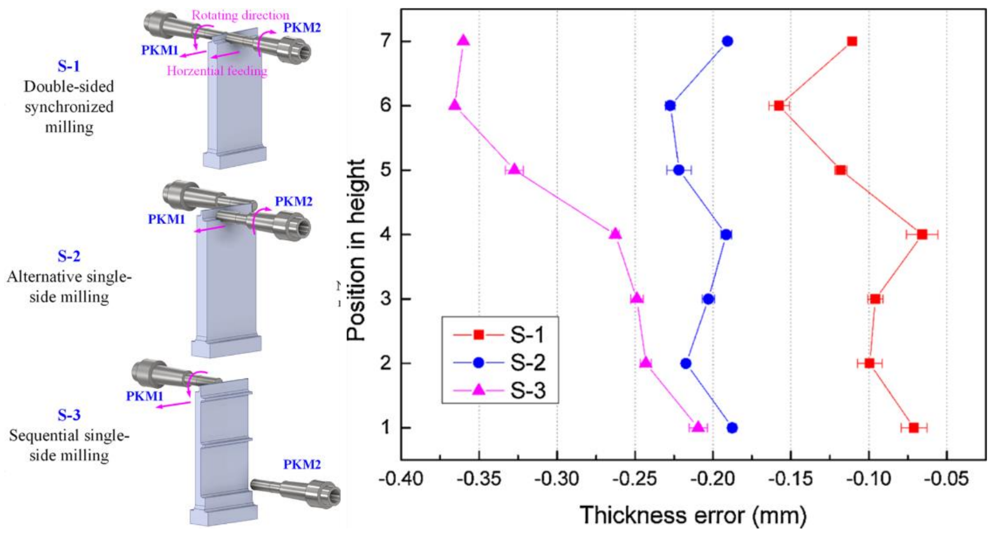

Figure 2.12 Double-sided machining strategies (left) and thickness errors across the workpiece height [85].

While the synchronised double-sided milling strategy improves dimensional accuracy and stability, the study also highlights some limitations. Surface roughness (Ra) is higher on the PKM1 side in S-1 compared to S-2, likely due to vibration-induced forced vibrations, which can cause secondary cuts and affect surface quality. The dynamic performance of the workpiece is improved, with the introduction of the second PKM helping to dampen vibrations, but vibration-induced roughness remains an issue. Additionally, the study focuses on parts with symmetrical double-sided features, and further research is needed to extend this approach to more complex geometries or asymmetric parts, which may present challenges related to collision risk and dynamic performance. Another limitation is the absence of an active form error control method in the study. While the dual PKM collaborative machining improves static stiffness and reduces deformation during machining, active error control, which could dynamically compensate for form errors during the process, was not implemented.

2.6 Gap analysis and novel contributions

The literature suggests that limitations of robotic machining operations are significant and there are many sources of error contributing to the poor machining accuracy: environment dependent, robot-dependent and milling force induced. The aforementioned errors can be mitigated by optimisation and augmentation techniques. Optimisation techniques utilise the existing machining cell, while augmentation techniques involve the addition of new elements to the cell, which gives room for a greater range of possibilities. One of these avenues, rising in research popularity is the concept of robot co-operation, or more specifically robotic assisted milling, with the use of a cooperative robot to improve machining accuracy in the robotic cell. The concept has not only been investigated in robotic milling [10], but also in conventional milling [11], [20] and hybrid robotic milling [15].

However, having outlined the latest advances in robotic assisted milling in the last section (as shown in Table 2.1), to the author's knowledge, active, closed-loop form errors control methods have never been utilised on a collaborative robot in robotic milling applications.

Research papers	Robotic collaboration type	Single/double sided machining	Active form error control	Sensing	Closed loop system
Ozturk et al. [11]	Robot-CNC	Single	-	Support force	-
Torres et al. [10]	Dual serial robot	Single	-	Support force	-
Xiao et al. [15]	Dual parallel kinematic robot	Single	Implemented on machining robot	Endmost geometrical pose	-
Fu et al. [85]	Dual parallel kinematic robot	Double	-	-	-
Xu et al. [80]	Dual serial robot	Double	-	Robot normal stiffness	-
Zhang et al. [20]	Conventional mirror milling	Single	Implemented on machining robot	Remaining wall thickness; geometric pose	MSP-DOB
The author's work (including this thesis) [76], [86]	Robot-CNC & dual serial robot	Single	Implemented on collaborative robot	Support force; overall force on workpiece; remaining wall thickness	PID

Table 2.1 Summary table of relevant works in form error reduction highlighted in the literature review .

For this reason, the following novel contributions are made via this research.

1. Machine - robot collaboration to achieve reduced form error in peripheral and pocket milling.

Unlike earlier investigations, which primarily relied on passive support systems [10], [11], a force control algorithm is implemented on the collaborative robot and actively controls the supporting force, regulating the deformations on the workpiece and enhancing machining accuracy in CNC-robot collaboration. This analysis lies in the static interaction between the machine and the robot, offering a more adaptable and localised solution compared to traditional methods.

2. Investigation of novel form error control measures on the collaborative robot in robotic milling

This novelty addresses the challenge of improving form errors through active error compensation by focusing on the collaboration rather than the milling robot [20], [87] in dual-robot collaboration. The two proposed novel methods—force minimisation and thickness control—aim to counteract the inherent errors caused by positional inaccuracies in robotic milling. The introduction of these control measures, especially the thickness control method, marks a significant advancement in reducing form errors consistently across various machining scenarios. This control approach represents a new direction for reducing reliance on static and predetermined system conditions.

Chapter 3

Theoretical framework

3.1 Introduction

In previous sections, it was outlined that cutting force-induced errors are predominant in machining lightweight structures. Several error compensation methods have been investigated over the last decade [64], but active methods have proven most efficient and cost-effective, as they do not rely on the repeatability of machining trials but instead on real-time acquisition and compensation of errors [20], [34], [88]. Among contributions in this field, the concept of robotic-assisted milling has gained increasing attention, particularly following the research pioneered by Ozturk et al. [11], and further developed by the author prior to this research [19].

Despite the flexibility of use of industrial robotic arms, they face some challenges related to compliance and positional accuracy. As a result, research increasingly focuses on improving the machining accuracy of robotic systems [89]. This chapter establishes the theoretical framework for addressing these challenges by introducing the fundamental principles of milling dynamics, including cutting force models [24], workpiece material properties, and static stiffness considerations.

Two milling configurations—peripheral milling and face milling—are examined in detail, with a focus on their respective force interactions and tool-workpiece engagement characteristics. A key factor in face milling is the influence of tool geometry on axial cutting forces, particularly the effect of helix angle on the direction of cutting forces. As demonstrated in prior studies [90], reversing the sign of the helix angle alters the direction of axial cutting forces, crucial for maintaining contact between the robotic support and the workpiece in face milling applications.

Building upon these principles, this chapter also explores the modelling of form errors in robotic-assisted milling. This approach incorporates the effect of robotic support forces on the effective depth of cut, leading to more accurate predictions of surface location errors.

Finally, two novel form error control methods—force minimisation and thickness control—are introduced. The force minimisation method seeks to regulate the overall forces acting on the workpiece, ensuring stable machining conditions. Meanwhile, the thickness control method, inspired by techniques in dual-robot mirror milling [20], dynamically adjusts the support robot's position based on real-time thickness measurements to maintain machining accuracy.

The theoretical concepts and models presented in this chapter form the basis for the simulation and validation work discussed in the subsequent chapters.

3.2 Milling dynamics

In the realm of machining operations, milling emerges as a fundamental and widely employed process with profound implications for modern manufacturing industries. At its core, milling involves the precise removal of material from the periphery of a workpiece using a rotating cutting tool. The geometric intricacies of this operation are defined by the tool's cylindrical shape and its orientation with respect to the workpiece surface.

Throughout this investigation, exclusively end mills are used in milling trials. Two configurations are examined: peripheral and face milling. Both configurations are shown in Figure 3.1.

This section provides a comprehensive analysis, providing an in-depth and meticulous examination of the modelling of cutting forces encountered during the intricate milling operations. This profound understanding of cutting forces serves as a fundamental prerequisite, playing a pivotal role in the subsequent design and implementation of advanced control strategies tailored for the STAUBLI robot, which will be elucidated in the forthcoming sub-sections of this document.

As we navigate through the formulation of cutting forces in milling operations, valuable insight was gained to shape the strategies and algorithms to be employed in the control system of the STAUBLI robot, ultimately leading to optimised machining processes and enhanced productivity.

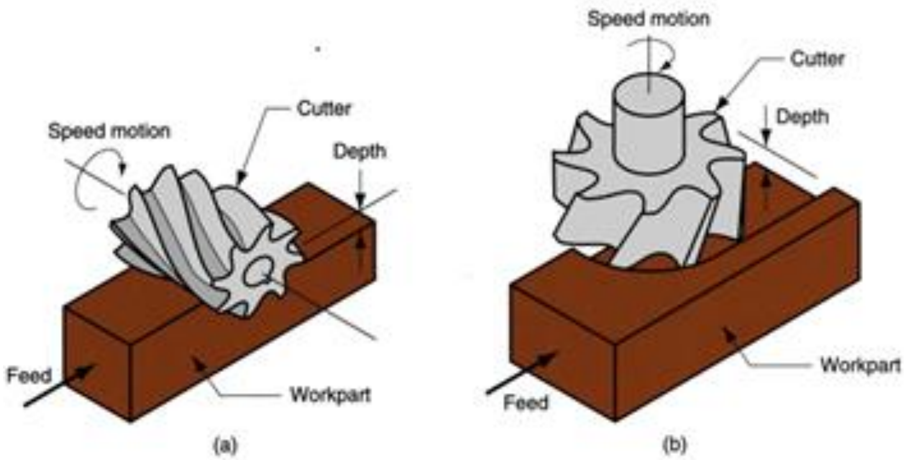

Figure 3.1 Forms of milling: (a) peripheral milling; (b) face milling [91]**.**

3.2.1 Cutting force model

The rigid force model, which was used in this investigation, can be used to accurately determine cutting forces from the uncut chip thickness. This formulation was outlined by Altintas et al [24]. In this formulation, the tool is modelled as a rotating body while the workpiece is stationary, as shown in Figure 3.2.

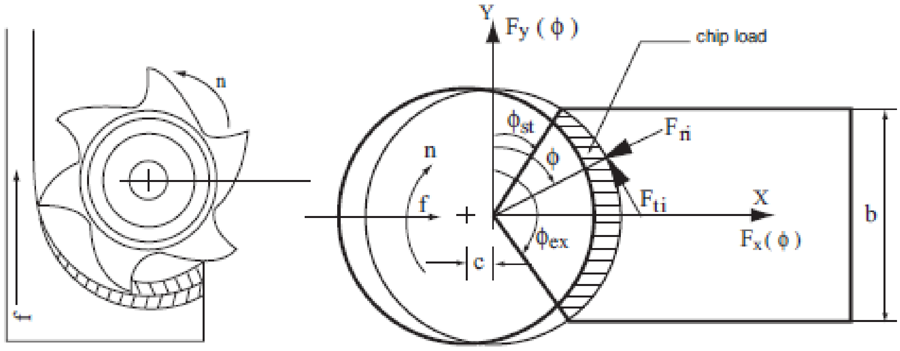

Figure 3.2 Geometry of milling process [24].

Following the derivations in [24], for milling, the milling tool is first divided along its axial length (Z-direction) into micro-discs of height dz. For each micro-disc, the tangential, radial, and axial forces on each tool are identified below.

$$\begin{cases} dF_{tj}(\phi, z) = \left(K_{tc}h(\phi_j) + K_{te}\right)dz \\ dF_{rj}(\phi, z) = \left(K_{rc}h(\phi_j) + K_{re}\right)dz \\ dF_{aj}(\phi, z) = \left(K_{ac}h(\phi_j) + K_{ae}\right)dz \end{cases}$$

Equation 3.1

where K_{tc}, K_{rc}, K_{ac}, K_{te}, K_{re} and K_{ae} are the cutting coefficients and h is the chip thickness. Its expression is given below.

$$h(\phi_j) = [c \sin \phi_j] g(\phi_j)$$

Equation 3.2

where ϕ_j is the instantaneous immersion angle of the jth tooth measured from the Y-direction at a specific height z

$$\phi_j(\phi, z) = \phi + (j-1) \times \frac{2\pi}{N} - \frac{2\tan\beta}{D} \times z$$

Equation 3.3

N is the number of flutes, β is the helix angle, D is the tool diameter, c is the feed rate per tooth and $g(\phi_j)$ is a unit step function which determines whether the cutter is within the cutting area.

$$\left.\begin{array}{r} g(\phi_j) = 1 \leftarrow \phi_{st} < \phi_j < \phi_{ex} \\ g(\phi_j) = 0 \leftarrow \phi_j < \phi_{st}\ or\ \phi_j > \phi_{ex} \end{array}\right\}$$

Equation 3.4

where ϕ_{st} and ϕ_{ex} are the start and exit angles for each tooth. For upmilling, these angles are

$$\begin{cases} \phi_{st} = 0 \\ \phi_{ex} = \cos^{-1}\left(\dfrac{D-2b}{D}\right) \end{cases}$$

Equation 3.5

For downmilling, these angles are

$$\begin{cases} \phi_{st} = \pi - \cos^{-1}\left(\dfrac{D-2b}{D}\right) \\ \phi_{ex} = \pi \end{cases}$$

Equation 3.6

Converting these forces to Cartesian coordinates, the cutting forces contributed by the jth tooth for each disc are as identified below.

$$\begin{cases} dF_{xj}(\phi,z) = -dF_{tj}(\phi,z)\cos\phi_j - dF_{rj}(\phi,z) \\ dF_{yj}(\phi,z) = +dF_{tj}(\phi,z)\sin\phi_j - dF_{rj}(\phi,z)\cos\phi_j \\ dF_{zj}(\phi,z) = -dF_{aj}(\phi,z) \end{cases}$$

Equation 3.7

The total milling forces acting on the milling tool are therefore a summation of all cutting forces contributed by all cutting flutes all along the axial depth of cut,

$$\begin{cases} F_x = \displaystyle\sum_{j=1}^{N-1}\left(\int_0^a g(\phi_j)dF_{xj}\right) \\ F_y = \displaystyle\sum_{j=1}^{N-1}\left(\int_0^a g(\phi_j)dF_{yj}\right) \\ F_z = \displaystyle\sum_{j=1}^{N-1}\left(\int_0^a g(\phi_j)dF_{zj}\right) \end{cases}$$

Equation 3.8

3.2.2 Workpiece material

3.2.2.1 Machinability of Al6082-T6

In this particular research, especially for simulation analysis, the workpiece material of choice is Aluminium 6082-T6 (Al6082-T6). It is a medium-strength alloy belonging to the 6000 series, widely regarded for its exceptional machinability, desirable mechanical properties, and strong resistance to corrosion [92], [93]. The "T6" designation refers to the tempering process, wherein the alloy is solution heat-treated and artificially aged to maximise its strength [94]. These attributes make it particularly well-suited for use in industries such as aerospace, automotive, and structural engineering, where lightweight and corrosion-resistant materials are critical [95], [96].

The alloy is notable for its excellent machinability, often rated at 70-80% when compared to free-machining brass, which is considered the benchmark for 100% machinability [97], [98]. Its relatively low hardness (approximately 95 HB) and soft characteristics enable high cutting speeds, low cutting forces, and extended tool lifespan, making it more favourable than harder materials such as titanium or stainless steel [99], [100]. This combination of properties makes Aluminium 6082-T6 an ideal material for research, prototyping, and production settings where efficiency is paramount. Furthermore, its high strength-to-weight ratio and outstanding corrosion resistance render it ideal for lightweight structural components [93], [96]. Its excellent thermal conductivity (around 180 W/m·°C) facilitates efficient heat dissipation during machining, which reduces tool wear and improves the quality of the surface finish [101]. These features are especially important in precision machining to ensure dimensional accuracy [102]. In addition to its performance characteristics, Aluminium 6082-T6 is readily available and significantly more cost-effective than materials like titanium Ti6Al-4V or stainless steel, making it a practical option for experimental and industrial machining processes [94], [96]. Its affordability also allows manufacturers and researchers to refine processes efficiently before transitioning to higher-cost materials [95], [103].

The alloy's moderate ductility and machinability allow thin-walled structures to be machined with minimal risk of deformation or chatter, which is critical for achieving precise dimensional tolerances [97], [104]. This makes it particularly advantageous for applications in the aerospace and automotive sectors [96]. Moreover, Aluminium 6082-T6 is compatible with standard machining tools, such as high-speed steel (HSS) and carbide tools, and works effectively with coatings like titanium nitride (TiN) [99], [105]. These tools perform well at higher cutting speeds and feed rates, thus reducing overall machining time [97], [99]. Unlike stainless steel, Aluminium 6082-T6 is less prone to work hardening, which ensures consistent machining outcomes [100].

By contrast, titanium Ti6Al-4V is a high-strength alloy designed for extreme environments requiring superior strength, resistance to corrosion, and excellent heat tolerance [106], [107]. However, its machinability is far lower than that of Aluminium 6082-T6, with a rating of only 20-30% [104], [108]. Titanium's high hardness (350-400 HB) and poor thermal conductivity contribute to accelerated tool wear, slower cutting speeds, and greater energy consumption during machining [107]. While titanium is essential for demanding applications such as aerospace and medical implants, Aluminium 6082-T6 is often a better choice in less extreme conditions due to its ease of machining and cost-effectiveness [103].

Similarly, stainless steels like 304 and 316 exhibit impressive corrosion resistance and higher mechanical strength compared to aluminium alloys [109]. However, their significantly greater density (~8 g/cm^3 versus ~2.7 g/cm^3 for aluminium) makes them unsuitable for applications where weight reduction is critical [110], [111]. Stainless steel also tends to work-harden during machining, reducing its machinability, which is typically rated at around 40-50% [104]. Despite its strength and durability, stainless steel is best suited for high-load or corrosive environments such as marine and chemical industries [112]. In contrast, Aluminium 6082-T6 offers a superior balance between machinability and performance for applications where lightweight and moderate strength are required [110].

A summative table of mechanical properties of Al6082-T6 is given in Table 3.1, comparing it to Ti 6Al-4V and stainless steel (grade 304). In conclusion, aluminium 6082-T6 is a highly suitable choice for this research, owing to its outstanding machinability, excellent thermal conductivity, and cost-effectiveness. Aluminium 6082-T6 allows for efficient experimental investigations and offers a reliable foundation for the development of machining strategies that can be adapted to more challenging materials. Its versatility ensures that the findings of this research retain relevance across a broad spectrum of industrial applications.

	Material		
Property	**Aluminium (6082-T6)**	**Titanium (Ti 6Al-4V)**	**Stainless steel – Grade 304**
Density (g/cm^3)	2.70	4.43	8.00
Tensile yield strength (MPa)	310	880	215
Tensile ultimate strength (MPa)	340	950	505
Young's modulus (GPa)	70	113.8	200
Elongation at break (%)	12	14	40
Poisson's ratio (-)	0.33	0.342	0.27
Shear strength (MPa)	200	550	310
Shear modulus (GPa)	26	44	77
Specific heat (J/kg/°C)	900	526.3	500
Thermal conductivity (W/m/°C)	180	6.7	16
Coefficient of linear thermal expansion (µ°C^{-1})	24	8.6	17
Melting temperature (°C)	555	1660	1450

Table 3.1 Mechanical properties of aluminium 6082-T6, titanium Ti 6Al-4V, and stainless steel [93], [94], [99], [104], [109], [110], [113], [114].

3.2.2.2 Cutting force coefficients

The mechanistic force model applied in this study (Equation 3.1) operates under the assumption that cutting forces are directly proportional to the uncut chip thickness. However, this assumption does not hold true in all milling scenarios, necessitating the adoption of non-linear models for a more accurate representation of the process [115], [116], [117], [118]. To evaluate the validity of the linearity assumption, Altintas proposed a method in [24] where average forces are correlated linearly with the feed per tooth, allowing cutting force coefficients to be determined from the slopes of the resulting lines.

A round of trials was carried out for one 2-flute tool of 20mm of diameter and helix angle of 25° to determine cutting force coefficients for peripheral milling scenarios. The trials were carried out at a singular spindle speed of 7000rpm, for an axial depth of cut of 10mm, and a radial depth of cut of 2mm, and at feed-per-tooth values of 0.05, 0.1, 0.15 and 0.2 mm/tooth. Radial and tangential cutting force coefficients are given in Table **3.2**.

Spindle speed (rpm)	Cutting speed (m/min)	K_{tc} (N/mm²)	K_{rc} (N/mm²)	K_{ac} (N/mm²)	K_{te} (N/mm)	K_{re} (N/mm)	K_{ae} (N/mm)
7000	439.82	1168.00	632.00	/	0.75	0.27	/

Table 3.2 **Cutting force coefficients for a two-flute tool of 25° of helix angle.**

Following this, one 3-flute tool of 12mm of diameter and helix angle of 35° was employed to determine the cutting force coefficients for face milling scenarios. The entire procedure was carried out at spindle speeds of 1300, 2300, 3300 and 4300rpm to investigate any variation due to cutting speed. For every spindle speed, a group of full-slotting trials at 2mm of axial of depth of cut was performed at similar feed-per-tooth values as the previous trials. The minimum cutting speed recorded was therefore of 49 m/min and the maximum speed was of 162 m/min. Table **3.3** summarises the results obtained from these experimental trials.

Spindle speed (rpm)	Cutting speed (m/min)	K_{tc} (N/mm²)	K_{rc} (N/mm²)	K_{ac} (N/mm²)	K_{te} (N/mm)	K_{re} (N/mm)	K_{ae} (N/mm)
1300	49.01	834.00	103.67	136.24	21.78	29.80	1.06
2300	86.71	832.67	514.80	125.09	22.62	38.85	-0.58
3300	124.71	993.07	281.37	138.86	61.23	21.89	-0.11
4300	162.11	773.87	294.88	133.19	47.88	24.77	-0.11

Table 3.3 **Cutting force coefficients for a three-flute tool of 35° helix angle.**

Subsequently, Figure 3.3 shows the relationship between the average forces for the 3-flute tool and the feed per tooth at 1300rpm. There is a clear proportionality between the average forces and the feed per tooth values in all directions. Hence, the assumption of a linear-force model with this metal is acceptable.

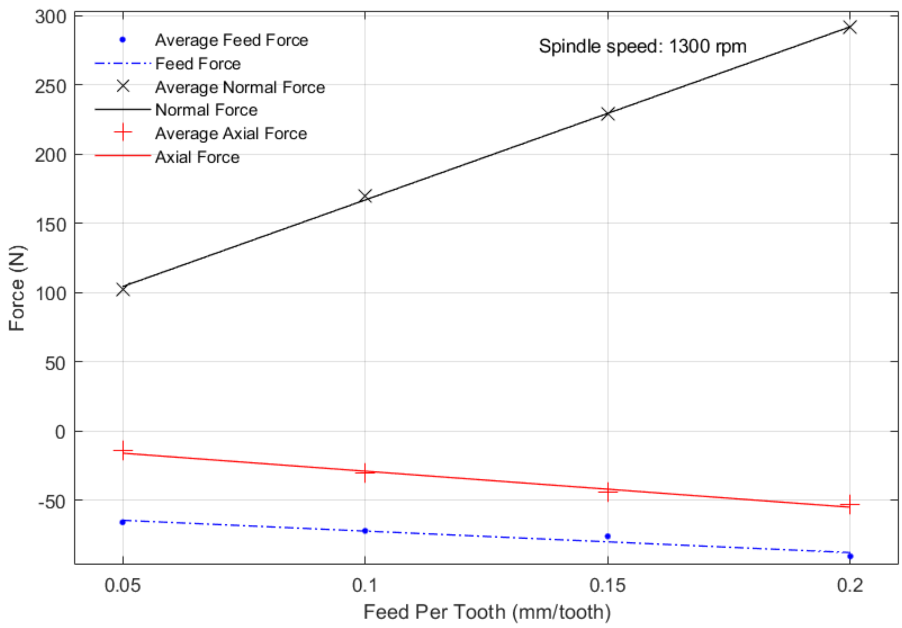

Figure 3.3 Experimental results showing the proportionality between the feed-per-tooth and the average cutting forces for a three-flute tool with 35° helix angle, at 1300rpm.

Similar patterns are observed at all other spindle speeds (2300rpm, 3300rpm and 4300rpm), as shown in Appendix A.1.

3.2.2.3 Static stiffness

The main workpiece of choice in this investigation was a T-profile from Aluminium 6082-T6, of which the length, thickness, and height were 250mm, 9.5mm and 101.6mm respectively, as shown in Figure 3.4.

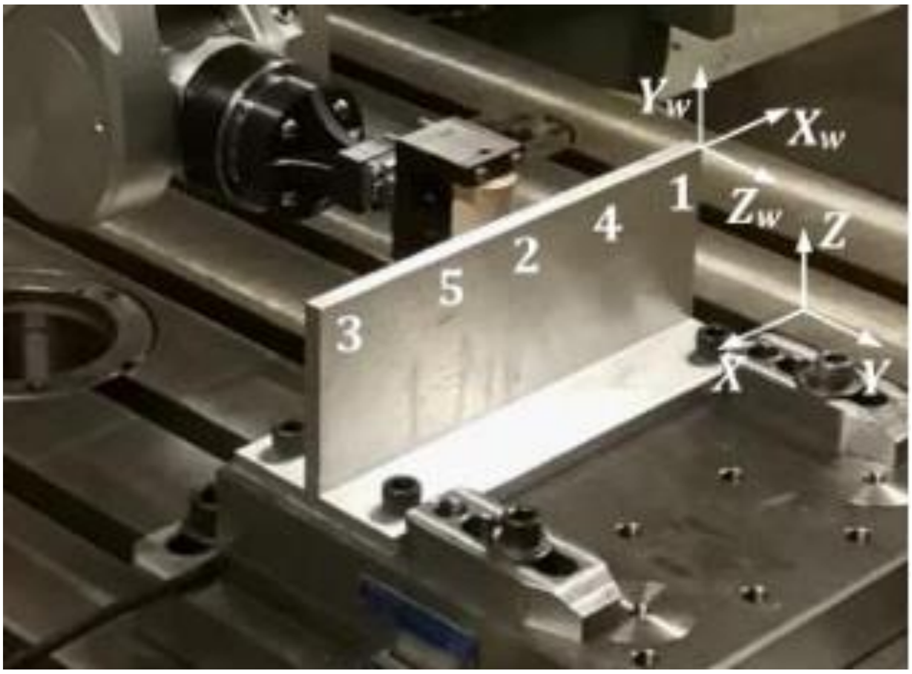

Figure 3.4 T-shaped workpiece from Aluminium 6082-T6 [76]**.**

Static stiffness values of the workpiece were measured using laser displacement sensor and load cell attached to a Staubli TX-90 robotic arm. The robot applied specific force values on one face of the workpiece, namely 25N, 50N, 100N and 200N, and the laser displacement sensor recorded the static deflection at the backface of the workpiece. The probing locations were at 57.5mm increments between -10mm and -240mm along the workpiece coordinate Xw. These points were 6mm below the top face of the workpiece (Yw=-6mm). Static stiffness values were obtained by obtaining slope values across force-deflection measurements at each probing location.

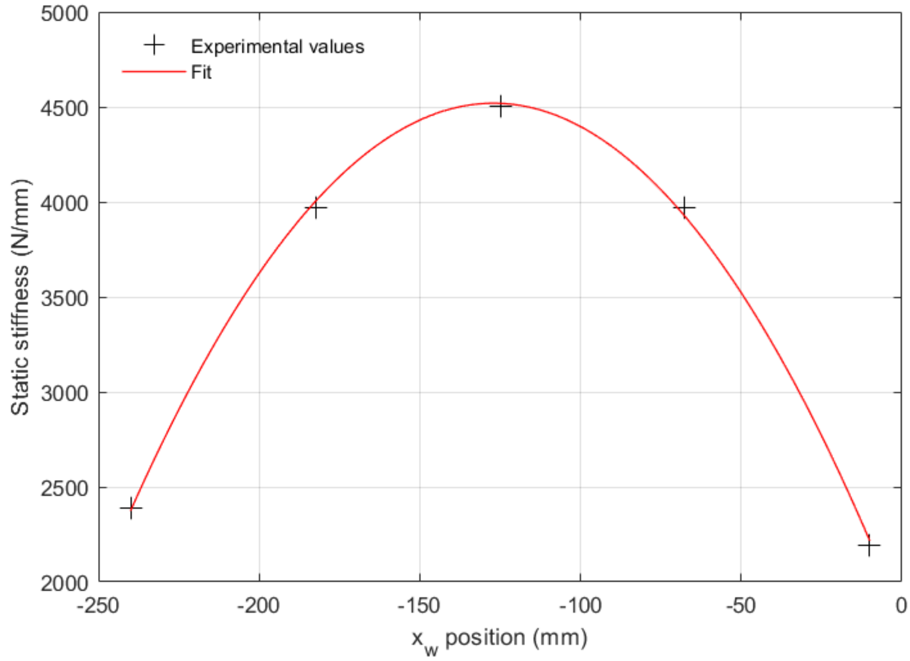

Figure 3.5 Static stiffness measured along the workpiece x-axis.

The values are plotted in Figure 3.5; a parabolic fit was made on this set of values. This fit is later used for simulation work.

3.2.3 Case studies & milling tool choice

Throughout the entirety of the simulation trials, two case studies were investigated, depending on the position of the tool relative to the workpiece: peripheral milling and face milling. Machining conditions are given in the following sections.

3.2.3.1 Peripheral milling

The first case scenario is peripheral milling, where the tool's axis of rotation is parallel to the surface of the machine workpiece. This is shown in Figure 3.6. There are two forces acting on the workpiece: F_c and F_s. They represent the cutting force and support force exerted by the robotic arm on the workpiece respectively. To prevent contact loss with the robotic end effector, F_c needs to be in the negative y-direction. Therefore the cutting force acting on the tool (opposing that acting on the workpiece) needs to be exerted in the positive y-direction.

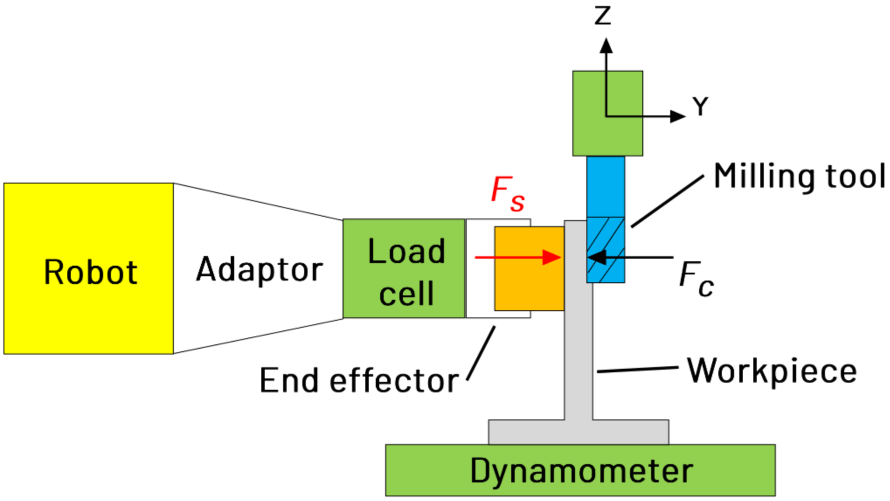

Figure 3.6 Setup of robotic assisted machining in peripheral milling trials.

The chosen cutting conditions are highlighted in Table 3.4.

Cutting parameters	Value
Tool geometry	Straight end
Milling operation	Down milling
No. of milling flutes (N)	2
Tool helix angle (β)	25°
Tool diameter (D)	20 mm
Feed rate per tooth (c)	0.107 mm/rev/flute
Spindle speed (n)	7000 rpm
Axial depth of cut (a)	10 mm
Radial depth of cut (b)	2 mm
Workpiece material	Aluminium 6082-T6
Tangential cutting coefficient (K_{tc})	1168 N.mm^{-2}
Radial cutting coefficient (K_{rc})	632 N.mm^{-2}
Tangential edge cutting coefficient (K_{te})	0.75 N.mm^{-1}
Radial edge cutting coefficient (K_{re})	0.27 N.mm^{-1}

Table 3.4 Peripheral milling simulation parameters.

The code given in Appendix B.1 was used to simulate the cutting forces acting on the tool in the x- and y- directions given the cutting conditions in Table 3.4; they are shown in Figure 3.7.

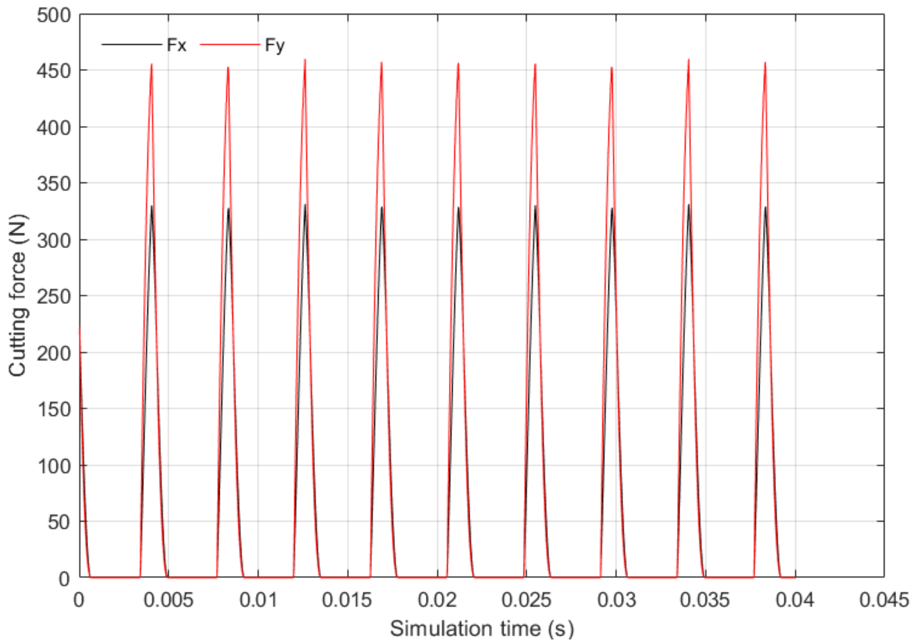

Figure 3.7 Simulation results showing the cutting forces of a 2-flute tool with 25° helix angle, 2mm of radial depth of cut and 10mm of axial depth of cut, at a spindle speed of 7000rpm.

As shown in Figure 3.7, the cutting forces acting on the tool in the y-direction are positive. This satisfies the condition for there not to be any contact loss between the cobot and workpiece.

3.2.3.2 Face milling

The second case scenario is face milling, where the tool's axis of rotation is perpendicular to the surface of the machine workpiece. This is shown in Figure 3.6. Two forces, F_c and F_s are acting on the workpiece. To prevent contact loss with the robotic end effector, F_c needs to be in the negative z-direction. Therefore the cutting force acting on the tool (that opposes the force acting on the workpiece) needs to be exerted in the positive z-direction.

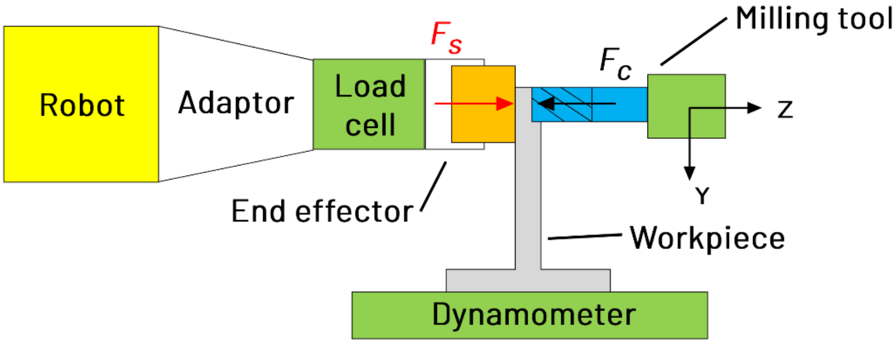

Figure 3.8 Setup of robotic assisted machining in face milling trials.

The chosen cutting conditions are highlighted in Table 3.5.

Cutting parameters	Value
Tool geometry	Straight end
Milling type	Slotting
No. of milling flutes (N)	3
Tool helix angle (β)	35˚
Tool diameter (D)	12 mm
Feed rate per tooth (c)	0.2 mm/rev/flute
Spindle speed (n)	4300 rpm
Axial depth of cut (a)	2 mm
Radial depth of cut (b)	12 mm
Workpiece material	Aluminium 6082-T6
Tangential cutting coefficient (K_{tc})	773.87 $N.mm^{-2}$
Radial cutting coefficient (K_{rc})	294.88 $N.mm^{-2}$
Axial cutting coefficient (K_{ac})	133.19 $N.mm^{-2}$
Tangential edge cutting coefficient (K_{te})	47.88 $N.mm^{-1}$
Radial edge cutting coefficient (K_{re})	24.77 $N.mm^{-1}$
Axial edge cutting coefficient (K_{ae})	-0.11 $N.mm^{-1}$

Table 3.5 Face milling simulation parameters.

Based on the cutting parameters in Table 3.5, the cutting forces acting on the tool are simulated on MATLAB via the code in Appendix B.1 and plotted in Figure 3.9.

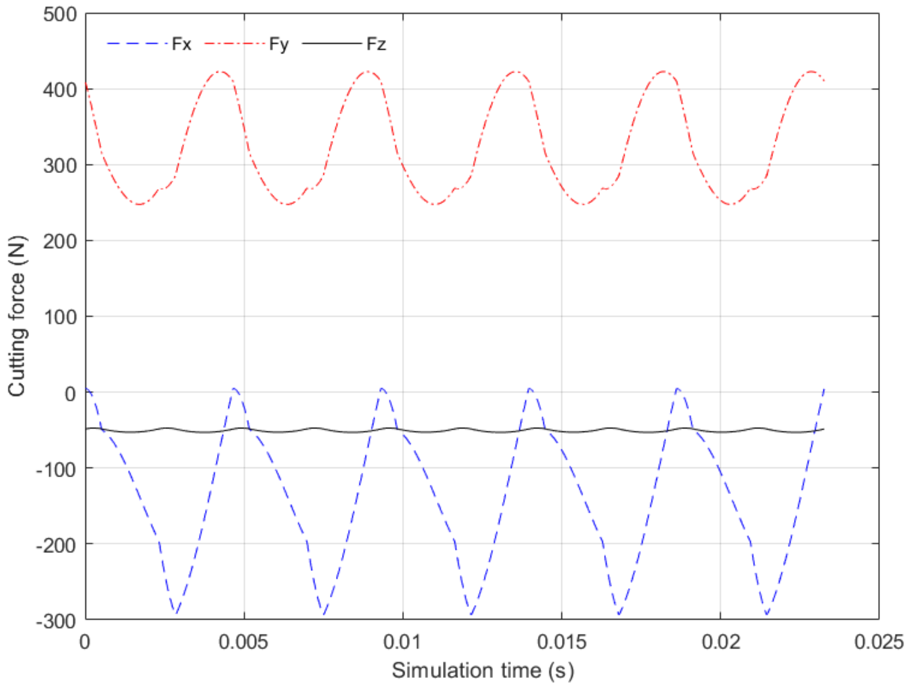

Figure 3.9 Simulation results showing the cutting forces of the slotting of a 3-flute tool with 35° helix angle and 2mm of axial depth of cut, at a spindle speed of 4300rpm.

As shown in Figure 3.9, the cutting forces acting on the tool in the z-direction are negative. This would result in the cutting tool pulling the workpiece away from the STAUBLI robot. It is therefore important to find an alternative to the current tool to maintain contact between the robot and workpiece.

An investigation by Ozturk et al showed that the sign of the helix angle affects the axial cutting forces [90]. Throughout their study, five tools with different helix angles were tested and the cutting force coefficients are plotted in Figure 3.10.

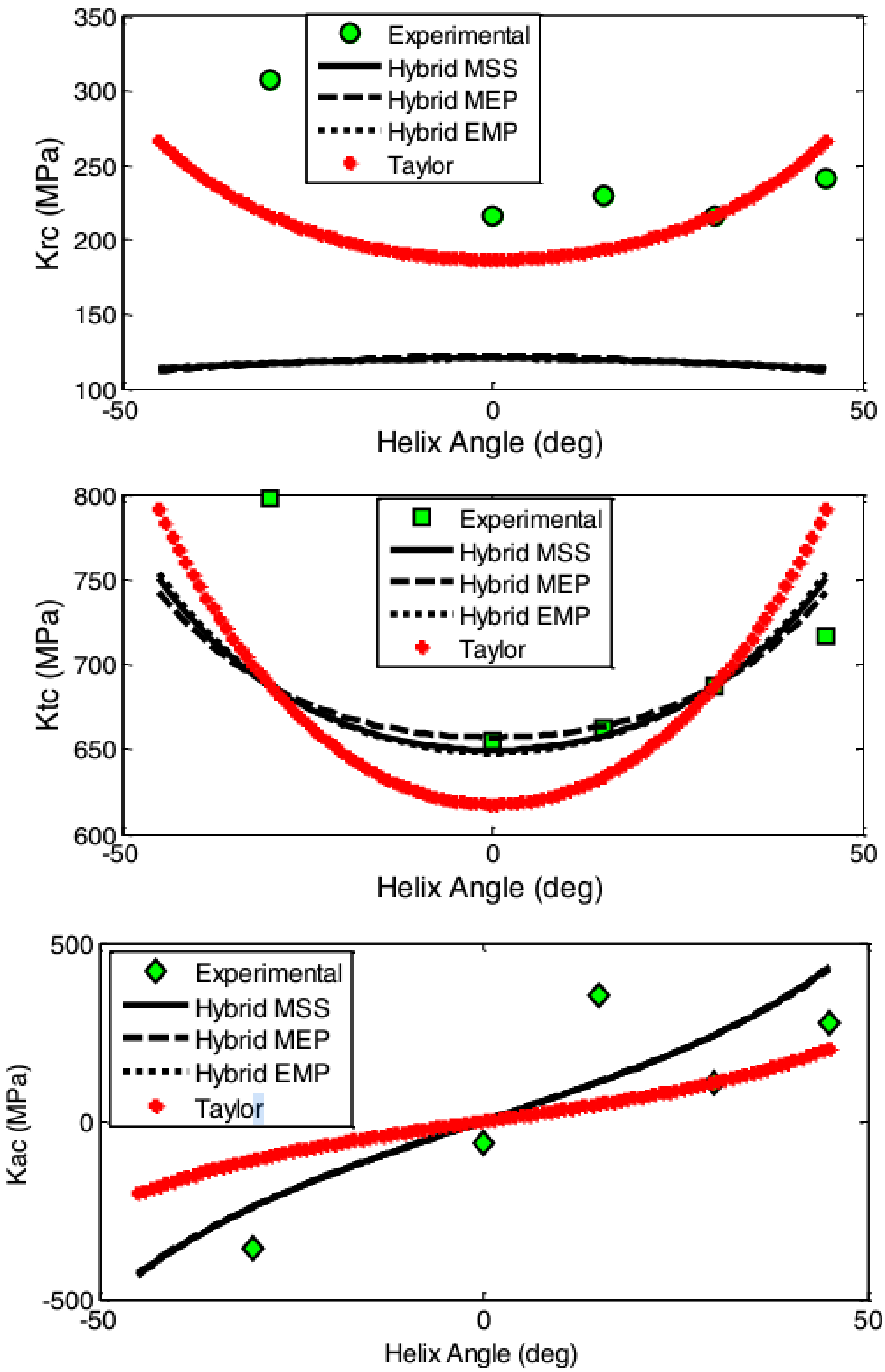

Figure 3.10 Experimental results showing the relationship between cutting coefficients and helix angle [90]**.**

According to Figure 3.10, the third graph shows that the sign of the helix angle affects the sign of K_{ac}. Looking at equations Equation 3.1, Equation 3.7 and Equation 3.8, cutting forces F_z are directly proportional to the axial cutting coefficient K_{ac}; therefore a negative helix angle would influence the sign of the z-forces. This has been integrated in the MATLAB code by multiplying the differential dFa by $sign(helix)$ on line 104 in Appendix B.1, to take into account the sign of the helix angle.

Upon changing the sign of the helix angle in simulation environment (from 35° to -35°), the cutting forces were obtained and plotted in Figure 3.11.

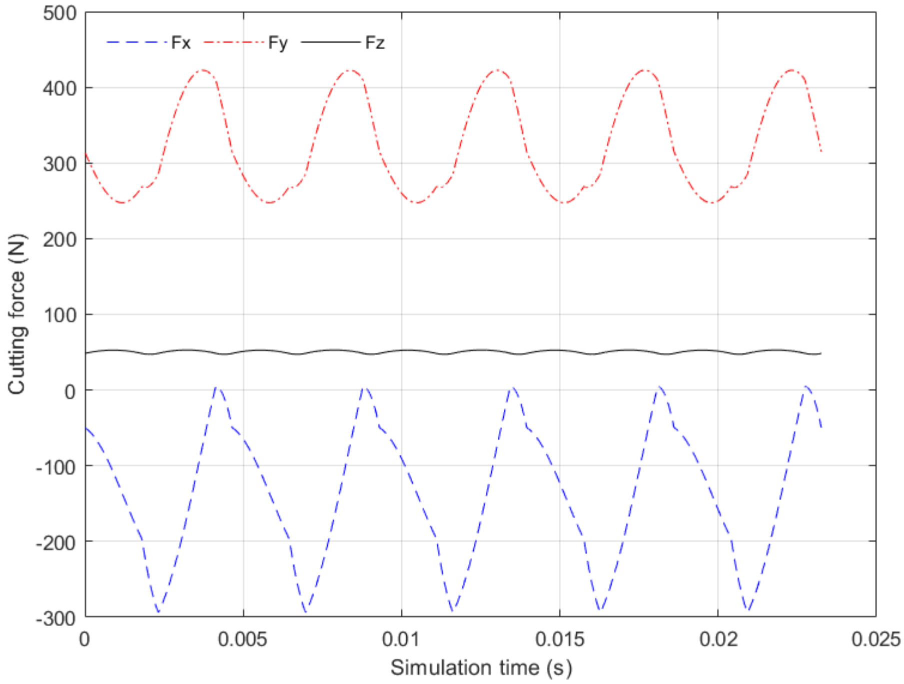

Figure 3.11 Simulation results showing the cutting forces of the slotting of a 3-flute tool with -35° helix angle and 2mm of axial depth of cut, at a spindle speed of 4300rpm.

As shown in Figure 3.11, the sign of the cutting forces in the z-direction has changed from negative to positive (when compared to Figure 3.9). This results in the cutting tool pushing the workpiece towards the robot, therefore preventing contact loss between the robot and workpiece. For this reason, for the rest of the simulation work in face milling, the tool helix angle has been changed to a negative angle of -35°.

3.3 Form errors in robotic assisted thin-wall milling

In section 3.2.1 the mechanistic cutting force model was presented to formulate cutting forces acting upon the tool in milling operations. As the aim of this investigation is to minimise surface location errors (SLEs) in milling, it is important to determine these errors analytically, in robotic assisted milling.

In traditional milling processes, with no robotic support, form error prediction models have been developed in both time domain [119], [120] and frequency domain [121]. However, these models did not involve a mobile fixture. Following the concept of robotic assisted milling proposed by Ozturk et al. [11], Sun et al. [76] proposed three different form error prediction models for robotic assisted milling (peripheral milling); however, these models did not involve static deflection from the robotic support. In effect, as shown in Figure 3.12, the support force provided by the robotic arm causes deflection on the workpiece part, hence influencing the form error on the machined surface.

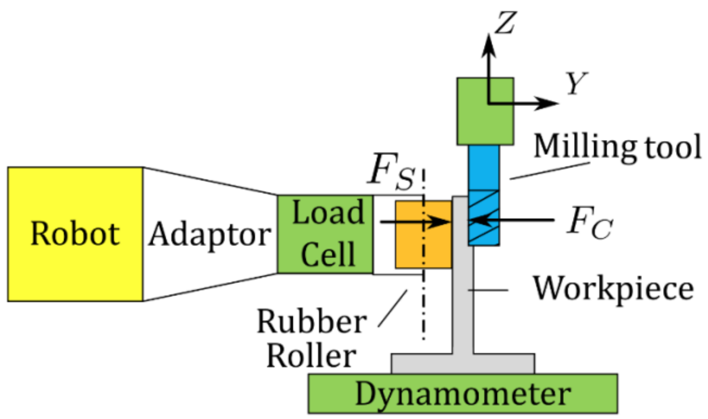

Figure 3.12 Robotic assisted milling setup (peripheral milling) [11].

Furthermore, several past investigations including the integral method published by Altintas [24], have focused on calculating cutting forces and form errors using a constant radial depth of cut and dynamic characteristics of the workpiece [122], [123], [124], [125], [126], [127]. An improved version of the basic constant radial depth of cut (in peripheral milling) involves considering the impact that plastic deformation of the workpiece has on the radial depth of cut when subjected to cutting forces. Recent investigations were carried out to include a time-varying radial depth of cut considering the dynamic deformation of the workpiece [128], [129], [130], [131], [132] and the static parameters of the workpiece [133], [134], [135], [136], [137].

In this section, in formulating surface form errors, the value of the time-varying depth of cut is determined considering the static stiffness of the part. In thin-walled milling, the cutter is considered a rigid body and the workpiece an elastic body, with only its static stiffness considered, hence the process illustrated in Figure 3.13, for an unsupported workpiece in peripheral milling.

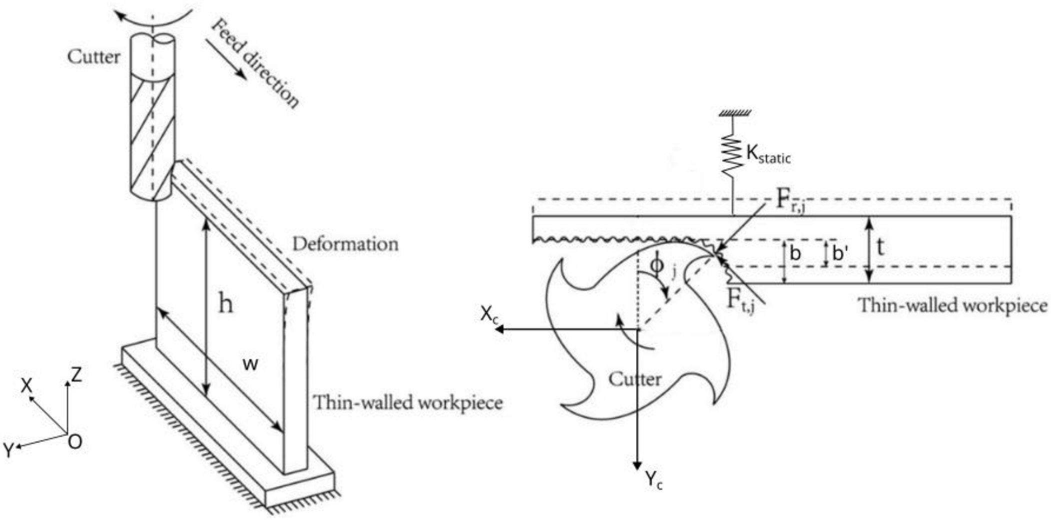

Figure 3.13 Revised milling force model in peripheral milling.

In Figure 3.13 the thin-walled part is deformed only in the Y-direction. In an undeformed scenario, the figure highlights the workpiece by solid lines, with a radial depth of cut b. When deformed, the part is outlined by dotted lines and the effective radial depth of cut is now b'. Deformation in other axes is not considered. The deformation in the Y-direction caused by forces acting upon the workpiece results in a variation of the radial depth of cut, further affecting the milling forces.

To simplify the formulation, only steady cutting processes are considered where the workpiece maintains a stable periodic forced vibration [129].

When the process is stable, there is relationship between the time-varying radial depth of cut b', the deformation of the workpiece δb and the milling force F_c.

$$b' = b_0 + \delta b$$

Equation 3.9

where b_0 is the nominal radial depth of cut.

For a supported workpiece, the deformation of the workpiece is proportional to the total force exerted on the workpiece. This total force is obtained as a difference between the cutting force F_c acting on the workpiece and F_s exerted by the robot on the workpiece. δb is calculated by the equation below

$$\delta b = \frac{F_s - F_c}{k_s}$$

Equation 3.10

where k_s is the static stiffness of the workpiece; this value changes along the workpiece as shown in experimental measurements from Figure 3.5.

In peripheral milling, the change in radial depth of cut affects the start and exit angles of cut by substituting b' into Equation 3.5 and Equation 3.6. The cutting forces F_c are calculated from Equation 3.8 for straight end mills.

In face milling, the axial depth of cut is affected by the deflection of the tool as shown below.

$$a' = a_0 + \delta a$$

Equation 3.11

where a_0 is the nominal radial depth of cut and δa is the static deformation of the workpiece. It is expressed as

$$\delta a = \frac{F_s - F_c}{k_s}$$

Equation 3.12

The resulting cutting forces are calculated and updated by substituting a' in Equation 3.8 for straight end mills.

In summary, surface location errors are calculated as the opposite of these deformations, i.e. if the cutting force is greater than the support force in face milling ($\delta a < 0$), undercut will be observed, characterised by a positive SLE value; the following equation therefore highlights the defining relationship between the cutting and support forces acting on the workpiece

$$SLE = -\delta a = \frac{F_c - F_s}{k_s}$$

Equation 3.13

The block diagram below shows the relationship between the form error (SLE), the cutting forces (F_c) and the support forces (F_s).

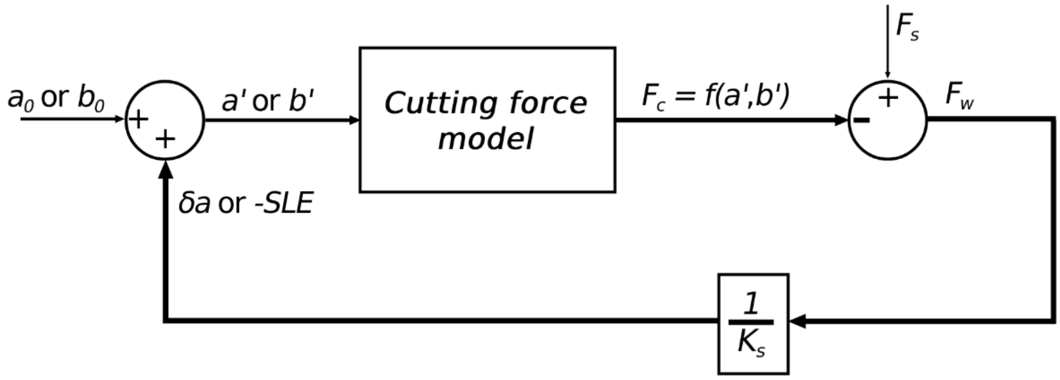

Figure 3.14 Block diagram of calculation of surface location errors.

According to the block diagram, the form errors are calculated at every time sample; so is the time-varying depth of cut. In the next section, control methods are presented to minimise these errors in milling operations.

3.4 Control theory

3.4.1 Objective of control approaches

The objective of the research is to provide approaches that minimise form error values during the milling process of thin-walled parts. In the previous section, form errors are determined analytically through the consideration of time-varying depths of cut during the milling process.

$$SLE = \frac{F_c - F_s}{k_s}$$

Equation 3.14

Based on Equation 3.14, three control approaches are investigated: force control, force minimisation and thickness control. Overall, the form error values are equated to the deformation of the thin-walled part due to both cutting and support forces exerted on the part.

PID (Proportional-integral-derivative) control was used in this research to design the error compensations methods. PID control is one of the most widely used control methods, utilising three control parameters to compensate errors between a measured variable and its target value [138], [139]. It has also been successfully implemented previously to reduce form error values in milling operations [19], [20], [76], [86].

3.4.2 Force control

This control method was first proposed by the author in [19] and implemented in robotic-assisted milling. Its objective is to keep the support force exerted by the cobot at the backface of the workpiece constant. The support force is measured by the load cell attached to the robot's end effector, as shown in Figure 3.15. The use of the robotic arm was shown as advantageous in Figure 2.3, however without control of the contact force between cobot and workpiece, this force can grow exceedingly large (see Figure 2.5). The PID force control therefore keeps the force F_s at a target value; its impact will be investigated in the following chapter (see section 4.2.1).

3.4.3 Force minimisation

According to Equation 3.14, the second approach to decrease the form error values incurred during the milling of thin-walled parts aims to decrease the overall force exerted on the system. This force can otherwise be called F_w and obtained as shown below.

$$F_w = F_s - F_c$$

Equation 3.15

A practical way to measure this force is by setting up a table dyno on the machining table of the robotic cell, as shown in Figure 3.15. Unlike the method proposed in section 3.4.2 [19], the table dyno will be used to measure the overall force on the part and a PID controller developed to modify the robotic push distance, that is the static deflection caused by the cobot on the workpiece. In Figure 3.15, the cobot moves in the z-direction. This distance is altered to get F_w as close to a null value as possible. The change in z-coordinate on the collaborative robot will in turn affect the supporting force on the workpiece and, based on the block diagram in Figure 3.15, also influence the cutting forces acting upon the workpiece.

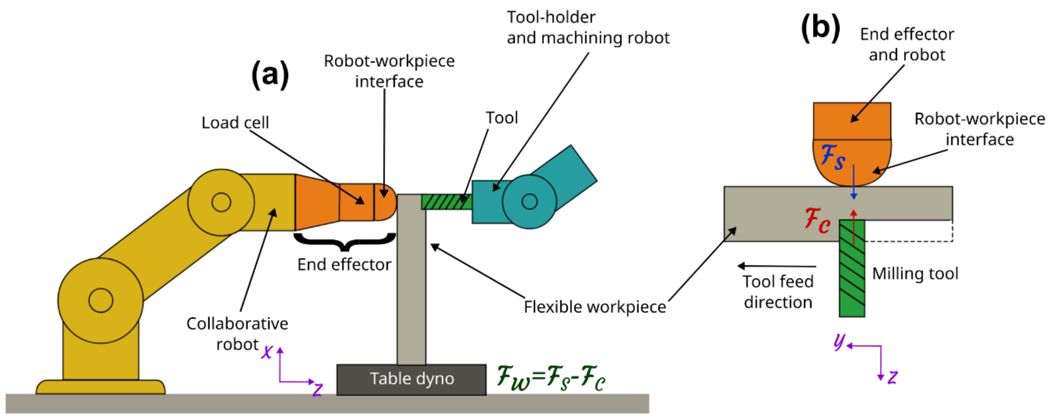

Figure 3.15 Table dyno and load cell on workpiece setup in face milling applications – (a) side view; (b) top view.

The table dyno is used instead of the load cell as the load cell primarily measures the supporting force exerted by the collaborative robot. The load cell is attached to the collaborative robot end effector to ensure that contact is always maintained between the supporting robot and the back face of the workpiece. The table dyno on the other hand is a commonly known device used to measure overall forces acting on a part during milling processes.

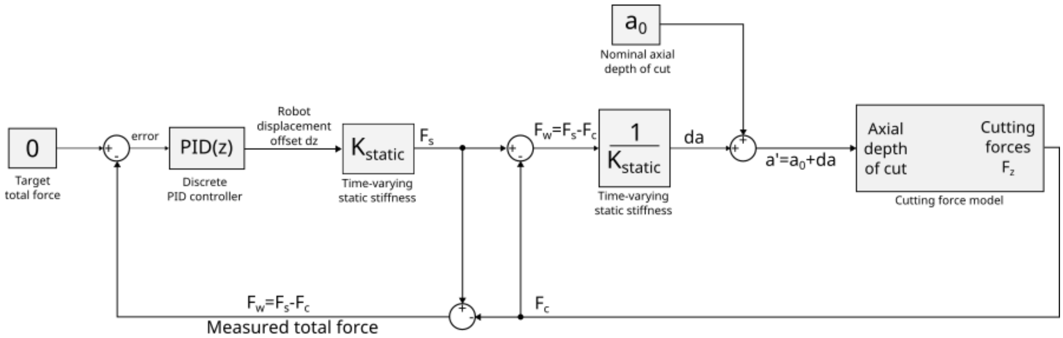

Figure 3.16 Block diagram of PID force minimisation technique.

As shown in the block diagram in Figure 3.16, the objective of the PID force minimisation controller is to keep the overall force F_w on the workpiece at 0 (0 being the set target force). The output of the controller is dz, the distance by which the cobot moves to reach the desired overall force. By multiplying this value (dz) by the local static stiffness on the workpiece, the robotic support force F_s is calculated, and the overall force $F_w = F_s - F_c$ is obtained. According to Equation 3.14, the form error ($-da$) is obtained as a quotient between F_w and the local static stiffness K_{static}, and the time-varying axial depth of cut a' is obtained by adding the SLE to the nominal axial depth of cut a_0. Cutting forces are in turn generated according to section 3.2.1 for that given depth of cut. Errors between the overall force and the target force (0N) are in turn fed in a feedback loop and compensated via PID control.

3.4.4 Thickness control

In theory, one of the drawbacks of the force minimisation approach is the introduction of position errors in dual robot configurations. In effect, the main challenge encountered in robotic milling is the position error incurred in the use of robotic arms. Taking into account the position errors δ_{pe}, the generalised formulation of these form errors is therefore

$$SLE = -\frac{F_s - F_c}{k_{static}} + \delta_{pe} = -\frac{F_w}{k_{static}} + \delta_{pe}$$

Equation 3.16

It is therefore expedient to submit a different form error control approach that enables the error to be accurately measured and minimised. The error is accurately measured by recording the remaining thickness of the workpiece in real-time.

$$SLE = t_{actual} - t_{target}$$

Equation 3.17

An example setup to measure the remaining wall thickness in real-time is a set of laser sensors attached to both milling and supporting robots, as shown in Figure 3.17. As shown in the figure, the distance h_{2a} is the default distance between the source of the beam and the face of the workpiece, with no axial engagement of the tool into the workpiece; this value is known. In cutting conditions, the laser reading will change to h_{2b} depending on the axial depth of cut and cutting force induced errors. Moreover, in order to ensure there is contact between the cobot and the workpiece, the contact force of the robot is measured by the load cell attached to the robot as shown in Figure 3.15; for a successful implementation of the robotic assisted method, the contact force is meant to be non-null.

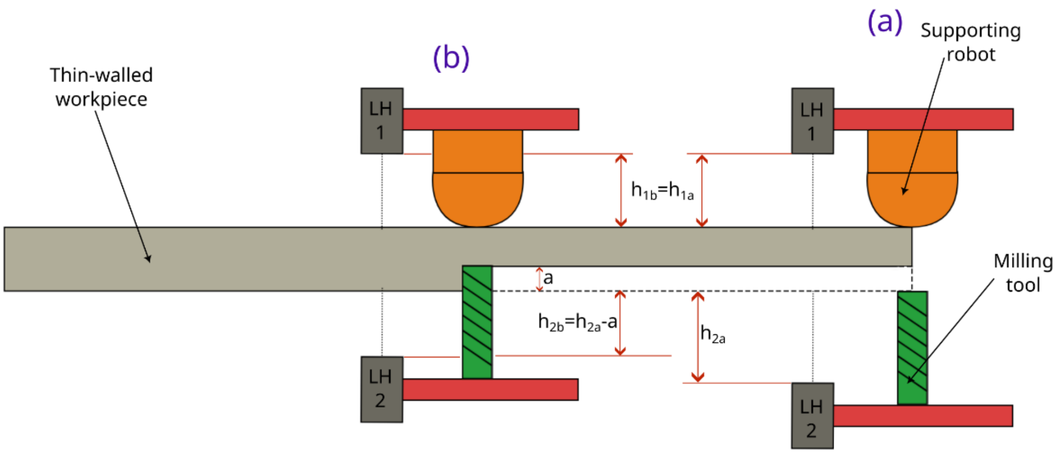

Figure 3.17 Use of laser heads (LH_1 on supporting robot and LH_2 on milling robot) to measure the remaining wall thickness – (a) before machining; (b) after machining.

The value h_{2b} corresponds to the value a' in the block diagram in Figure 3.18. This depth of cut influences the cutting forces acting upon the tool. The remaining thickness is compared to the target wall thickness; the error is then measured and compensated through the PID controller, that generates as output, a robotic push distance dz. This push generates a robotic force applied on the workpiece; the overall force on the workpiece generates a static deflection on the workpiece and affects the axial engagement of the tool into the workpiece.

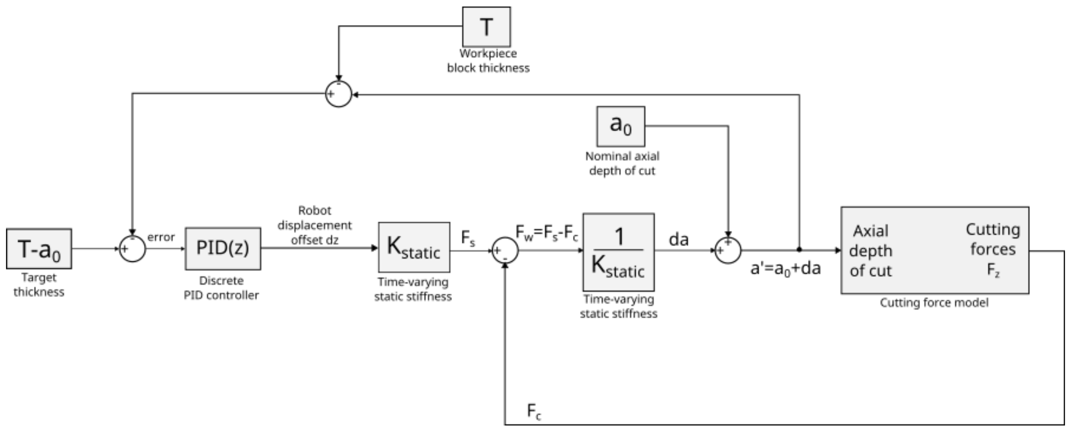

Figure 3.18 Block diagram of PID thickness control.

3.5 Summary

This chapter has established the theoretical framework underpinning the investigation of active form error control in robotic-assisted milling. It introduced the fundamental principles of milling dynamics, including cutting force modelling, material properties of Aluminium 6082-T6, and static stiffness considerations—key factors influencing machining accuracy in thin-walled structures.

Whilst the modelling of cutting forces for both peripheral and face milling operations follows well-established principles, this chapter provided a detailed analysis of how these forces interact with robotic support systems. Particular attention was given to the influence of the helix angle on axial cutting forces, demonstrating that reversing the helix angle's sign significantly affects the force direction. This insight is critical for maintaining continuous contact between the workpiece and the supporting robot during face milling, thereby improving process stability.

In addition, this chapter revisited existing form error prediction models, enhancing their application within the context of robotic-assisted milling. By incorporating the effects of static deflection induced by robotic support forces, the models offer improved accuracy in predicting surface location errors compared to conventional approaches that primarily focus on cutting force-induced deflections [76]. This adjustment ensures a more comprehensive understanding of the factors contributing to form errors in dynamic machining environments.

Furthermore, two innovative form error control methods were introduced:

- Force Minimisation Method (FMM): This method regulates the overall forces acting on the workpiece, aiming to maintain them close to zero to reduce deformation during milling.
- Thickness Control Method (TCM): Inspired by dual-robot mirror milling strategies [20], this approach dynamically adjusts the support robot's position in real time based on wall thickness measurements, ensuring consistent machining accuracy without relying on prior knowledge of workpiece stiffness or robotic position errors.

Both methods represent significant advancements in the field of robotic-assisted milling, with the thickness control method showing particular promise for achieving high accuracy across varying machining conditions.

The theoretical concepts and models presented in this chapter form the foundation for the simulation studies in the next chapter, where their effectiveness will be rigorously evaluated and benchmarked.

Chapter 4

Simulation work

4.1 Introduction

This chapter outlines the simulation work carried out in designing and implementing control approaches with the aim of minimising form error in milling operations. The theoretical framework highlighted in the previous chapter constitutes the platform upon which the simulation model has been designed.

With regards to the cutting forces generated in milling applications, a cutting force model was implemented in both MATLAB and SIMULINK environments. Cutting condition variables were initialised in MATLAB and utilised in SIMULINK environment to obtain cutting force profiles. The code presented in Appendix B was designed to take into account the milling operation (peripheral or face milling).

Simulation tests are run in SIMULINK environment, embedding the surface location error (SLE) model given in section 3.3, to generate form error values. Such tests were carried out for peripheral and face milling scenarios. Form error control techniques are also designed, implemented and their performance assessed.

Simulation results from all form error control methods are provided and compared. Furthermore, position errors were introduced in the model to replicate inaccuracies encountered in robotic milling; these position errors were modelled in the form of disturbances on the axial depth of cut (in face milling scenarios).

4.2 Peripheral milling simulations

The first set of simulations was conducted in peripheral milling conditions, as shown in Figure 3.6. The cutting conditions were first presented in section 3.2.3.1 and given in Table **4.1**.

Cutting parameters	**Value**
Tool geometry	Straight end
Milling operation	Down milling
No. of milling flutes (N)	2
Tool helix angle (β)	25°
Tool diameter (D)	20 mm
Feed rate per tooth (c)	0.107 mm/rev/flute
Spindle speed (n)	7000 rpm
Axial depth of cut (a)	10 mm
Radial depth of cut (b)	2 mm
Workpiece material	Aluminium 6082-T6
Tangential cutting coefficient (K_{tc})	1168 N.mm^{-2}
Radial cutting coefficient (K_{rc})	632 N.mm^{-2}
Tangential edge cutting coefficient (K_{te})	0.75 N.mm^{-1}
Radial edge cutting coefficient (K_{re})	0.27 N.mm^{-1}

Table 4.1 **Peripheral milling simulation parameters.**

Cutting conditions are initialised in MATLAB environment via the code given in Appendix B.2. As shown in Equation 3.12, the form error values are obtained from the overall force exerted on the workpiece and the local static stiffness of the workpiece. Static stiffness values are obtained from the parabolic fit highlighted in

Figure 3.5, and extrapolated to the entire length of the workpiece (from X-250mm to X-0mm) as shown in Figure 4.1.

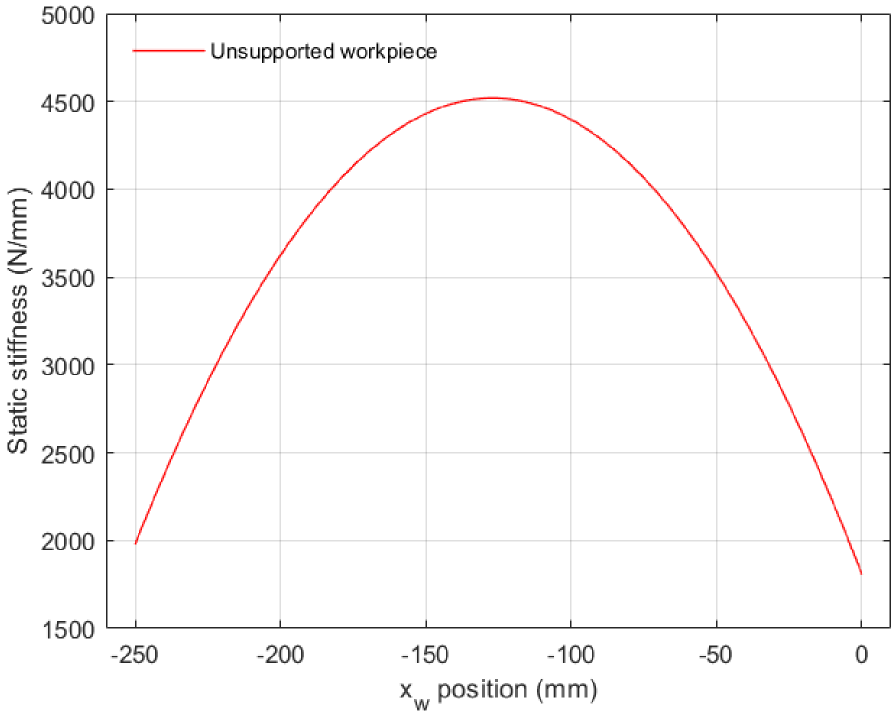

Figure 4.1 Profile of the static stiffness of the workpiece across its length.

In the following sections, cutting forces and form errors are obtained via simulations for the unsupported workpiece (under no loading from the STAUBLI robotic arm). The investigation is continued by analysing the effect of the robotic support force on the resulting form error values obtained via simulation runs, as the force control method is implemented.

4.2.1 Unsupported workpiece

Simulations were run with the cutting conditions highlighted in Table **4.1**, for the unsupported workpiece. Figure 4.2 illustrates the cutting forces exerted upon the tool in the tool Y-axis. As seen, the cutting forces acting on the tool are positive; this is a requirement to ensure that the workpiece is pushed towards the robotic end effector, thereby preventing contact loss between workpiece and robot. In this simulation run, the tool travels the full length of the workpiece, from X-250 mm to X0 mm relative to datum.

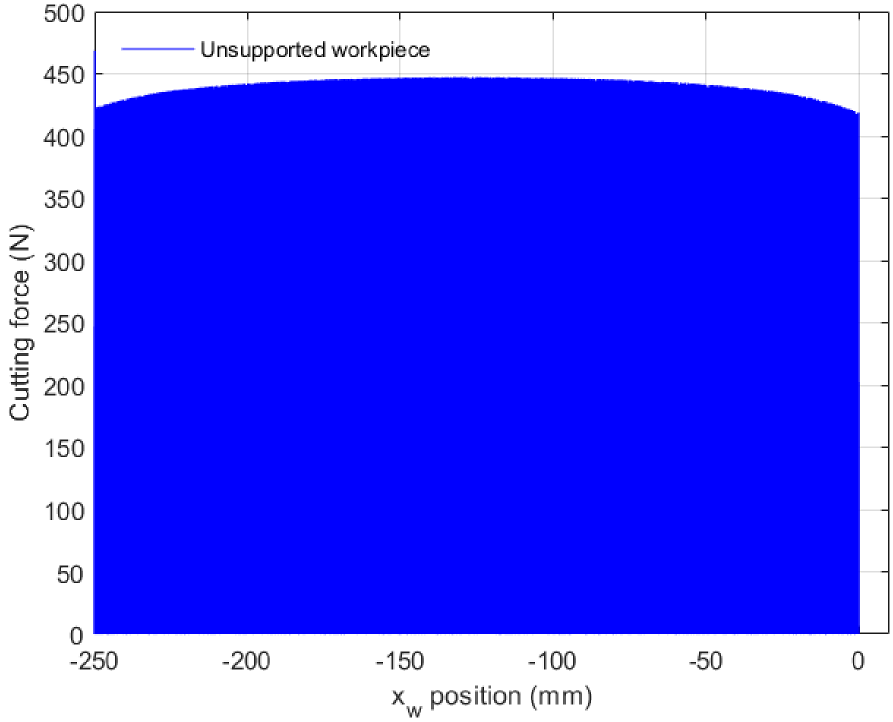

Figure 4.2 Simulated cutting forces acting on the tool in the y-direction in peripheral milling.

As seen in Figure 4.2 the cutting forces have a concave profile. This is due to the parabolic trend of the static stiffness shown in Figure 4.1. At the edges (X-250mm and X0mm), the stiffness values are minimal, resulting in a larger static deflection, hence reducing the peripheral engagement of the tool in the workpiece (as the workpiece deflects away from the tool). The highest force value is recorded halfway across the workpiece, where the static stiffness has the highest value.

This is further investigated by looking at the resulting form error values plotted in Figure 4.3. SLE follows a parabolic profile similar to the static stiffness, with a minimum error of 0.098mm at X=-125mm and a maximum SLE value of 0.231mm at X=0mm; positive form error values signify undercutting.

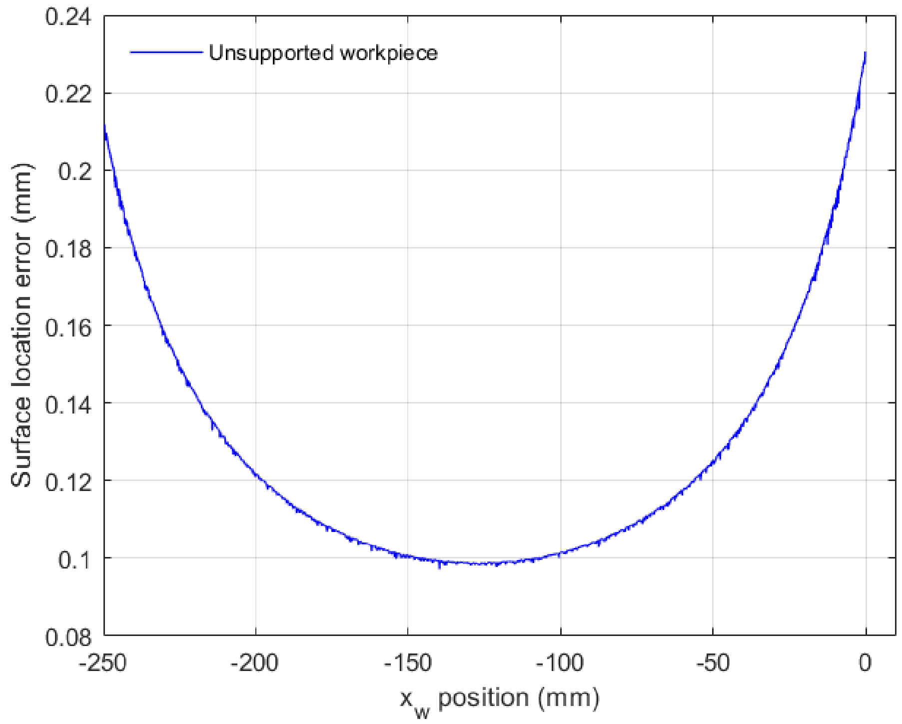

Figure 4.3 Simulated form error values on the unsupported workpiece in peripheral milling.

In the next section, the effect of robotic support force on surface location errors recorded during milling trials is investigated.

4.2.2 Investigation of robotic supporting force on form error values

In this section, the performance of force control method (outlined in section 3.4.2) is investigated in simulation environment. This is done by applying various robotic support force values to the tool-workpiece system, maintaining these force values constant as the tool travels the entire length of the workpiece and analysing the form errors incurred throughout milling operations. Milling trial simulations were run for the following robotic supporting forces: 0N (unsupported), 60N, 120N, 200N and 280N. These runs are conducted with the same static stiffness profile given in Figure 4.1.

Figure 4.4 presents a comparative analysis of the results; for each robotic force, the following variables are compared.

- Robotic push distance: this is the distance by which the cobot moves from its initial position to apply the target support force. In the case with no robotic support, this value is 0.
- Cutting force: this is the cutting force acting upon the tool in the y-direction, according to the diagram shown in Figure 3.6.
- Surface location error: this is the deviation from the target depth of cut in machining trials.

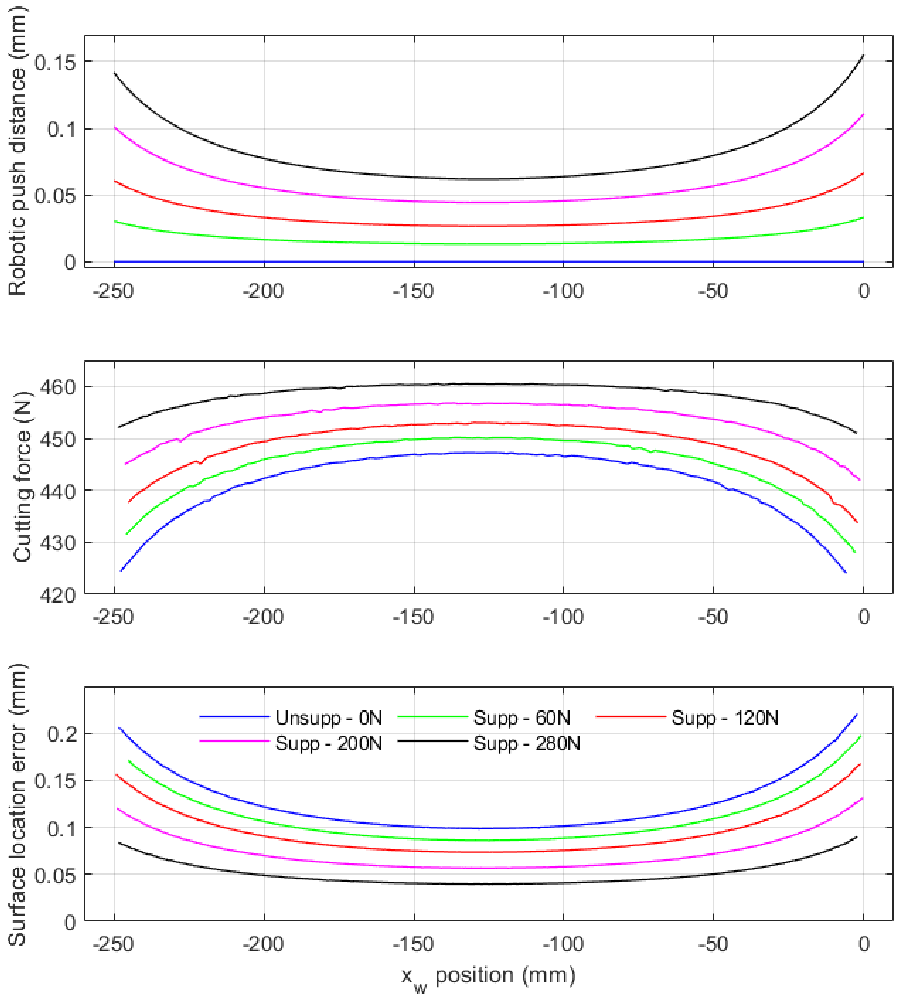

Figure 4.4 Comparative analysis of simulated results across robotic supporting forces of 0-280N: robotic push distance (top), cutting forces on the tool (middle) and form errors (bottom).

As shown in Figure 4.4, the robotic push distance increases as the robotic push force increases, with it following a parabolic profile for all values; due to the low static stiffness at the edges, there is more push needed to maintain the support force constant, while this distance reaches its minimum at the centre of the tool path (where the static stiffness is at its maximum). At 280N of robotic support force, this push varies between 0.062mm and 0.155mm. This results in an increase in cutting force, as shown in the middle graph due to the increase in radial engagement as the robot pushes the workpiece towards the tool. The change in force is however very small, with the maximum cutting force varying from 447N (unsupported) to 460N (with 280N support force), about 3% increase. That being said, the robotic push yields promising results in reduction in form error. With a robotic support force of 280N, there is an average decrease in SLE of 0.071mm, corresponding to nearly a 60% decrease. This indicates that a higher support force leads to a decrease in form error incurred during machining trials. It is also important to note that, as the robotic force increases, there is a steady change in curvature on the form error profile. Extending the simulations to higher forces is therefore necessary, to investigate the impact on the form errors.

Simulations are extended to additional support forces of 450N and 600N. Findings related to robotic push distance, cutting force and form error are summarised in Figure 4.5 for the following support forces: 0N (unsupported), 120N, 280N, 450N and 600N.

As seen in Figure 4.5, with a further increase in robotic support force, the robotic push effort also increases. It is interesting to note a change of curvature in both cutting forces and surface location errors. With regards to cutting forces, only an 8% increase in value is recorded at 600N of robotic push. However, at around 450N of support force, the force profile flattens and changes curvature beyond that (especially at 600N). At this specific force value (450N), the form errors are nearly null. This is because the overall force on the workpiece is almost zero, as the robotic push force approaches the average cutting forces on the workpiece (around 468N for that scenario). Beyond 450N however, overcutting is experienced, as the support force (600N) overpowers the cutting forces (478N). This results in the workpiece being pushed beyond its neutral axis towards the tool.

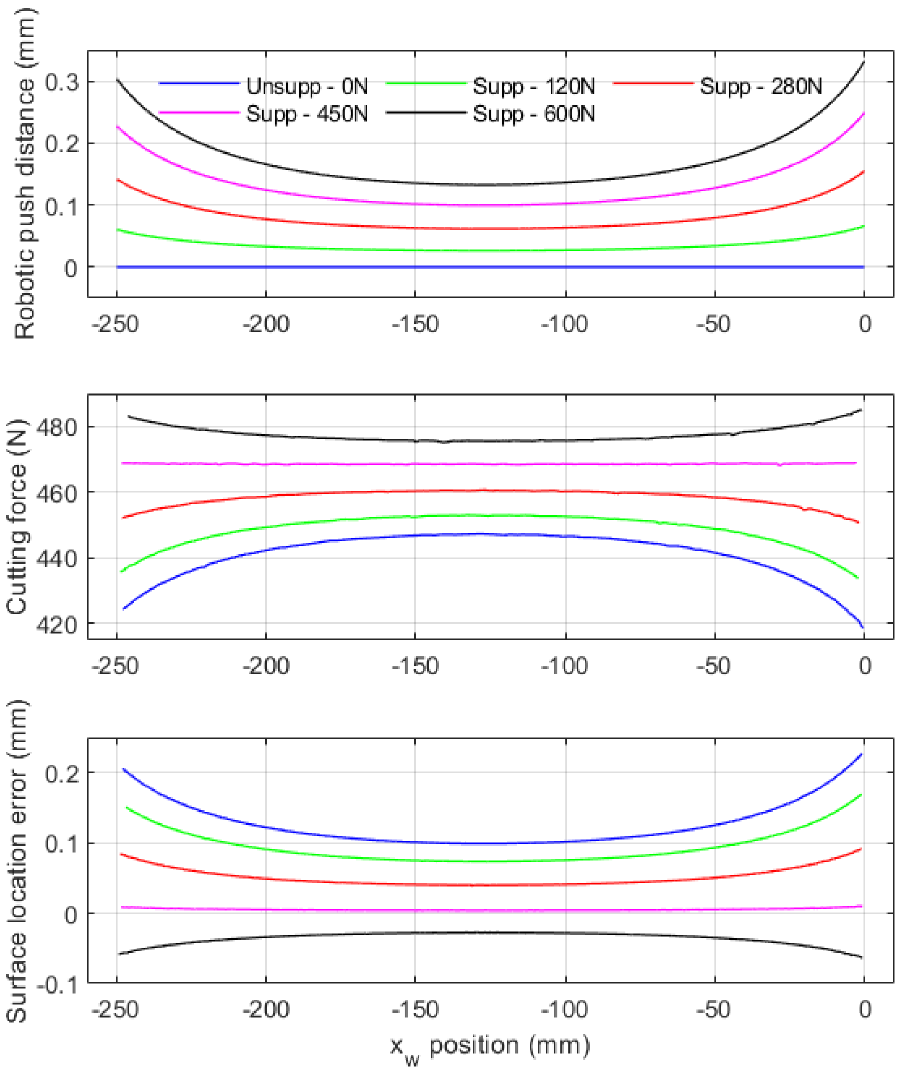

Figure 4.5 Comparative analysis of simulated results across robotic supporting forces of 0-600N: robotic push distance (top), cutting forces on the tool (middle) and form errors (bottom).

In conclusion, there is a positive effect in form error reduction with an increasing robotic push effort; however, the impact can be optimised through an actual knowledge of the cutting forces acting upon the workpiece in real-time; otherwise, overcutting may happen with high support forces. It is therefore important to go beyond the force control method, and investigate other control methods, namely one where the overall force on the workpiece is minimised. In the next section, two control methods are investigated: force minimisation method which aims to minimise the overall force on the workpiece, and thickness control method which aims to minimise remaining wall thickness errors. These methods will be compared in face milling simulations.

4.3 Face milling simulations

Further simulation investigations are carried out in face milling conditions, as shown in Figure 3.8. As shown in section 3.2.3.2, there is a need to use a cutting tool with a negative helix angle to prevent contact loss with the cobot. Cutting conditions used in this section are presented in Table 4.2.

Cutting parameters	Value
Tool geometry	Straight end
Milling type	Slotting
No. of milling flutes (N)	3
Tool helix angle ($\boldsymbol{\beta}$)	-35°
Tool diameter ($\boldsymbol{D}$)	12 mm
Feed rate per tooth ($\boldsymbol{c}$)	0.2 mm/rev/flute
Spindle speed ($\boldsymbol{n}$)	4300 rpm
Axial depth of cut ($\boldsymbol{a}$)	2 mm
Radial depth of cut ($\boldsymbol{b}$)	12 mm
Workpiece material	Aluminium 6082-T6
Tangential cutting coefficient ($\boldsymbol{K_{tc}}$)	773.87 $N.mm^{-2}$
Radial cutting coefficient ($\boldsymbol{K_{rc}}$)	294.88 $N.mm^{-2}$
Axial cutting coefficient ($\boldsymbol{K_{ac}}$)	133.19 $N.mm^{-2}$
Tangential edge cutting coefficient ($\boldsymbol{K_{te}}$)	47.88 $N.mm^{-1}$
Radial edge cutting coefficient ($\boldsymbol{K_{re}}$)	24.77 $N.mm^{-1}$
Axial edge cutting coefficient ($\boldsymbol{K_{ae}}$)	-0.11 $N.mm^{-1}$

Table 4.2 Face milling simulation parameters.

4.3.1 Unsupported workpiece

Simulations were run with the cutting conditions highlighted in Table 4.2, for the unsupported workpiece. Figure 4.6 illustrates the cutting forces acting upon the tool in the z-axis and the form errors incurred during the tests.

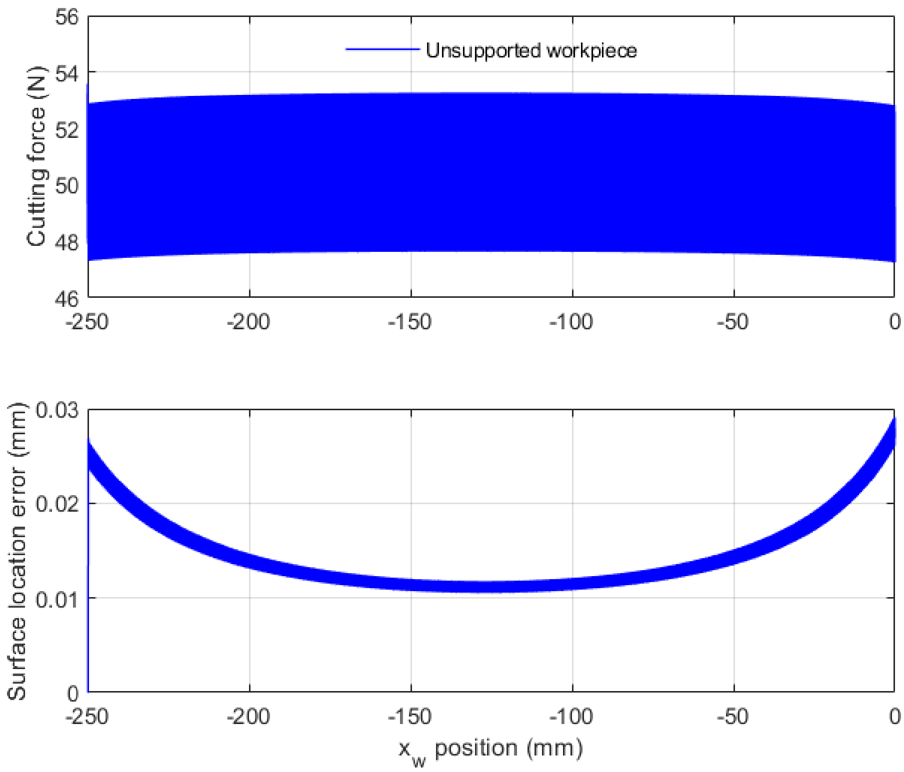

Figure 4.6 Simulated results of unsupported workpiece in face milling conditions: cutting forces acting on the tool in z-direction (top); surface location errors incurred (bottom).

As seen in Figure 4.6 the cutting forces are positive; this means that the workpiece is pushed away from the tool, thereby keeping contact with the end effector of the cobot. This justifies the choice of the tool with a negative helix angle. A similar parabolic profile is observed for both cutting forces and form errors, due to the parabolic static stiffness profile shown in Figure 4.1. Undercutting was observed, with form errors varying between 0.011mm and 0.030mm. This set of results represents the benchmark for the upcoming series of tests.

In the following sections, the design and implementation of two novel form error control methods is presented; their performance will also be investigated and compared to the unsupported case.

4.3.2 Preliminary control design and implementation

4.3.2.1 Control design specification and tuning method

Design specifications are identified to ensure the successful design of control methods and their efficiency when implemented on the machining setup described in section 5.3. While the milling trials are modelled as a continuous function (see *cutting force model* block in Figure 3.16), the controller is designed as a discrete-time PID controller due to the execution loop time of Beckhoff PLC, a third-party controller proposed to be used to coordinate the motion of both robots in dual-robot collaboration. This time is set as 10ms during which the robot displacement z-offset is computed, hereby controlling the motion of the supportive robot in a periodic manner.

Moreover, the PID controllers are designed in a SIMULINK environment and tuned with PID Tuner, a single-loop PID tuning method embedded within the same platform. This method helps to tune the PID controller parameters to achieve a robust design with the desired response time [140]. The desired settling time is set to 100ms. This time corresponds to the update cycle time during which the xy- coordinates of the supportive robot are computed by the Beckhoff PLC from the coordinates of the machining robot to achieve a mirrored, dual robot system. More details about the setup will be given in section 5.3.

4.3.2.2 Performance of force minimisation

The objective of the force minimisation method (FMM) is to minimise the total force on the workpiece by altering the robot push distance from its nominal path, as explained in section 3.4.3. The FMM block diagram is illustrated in Figure 3.16. Based on the design restrictions mentioned in section 4.3.2.1, the controller is designed and tuned; the controller parameters are the following

$$K_p = 9.86 \times 10^{-5}, K_i = 1.97 \times 10^{-2}, K_d = 0$$

Equation 4.1

Figure 4.7 shows the step response of the FMM controller, with rise and settling times of 0.06s and 0.1s respectively.

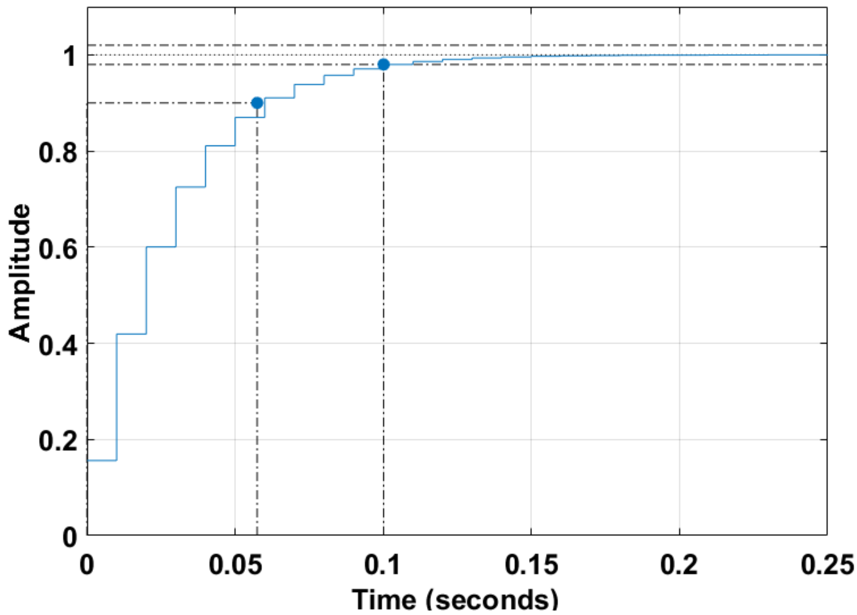

Figure 4.7 Step response of the FMM controller.

Upon implementation of the force minimisation method in machining conditions outlined in Table 4.2, Figure 4.8 shows the cutting forces acting on the tool, the robotic support force and the overall force on the workpiece. The collaborative robot moves forward to keep the overall force close to zero; the average total force measured during the simulation is 1.95N (about 4% of the cutting forces on the tool).

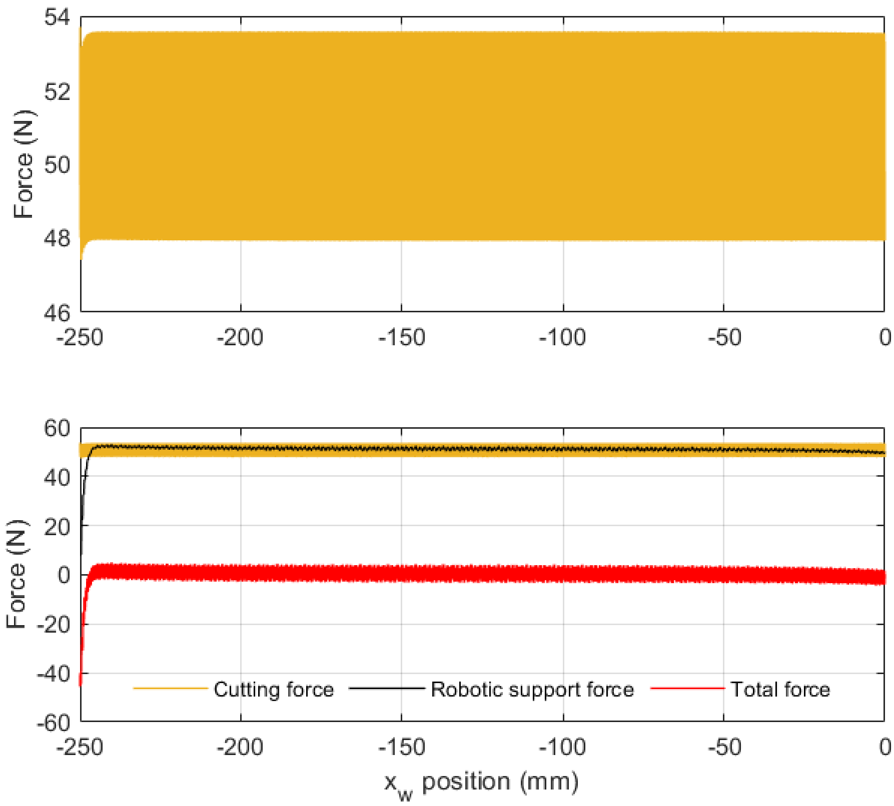

Figure 4.8 Performance of the force minimisation method – cutting forces acting upon the tool (top); forces acting upon the workpiece: cutting force, robotic support force, and total force on workpiece (bottom).

Moreover, a comparative analysis is carried out to assess the performance of TCM with regards to the unsupported case (in section 4.3.1). The results are outlined in Figure 4.9, namely the robotic push performed through FMM by the cobot, the comparison in cutting forces acting upon the tool in z-forces for both the unsupported case and through FMM, and the form error values in both cases.

According to Figure 4.9, the robotic push followed a parabolic profile in order to keep the overall force on the workpiece close to 0. This yields an average increase of 14.8μm in axial engagement (around 0.7% of the axial depth of cut). This justifies the very little change in cutting forces after the implementation of the control method, with a slight increase of about 1% in forces.

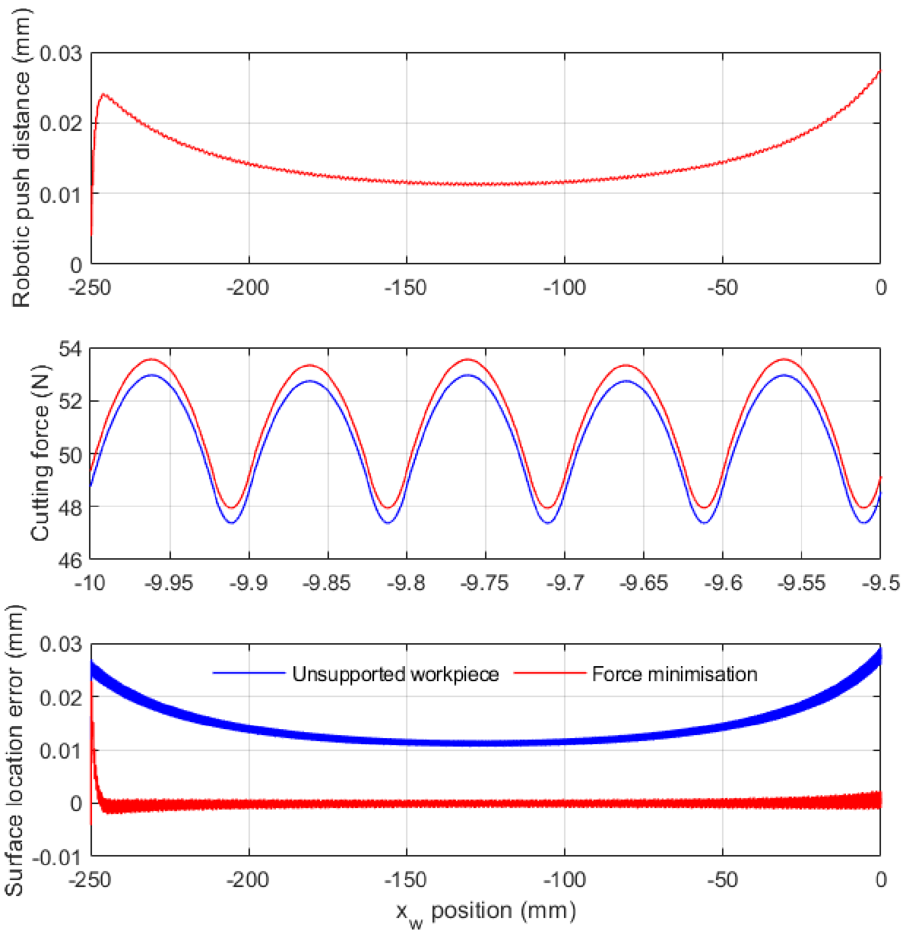

Figure 4.9 Comparative analysis of the performance of force minimisation method (FMM) – robotic push distance in FMM (top); close-up of cutting forces for unsupported workpiece versus FMM (middle); SLE values for unsupported workpiece and FMM (bottom).

However, there is a noticeable improvement in form error. A 99% reduction in average form errors is observed with the help of FMM, with a slight overcut of 0.54μm.

4.3.2.3 Performance of thickness control

The thickness control method (TCM) aims to keep the remaining wall thickness at a setpoint value, as explained in section 3.4.4, by altering the robotic push distance from its nominal path. The control method is illustrated by a block diagram in Figure 3.18. Based on the design restrictions given in section 4.3.2.1, the TCM controller is designed and tuned; its final parameters are given below.

$$K_p = -1.92 \times 10^{-1}, K_i = -3.83 \times 10^{1}, K_d = 0$$

Equation 4.2

Figure 4.10 shows the step response of the TCM controller, with rise and settling times of 0.06s and 0.1s respectively.

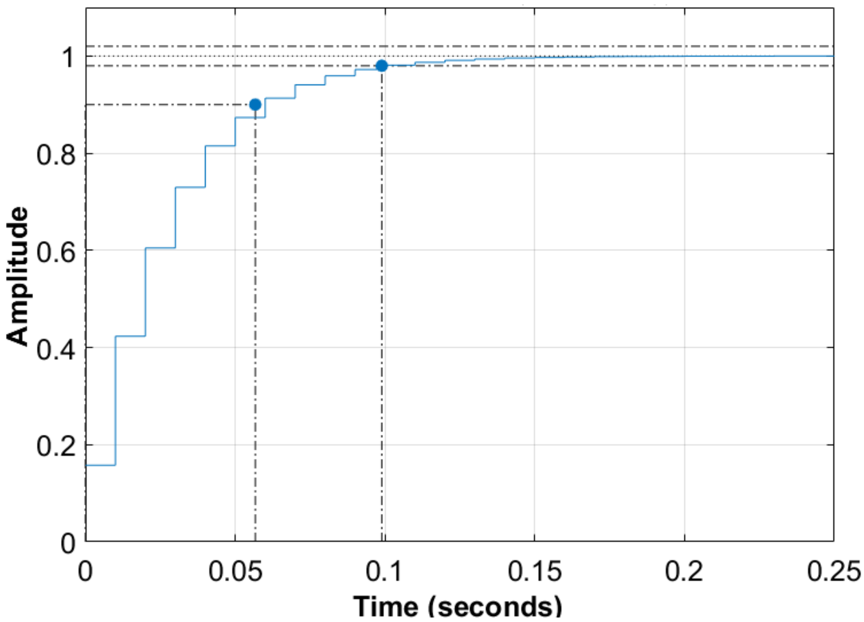

Figure 4.10 Step response of the TCM controller.

Similarly, TCM is implemented in face milling conditions outlined in Table 4.2. Figure 4.11 presents simulation results, namely the robotic push, the comparison in cutting forces acting upon the tool in z-forces for both the unsupported case (in section 4.3.1) and through TCM, and the form error values in both cases.

According to Figure 4.11, the robotic push followed a parabolic profile across the entire workpiece length, with an average value of 14.7µm. However, due to the low change in axial engagement, this push had very little influence on the cutting forces on the tool, as there was a slight increase of 7% in average cutting forces (as shown in the middle graph). The noticeable change is perceived on form errors where a 99% reduction is observed with a change from undercut to an average overcut of 0.49µm across the workpiece.

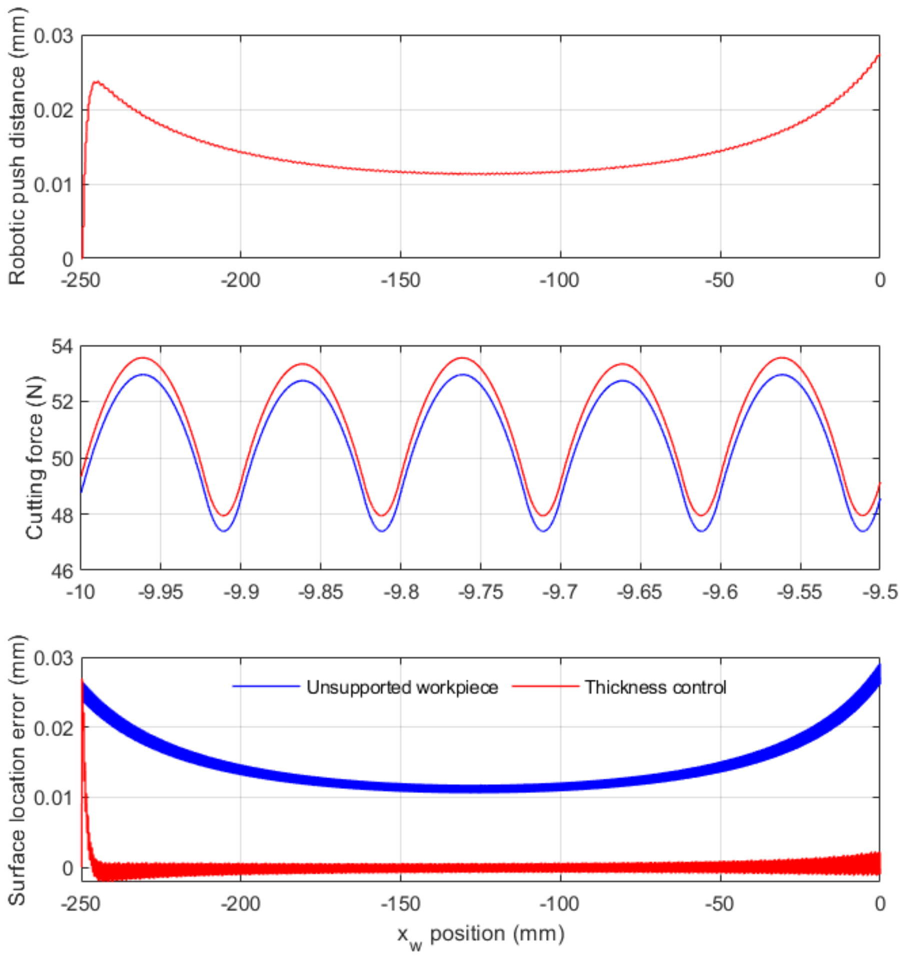

Figure 4.11 Comparative analysis of the performance of TCM – robotic push distance in TCM (top); close-up of cutting forces for unsupported workpiece versus TCM (middle); SLE values for unsupported workpiece and TCM (bottom).

Furthermore, when comparing the performance of both FMM and TCM methods along with the unsupported workpiece, it is clear that there is little to no difference in form error values, as highlighted in the top graph in Figure 4.12.

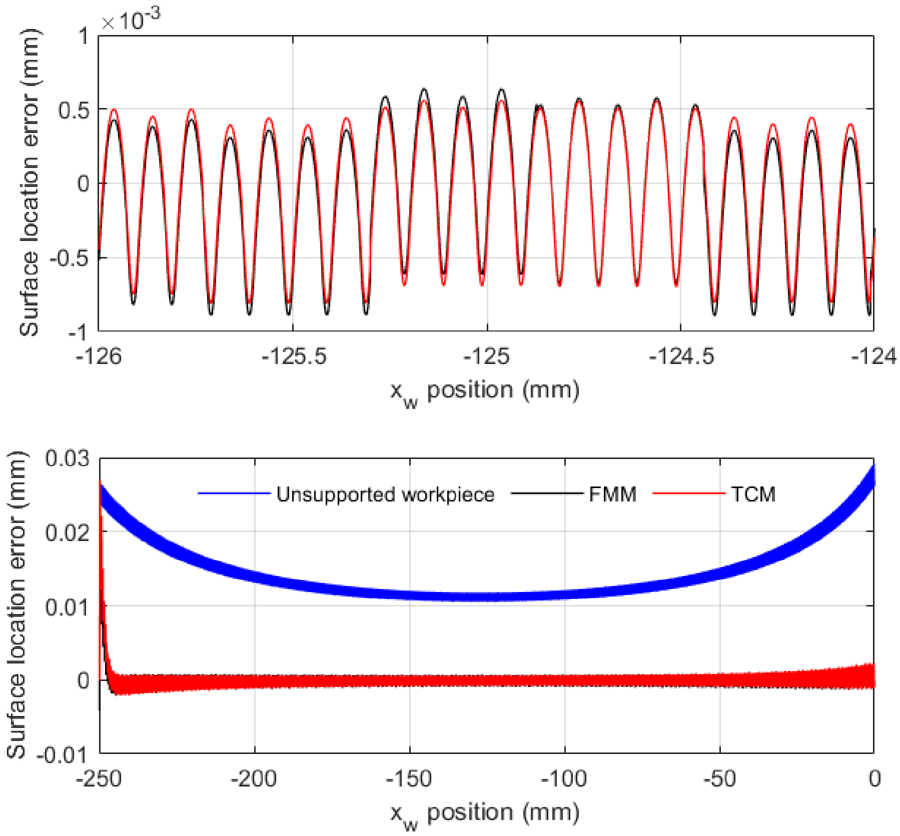

Figure 4.12 Form error comparison of both control methods along with unsupported case with no position errors in face milling – close-up view (top); comparison of all three scenarios (bottom).

This is justified by taking a look at the equation given in section 3.3 to obtain form error values, as shown below

$$SLE = \frac{F_s - F_c}{k_s}$$

Equation 4.3

This equation applies when there are no position errors in the setup. Therefore, in order to reduce form error values, one can either reduce the overall force on the workpiece (objective of FMM) or measure and nullify the remaining wall thickness error (objective of TCM). This is why both methods perform relatively the same when position errors are not taken into account.

This is however not realistic in a real system, even more so in robotic milling, where position errors are the main issue under milling conditions. In the next section, the robustness of both control methods is investigated by introducing position errors on the machining head.

4.3.3 Machining robot position errors in dual robotic milling

In robotic machining applications, the main challenge to be addressed originates from TCP position errors [46], resulting in errors ranging up to 1mm [57], [58]. It is therefore important to investigate how the novel control methods address this issue.

Figure 4.12 presented the performance of FMM and FMM with no position errors, but this case is not realistic as position errors are inherent in the milling robot. It is therefore important to test the performance of the two controllers proposed, by employing position errors as a disturbance in the system. For the sake of analysis, the previous scenario where no position errors were considered is labelled as 'Case 0'.

Two additional case scenarios are considered and obtained from actual position errors measured on the ABB IRB6640 during milling trials carried out by Onawumi et al. in AMRC (Advanced Manufacturing Research Centre) in Sheffield [141].

- Case #1 – a constant position error of -0.1161mm is introduced (corresponding to the average of position errors across the milling trials conducted in [141]). The negative sign signifies an undercut.
- Case #2 – a varying pattern of position errors is introduced across the workpiece profile. The errors vary between -0.204mm and -0.054mm [141].

All machining robot error profiles are plotted in Figure 4.13.

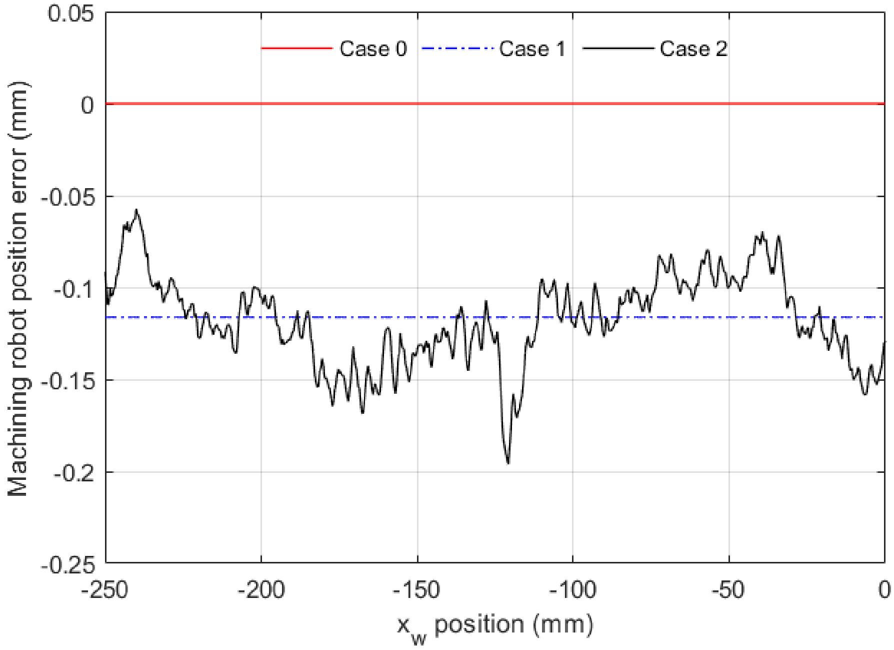

Figure 4.13 Profiles of machining robot position errors introduced as disturbances on the axial depth of cut.

It is also important that the same controller parameters are used in all scenarios.

The control block diagrams are revised in Figure 4.14; the machining robot position errors are introduced as a disturbance on the axial depth of cut. As the position errors affect the axial engagement of the tool, they are also indirect disturbances on the cutting forces acting on the tool in milling trials.

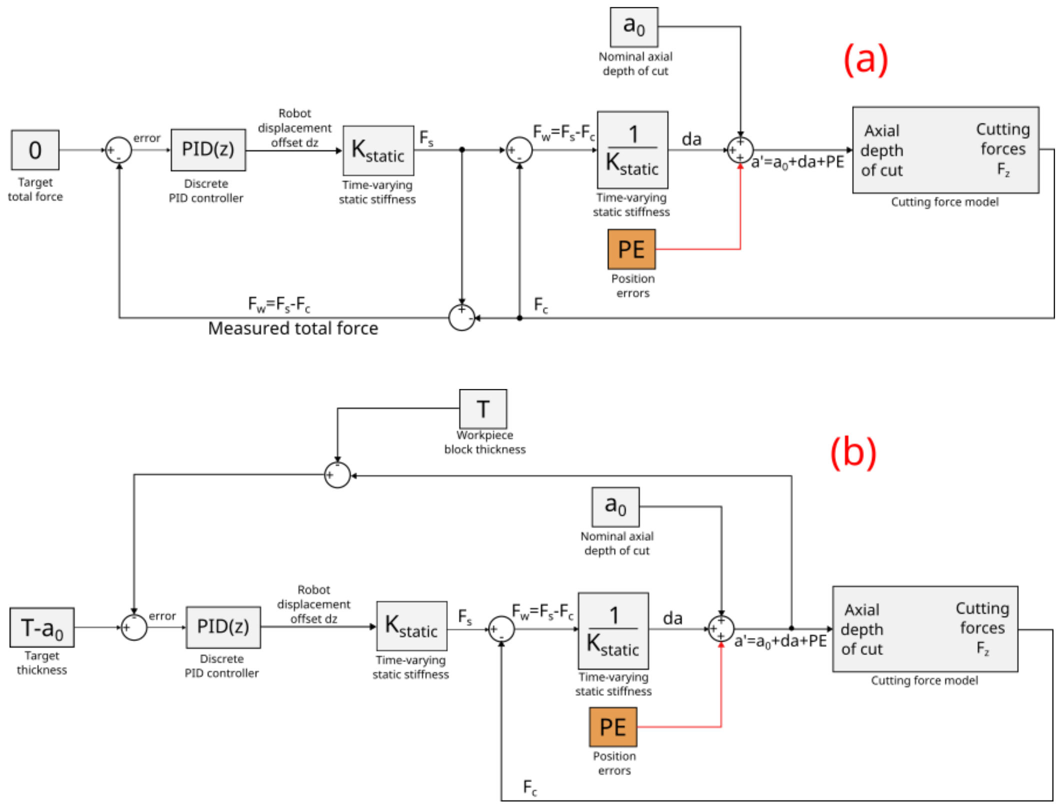

Figure 4.14 Revised block diagrams of form error control methods: (a) force minimisation method (FMM); (b) thickness control method (TCM).

4.3.3.1 Case #1 – constant position error

The first case scenario in this section illustrates the introduction of a constant value of position errors from the machining robot, of -0.1161mm (see Figure 4.13). Figure 4.15 illustrates the performance of both control strategies. Overall, there is an improvement in form error with both approaches; however, the thickness control method (TCM) yields over 99% decrease with a slight overcut, while the force minimisation method (FMM) only yields a 11% decrease.

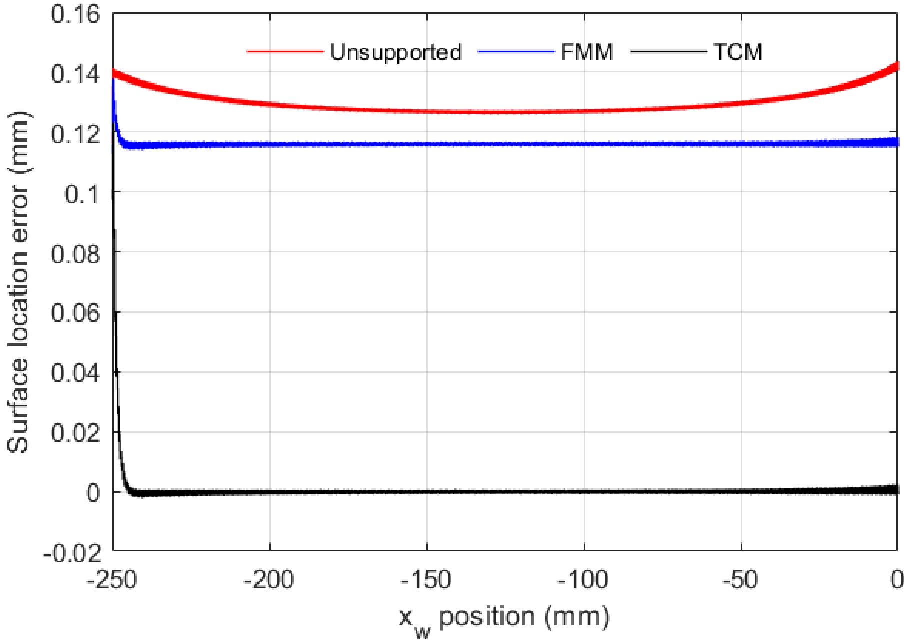

Figure 4.15 **Case #1 – comparison of form error values across all milling scenarios (unsupported, TCM and FMM).**

A closer look at the controller outputs of both strategies, i.e., the change in robotic push distance, reveals that only the TCM focuses on the compensation of the position errors originating from the machining robot (see Figure 4.16).

The low performance of the FMM is due to the nature of its objective: it aims to nullify the overall force on the workpiece. The latter is not a metric that takes into account the position errors present within the machining robot.

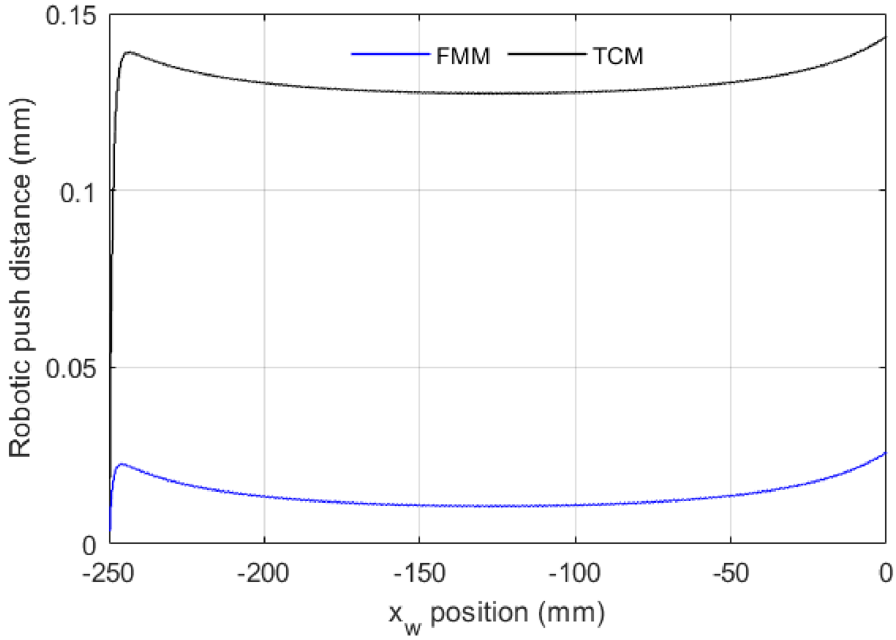

Figure 4.16 Case #1 – Robotic push distance in both control strategies (in the z-direction).

Another way to appreciate the stark difference between both approaches is by comparing the support force exerted by the collaborative robot at the back face of the workpiece (see Figure 4.17). The FMM yields about 48N of robotic support force while the TCM yields an average of about 472N of force. The former value is relatively close to the cutting forces measured during the milling operation of the unsupported workpiece (see Figure 4.9).

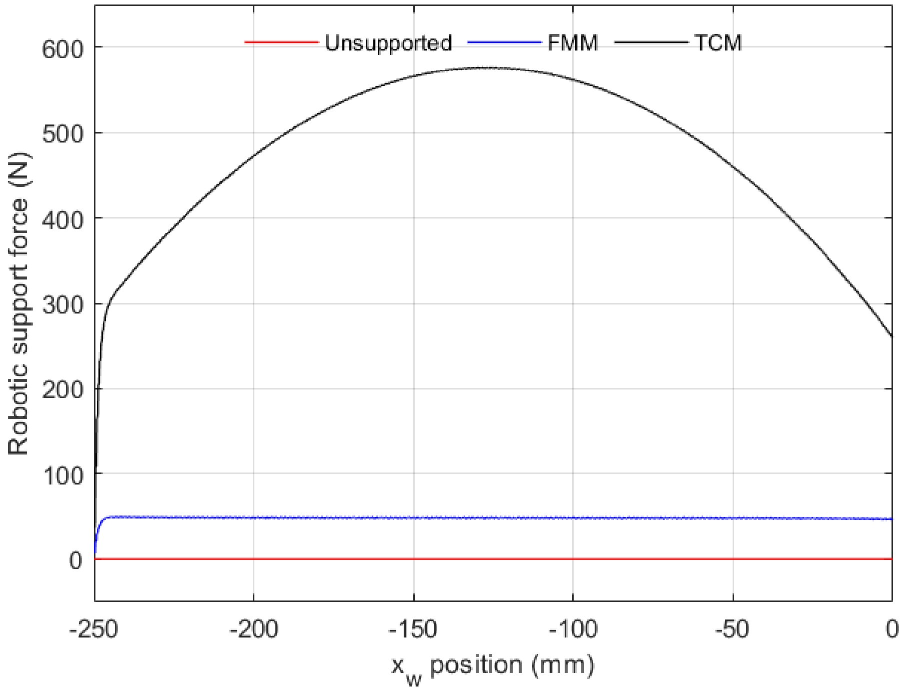

Figure 4.17 Case #1 – comparison of robotic support forces across all milling scenarios (unsupported, TCM and FMM).

4.3.3.2 Case #2 – time-varying position error

The performance of both compensation methods was also evaluated for time-varying position errors on the machining robot (see the position error profile in Figure 4.13). Figure 4.18 gives a summative illustration of the simulated results.

Similar to Case #1, TCM performed the best with a decrease in form error of over 99% with a slight undercut while only 11% decrease is observed with the FMM. However, with the implementation of the thickness control method, robotic support forces reach just under 900N. Another interesting observation is the decrease in amplitude of form errors with the implementation of TCM; there is an overall decrease of amplitude of SLE of 56% from unsupported milling conditions while the amplitude remains relatively unchanged in the FMM case.

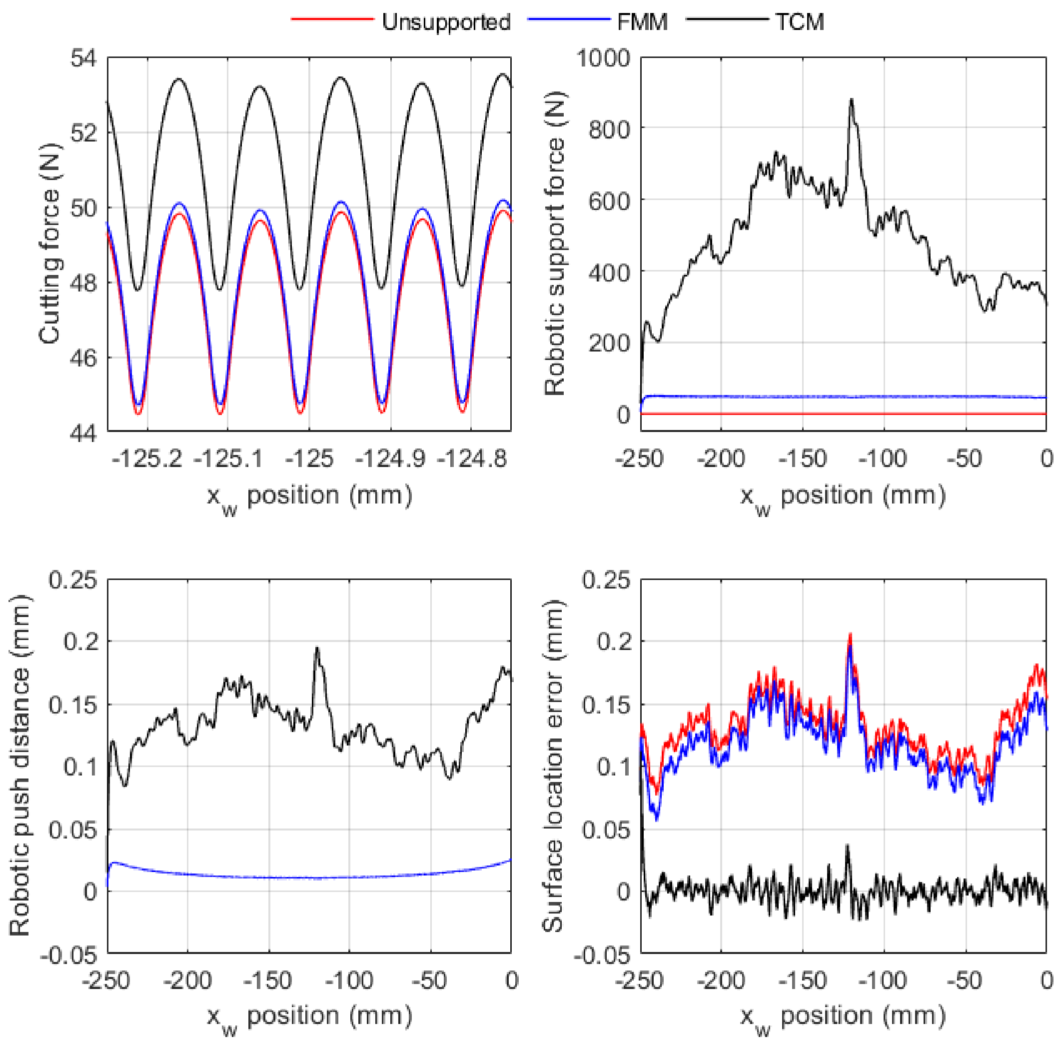

Figure 4.18 Case #2 – comparison of both compensation methods – close-up of cutting forces acting on the tool between X-125.25mm and X-124.75mm (top left); robotic support force (top right); robotic push distance (bottom left); form error values (bottom right).

Looking at all cases, a summative table of average form error values is illustrated below. Case 0 refers to no position errors. The percentages refer to improvements in form error.

According to Table **4.3**, TCM performed the best for all cases, except Case 0 where it performed relatively the same to FMM.

Position error case	No support	FMM	TCM
Case 0	1.41×10^{-2}	-5.36×10^{-4} (104%)	-4.88×10^{-4} (103%)
Case 1	1.29×10^{-1}	1.16×10^{-1} (10.7%)	-6.39×10^{-5} (100%)
Case 2	1.31×10^{-1}	1.17×10^{-1} (10.6%)	5.99×10^{-5} (100%)

Table 4.3 **Comparative table of form errors in milling scenarios in mm (unsupported, FMM, TCM) across all three position error cases.**

4.3.4 Machining conditions in dual robotic milling

Besides positional errors from robotic milling, it is also important to assess the performance of the proposed error compensation strategies with changing machining conditions. In the following section, this investigation is carried out considering the parameters below.

- ❖ Varying static stiffness values, as they are one of the key variables in the newly proposed form error prediction model (see Equation 3.16).
- ❖ Force limits on the support robot.
- ❖ Radial engagement of the tool.

4.3.4.1 Static stiffness of workpiece

For most part of the exposition of simulation results, the profile of the static stiffness of the workpiece (see Figure 3.5) was assumed to be the same for both peripheral (section 4.2) and face milling (section 4.3) simulation runs. This was done to have a set of coherent results.

To further evaluate the performance of both novel form error control methods, it is important to evaluate their robustness to changes in local static stiffness of the workpiece as the tool travels the part. Up until now, only straight cuts have been considered as the tool travels across the top part of the workpiece, and the static stiffness profile considered for simulations has been measured across the whole length of the workpiece, at Yw=-6mm; this profile is shown in Figure 4.1. For more complex milling paths, there will be variations in static stiffness. The performance of both control methods is therefore important to be investigated for complex paths.

Through finite element analysis (FEA), the average static stiffness values of the aluminium part can be evaluated. The workpiece is modelled as a 21-element cantilever beam clamped on one end. The stiffness values were evaluated at the top element of the beam, by inputting a static force of 25N and obtaining the steady deflection at the end of the simulation (see code in Appendix B.4). Figure 4.19 shows the average static stiffness of the workpiece along the workpiece height.

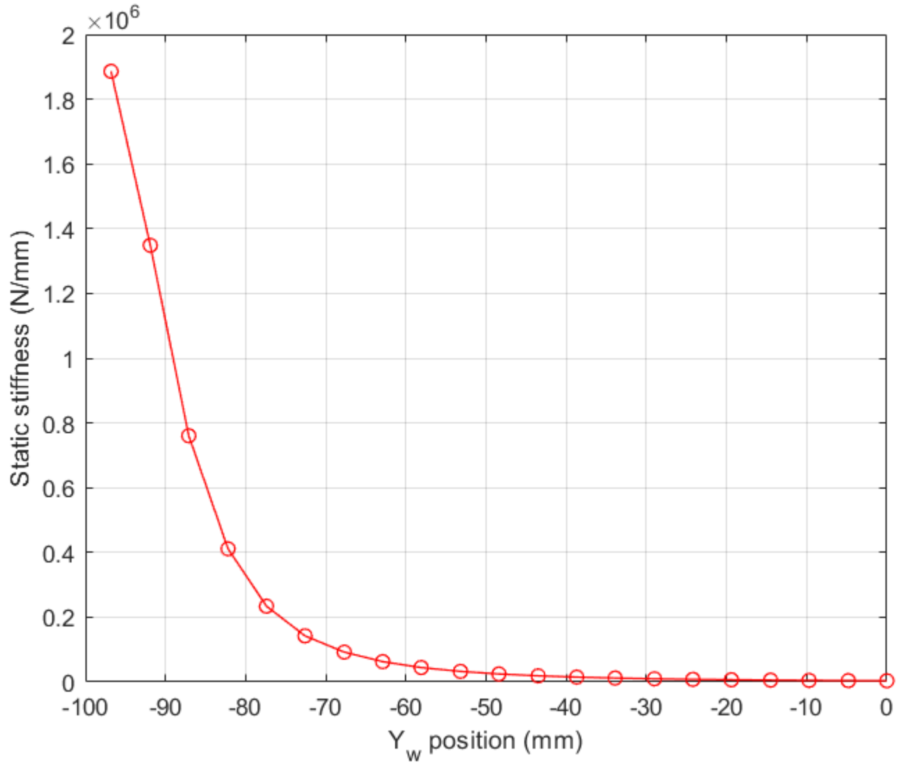

Figure 4.19 Average static stiffness of the unsupported workpiece across the workpiece length axis (Yw). The top of the workpiece is considered as datum.

According to Figure 4.19, the static stiffness varies from 1 to over 500 times the average value at the top of the workpiece (Yw=0mm), which is a wide range across the workpiece. It is therefore imperative to assess the impact of a change in workpiece static stiffness on the performance of both error compensation methods. For this investigation, a range of static stiffness multiples of the experimental stiffness profile (in Figure 4.1) was identified. These values are stated below.

$$k/_{k_{static}} = \left\{\frac{1}{5}, \frac{1}{4}, \frac{1}{3}, \frac{1}{2}, 1,2,3,4,5\right\}$$

Equation 4.4

Preliminary tests of both methods were carried out by identifying both rise and settling times of the step response of both controllers in the closed-loop system with each control method (FMM and TCM), as shown in Figure 4.20, across various multiples of the experimental static stiffness profile. In control theory, rise time is defined as the time it takes for the response signal to transition from 10% to 90% of the final value, while the settling time is the time it takes for the error to stay below 2% of the final value.

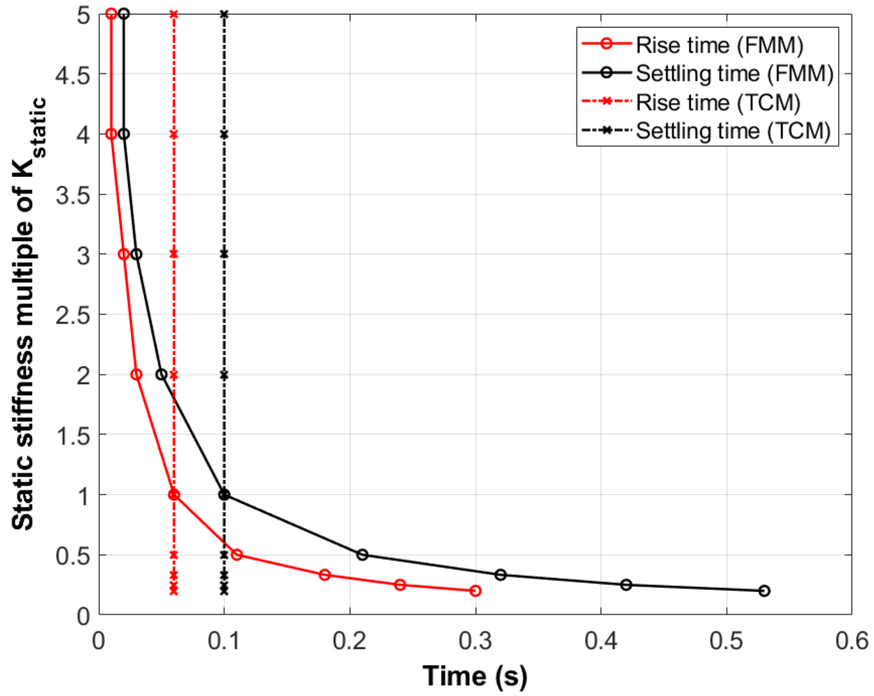

Figure 4.20 Rise and settling times of FMM and TCM control methods across various workpiece static stiffness values.

According to Figure 4.20, the performance of the thickness control method is not affected by the change in stiffness, whereas the performance of the force minimisation method exponentially increases as the static stiffness increases. This is because, with regards to TCM, the controller input is the wall thickness error, and its output is the robotic push distance; both variables are not dependent on the static stiffness, hence why changes in static stiffness do not affect its performance. With FMM however, the input is the error in overall force on the workpiece and its output is the robotic push distance; both variables are related to static stiffness through Equation 3.13. It therefore shows that static stiffness is a crucial variable to measure in order to implement the FMM, but it is not needed to implement TCM.

A further analysis was conducted by measuring the form errors in milling trial simulations. The simulations were conducted across the range of stiffness values, for both control methods. A comparative graph of all results is shown in Figure 4.21 for the first 5mm of milling path covered by the milling robot. A constant value of -0.1161mm in machining position errors was also introduced (similar to Case#1 in section 4.3.3.1).

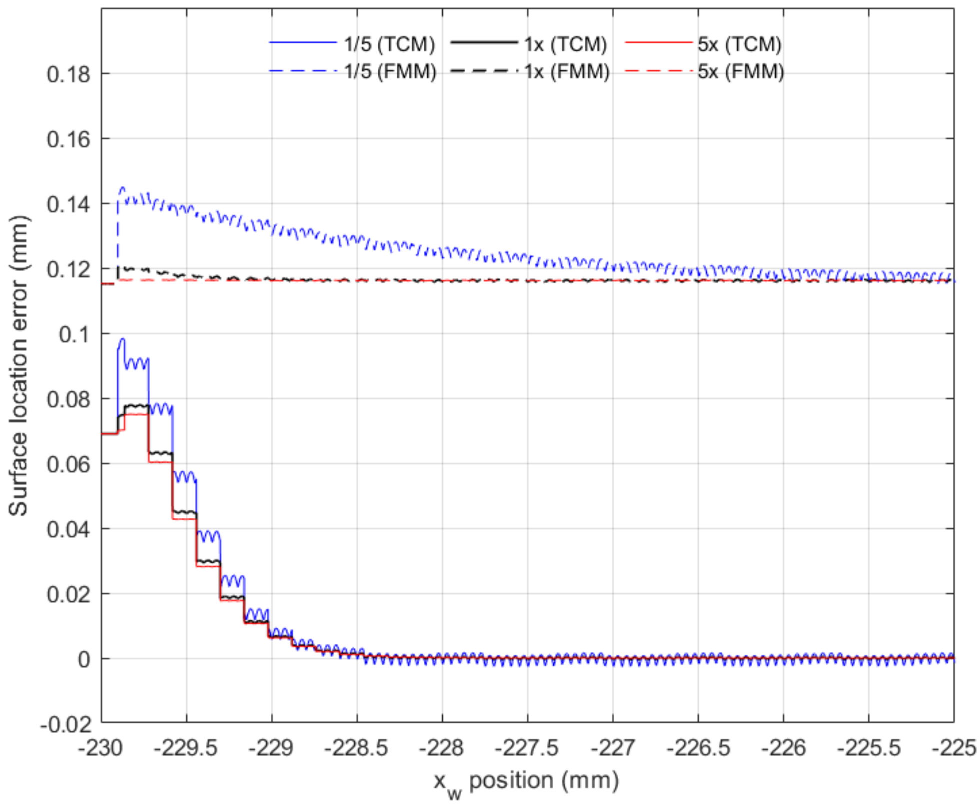

Figure 4.21 Form error comparison between TMC and FMM across various static stiffness values; results are presented for multiple in static stiffness of 1/5x, 1x and 5x of the experimental static stiffness profile.

According to Figure 4.21, the thickness control method performs the best and is also consistent in its response across all stiffness scenarios, with the SLE nearing 0 at Xw=-228mm. However, with the force minimisation method, as the stiffness decreases, it takes longer for the controller to reach steady state; however the response is much quicker as the stiffness value increases. This is because the cobot is required to cover less distance to reach a certain support force as the stiffness increases. Both these observations highlight the superiority in robustness of the TCM as changes in stiffness arise in the milling system. However, this analysis is carried out provided that the system has an infinite force capacity; in the real system, it will not be the case; it is therefore important to assess how both control methods perform when there is a limit in force capacity applied by the supporting robot.

4.3.4.2 Force limitations

So far, FMM and TCM control algorithms have shown promising results; both methods control the robot to push the workpiece towards the cutter, altering the neutral axis of the part, depending respectively on the overall force on the workpiece and the remaining wall thickness error. However, in section 4.3.3, in the presence of position errors, the thickness control method had a far more outstanding performance, as the controller effort was to directly mitigate surface location errors, therefore taking into account position errors, unlike FMM. For example, for Case #2 in section 4.3.3.2 where the position errors varied along the milling path, the resulting SLE values were plotted in Figure 4.18, with TCM performing 10x better than FMM.

However, a concerning observation is made on the simulated robotic support force exerted by the cobot, in its effort to compensate errors; support forces reach up to ~900N. Despite it being way below the load rating of the load cell, which is about 3kN in the z-direction (of the robot end effector), the ball caster has in reality much stricter constraints. In effect, the load rating of the ball caster is 380N, beyond which plastic deformation will start to occur on the plastic spherical caster [142]. It is therefore important to investigate the performance of both methods under force capacity limits. In this investigation, the limit is set to 350N.

In order to assess the performance, simulation results were obtained with both control methods running under two sets of conditions: *'normal'* (with no force limit) and *'safe'* (with a robotic support force limit of 350N). This implies that the robotic support force is checked throughout the simulated milling trial and, where its value based on the controller output exceeds 350N, the robotic push distance will be capped. In practice, this means that both methods would be used in conjunction with the previously proposed force control method (FCM) presented in section 3.4.2.

Furthermore, in light of the performance of both methods across varying static stiffnesses in section 4.3.2.1, it would be interesting to investigate how both methods will perform in complex milling paths as these paths will involve nonuniform changes in static stiffness. Two milling paths are therefore proposed: a rectangular path and a circular path.

- ❖ The rectangular path has the following coordinates as corners: (-160,0), (-160,-5), (-90,0) and (-90,0).
- ❖ The circular path has a centre of coordinates of (-125,-50) and radius of 25mm.

Both are shown in Figure 4.22.

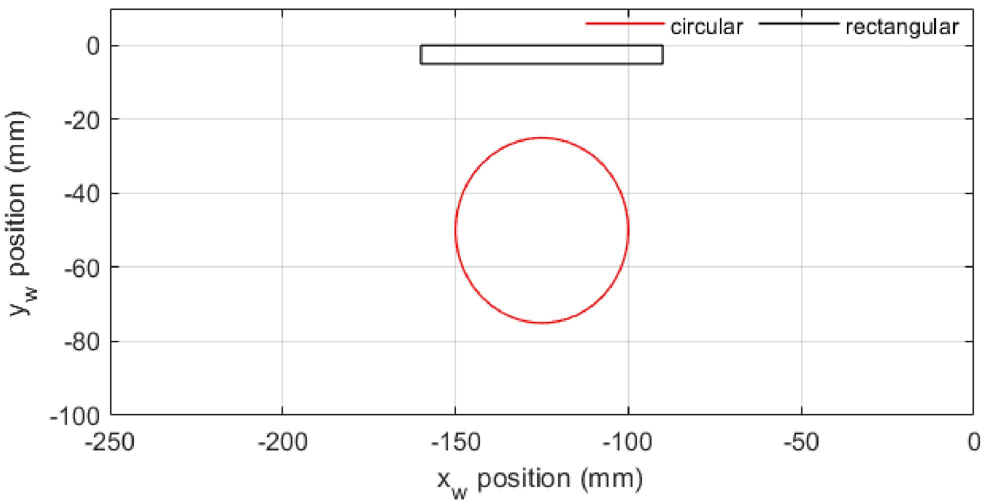

Figure 4.22 Complex machining paths.

The simulation results are presented in Figure 6.4 and Figure 6.5 and show the position errors, static stiffness values, cutting forces, robotic support forces and surface location errors across the milling paths; *'FMM-safe'* and *'TCM-safe'* respectively refer to force minimisation and thickness control methods applied with a maximum force limit. From the results, the performance of both control methods in both force limit scenarios is more clearly analysed by obtaining the average SLE values in all cases; these values are shown in Table **4.4**.

		Rectangular path	Circular path
Position error (mm)		-0.128	-0.127
Static stiffness (N/mm)		3.99×10^3	5.82×10^4
SLE for different scenarios (mm)	**Unsupported**	0.140	0.129
	FMM	0.128 (9%)	0.127 (2%)
	TCM	4.24×10^{-4} (100%)	7.25×10^{-4} (99%)
	FMM_safe	0.128 (9%)	0.127 (2%)
	TCM_safe	5.25×10^{-2} (62%)	0.111 (14%)

Table 4.4 **Comparative table of average form errors, position errors and static stiffness across both circular and rectangular paths in both normal and safe running conditions.**

According to Table **4.4**, for the rectangular path, TCM performs the best in normal conditions with a near perfect mitigation of form errors, while FMM only achieves a 9% reduction in SLE. However, under *safe* conditions, the performance of the TCM slightly drops from near perfect to 62% improvement in SLE, while the FMM's performance is unchanged. In order to understand the trend observed, it is important to take a closer look at the robotic support force in Figure 6.4. In effect, the robot is pushed to exert on the workpiece forces higher than 500N, considerably larger than the limit of 350N; hence why the performance is slightly reduced under *safe* conditions. FMM on the other hand, whose objective is to use the robot to counter cutting forces (averaging ~50N) does not require the robot to exert such high forces; hence why there is no change between *normal* and *safe* conditions. Nevertheless, TCM still outperforms FMM in both conditions.

Furthermore, for the circular path, a similar trend is observed with TCM, which perfects with a near perfect improvement of form errors in *normal* conditions; however, the drop in performance here is more drastic with only 14% improvement in SLE recorded under *safe* conditions. FMM achieves a marginal 2% improvement in SLE in both conditions. Upon inspection of the robotic support forces in Figure 6.5, under *normal* conditions, TCM leads the cobot to exert forces up to 35kN, which is way outside the load rating of the ball caster; this is why the performance is greatly impacted under *safe* conditions. On the contrary, the forces exerted by the cobot through FMM are very low (~50N); hence why this control method performs the same under both conditions.

It is important to highlight that, despite the loss in performance of the TCM with a force limit, it still outperforms FMM across both machining paths, making it the favourite active error compensation method in this investigation. Looking at the average static stiffness values for both machining paths, it is understandable that the circular path, that is covering an area that is much closer to the base of the part (as shown in Figure 4.22), where the static stiffness is considerably higher (as shown in Figure 4.19), it is understandable that any small push distance from the cobot will yield large robotic support force. In order to improve the performance of TCM under *safe* conditions, the following remedies can be investigated.

- ❖ Implement the control method on thinner parts where the static stiffness will be much lower; the current part is 9.5mm thick, which is on the thicker end for thin-walled milling applications.
- ❖ Source out a ball caster with higher load rating while keeping plastic as the ball material.

4.3.4.3 Radial engagement of the tool

Throughout section 4.3, face milling simulations were only carried out in slotting conditions. Due to a full radial immersion, the cutting forces are exclusively non-null (as shown in Figure 4.6). However, for any other radial immersion (less than 100%), the cutting forces will be zero as the immersion angle is outside the cutting region (as shown in Figure 3.2 and through Equation 3.4). This is not a problem with TCM as its objective is to compensate wall thickness error (in the z-direction). However, it may become a problem with FMM where the objective is to counteract cutting forces; in the event that milling forces are null, the cobot can be led to withdraw from the workpiece, causing contact loss with the part. Moreover, the controller might not be able to keep up with the high frequency oscillation between null and non-null values, as the tool travels along its milling path. It is therefore important to investigate how the FMM performs with various radial immersion percentages. For this reason, simulations are run from full immersion (100%) downwards, with all other simulation conditions highlighted in Table 4.2, until a simulation error registers, thereby showing the inability of the FMM to perform; no position error is introduced in this set of trials. The simulation trials are tabulated in Table **4.5** according to the radial immersion of the tool and whether or not the FMM was viable (whether or not a simulation error message popped up in simulation environment).

Tool radial immersion (%)	**Successful control performance**
100	✓
90	✓
80	✓
70	✓
60	✗
69	✓
68	✓
67	✓
66	✓
65	✓
64	✗

Table 4.5 **Machining trials checklist to assess the point of failure of performance of FMM across various radial immersions of the tool.**

According to Table **4.5**, the FMM stopped operating at 65% radial immersion. Upon close inspection of the cutting forces during the simulation trials as shown in Figure 4.23, it is evident that, at this specific immersion (64%), the cutting forces quickly oscillate between 53.5N and 0N; hence the failure of the control method. This method is therefore recommended for full immersion trials.

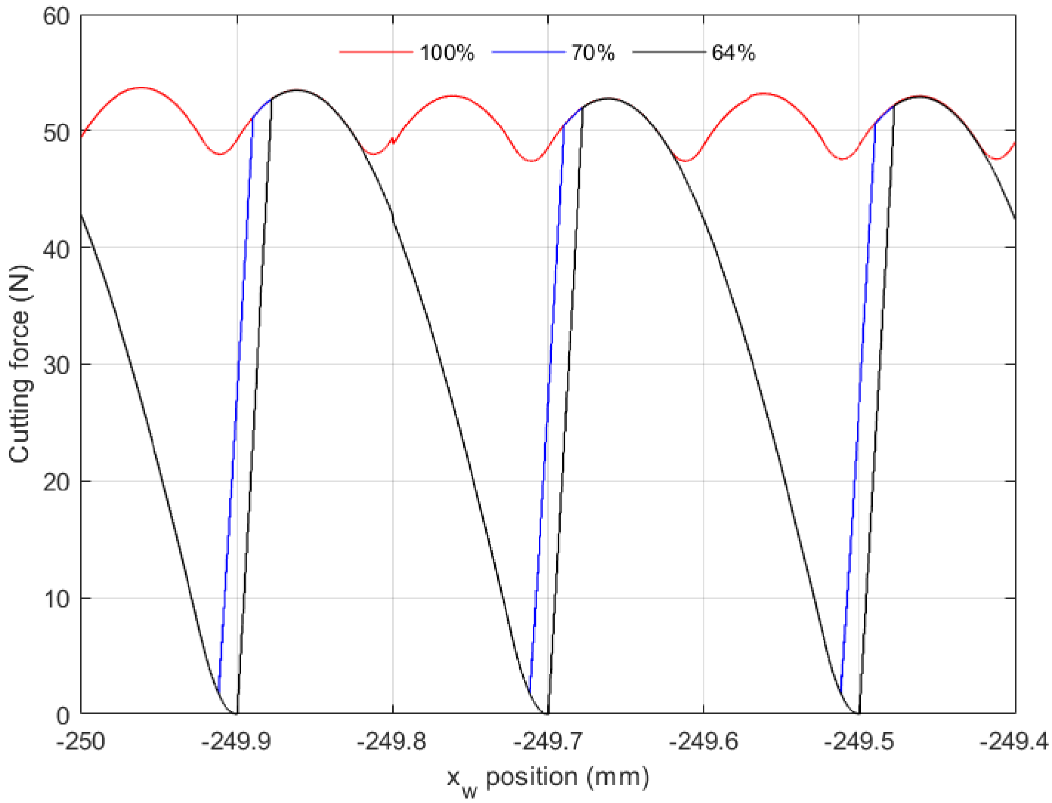

Figure 4.23 Close-up of cutting forces in robotic assisted milling operations for face milling given various radial immersions.

4.4 Summary

The chapter focuses on the simulation studies evaluating the proposed control methods for reducing form errors in robotic-assisted milling operations, including both peripheral and face milling. It explores the effects of robotic support forces, position errors, workpiece stiffness, and force limitations. Simulations were conducted using MATLAB and SIMULINK to model cutting forces and resulting form errors. These environments were used to replicate real-world milling conditions, incorporating variables like machining parameters and robotic support influences.

Compared to previous literature, the work described in this chapter also made the following contributions to knowledge.

- The implementation of the previously proposed force control method on the support robot led to significant decrease in form errors in peripheral milling trials. As the support force increased from 60-280N, a 69% reduction in form errors was achieved, confirming its effectiveness.

- ❖ Two novel form error control methods – force minimisation and thickness control methods, were tested in face milling conditions, significantly better than the conventional unsupported robotic milling case. After taking into account robotic position errors, it was shown that the thickness control method (TCM) dynamically adjusted the support robot's position based on real-time thickness measurements, outperforming force minimisation in most cases, with an improvement in form errors of over 95% and 10% respectively, compared to unsupported cases.
- ❖ Upon analysis of the robustness of both methods with respect to changes, results indicated that while position errors affect milling accuracy, the control methods, especially the thickness control method, could compensate for these variations, maintaining consistent form errors reductions. Unlike the force minimisation method whose performance was very much affected by changes in static stiffness, TCM proves insensitive to variations in workpiece stiffness, which means that upon tuning of the algorithm for a set of machining conditions, no further knowledge of static stiffness is needed, as long as workpiece parameters do not change drastically.
- ❖ Further analysis of the impact of force limits that arise when using ball casters (that do not have unlimited load ratings) reveals that the performance of both methods is greatly capped by the end effector force limits. Running simulations for both methods over rectangular and circular paths across the workpiece face revealed that TCM still outperformed FMM, with lower reductions in form error of respectively 62% and 9% for the rectangular path, and 14% and 9% for the circular paths. The much lower TCM performance in circular performance is due to the location of the path on the workpiece face, especially where the static stiffness is high, and therefore very low robotic push effort can be made within the force limits. Taking into account force limits gives rise to a hybrid algorithm that combines either TCM or FMM with FCM (force control method).

- ❖ When it comes to changes in radial engagement of the tool, the FMM method encounters great challenges as it could not be implemented below 65% of radial immersion.

The simulation tests highlighted the need for further refinement in the models as well as the benchmarking of these results against experimental results. This is discussed in the next chapter.

Chapter 5

Validation tests

5.1 Introduction

This chapter investigates and implements a force-based control method aimed at reducing form error and enhancing stability, by maintaining a force setpoint value, in two milling scenarios: peripheral milling and pocket milling. Unlike previous studies that primarily focused on using robotic-assisted fixturing to suppress chatter [11], [19], this research provides a comprehensive investigation into the direct impact of force-controlled robotic support on form accuracy. By actively regulating the supporting force exerted by a collaborative robotic arm, this approach not only stabilises the workpiece but also systematically minimises machining deviations, addressing a critical gap in the field of robotic-assisted milling.

The investigations presented in this chapter seek to address this gap by systematically evaluating the impact of force-controlled robotic support on form error mitigation. Experimental trials are conducted to assess the performance of the control approach under various force setpoints and machining conditions. Comparative analyses between different robotic support strategies—including unsupported cases, passive support, and active PID-controlled support—highlight the effectiveness of force control in reducing form deviation. Additionally, the accuracy of the developed simulation models is benchmarked against experimental results, further validating the approach. Key findings from this research have been disseminated in conference proceedings [76], [86]. These research papers are presented in Appendix D.

Beyond these investigations, this chapter also introduces the concept of dual robot collaboration, where a second robotic arm is integrated into the machining setup to further improve form accuracy. This proposed system builds on the findings from peripheral and pocket milling trials and aims to actively compensate for machining deviations by employing a synchronised robotic support mechanism. A preliminary framework for this dual-robot system is outlined, detailing the control strategies, equipment selection, and challenges involved in its implementation. Although the physical setup is still under development, its potential benefits in minimising form errors are discussed in comparison to the single-robot approach.

The remainder of this chapter details the methodology, experimental setup, results, and comparative analysis, providing insights into the potential of force-controlled robotic support and dual-robot collaboration for precision machining applications.

5.2 Machine-robot collaboration

This section covers the application of force control in peripheral and pocket milling trials, where the workpiece is machined by a conventional CNC milling machine and supported by an industrial robotic arm. The experimental results are compared with the simulation results in section 4.2.

5.2.1 Peripheral milling trials

5.2.1.1 Experimental results

The first set of experimental trials was carried out to assess the performance of the force control in peripheral milling conditions. The experimental setup in this research is identical to previous work carried out by Ozturk et al [11]. In earlier research, a force control strategy was developed by implementing PID control to stabilise the supporting force applied by a robotic arm on the backface of an aluminium workpiece, in peripheral milling conditions [19]. The experimental setup consists of a STAUBLI TX-90 robotic arm at the back of a T-shaped Al6082-T6 workpiece (see Figure 5.1). A soft rubber roller was the point of contact between the workpiece and the cobot (STAUBLI TX-90), while the supporting force F_s was measured by a KISTLER 9317C load cell attached to the arm's end effector.

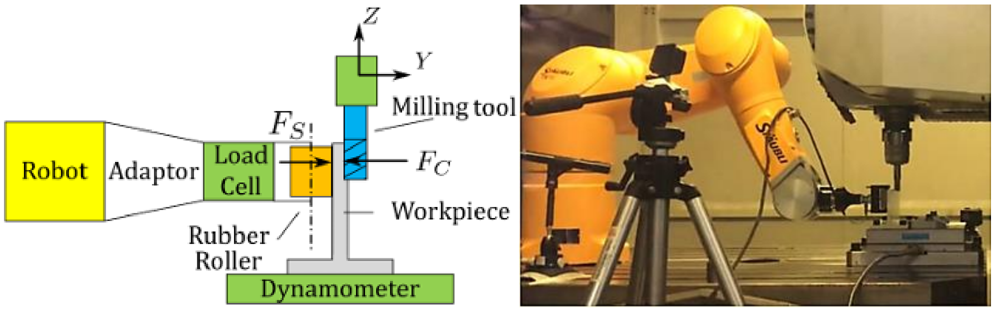

Figure 5.1 Solution developed in robotic assisted milling [11].

The load cell force was acquired by the load cell through a standalone National Instruments cDAQ-9133 data acquisition device (operating in LabVIEW environment) and transmitted via MODBUS, an Ethernet based communication protocol, to the robot controller. PID control was implemented within the robot motion code, and the robot moved axially by a distance Y_c to stabilise the load cell to a pre-defined value F_s. The block diagram for the implemented control approach is shown in Figure 5.2.

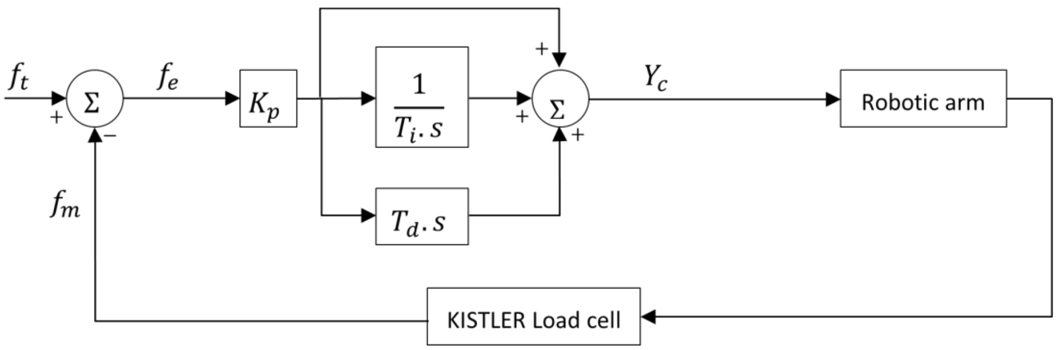

Figure 5.2 PID control block diagram [19].

The transfer function of the PID controller is given in Equation 5.1 and the resulting discretisation formula (Equation 5.2) is implemented in the robot motion code and executed periodically, every $T = 4ms$. Appendix C.4 gives the detailed derivation of the discretisation formula.

$$G_{pid}(s) = K_p\left(1 + \frac{1}{T_i s} + T_d s\right)$$

Equation 5.1

$$Y_c[k] = f_c[k-1] + K_p.\left\{f_e[k]\left(1 + \frac{T}{T_i} + \frac{T_d}{T}\right) - f_e[k-1]\left(1 + 2\frac{T_d}{T}\right) + f_e[k-2]\left(\frac{T_d}{T}\right)\right\}$$

Equation 5.2

After fine-tuning the PID controller via the Ziegler-Nichols method, various tests were carried out. Firstly, the capability was tested for various force setpoint profiles. It is important to note that this set of tests was carried out as the rubber roller moved across the workpiece profile and no milling operation was performed.

- Constant: the target force was set to 100N (see Figure 5.3)
- Linear: the target force was ramped up linearly from 100N to 200N and right down to 100N (see Figure 5.4)
- Parabolic: the target force profile followed a parabolic, concave-down curve as shown in Figure 5.5.

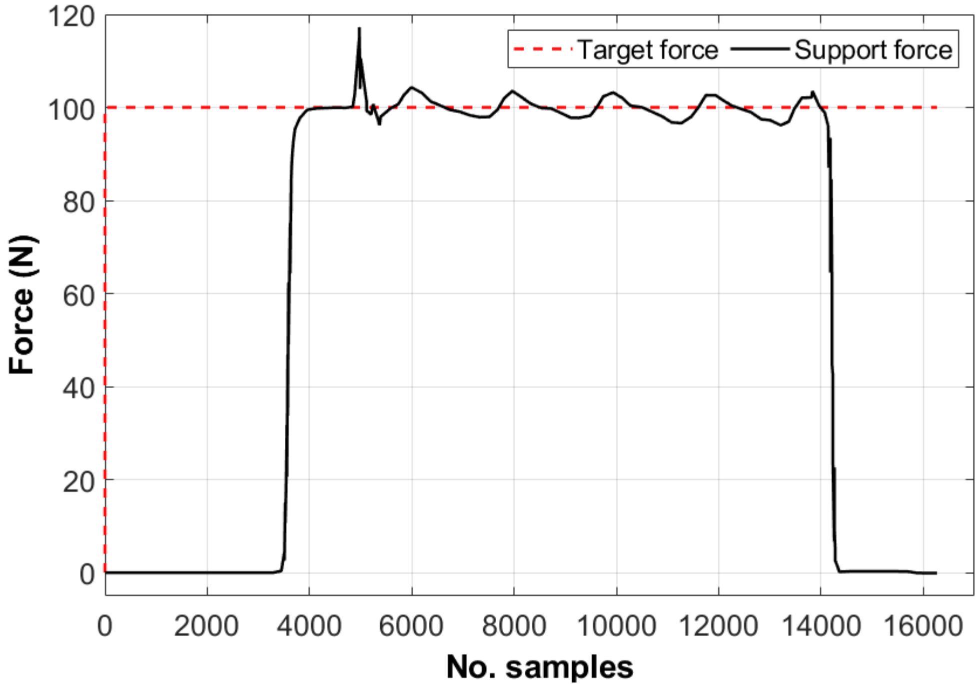

Figure 5.3 Force profile (constant force target).

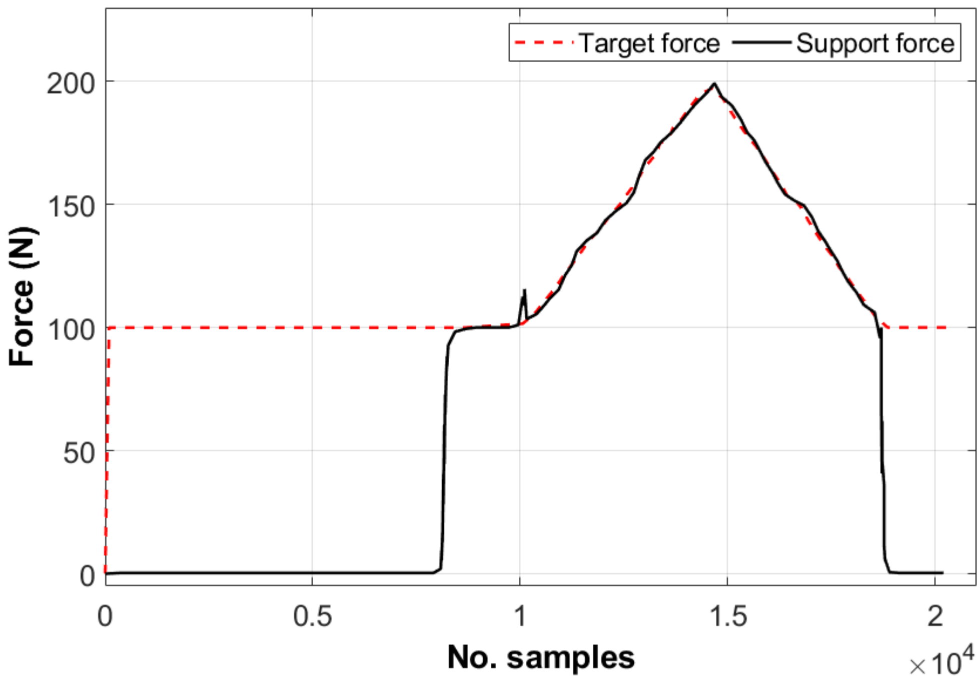

Figure 5.4 Linear target force profile.

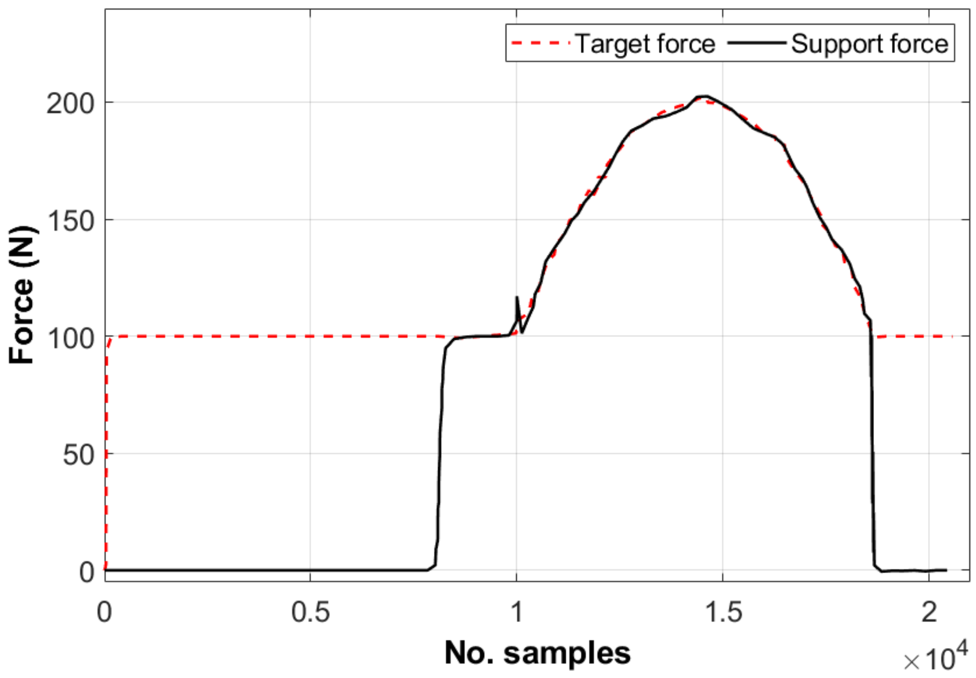

Figure 5.5 Parabolic target force profile.

As seen in this set of trials, there appeared to be a spike with all target force profiles; this is because rubber rollers exhibit higher coefficients of friction than harder materials like steel or nylon. This is primarily due to material properties of rubber, allowing for greater deformation and surface contact, hence leading to increased frictional forces, especially upon initial motion of the robot [143]. Moreover, the average percentage errors between target and actual force values were: 2.45% (constant), 2.64% (linear) and 2.83% (parabolic).

Secondly, the impact of the PID force control algorithm on the form error was assessed by comparing it with two cases: "no support" (no robotic support at the back of the workpiece) and "without force control" (robot initially applied a supporting force on the workpiece but this force was not controlled by the PID algorithm as time went by). In this set of trials, the STAUBLI robot was instructed to follow a STARRAG STC1250 5-axis milling machine, with a 20mm diameter carbide end mill with 2 flutes, in down milling. Spindle speed, feed per tooth, radial and axial depths of cut were respectively 7000 rpm, 0.107mm/tooth, 2mm, and 10mm. The target force value was 120N. The form error results are presented in Figure 5.6.

As shown below, the robotic support led to an average decrease in form error of 22% (without force control) and 38% (with force control), the latter yielding the best results. Moreover, the best improvement was seen in the amplitude of form error values across the workpiece profile during the milling operation; the amplitudes were 0.11mm and 0.055mm for "without force control" and "with force control" respectively.

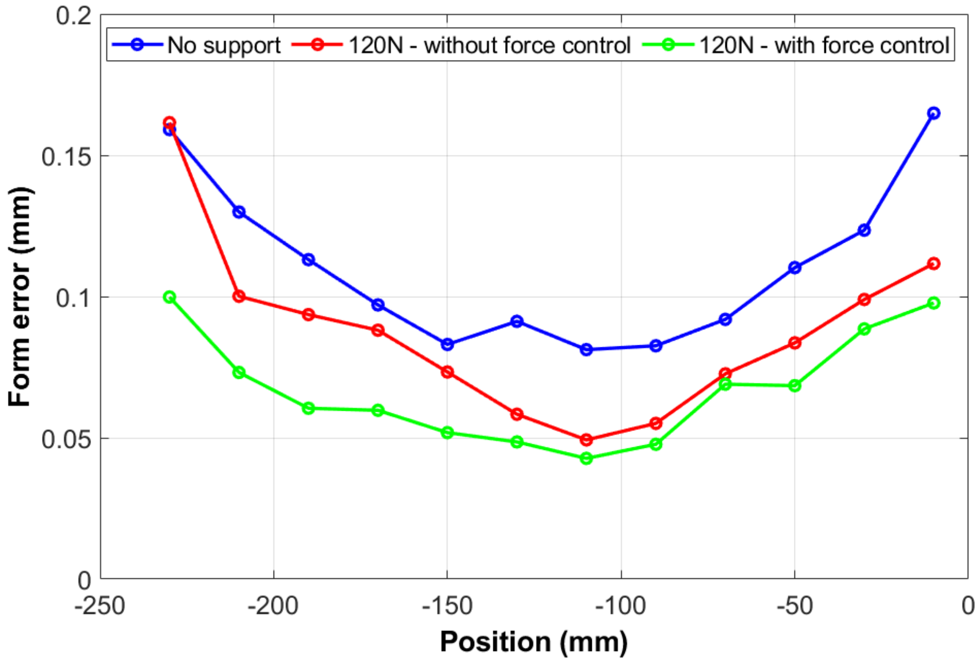

Figure 5.6 Form error comparison between "no force control" and "with force control" tests.

More trials were conducted while progressively increasing the robotic support force from 0N (i.e., there was no support from the robot at the back of the workpiece) to 280N.

The form errors are measured between -230mm and -10mm along the length of the workpiece for each robotic support force; the results are compiled in Figure 5.7.

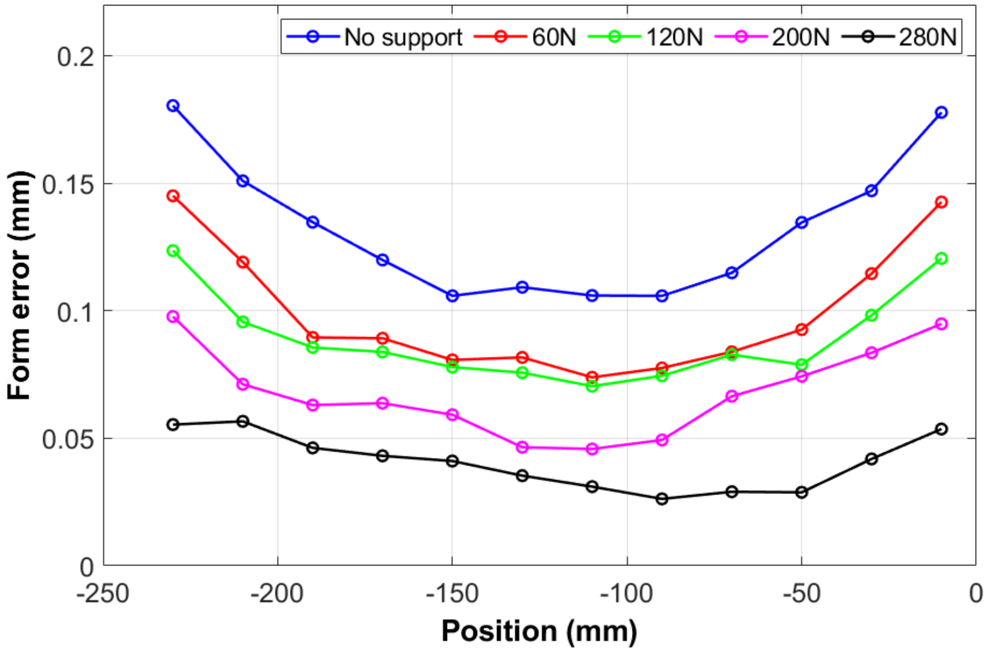

Figure 5.7 Measured form error results during peripheral milling trials in robotic assisted conditions at various robotic support forces: 0N (Unsupported), 60N, 120N, 200N, 280N.

The highest and lowest form error values recorded were respectively achieved with the unsupported workpiece trial and the case with a supporting force of 280 N, with values steadily decreasing from the former case to the latter (69% decrease in form error). This trend highlighted the impact that the robotic support force has on the forms error observed in peripheral milling. The robotic push from the cobot (STAUBLI TX-90) resulted in a static deflection that increased with the force applied on the backface of the workpiece. It is therefore observable that the maximum robotic support force of 280N applied on the workpiece resulted in an average static deflection of 0.1mm towards the tool. No deformation or stress measurement was carried out after these trials; nevertheless, no plastic deformation was visibly observed on the parts.

The same control approach was also implemented and investigated in pocket milling trials. The major contribution that the static deflection (from the robotic arm) has on the overall form error was observed on the workpiece in peripheral milling, validated previous investigations and further highlighted the influence of a supporting force on the form error observed on the workpiece in peripheral milling. It was then important to investigate the same control approach in other milling operations.

5.2.1.2 Comparative benchmarking of experimental and simulation data

This section presents a detailed comparative benchmarking of simulation and experimental data, respectively in sections 4.2 and 5.2.1.1, to assess the accuracy of the developed simulation models and the performance of the force control method applied in peripheral milling tests.

As an initial observation, the maximum cutting force values in the y-direction were respectively 447N (see Figure 4.2) and 467N from simulation and experiments [76], resulting in 4.2% error in simulation. Moreover, Figure 5.8 presents a comparative analysis of both experimental and simulation form error data for the following supporting forces: 0N (unsupported), 60N, 120N, 200N and 280N. This comparison is made between X-230mm and X-10mm.

According to Figure 5.8, the form error values steadily decreased as the supporting force value increased, in both simulation and experimental data. The maximum errors between simulated and experimental values ranged from 0.028mm to 0.055mm. The simulation model generally overestimates the form error values in all cases. The consistent positive errors could come from dynamic vibrations on the workpiece, machine tool positioning accuracy (0.005mm), cutter radius error, including runout (0.014mm) and probing measurement errors (0.001mm) [76]. However, runout has not been considered in the model; this is because of the low resolution in acquisition of SLE measurements along the milling path.

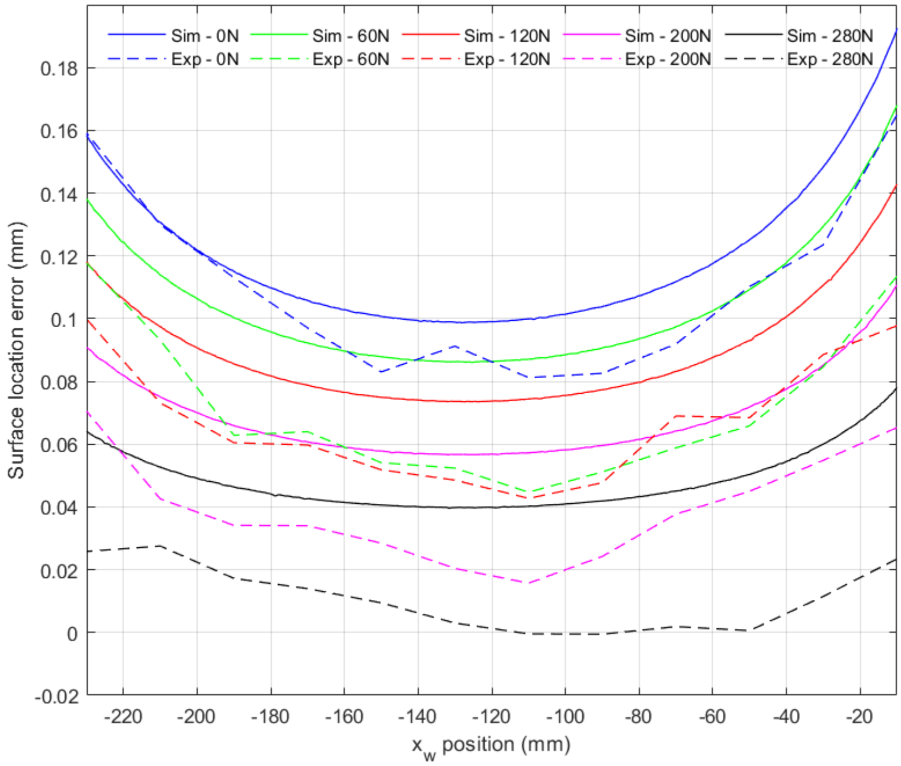

Figure 5.8 Comparative analysis of form error values between X-230mm and X-10mm – simulated (solid line) and experimental (dotted line) at various robotic support forces: 0N (unsupported), 60N, 120N, 200N and 280N.

Furthermore, the simulation model was compared with three form error prediction models proposed by Sun et al [76]. These models were proposed and investigated with the same cutting conditions used in these trials. They are presented below.

❖ Static deflection model: form errors are generated as a static deflection on the part, caused by both cutting forces F_c and robotic support force F_s. They can be calculated by Equation 5.3.

$$\delta(t) = \frac{F_s - F_c}{k_s}$$

Equation 5.3

where k_s is the static stiffness of the workpiece.

- Frequency domain model: form error values are dependent on both the overall forces acting upon the tool and the dynamic characteristics of the workpiece.

The overall force F_w on the workpiece acting upon the workpiece can be expressed as shown in the equation below

$$F_w(\phi) = F_s - F_c(\phi)$$

Equation 5.4

where ϕ is the instantaneous angle of immersion of the tool

The form error values can then be calculated in frequency domain using a Fourier series.

$$\delta(\omega) = F_w(\phi). \Phi(\omega) = \mathcal{F}\{F_w[\phi(t)]\}. \Phi(\omega)$$

Equation 5.5

where $\Phi(\omega)$ is the frequency response function of the workpiece.

The SLE values in time domain $\delta(t)$ can then be calculated through inverse Fourier transform of $\delta(\omega)$. At any given time as the cutter advances into the workpiece, the form error can be calculated by the equation below, where ω_n is the spindle speed in rad/s.

$$\delta(t) = \delta(\phi/\omega_n)$$

Equation 5.6

- Hybrid model: this model utilises both static and dynamic characteristics of the workpiece. It is assumed that the support robot exerts a static force on the structure while the cutting forces affect the system dynamically. The overall SLE can be calculated by the equation below.

$$\delta(t) = \delta_S - \delta_C$$

Equation 5.7

The deflection caused by the support force (δ_S) can be calculated by Equation 5.8, while the deflection caused by cutting forces are obtained using Equation

5.4~Equation 5.6 by substituting the total force $F_w[\phi(t)]$ exerted on the workpiece with the cutting force F_c.

$$\delta_S = \frac{F_S}{k_S}$$

Equation 5.8

Figure 5.9 presents a comparative bar graph of the maximum SLE discrepancies between experimental data and each model, for three cases: 'no support' (no robotic support), '120N support', and '280N support'. For both frequency domain and hybrid models, the static stiffness was identified for the unsupported workpiece, as shown in Figure 4.1, and the dynamic characteristics were measured as shown in Appendix C.5. Positive values here signify overestimation from the models when compared to the experimental results.

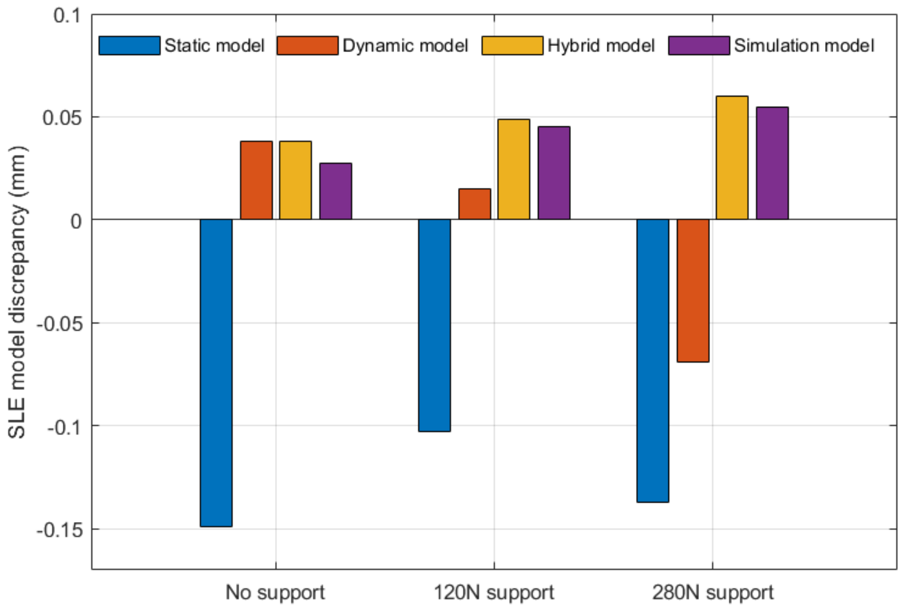

Figure 5.9 Comparative analysis of maximum SLE discrepancies between experimental data and four models, for three cases – unsupported, 120N support, 280N support.

According to Figure 5.9, it is not clear which model is the most accurate in determining form error values. Out of the three models formerly proposed in [76], the hybrid one was found to be the most reliable out of the three in his investigations, as it was consistently overestimating. In that regard, the model results presented in this thesis are slightly better in that they consistently overestimate, but do not provide the smallest discrepancies.

A further look at comparative results in Figure 5.8 reveals that the difference between simulated and experimental results is consistent for cases where the workpiece is supported (60N, 120N, 200N, 280N); the average discrepancy for these cases is around 0.03mm. In comparison, the average discrepancy for the unsupported workpiece is around 0.01mm. This signifies a correlation between cases where the workpiece was supported. This observation may be due to the fact that the impact of the robotic support on the static stiffness of the workpiece had not been investigated up until now; the static stiffness profile of the unsupported workpiece was adopted for all cases in simulation environment. It is therefore important to investigate how the static stiffness changes under different static loadings.

Unfortunately, the static stiffness of the workpiece was not experimentally measured as it ought to be; nevertheless, it is possible to analytically investigate their values. With the robotic support, the workpiece static stiffness changes from k_0 (for the unsupported workpiece) to k_s, which is much higher, as shown in Figure 5.10.

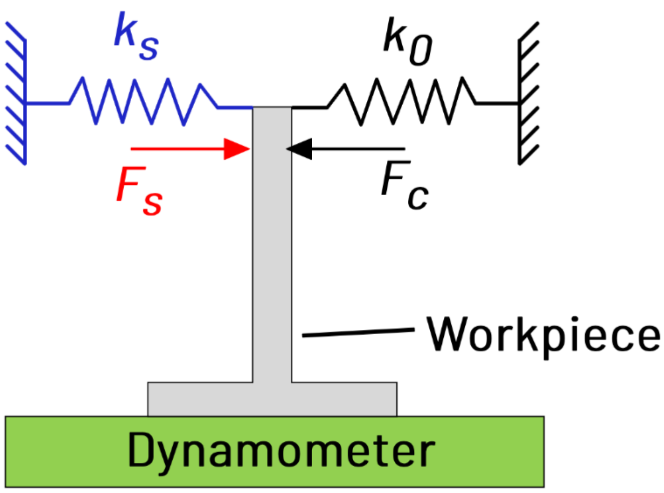

Figure 5.10 Workpiece static stiffness change due to the robotic support.

According to Figure 5.10, the support force and cutting force are each therefore under different static stiffness; the updated relationship between the surface location error, the cutting forces, the support forces and the static stiffnesses, is shown in Equation 5.9.

$$SLE = \frac{F_c}{k_s} - \frac{F_s}{k_0}$$

Equation 5.9

For a given static loading of F_s, the static stiffness can therefore be obtained by deriving it as shown below, at any point across the milling path.

$$k_s = F_c \times \frac{1}{\frac{F_s}{k_0} + SLE}$$

Equation 5.10

For each set of experimental results, a parabolic fit was made; these fits can be observed in Appendix C.6 (see Figure 6.8). Table 6.4 provides a point-based summary of the interpolated values of SLE values for each force. These values are substituted into Equation 5.10 to obtain the static stiffness values. For the unsupported workpiece, the maximum experimental cutting force value is used as F_c; this value is 467N [76]. Figure 5.11 presents the static stiffness of the workpiece obtained in two ways between X-230mm and X-10mm: experimentally (as explained in section 3.2.2.3) and analytically (through Equation 5.10). Figure 5.11 shows that there is about a 20% difference between both profiles.

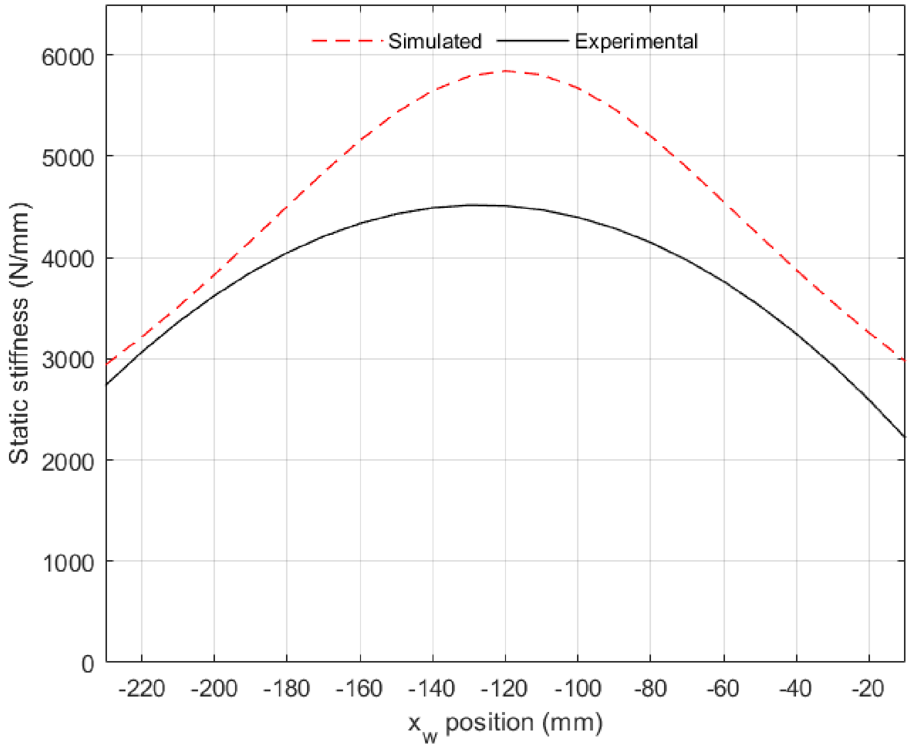

Figure 5.11 Comparative analysis of static stiffness profiles between X-230mm and X-10mm for the unsupported workpiece – experimentally obtained (solid line) and analytically determined (red dotted line).

Furthermore, based on the simulations carried out in section 4.2.2, there was only a 3% increase in cutting forces from 0N (unsupported) to 280N. It is therefore assumed that F_c is constant for the supported cases (60-280N) when computing the static stiffness values and the computed static stiffness values are given in Table 6.5, and presented in Figure 5.12.

According to Figure 5.12, the static stiffness profiles follow a Gaussian pattern. Moreover, there is an increase of 10-28% in static stiffness from the unsupported case to the supported case; however, there is no direct correlation between the support force and the value of the static stiffness. The average static stiffness under robotic support shows a 20% increase from the unsupported case.

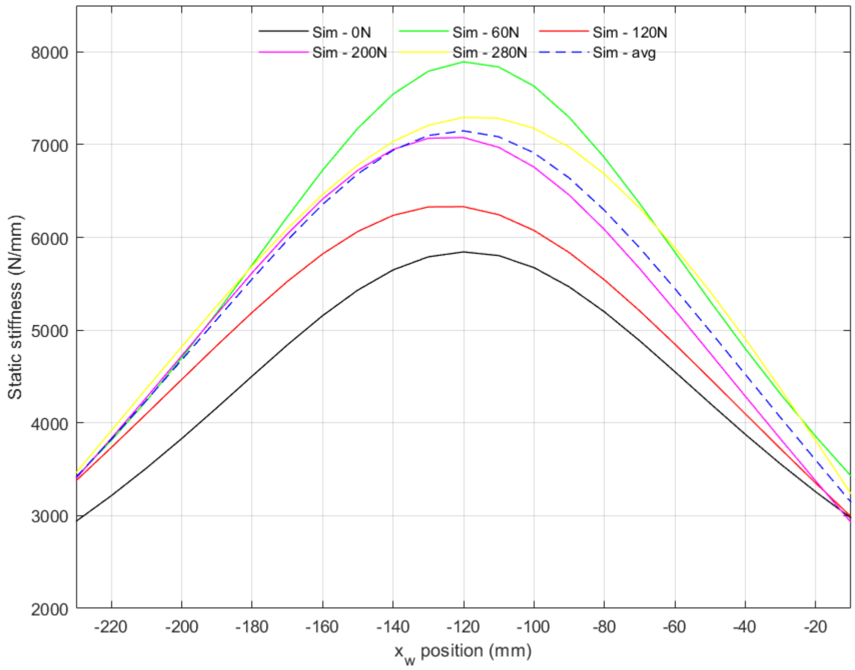

Figure 5.12 Analytically determined static stiffness profiles various robotic support forces: 0N (unsupported), 60N, 120N, 200N, 280N. The average stiffness profile for supported cases is also plotted in blue dotted lines.

An updated simulation is obtained by feeding these individual static stiffness profiles for each static loading, and the simulated form error values are obtained and compared against the experimental results, as shown in Figure 5.13.

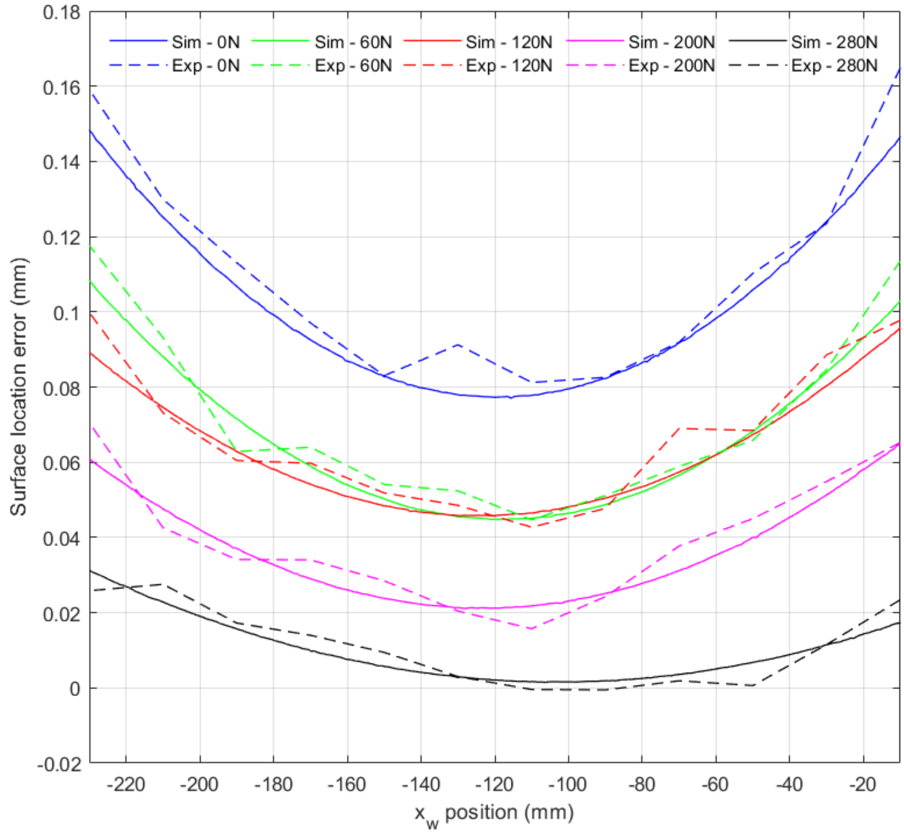

Figure 5.13 Comparative analysis of form error values between X-230mm and X-10mm – updated simulation data (solid line) and experimental (dotted line) at various robotic support forces: 0N (unsupported), 60N, 120N, 200N and 280N.

As shown in Figure 5.13, the updated simulation results are a lot more in line with the experimental results. In fact, the model now underestimates on average by about 4%. This highlights the importance of knowing the static characteristics of the workpiece under different loadings.

A further comparison is made between the updated model, its previous iteration, and the three models proposed by Sun et al [76]. This comparison is presented in Figure 5.14, where the maximum discrepancies between each model and experimental values are highlighted. The former iteration is referred to as *'Early Proposed Model'* (EPM) and the updated model as *'Newly Proposed Model'* (NPM). With the updated model, there is a 62% average improvement in accuracy from the initial model. Moreover, out of all five models, the updated model yielded, in all three loading scenarios, the highest accuracy (when compared to experimental results).

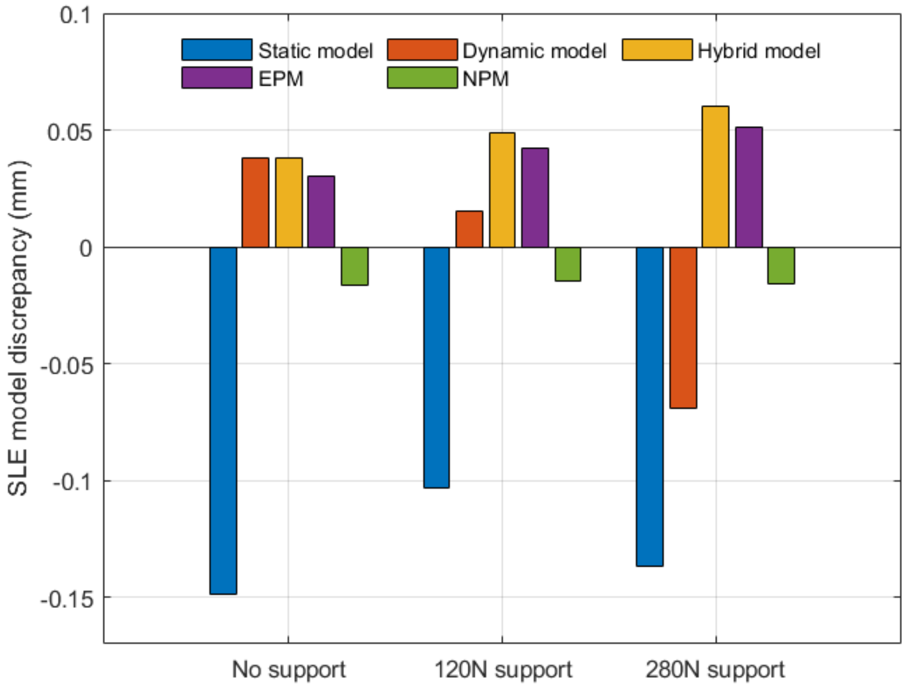

Figure 5.14 Comparative analysis of maximum SLE discrepancies between experimental data and five models, for three cases – unsupported, 120N support, 280N support.

Furthermore, simulations were run with the average static stiffness profile (blue dotted line in Figure 5.12). This is to determine how accurate the form errors can be in supported cases, without having to measure the static stiffness for each static loading. Form error results are obtained in Figure 5.15. The simulated cases are generally lining up with the experimental cases except from the case with 120N of robotic support.

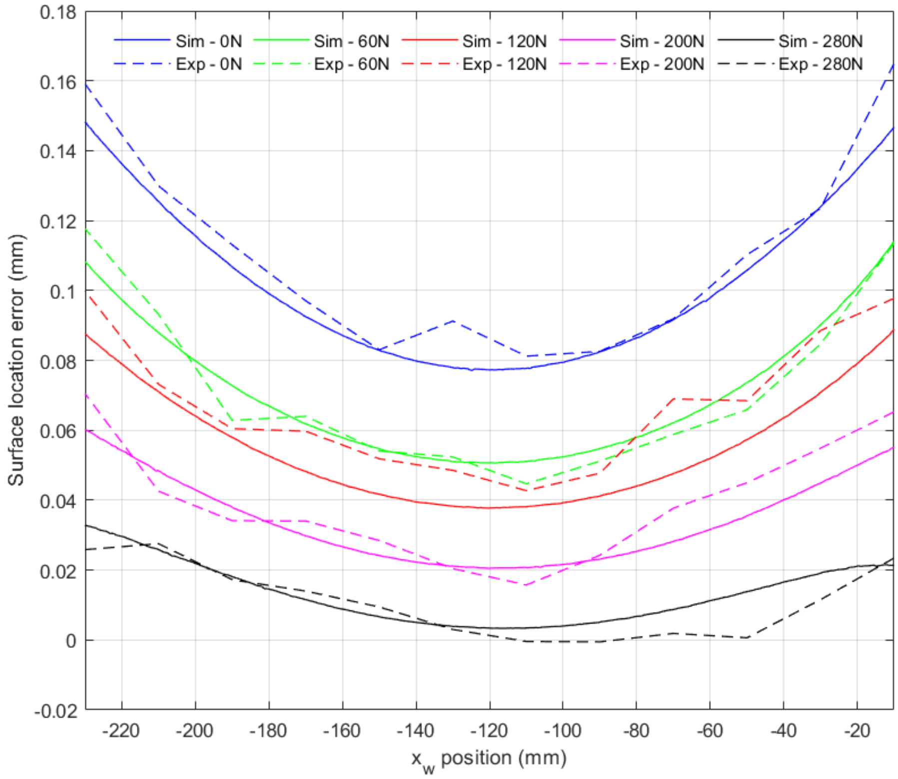

Figure 5.15 Comparative analysis of form error values between X-230mm and X-10mm – updated simulation data (solid line) and experimental (dotted line) at various robotic support forces: 0N (unsupported), 60N, 120N, 200N and 280N.

A further comparison with previous iterations of simulation results is given in the bar chart in Figure 5.16. This iteration is referred to as *'Newly Proposed Model-mean'* (NPM-m) because of the average static stiffness value used. Out of the 6 models compared, it is the second-most accurate model, behind the NPM, with a 56% improvement from the early proposed model (EPM), only 6% less accurate than NPM. This may decrease the number of static stiffness measurements before approximating form error values and configuring control methods to minimise these errors.

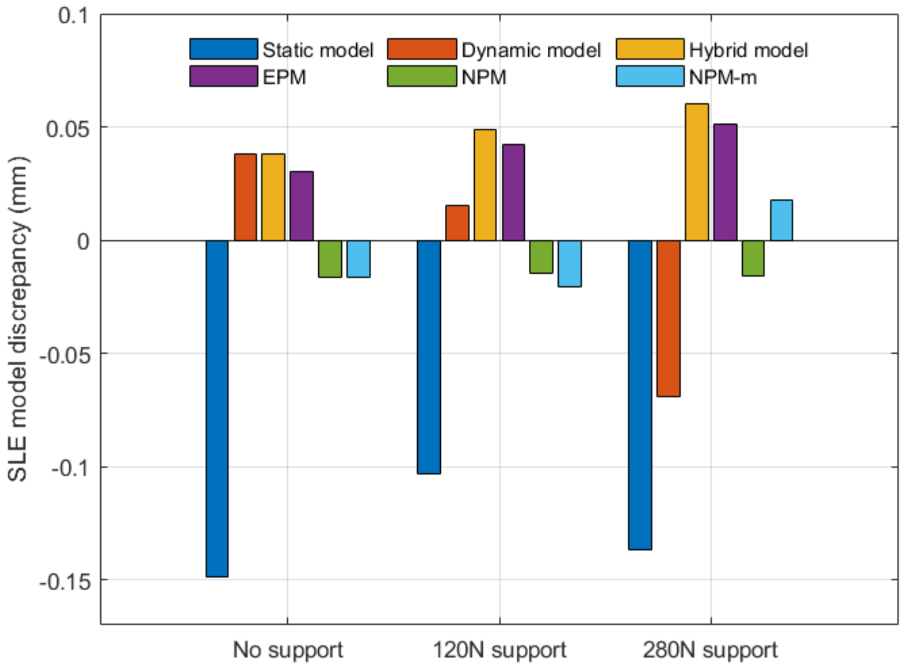

Figure 5.16 Comparative analysis of maximum SLE discrepancies between experimental data and five models, for three cases – unsupported, 120N support, 280N support.

5.2.2 Pocket milling trials

Further trials were carried to assess the efficacy of the PID force control on form error values in pocket milling. 8-pocket, L-shaped aluminium profiles were machined on a SORALUCE FX1200 as the Staubli TX-90 robot provided supporting force at the back face of the parts (Figure 3.8). A new end effector was designed, made of a rubber pad to support the floor of each pocket. It is important to mention that, unlike the peripheral milling tests, where the roller was moving and following the milling tool, the rubber pad was fixed throughout the machining of each pocket and progressively moved to the next pocket locations. Coolant was used in these trials to avoid built up edge on the tool. The same control approach was implemented here.

Figure 5.17 SORALUCE machining setup for pocket milling.

In machining trials, the selection of cutting parameters is very crucial to strike a good balance between productivity and avoidance of unstable cuts. The objective of this round of experimental trials is to determine whether the implementation of a force controlled robotic support can substitute the selection of conservative cutting parameters, in order to both minimise form errors and achieve a high productivity in cutting trials. Two sets of machining conditions were therefore selected: aggressive (high productive conditions) and conservative (moderate cutting conditions) and outlined in Table 5.1. Three parts were machined, as explained below.

- Aggressive unsupported (AU): the workpiece is machined in high productive conditions without robotic support.
- Conservative unsupported (CU): the part is machined in moderate cutting conditions without robotic support.
- Aggressive supported (AS): the part is machined in high productive conditions with robotic support of 60N at the backface of each pocket.

The support force was not determined analytically as cutting force coefficients were not determined for these cutting coefficients (Al7075-T6 was used in this set of trials instead of Al6082-T6 used in peripheral milling trials). The force value was selected with the sole purpose of providing robotic support with no contact loss.

Machining conditions	**Aggressive**	**Conservative**
Workpiece material	Aluminium 7075-T6	
Spindle speed (rpm)	4000	
Depths of cut for roughing (mm) - axial/radial	29.5/2	
Feed per tooth for roughing (mm)	0.30	0.15
Stock allowance for finishing (mm) - bottom/side walls	0.5/0.2	
Feed per tooth for finishing (mm)	0.075	
Cutting tool	3 flutes; diameter = 16mm; corner radius = 4mm; cutting length = 32mm; helix angle = 30°.	

Table 5.1 SORALUCE machining conditions.

Figure 5.18 shows the maximum form error values for pocket floors across all three parts, out of 72 probing measurements per workpiece. The lowest value was recorded in aggressive-supported case (AS), with a 63% decrease in form error from the conservative-unsupported case (CU). This shows that, despite the high productive conditions, the force control method yielded the best results on the pocket floors; this finding is further strengthened with the fact that, in "aggressive" conditions, there is an overall increase of 37% in productivity during milling (because of the high feed per tooth in roughing).

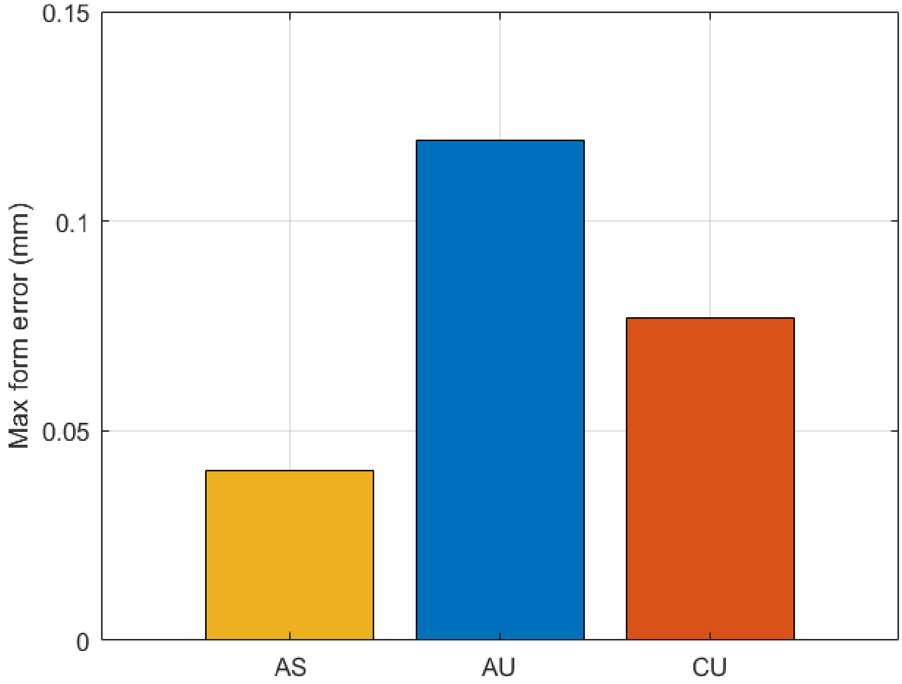

Figure 5.18 Comparison of maximum form errors measured on pocket floors in three case scenarios: AS (Aggressive supported), AU (Aggressive unsupported) and CU (Conservative unsupported).

However, the same results were not observed with side walls. Figure 5.19 shows the maximum form error values for side walls across all three parts. The best results (6% decrease in error) were rather achieved with moderate cutting conditions without robotic support. The use of robotic support only achieved a 1% reduction in SLE. One of the possible reasons was the inadequacy of the designed end effector in pocket milling; the applied force was only in the floor direction.

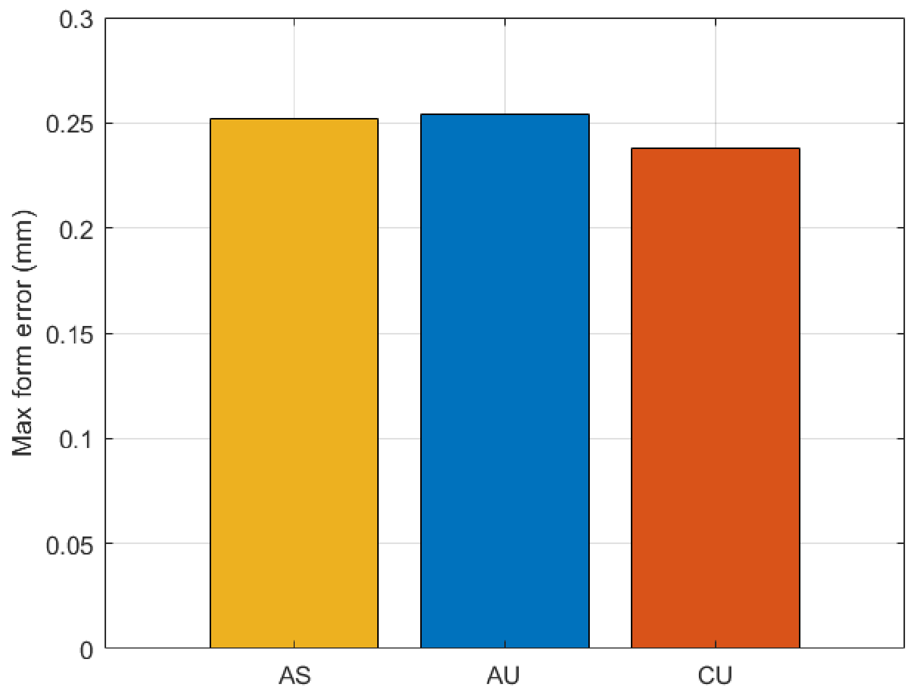

Figure 5.19 Comparison of maximum form errors measured on pocket side walls in three case scenarios: AS (Aggressive supported), AU (Aggressive unsupported) and CU (Conservative unsupported).

5.3 Dual robot collaboration

5.3.1 Motivation of the dual robot system

In this section, the concept of a *dual robot collaboration* is investigated. It consists of the addition of a collaborative robot in a robotic cell. In the last chapter, the collaborative robot was used to exert a supporting force at the backface of a thin-walled part during peripheral and pocket milling operations. The support robot, through its contact with the part, provided an overall increase in stiffness and damping to the structure, leading to a significant reduction of the frequency response on the part, irrespective of the supporting force applied (see Appendix C.5). In a similar setup like mirror milling, the contact between the supporting head and the workpiece affects the contact stiffness and boundary conditions of the system and influences the stability of the system during milling operations. [144]

Moreover, not only is the dynamic behaviour affected, but the addition of a supporting force to the system affects the form error incurred in the machining process. For example, in peripheral milling, as shown in Figure 5.7, there is a noticeable decrease in form error as milling tests were carried out with increasing support forces. In fact, the form error decreased by 69% by increasing the supporting force from 0N (no support from the collaborative robot) to 280N exerted by the supporting robot.

One of the first instances of a collaborative robot in robotic milling was implemented by Torres et al. [10], where a KUKA LBR iiwa robotic arm was used as a collaborative robot. The machining robot was a KUKA KR270 2700 Quantec Ultra. The experimental results showed that the robotic support countered the push off created by the cutting forces on the workpiece. This resulted in the part being brought closer to the programmed depth of cut, hence reducing form error values of the thin-walled part during machining by 50%. However, no compensation technique was developed and implemented on the system.

A similar setup is hereby proposed with two robotic arms, as illustrated in Figure **5.20**. The control strategies are implemented on the Z-position of the collaborative robot end effector in order to minimise form error values in milling operations.

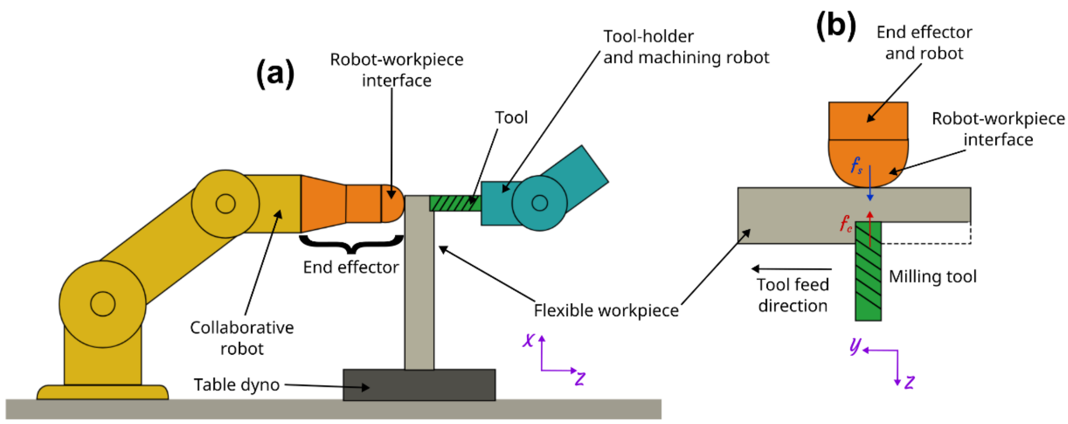

Figure 5.20 **Conceptual illustration of robotic assisted form error control during robotic milling. (a) Side view; (b) top view, showing the cutting force f_c and robot support force f_s.**

The main prerequisite for this setup to be operational is the maintenance of contact between the back face of the workpiece and the robot-workpiece interface (as shown in Figure **5.20**). This can only be ensured through the following conditions being satisfied.

- ❖ The collaborative robot needs to exert a force against the workpiece. This is monitored by a load cell attached to the supporting robot end effector. The loss of contact may cause a drastic change of the local damping and stiffness on the workpiece.
- ❖ The workpiece needs to be pushed against the robot-workpiece interface. This is dependent on the direction of the cutting forces exerted on the workpiece during milling operations. As forces acting upon the tool and workpiece are opposite to one another, this implies that cutting forces acting on the tool must be positive for the workpiece to be pushed towards the supporting robot. This is in fact the cornerstone of the solution, without which this solution cannot be successfully implemented. This is later ensured by a careful selection of the cutting tool geometry.
- ❖ Both robotic end effectors should be aligned coaxially. The mirror-synchronous support of the collaborative robot reduces workpiece deformation [20] and prevents distortion errors caused by misaligned robots.

It is also important to note that only dry milling conditions are considered in this dual robot configuration.

5.3.2 Dual robot configuration

As shown in Figure 5.21, the machining setup considered here is made up of an ABB IRB6640 robotic arm (milling robot) and a STAUBLI TX-90 robotic arm (support or collaborative robot). They are to be set up in a robotic cell to work and move synchronously, and effectively work as a mirror milling system, able to perform single-sided milling along curved or straight paths. However, in the simulation section, only straight paths were investigated.

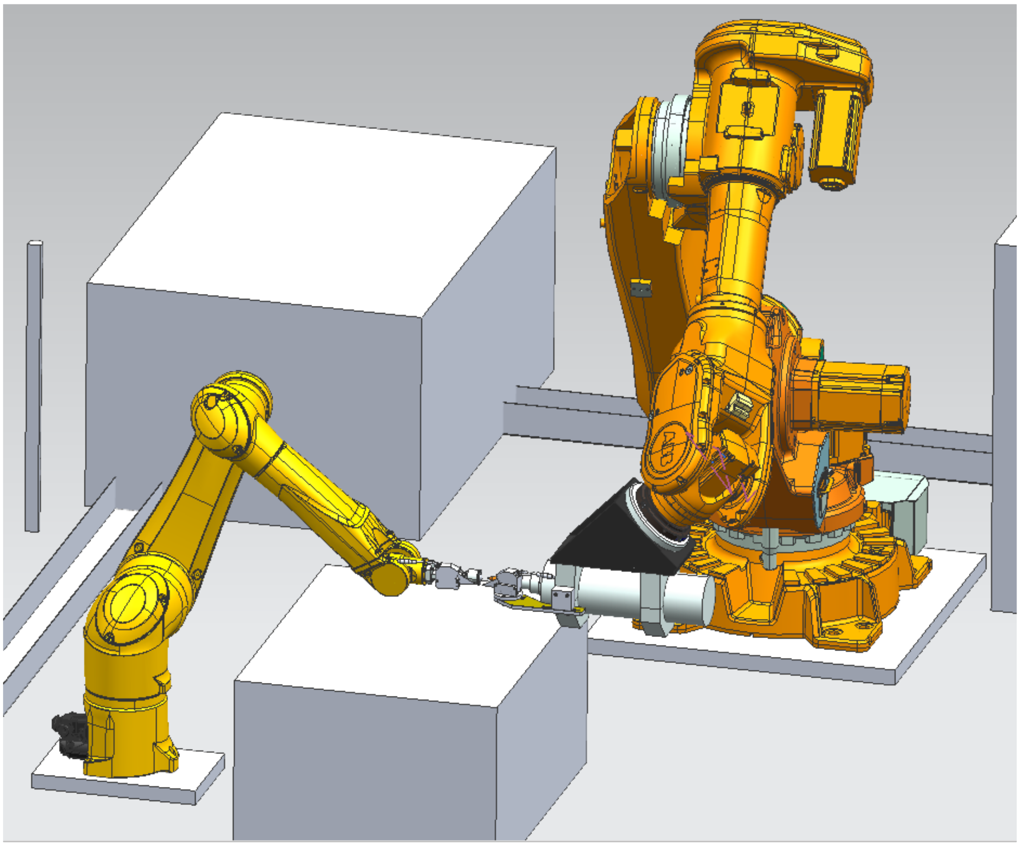

Figure 5.21 3D rendering of robot integration - STAUBLI TX-90 (left); ABB IRB6640 (right).

A third-party controller is needed to control both movements of the two robots above mentioned. The controller chosen is a Beckhoff controller. It is used to both control the robots and as the hub to implement the control approaches for active form error control in machining trials. Moreover, the controller is to be used to compute every 100ms the coordinates of the collaborative robot from the position of the milling robot.

5.3.3 Choice of equipment

A closer look at the dual robot configuration reveals the use of different end effectors and sensors, as shown in Figure 5.22. This equipment is necessary for the implementation of the active form error measures developed in the upcoming sections.

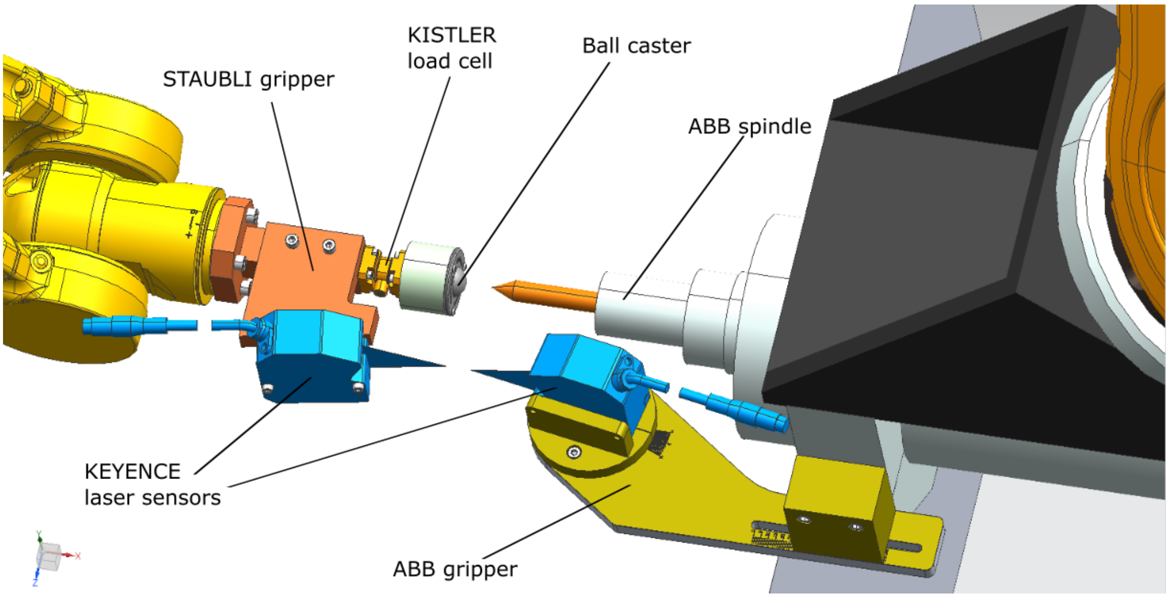

Figure 5.22 Components of the experimental setup.

5.3.3.1 Ball caster

The ball caster is to be used as the primary point of contact between the workpiece and the collaborative robot. In past applications, as presented in section 5.2, two types of end effectors were used as end effectors to provide robotic support in peripheral and pocket milling conditions (see Appendix C.3); however, they had some restrictions.

In pocket milling, the rubber pad was used to provide stationary support when a pocket was machined; once a specific pocket was machined, the support robot would then change location to provide support for the next pocket.

In peripheral milling, a rubber roller was used, enabling the robotic support to both be localised and follow the milling tool along the workpiece. This was very effective with simple milling paths (along a straight line) but proved to be ineffective for more complex paths. Moreover, the low hardness of the roller led to plastic deformation when the end effector is pushed against the workpiece. This resulted in some irregularities in the support force applied by the robot (see Figure 2.5). Moreover, the high coefficient of friction of the rubber roller led to spikes upon the initial motion of the robot (see Figure 5.3).

It is therefore important to select an end effector that provides increased mobility and a lower coefficient of friction. The ball caster was hence selected, allowing 3D motion across the backface of the workpiece, and a smaller surface contact with the workpiece, preventing spikes during the motion of the robot. The ball caster chosen is made of copolymer acetal to avoid marks on the workpiece.

5.3.3.2 Force sensors

Similar to the machine-robot collaboration presented in the previous chapter, a KISTLER 9317C load sensor is to be used and attached directly to the ball caster. In previous applications, it was used to measure the contact force between the workpiece and the support robot; however, in the application, it is used to ensure that there is contact between the ball caster and the workpiece. It is therefore expected for its data reading to be non-null throughout the milling operations. Its force data is not used in the control measures developed.

In addition to the previous load cell, a table dyno (KISTLER 9255C) is to be used to measure the overall forces acting on the workpiece. It is fitted on the machining table and the workpiece mounted on it (see Figure 5.20). This force data will be used to implement the force minimisation method, one of the error compensation methods developed and presented in earlier sections of this thesis.

5.3.3.3 Thickness sensors

The remaining wall thickness is a crucial input in the implementation of the thickness control method (TCM) presented in section 3.4.4 and investigated in section 4.3. Thickness measurements are commonly conducted using ultrasonic [145], [146], [147], [148], [149], electromagnetic [150], [151], positional [15], [152], [153], and optical [154] methods. In the conceptual design of dual robot setup, two KEYENCE laser displacement sensors are proposed to be mounted on both robots to measure the wall thickness during milling operations (see Figure 5.22). However, it is important to determine experimentally the best thickness sensor in future research.

5.3.4 Workpiece material

The workpiece material of choice in the dual robot system is Aluminium 6082-T6. Its structural properties were presented in section 3.2.2. A thin-walled workpiece will be fixed to the table dyno mounted on the machining table, just as shown in Figure 5.20.

5.3.5 Challenges with the setup

The dual robot setup presented in the previous sections is currently under completion (at the time this manuscript is written). A contractor has been hired to complete the commissioning of the cell; however, it is not yet complete, due to some challenges encountered. The main bottleneck is the synchronisation between both robots, as there is currently an error in computing the STAUBLI coordinates from the ABB robot coordinates via the Beckhoff controller.

As a result, no experimental tests have been carried out to validate the simulation results obtained in section 4.3 through FMM and TCM control methods.

5.4 Summary

This chapter has presented a novel investigation into the use of force-controlled robotic support for reducing form errors in milling operations. Through a systematic evaluation of peripheral and pocket milling trials, the results have demonstrated the significant influence of controlled robotic support on machining accuracy. Additionally, a comprehensive benchmarking analysis was conducted to assess the accuracy of the developed simulation models against experimental results, providing further validation of the approach and the simulation results in Chapter 4.

Key observations from this study include:

- The localised support provided by the collaborative robot induces a static deflection of the workpiece towards the milling tool, effectively increasing the axial depth of cut. This was confirmed by experimental trials where an increase in the supporting force from 0N (unsupported) to 280N led to a 69% reduction in average form error values (Figure 5.7), validating earlier findings in [19].
- The implementation of PID force control further improved machining accuracy by minimising variations in form error values across the workpiece.

As shown in Figure 5.6, the force-controlled approach resulted in a 50% reduction in the amplitude of form errors compared to cases where the robotic support was applied but not actively controlled.

- ❖ The robustness of the force control method was further assessed in pocket milling under harsher cutting conditions, with an increased material removal rate. Despite the more aggressive machining parameters, the force-controlled robotic support still yielded the best performance, reducing maximum form error values by 47% (Figure 5.18). However, this improvement was primarily observed on pocket floors, with no significant effect on pocket side walls, highlighting an area for further investigation (Figure 5.19).
- ❖ A detailed benchmarking analysis was carried out, comparing experimental results with multiple simulation models to evaluate their predictive accuracy. While all models overestimated form error values to some extent, the newly proposed model, which accounts for variations in static stiffness under different robotic support forces, provided the highest accuracy, with an average improvement of 62% over the initial simulation model (Figure 5.14). This underscores the importance of incorporating realistic stiffness variations in machining simulations.

Beyond these findings, this chapter has also introduced the dual robot collaboration concept, proposing an advanced machining setup where two robotic arms work synchronously to actively compensate for machining deviations. While the experimental validation of this system is still in progress, the proposed framework lays the groundwork for a future extension of robotic-assisted milling, with the potential to further enhance machining precision.

Future investigations may focus on extending these findings to face milling operations, continuing the exploration of more active form error control methods in robotic support and its broader applications in precision machining. In the next chapter, a summary of the research is given as well as areas of future investigations beyond the findings of this thesis.

Chapter 6

Discussion

6.1 Summary of thesis

This thesis explores the use of collaborative robots in robotic-assisted milling to improve machining accuracy, focusing on form error reduction in both conventional CNC and robotic milling systems. In the introductory chapter, the research motivation is established, highlighting the increasing adoption of industrial robots in manufacturing and the challenges they face in achieving high machining accuracy, particularly for thin-walled parts. The chapter identifies the key limitations of robotic machining, such as positional errors and low stiffness, which hinder precision. These challenges lead to the exploration of robotic-assisted milling as a solution, with the aim of investigating active form error control using collaborative robots. Two novel compensation methods, force minimisation and thickness control, are proposed to address positional inaccuracies and workpiece deformations.

The second chapter reviews existing literature on robotic milling and robotic-assisted milling, providing a comprehensive overview of the development of robotic machining technologies. The chapter examines the advantages of industrial robots, such as flexibility of use, large working envelopes, and multi-station capabilities, which make them attractive alternatives to conventional CNC machines. However, the limitations of robots, particularly in terms of positional accuracy and structural stiffness, are highlighted. Various error reduction methods are explored, including optimisation techniques such as robot trajectory modification and augmentation strategies like the addition of sensors and secondary robotic systems. The chapter concludes with a gap analysis, identifying the need for active form error control in robotic-assisted milling, particularly using collaborative robots.

The theoretical framework in chapter three delves into the key concepts underlying the research, including the dynamics of milling operations, cutting force models, and form error modelling. The chapter discusses the factors influencing form errors in robotic milling, such as cutting forces, workpiece material properties, and static stiffness. Two novel error control methods—force minimisation and thickness control—are introduced, aiming to mitigate the errors caused by positional inaccuracies in robotic milling. These methods are framed within the broader context of control theory, providing a foundation for the subsequent simulation and experimental work presented in later chapters.

Chapter four presents the simulation studies that evaluate the effectiveness of the proposed error control methods. The simulations investigate peripheral and face milling operations, examining the impact of robotic support forces and various machining conditions on form errors. A comparative analysis of the force minimisation and thickness control methods is conducted, with the latter demonstrating superior performance in reducing form errors. The chapter also explores the influence of robotic position errors, workpiece stiffness, force limits on the robotic end effector and other machining parameters, on the accuracy of the milling process, providing valuable insights into the potential of these control methods to improve robotic milling.

In chapter five, the experimental setup and validation tests are described, focusing on the machine-robot collaboration setup. The use of a collaborative robot with force control algorithms is detailed, and the results from peripheral and face milling trials are presented. Although the experimental validation was not fully completed at the time of writing, the tests demonstrate the potential for the proposed control methods to reduce form errors. The chapter also discusses the challenges encountered in the experimental setup of dual-robot configuration and outlines plans for future work to complete the validation of the control strategies.

6.2 Conclusions

In this thesis, approaches to mitigate form errors in robotic milling were investigated. It can be concluded that:

1. The introduction of a support robot greatly improves the productivity of machining in both conventional CNC milling.

The introduction of a support robot significantly enhances machining productivity in both conventional CNC milling due to its ability to minimise form errors and stabilise the workpiece during high-speed operations. Experimental pocket milling trials in section 5.2.2 demonstrate that utilising a force-controlled robotic support allows for more aggressive cutting conditions while maintaining superior machining accuracy. In high-productive scenarios, robotic support led to a 63% decrease in form error on pocket floors compared to conservative conditions without robotic assistance, while also increasing overall milling productivity by 37%. This improvement is attributed to the robot's capacity to counteract deformations and vibrations that typically arise in thin-walled and flexible structures, reducing machining errors without the need for overly conservative cutting parameters.

2. Thickness data is more efficient than force data in assessing more accurately position errors on the milling robot head.

The thickness control method consistently outperformed the force minimisation method across various parameters to test their robustness. Upon the introduction of robotic position errors, TCM caused the cobot to compensate errors almost entirely while FMM only managed to achieve a 10% reduction in form error from unsupported milling trials.

6.3 Original contributions

This thesis presents two key contributions to the field of robotic-assisted milling, with a particular focus on enhancing machining precision through the active integration of collaborative robots. The original contributions to knowledge found in this work are as follows:

1. Machine-robot collaboration to achieve reduced form error and increase stability in peripheral and pocket milling.

The novel contribution of this research lies in the implementation of an active force control algorithm within a machine-robot collaborative setup. Unlike traditional approaches that employed passive support systems, this research introduces a collaborative robot actively regulating the support force applied to the back face of the workpiece during CNC-robot collaboration. Experimental results show that the force control system significantly reduces form errors by minimising deformation during machining. In peripheral milling, a reduction in form error by 69% was achieved compared to traditional unsupported milling when increasing the support force value from 60N to 280N, while in pocket milling, form error reduction was 63% with a support force of 60N.

These improvements were directly correlated with the ability of the collaborative robot to maintain a constant support force, providing a dynamic and localised solution to form error control.

2. Investigation of novel form error control measures on the collaborative robot in face milling.

This research introduces two innovative error compensation strategies designed to improve machining accuracy in robotic milling: Force Minimisation and Thickness Control. Both methods were rigorously tested in simulation and validated experimentally, demonstrating their effectiveness in reducing form errors in robotic milling tasks.

❖ Force Minimisation method (FMM): the FMM aims to reduce the overall force acting on the workpiece by dynamically adjusting the robotic support forces during milling. Simulations showed that, under robotic end effector force limits, the FMM reduced form errors by 9% when compared to unsupported robotic milling. This method was effective across various cutting conditions, including varying workpiece stiffness and robot position errors.

- Thickness Control Method (TCM): the thickness control method, a first in the field, leverages real-time measurements of the remaining workpiece thickness to adjust the position of the collaborative robot. Under force limits, this control method proved to be highly effective, reducing form errors by up to 62% across different scenarios, including rectangular and circular milling paths. The TCM outperformed the FMM in terms of form error reduction, especially under complex machining conditions involving varying material properties and robot-induced position errors. In comparison to unsupported milling trials, the TCM significantly improved dimensional accuracy, by dynamically correcting errors due to the deformation of thin-walled structures.

These contributions represent a substantial advancement in robotic-assisted milling, particularly in terms of improving machining precision and mitigating form errors during high-precision tasks. The integration of active form error control strategies via collaborative robots offers a significant improvement over traditional methods, especially for applications requiring consistent dimensional accuracy across a wide range of materials and cutting conditions. These methods not only reduce reliance on static error compensation but also ensure adaptive and robust error correction during real-time machining processes.

6.4 Publications

The thesis findings were published and presented in the conference proceedings. Below are the published conference proceedings available in the literature:

1. C. Sun, P. L. F. Kengne, A. Barrios, S. Mata, and E. Ozturk, ‘Form error prediction in robotic assisted milling’, *Procedia CIRP*, vol. 82, pp. 491–496, 2019, doi: 10.1016/j.procir.2019.04.335.

2. P. L. F. Kengne, C. Sun, S. Pope, and E. Ozturk, 'Integration and demonstration of force controlled support in pocket milling', *Procedia CIRP*, vol. 101, pp. 158–161, 2020, doi: 10.1016/j.procir.2021.05.151.

6.5 Discussions and future works

Based on the findings throughout this research, it is important to point out the following aspects to look into as future works.

1. Validation in dual-robot configurations

One of the key future directions involves extending these findings to dual-robot configurations. Although the concept has been developed, experimental trials in dual-robot face milling are still in progress. Future work should focus on finalising the dual robot setup and testing the system's performance. The concept holds the potential to further reduce form errors by enabling synchronised corrective actions between two robotic arms.

Additionally, the influence of tool geometry and various cutting conditions on form error control needs further exploration. While the current study focused on specific parameters, such as radial depth of cut and cutting speed, future experiments should systematically vary these parameters to understand their impact on the effectiveness of the control strategies. This could help optimise the system for different machining setups and materials.

Furthermore, it would be interesting to test the control methods on various workpiece shapes. In effect, under force limits from the end effector, the performance of the thickness control method was limited; one way to deal with it is by decreasing the wall thickness of the original workpiece, leading to lower static stiffness and more leverage for the cobot to push the workpiece and compensate errors during milling operations. Furthermore, a broader application of the proposed control methods across curved surfaces and various workpiece materials could enhance their industrial relevance.

2. Exploration of additional control methods

The current work used PID control to regulate robotic support forces and wall thickness errors, but future research should investigate alternative control algorithms to further enhance robustness. Adaptive control methods, model-based controllers, and machine learning approaches could potentially provide more precise error compensation, especially under complex machining conditions.

3. Sensor integration and real-time error compensation

The effectiveness of the thickness control method can be further enhanced by integrating advanced sensors, such as optical or ultrasonic sensors, for real-time feedback. Future investigations should explore multi-sensor systems to improve the accuracy of remaining thickness measurements and allow for more responsive and dynamic compensation during milling operations.

4. Industrial adoption and scalability

Finally, the practical application of this research in industrial settings remains a crucial next step. Future work should explore the scalability of the proposed methods to real-world production environments, focusing on cost-effectiveness, ease of integration, and compatibility with existing robotic systems and CNC machines. Collaborative projects with industrial partners could help accelerate the development of commercially viable robotic-assisted milling systems.

Appendix A

Cutting force coefficients

A.1 Al 6082-T6 trial results

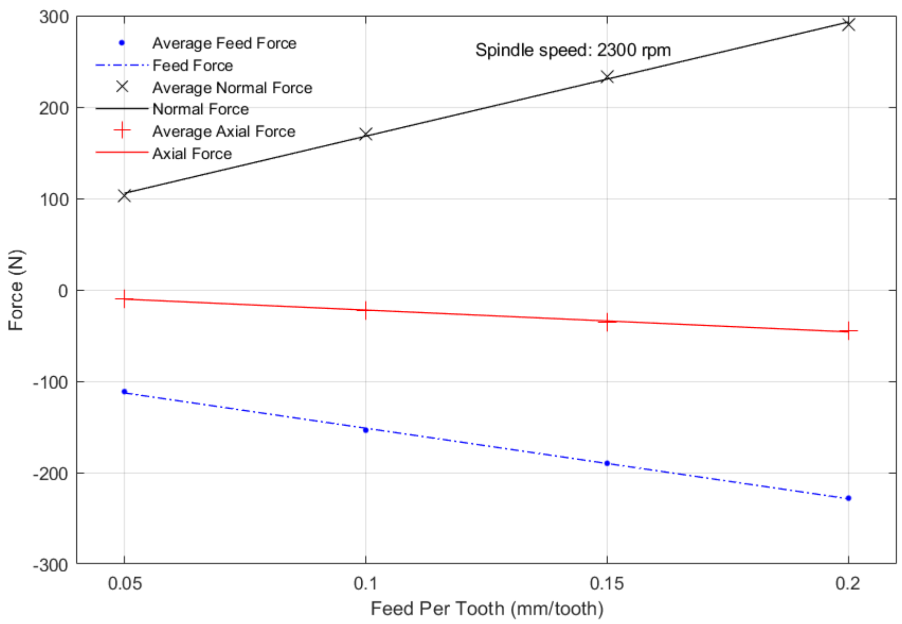

Figure 6.1 Experimental results showing the proportionality between the feed-per-tooth and the average cutting forces for a three-flute tool with 35° of helix angle, at 2300rpm.

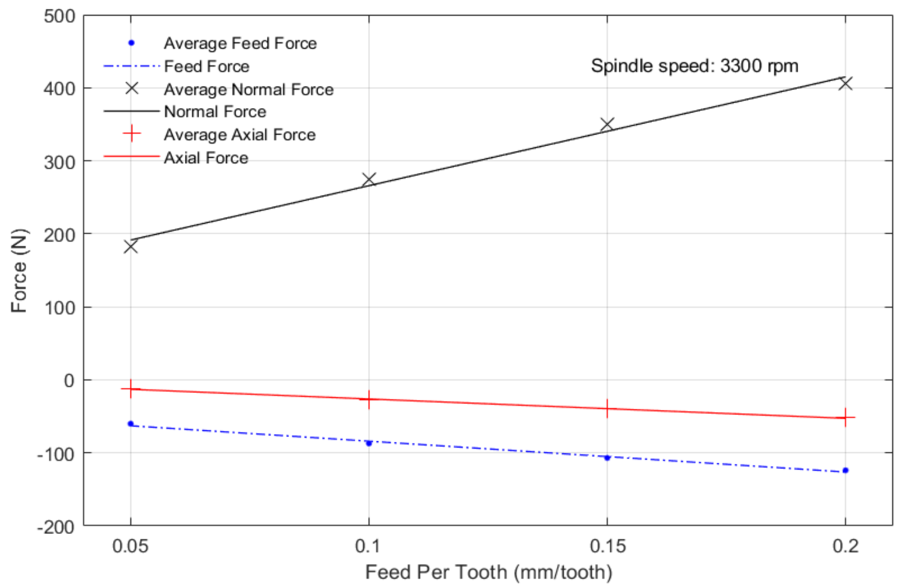

Figure 6.2 Experimental results showing the proportionality between the feed-per-tooth and the average cutting forces for a three-flute tool with 35° of helix angle, at 3300rpm.

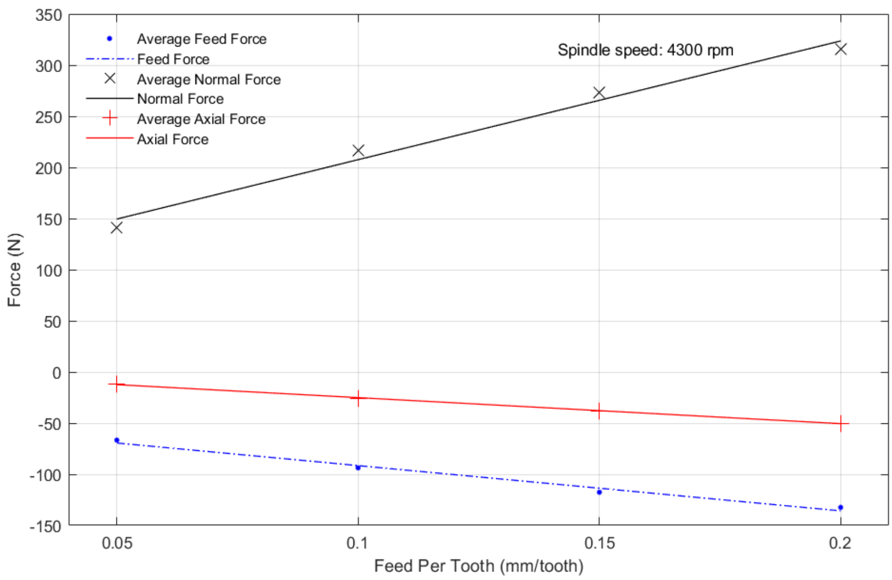

Figure 6.3 Experimental results showing the proportionality between the feed-per-tooth and the average cutting forces for a three-flute tool with 35° of helix angle, at 4300rpm.

Appendix B

Simulation work

B.1 MATLAB code for milling force calculation

This code helps generate cutting forces in machining trials given machining conditions in MATLAB environment. As an output, a figure of cutting forces acting on the tool in all directions is obtained.

```
%%% Milling Force Simulation Algorithm %%%

%% Inputs %%

% Machine and Tool geometry %
N = 3; %%% number of flutes
pitch = 2*pi/N; %%% cutter pitch angle - in rad
helix = -35; %%% helix angle - in deg
beta = helix*pi/180.; %%% helix angle - in rad
D = 12; %%% diameter of cutting tool

% Cutting conditions %
c = 0.2; %%% feed rate - mm/rev-flute
n = 4300; %%% spindle speed - rpm
a = 2; %%% axial depth of cut - mm
w = n*pi/30.; %%% angular velocity - rad/s
b = 12; %%% radial depth of cut - mm
UpDown = -1; %%% -1 for up-milling; 1 for down-milling

if UpDown<0 %%% up-milling
    theta_start = 0; %%% start angle of immersion - in rad
```

```
        theta_exit = acos(1-(2*b/D)); %%% exit angle of immersion - in rad
    else %%% down-milling
        theta_start = pi-acos(1-(2*b/D)); %%% start angle of immersion - in rad
        theta_exit = pi; %%% exit angle of immersion - in rad
    end

    Vc = pi*D*n/1000.; %%% cutting speed - mm/min

    % Workpiece conditions - Cutting coefficients %
    Ktc = 773.87; %%% - N/mm^2 - 773.87
    Krc = 294.88; %%% - N/mm^2 - 294.88
    Kac = 133.19; %%% - N/mm^2 - 133.19
    Kte = 47.88; %%% - N/mm - 47.88
    Kre = 24.77; %%% - N/mm - 24.77
    Kae = -0.11; %%% - N/mm - -0.11


    %% Simulation Variables %%

    % Initialise the x-axis, angle or time %
    theta = [];
    time = [];

    % Feed %
    FS = n*c*N; %%% feed speed - mm/min
    CutDistance = 1; %%% Length of cut - mm
    MTime = (CutDistance/FS)*60.; %%% Machining Time - seconds
    TPF=n*N/60.;
    t_rev = 60./n; % time for one revolution

    % Integration angle - in deg %
    K = 1800; %%% number of angular integration steps - angle in deg
    % r = 5; %%% number of revolutions
    r = MTime/t_rev; %%% number of revolutions according to machining time
    delta_theta = r*2*pi/K;

    % Integration height %
    L = 100; %%% number of axial integration steps
    delta_a = a/L;



    %% Outputs %%

    % Cutting force history %
    Fx = []; %%% feed force dependant on angle of immersion
    Fy = []; %%% normal force dependant on angle of immersion
    Fz = []; %%% axial force dependant on angle of immersion
    F = []; %%% resultant force
    Ft = [];
    h1 = [];
```

```
% Cutting torque and power history %
Tc = []; %%% cutting torque
Pc = []; %%% cutting power



%% Angular integration loop %%
for i=1:K %%%
    theta(i) = i*delta_theta; %%% immersion angle of flute's bottom edge
    time(i) = theta(i)/w; %%% time elapsed
    Fx(i) = 0.0;
    Fy(i) = 0.0;
    Fz(i) = 0.0;
    Ft(i) = 0.0;
%     h1(i) = 0.0;
%     theta_start = 0; %%% start angle of immersion - in deg
%     theta_exit = 6.03*pi/180.; %%% exit angle of immersion - in deg - 6.03
    for k=1:N %%% calculate force contribution of all teeth
        theta1 = theta(i)+(k-1)*pitch; %%% immersion angle for tooth k
        theta2 = theta1; %%% memorise the present immersion
        for j=1:L %%% integrate along the axial depth of cut
            a_j = j*delta_a; %%% axial position
            theta2 = theta1-(2*tan(beta)/D)*a_j; %%% update the immersion angle due helix
            theta2 = mod(theta2,2*pi);

            if (theta_start<=theta2)&&(theta2<=theta_exit) %%% if the edge is cutting
                h = c*sin(theta2); %%% chip thickness at this point

                dFt = delta_a*((Ktc*h)+Kte); %%% differential tangential force
                dFr = delta_a*((Krc*h)+Kre); %%% differential radial force
                dFa = delta_a*((sign(helix)*Kac*h)+Kae); %%% differential axial force

                dFx = -dFt*cos(theta2)-dFr*sin(theta2); %%% differential feed force
                dFy = dFt*sin(theta2)-dFr*cos(theta2); %%% differential normal force
                dFz = -dFa; %%% differential axial force

                Fx(i) = Fx(i)+dFx; %%% sum all cutting forces contributed by all active edges
                Fy(i) = Fy(i)+dFy; %%% sum all cutting forces contributed by all active edges
                Fz(i) = Fz(i)+dFz; %%% sum all cutting forces contributed by all active edges
```

```
                Ft(i) = Ft(i)+dFt; %%% sum all cutting forces contributed by all active edges
            else
                h = 0;
                dFt = 0;
                dFr = 0;
                dFa = 0;
                dFx = 0;
                dFy = 0;
                dFz = 0;
            end
        end
    end
end



disp("Machining time: "+MTime+"s.")
disp("ABB robotic arm speed needed: "+FS/(60.)+"mm/s.")

figure(1)
%% Force vs. Time %%
plot(time,Fx, ...
    'DisplayName', 'Fx',"Color",'b','LineStyle','--')
hold on
plot(time,Fy, ...
    'DisplayName', 'Fy',"Color",'r','LineStyle','-.')
hold on
plot(time,Fz, ...
    'DisplayName', 'Fz',"Color",'k','LineStyle','-')
hold off
grid
% title("Forces")
xlabel('Simulation time (s)')
ylabel('Cutting force (N)')

legend('Location','northwest')
legend('Orientation','horizontal')
legend('boxoff')
```

B.2 MATLAB initialisation code for milling trials

This code is used to initialise machining conditions in MATLAB workspace that will be used to run milling simulations later on in SIMULINK environment.

```
%%% Milling Force Simulation Algorithm %%%
close all
clear all;

```

```
%% Inputs %%

% %%%--- PERIPHERAL MILLING ---%%%
%
% % Workpiece conditions - Cutting coefficients %
% Ktc = 1168; %%% - N/mm^2
% Krc = 632; %%% - N/mm^2
% Kac = 0; %%% - N/mm^2
% Kte = 0.75; %%% - N/mm
% Kre = 0.27; %%% - N/mm
% Kae = 0; %%% - N/mm
%
% % Machine and Tool geometry %
% N = 2; %%% number of flutes
% h1 = zeros(N);
% h1 = h1(1,:);
% pitch = 2*pi/N; %%% cutter pitch angle - in rad
% helix_deg = 25; %%
% helix = helix_deg*pi/180.; %%% helix angle - in rad
% D = 20; %%% diameter of cutting tool - mm
% CR = 0; %%% corner radius - mm
%
% % Cutting conditions %
% BlockThickness = 10; %%% initial block thickness - in mm
% c = 0.107; %%% feed rate - mm/rev-flute
% n = 7000; %%% spindle speed - rev/min
% % a = 10; %%% axial depth of cut - mm
% % b = 2; %%% radial depth of cut - mm


% %%%--- FACE MILLING ---%%%
%
% % Workpiece conditions - Cutting coefficients %
% Ktc = 773.87; %%% - N/mm^2
% Krc = 294.88; %%% - N/mm^2
% Kac = 133.19; %%% - N/mm^2
% Kte = 47.88; %%% - N/mm
% Kre = 24.77; %%% - N/mm
% Kae = -0.11; %%% - N/mm
%
% % Machine and Tool geometry %
% N = 3; %%% number of flutes
% h1 = zeros(N);
% h1 = h1(1,:);
% pitch = 2*pi/N; %%% cutter pitch angle - in rad
% helix_deg = -35; %%
% helix = helix_deg*pi/180.; %%% helix angle - in rad
% D = 12; %%% diameter of cutting tool - mm
% CR = 0; %%% corner radius - mm
%
% % Cutting conditions %
% BlockThickness = 10; %%% initial block thickness - in mm
% c = 0.2; %%% feed rate - mm/rev-flute
% n = 4300; %%% spindle speed - rev/min
```

```
% a =2; %%% axial depth of cut - mm
% b = 12; %%% radial depth of cut - mm

%%%--- POCKET MILLING ---%%%

% Workpiece conditions - Cutting coefficients %
Ktc = 660; %%% - N/mm^2
Krc = 250; %%% - N/mm^2
Kac = 180; %%% - N/mm^2
Kte = 0; %%% - N/mm
Kre = 0; %%% - N/mm
Kae = 0; %%% - N/mm

% Machine and Tool geometry %
N = 3; %%% number of flutes
h1 = zeros(N);
h1 = h1(1,:);
pitch = 2*pi/N; %%% cutter pitch angle - in rad
helix_deg = 30; %%
helix = helix_deg*pi/180.; %%% helix angle - in rad
D = 16; %%% diameter of cutting tool - mm
CR = 4; %%% corner radius - mm

% Cutting conditions %
BlockThickness = 10; %%% initial block thickness - in mm
c = 0.3; %%% feed rate - mm/rev-flute
n = 4000; %%% spindle speed - rev/min
a =29.5; %%% axial depth of cut - mm
b = 2; %%% radial depth of cut - mm

omega = n*pi/30.; %%% angular velocity - rad/s
w = n*pi/30.; %%% angular velocity - rad/s
freq = n*N/60.; %%%tooth passing frequency
t2 = 1/freq;
freq1 = [1 2 3 4 5]*freq;

% Cutting speed and feed %
Vc = pi*D*n/1000.; %%% cutting speed - mm/min
FS = n*c*N; %%% feed speed - mm/min
% CutDistance = 250; %%% Length of cut - mm
CutDistance = 500; %%% Length of cut - mm
MTime = (CutDistance/FS)*60.; %%% Machining Time - seconds
% MTime = 0.6;
factor = c/0.1;

%% Simulation Variables %%

% Integration angle - in deg %
delta_t1 = 1/(50*100); %% freq - 100KHz; gives 12002 instead of 402 samples like CutPro
delta_t = 30*delta_t1;
iters = round(60/(delta_t*n),0); %%% number of angular integration steps - angle in deg
```

```
% iters = 1800; %%% number of angular integration steps - angle in deg
cycles = 5*10*5; %%% number of revolutions - normally 5
Time2 = ((cycles+1/iters)/omega*2*pi);
%% (cycles+1/K)/pd.omega*2*pi
delta_theta = cycles*2*pi/iters;

% Integration height %
% delta_a = 0.01; %%% in mm
% L = a/delta_a;

L = 30;
% delta_a = a/L; %%% in mm

disp("ABB robotic arm speed needed: "+FS/(60.)+"mm/s.")
```

B.3 SIMULINK code for SLE calculation in milling trials

The code below is implemented in SIMULINK to calculate cutting forces for various types of milling operations, whether they may be face or peripheral milling, and straight or bull-nose end milling.

```
function [a1,b1,h,Fx,Fy,Fz]= fcn(a, b,da,db,phi,dx,dy,dz,N,pitch, c, D, L, helix, UpDown,h1, CR, Ktc, Krc, Kac, Kte, Kre, Kae)

a1 = a+da;
b1 = b+db;

delta_a = a1/L;
% L = a1/delta_a; %%% steps along axial depth


%%% Initialising forces
Fx = 0.0;
Fy = 0.0;
Fz = 0.0;
h = h1;
dh = 0.0;

if UpDown==-1
            phi_s = 0; %%% start angle of immersion - in rad
            phi_e = acos(max(min(1-(2*b1/D),1),-1)); %%% exit angle of immersion - in rad
        else
            phi_s = pi-acos(max(min(1-(2*b1/D),1),-1)); %%% start angle of immersion - in rad
            phi_e = pi; %%% exit angle of immersion - in rad
        end
```

```


    for k=1:N %%% calculate force contribution of all teeth
        phi1 = phi+(k-1)*pitch; %%% immersion angle for tooth k
        phi2 = phi1; %%% memorise the present immersion

        for z=1:L %%% integrate along the axial depth of cut

            a_j = z*delta_a; %%% axial position

            % Calculate kappa in the for loop -- DONE
            if CR>0
                if a_j < CR
                    kappa = acos((CR-a_j)/CR);
                    phi2 = phi1-(tan(helix)/CR)*a_j; %%% update the immersion angle due helix
                else
                    kappa = pi/2.;
                    phi2 = phi1-(2*tan(helix)/D)*a_j; %%% update the immersion angle due helix - version A
                end
            else
                kappa = pi/2.;
                phi2 = phi1-(2*tan(helix)/D)*a_j; %%% update the immersion angle due helix
            end

            phi2 = mod(phi2,2*pi);



            if (phi_s<=phi2)&&(phi2<=phi_e) %%% if the edge is cutting
                    % Generalise this to include bull-nose end milling -- DONE
                    if CR<=0
                        dh = dx*sin(phi2)+dy*cos(phi2)+c*sin(phi2); %%% chip thickness at this point - if negative FORCES ARE ZERO (CONTRIBUTION OF THAT TEETH
                    else

                        dh = dx*sin(phi2)*sin(kappa)+dy*cos(phi2)*sin(kappa)-dz*cos(kappa)+c*sin(phi2)*sin(kappa); %%% chip thickness at this point - bull-nose end milling
                    end

                if dh > 0
                    % Change and generalise these equations for bull-nose end
                    % milling by adding 1/sin (kappa) -- DONE
                    if CR<=0

                     dFt = delta_a*((Ktc*dh)+Kte); %%% differential tangential force
```

```
                     dFr = delta_a*((Krc*dh)+Kre); %%% differential radial force
                     dFa = delta_a*((sign(helix)*Kac*dh)+Kae); %%% differential axial force

                     dFx = -dFt*cos(phi2)-dFr*sin(phi2); %%% differential feed force

                     dFy = dFt*sin(phi2)-dFr*cos(phi2); %%% differential normal force

                     dFz = -dFa; %%% differential axial force
                    else

                    dFt = delta_a*((Ktc*dh)+Kte)/sin(kappa); %%% differential tangential force
                    dFr = delta_a*((Krc*dh)+Kre)/sin(kappa); %%% differential radial force
                    dFa = delta_a*((sign(helix)*Kac*dh)+Kae)/sin(kappa); %%% differential axial force

                    dFx = -dFt*cos(phi2)-dFr*sin(phi2)*sin(kappa)-dFa*sin(phi2)*cos(kappa); %%% differential feed force

                    dFy = dFt*sin(phi2)-dFr*cos(phi2)*sin(kappa)-dFa*cos(phi2)*cos(kappa); %%% differential normal force

                    dFz = dFr*cos(kappa)-dFa*sin(kappa); %%% differential axial force
                    end

                else
                    dh = 0;
                    dFt = 0;
                    dFr = 0;
                    dFa = 0;
                    dFx = 0;
                    dFy = 0;
                    dFz = 0;
                end

                Fx= Fx+dFx; %%% sum all cutting forces contributed by all active edges
                Fy=Fy+dFy; %%% sum all cutting forces contributed by all active edges
                Fz= Fz+dFz; %%% sum all cutting forces contributed by all active edges

            else
                dh = 0;
            end
        end
        h(k)=h(k)+dh;
```

```

end
```

B.4 SIMULINK code for finite element analysis

The code below is implemented in MATLAB to work out the static stiffness of the workpiece in MATLAB environment. This is done by having a FEA Euler-Bernoulli model of a simply supported beam; upon generation of the state space model, an input force is added to the system and the steady deflection at the top node is obtained; static stiffness is then obtained as a quotient of the force applied by the deflection measured.

```
%%% FEA Euler-Bernoulli model of a simply supported beam
% close all
clc

n1 = 22;          %%% The number of measurement points. Therefore there are n-1 mass elements - 22

%Al 6082-T6 - 250mm
l1 = 101.6e-3;    %%% Beam length = 1m / or height in y-direction -
b1 = 250e-3;      %%% Depth of beam = 0.22m/in x-direction
h2 = 9.5e-3;      %%% Width/Thickness of beam = 0.010m/in z-direction
ln1 = l1/(n1-1.);   %%% Length of each mass element = 0.1m
rho1 = 2700;      %%% Density (kg/m3) of mild steel - 7850; 2810 for Al7075-T6; 1410 for acetal; 2700 for Al6082-T6
E1 = 70000e6;    %%% Modulus of elasticity of mild steel - 210GPa; 71.7GPa for Al7075-T6; 2.7GPa for acetal;70GPa for Al6082-T6


%%% MAKE THE THICKNESS VARIABLE AND CHOOSE WHERE THE FORCE IS APPLIED %%%

%%% --- Make the thickness variable
%%% The nodes go from 1 (bottom segment) to n-1 (top segment)
thic1 = ones(1,n1-1);
MR_enabled=0; %% enable material removal

%%% material removal from vertical point i to point j (from the top) - 1 is to aim at the top %%%
i4 = 2;
j4 = 21; % force application point from the top

if MR_enabled>0
    for ii = i4:j4
```

```
            thic1(n1-ii)=thic1(n1-ii)-0.5;
        end
    end
    h3 = h2*thic1;% varying thickness

    %%% Choosing where the force is applied %%%
    % The size of u is 2*n1-1
    % The translational forces are access by choosing j so that Frobot is
    % applied to u(2*n-1-k, numel(t)) so that j = 1, 3, 5, ... (corresponding
    % to the 1st pt,2nd pt,nth pt from the top)
    Fpt = j4; % force application point from the top

    Mpt = Fpt; % point of measurement of displacement - same point of application
    % Mpt = 2; % point of measurement of displacement - different point of application

    %%% Setup variables
    K_dyno = 2e9; % stiffness of the table dyno
    Frobot = 25; % force applied by robot
    t_end = 5; % in seconds
    StaticDynamic = 0; % 0 for static


    %%% Assembles the Mass (M), Damping (C) and Stiffness (K) matrices
    %%% Note that the ordering of the elements in the vector X follows the
    %%% definition x1, theta1, x2, theta2, ..., xn, theta - where x is the
    %%% vertical displacement and theta is the angular displacement
    m = [];
    k = [];
    M = zeros(2*n1,2*n1);
    K = zeros(2*n1,2*n1);
    for ii = 1:n1-1
        S = b1*h3(ii);        %%% Cross section of beam
        I = b1*h3(ii)^3/12;   %%% Area moment of inertia of a rectangle


        m = (rho1*S*(ln1/2)/105)*[78 22*(ln1/2) 27 -13*(ln1/2);22*(ln1/2) 8*(ln1/2)^2 13*(ln1/2) -6*(ln1/2)^2;27 13*(ln1/2) 78 -22*(ln1/2);-13*(ln1/2) -6*(ln1/2)^2 -22*(ln1/2) 8*(ln1/2)^2];

        M(2*ii-1:2*ii+2,2*ii-1:2*ii+2) = M(2*ii-1:2*ii+2,2*ii-1:2*ii+2) + m;

        k = (E1*I/(2*(ln1/2)^3))*[3 3*(ln1/2) -3 3*(ln1/2);3*(ln1/2) 4*(ln1/2)^2 -3*(ln1/2) 2*(ln1/2)^2;-3 -3*(ln1/2) 3 -3*(ln1/2);3*(ln1/2) 2*(ln1/2)^2 -3*(ln1/2) 4*(ln1/2)^2];

```

```
    K(2*ii-1:2*ii+2,2*ii-1:2*ii+2) = K(2*ii-1:2*ii+2,2*ii-1:2*ii+2) + k;

end


%%% Uses Rayleigh damping
C2 = 1*(1*M + 0.00002*K);

%---- CLAMP SUPPORT ----%
% %%% Sets the clamp support boundary conditions
% K([1 2 2*n-1 2*n],:) = [];
% K(:,[1 2 2*n-1 2*n]) = [];
% C([1 2 2*n-1 2*n],:) = [];
% C(:,[1 2 2*n-1 2*n]) = [];
% M([1 2 2*n-1 2*n],:) = [];
% M(:,[1 2 2*n-1 2*n]) = [];

% %%% Creates the state space matrices, where the outputs are the list of
% %%% linear and angular displacements
% Ass = [-M\C -M\K;eye(2*n-4) zeros(2*n-4,2*n-4)];
% Bss = [inv(M);zeros(2*n-4,2*n-4)];
% Css = [zeros(2*n-4,2*n-4) eye(2*n-4)];
% Dss = zeros(2*n-4,2*n-4);

%---- CANTILEVER SUPPORT ----%

%%% Sets the cantilever support boundary conditions

% CODE TO REMOVE THETA1 FROM THE MATRIX %
K([2],:) = [];
K(:,[2]) = [];
C2([2],:) = [];
C2(:,[2]) = [];
M([2],:) = [];
M(:,[2]) = [];


K(1,1) = K(1,1)+K_dyno;

% ORIGINAL CODE %
% K([1 2],:) = [];
% K(:,[1 2]) = [];
% C([1 2],:) = [];
% C(:,[1 2]) = [];
% M([1 2],:) = [];
% M(:,[1 2]) = [];

%%% Creates the state space matrices, where the outputs are the list of
%%% linear and angular displacements

% % % REMOVING ONLY THETA1 BUT KEEPING X1 %
```

```
Ass = [-M\C2 -M\K;eye(2*n1-1) zeros(2*n1-1,2*n1-1)];
Bss = [inv(M);zeros(2*n1-1,2*n1-1)];
Css = [zeros(2*n1-1,2*n1-1) eye(2*n1-1); zeros(1,4*n1-2)]; %add dyno force
Css(2*n1,2*n1)=Css(2*n1,2*n1)+K_dyno;
Css1 = [Css(2*n1-2,:);Css(2*n1,:)]; %%% for Control design
% Css = [zeros(2*n-1,2*n-1) eye(2*n-1); zeros(2*n-1,2*n-1) zeros(2*n-1,2*n-1)]; %more rows to include forces as part of output
% Css = [zeros(2*n-2,2*n-2) eye(2*n-2)];
Dss = zeros(2*n1,2*n1-1); %just to add the base force
Dss1 = zeros(2,2*n1-1); %%% for Control Design
% Dss = [zeros(2*n-1,2*n-1); eye(2*n-1)]; %more rows to include forces as part of output
% Dss = zeros(2*n-2,2*n-2);
U0 = zeros(1,2*n1-3);

% % ORIGINAL CODE - REMOVING X1 AND THETA1 %
% Ass = [-M\C -M\K;eye(2*n-2) zeros(2*n-2,2*n-2)];
% Bss = [inv(M);zeros(2*n-2,2*n-2)];
% Css = [zeros(2*n-2,2*n-2) eye(2*n-2); zeros(2*n-2,2*n-2) zeros(2*n-2,2*n-2)]; %more rows to include forces as part of output
% % Css = [zeros(2*n-2,2*n-2) eye(2*n-2)];
% Dss = [zeros(2*n-2,2*n-2); eye(2*n-2)]; %more rows to include forces as part of output
% % Dss = zeros(2*n-2,2*n-2);
%


%%% Initialise simulation
t = 0:0.01:t_end; %simulation time



% u = [zeros(2*n1-3,numel(t)); Frobot*ones(1,numel(t)); zeros(1,numel(t))];
u = zeros(2*n1-1,numel(t));
u(2*n1-1-(2*Fpt-1),:)=Frobot*ones(1,numel(t));

x0 = zeros(4*n1-2,1);
[y,x] = lsim(Ass,Bss,Css,Dss,u,t,x0);
%
% % ORIGINAL CODE %
% G = ss(Ass,Bss,Css,Dss);
% t = 0:0.01:10; %simulation time
% u = [zeros(2*n-4,numel(t)); 120*ones(1,numel(t)); zeros(1,numel(t))];
% x0 = zeros(4*n-4,1);
% [y,x] = lsim(Ass,Bss,Css,Dss,u,t,x0);

H9=[];
dx1 = [];
Y_1 = [];
X_1 = [];
```

```
for jj = 1:size(t,2)
    Y_1(jj,1) = 0;
    X_1(jj,1) = y(jj,1);
    for ii = 2:n1
        a5 = 2*ii-2;
        X_1(jj,ii) = y(jj,a5);
        Y_1(jj,ii) = Y_1(jj,ii-1)+((ln1)^2-(X_1(jj,ii)-X_1(jj,ii-1))^2)^0.5;
    end
end

%%% Plot results
figure(1)
tiledlayout(3,3);

nexttile
a5 = 1;
text = "y1";
H9(1)=0;
dx1(1)=y(size(t,2),a5);
plot(t,1000*transpose(y(:,a5)),'DisplayName', text)
hold on

for ii = 1:n1-1
    a5 = 2*ii;
    b2 = ii+1;
    text = "y"+b2;
    H9(b2)=(b2-1)*ln1;
    dx1(b2)= y(size(t,2),a5);
    plot(t,1000*transpose(y(:,a5)),...
    'DisplayName', text)
    hold on
end
hold off
% %
grid
text = "Displacement at measurement points - "+Frobot+"N";
title(text)
xlabel('Time (s)')
ylabel('Displacement (mm)')
if n1<=20
    legend('Location','eastoutside')
end

nexttile(4)
a5 = 1;
text = "theta1";
% H(1)=0;
% dx(1)=y(size(t,2),a);
```

```
plot(t,zeros(1,size(t,2)),'DisplayName', text)
hold on

for ii = 1:n1-1
    a5 = 2*ii+1;
    b2 = ii+1;
    text = "theta"+b2;
%     H(b)=(b-1)*ln;
%     dx(b)= y(size(t,2),a);
    plot(t,transpose(y(:,a5)),...
    'DisplayName', text)
    hold on
end
hold off
% %
grid
text = "Angle at measurement points - "+Frobot+"N";
title(text)
xlabel('Time (s)')
ylabel('Angle (deg)')
if n1<=20
    legend('Location','eastoutside')
end

nexttile (7)
a5 = 2*n1;
b2 = 2*n1-1-(2*Fpt-1);
text = "Fz1";
plot(t,transpose(y(:,a5)),'DisplayName', "Fz (dyno)")
hold on
plot(t,u(b2,:),'DisplayName', "Fz (input)")
hold off
grid
title('Forces applied')
xlabel('Time (s)')
ylabel('Forces (N)')
legend('Location','eastoutside')

% figure(2)
nexttile(2,[3 2])

% plot(1000*dx,1000*H,'LineWidth',8,'DisplayName', "Practical")
% hold on

if StaticDynamic == 1

for jj=1:size(t,2)
    hold all
    plot(1000*X_1(jj,:),1000*Y_1(jj,:),'k','LineWidth',1)
%     hold on
%     grid
    text = "Dynamic deflection at "+Frobot+ "N";
    title(text)
%     xlim([0 l1*1250])
```

```
        ylim([0 l1*1250])
        xlabel('x (mm)')
        ylabel('y (mm)')
%       legend('Location','eastoutside')
        pause(0.001)
        if jj<size(t,2)
            plot(1000*X_1(jj,:),1000*Y_1(jj,:),'r','LineWidth',2)
            hold off
        end
    end
    % hold off
    else
%       plot(1000*dx,1000*H,'LineWidth',8)
    %%% for variable profile %%%
    for kk=1:n1-1
        T0 = 10;
plot(1000*X_1(size(t,2),kk:kk+1),1000*Y_1(size(t,2),kk:kk+1),'k','LineWidth',T0*thic1(kk))
        hold on
    end
    hold off
    grid
    text = "Static deflection at "+Frobot+ "N";
    title(text)
    % xlim([0 l1*1250])
    xlim([0 0.1])
    ylim([0 l1*1250])
    xlabel('x (mm)')
    ylabel('y (mm)')
    end
    Force_error = (1-y(size(t,2),a5)/u(b2,size(t,2)))*100;
    Mass_removed = (1-(sum(b1*(l1/(n1-1.))*h3,"all")/(b1*h2*l1)))*100;
    Deflection_amplitude = y(size(t,2),a5-(2*Mpt))*1000;
    Stat_Stiffness = Frobot/(Deflection_amplitude);
    data = [Mass_removed Deflection_amplitude Force_error];
    disp("The error between applied force at the top of the beam and the force measured by the dyno is: "+Force_error+"%.")
    disp("Mass removed: "+Mass_removed+"%.")
    disp("Force applied: "+Frobot+"N.")
    disp("Static deflection: "+Deflection_amplitude+"mm.")
    disp("Static stiffness: "+Stat_Stiffness+"N/mm.")
```

B.5 SIMULINK results for rectangular milling paths

The figure below shows the milling results for a rectangular milling path given changes in local workpiece static stiffness and position errors from the milling robot.

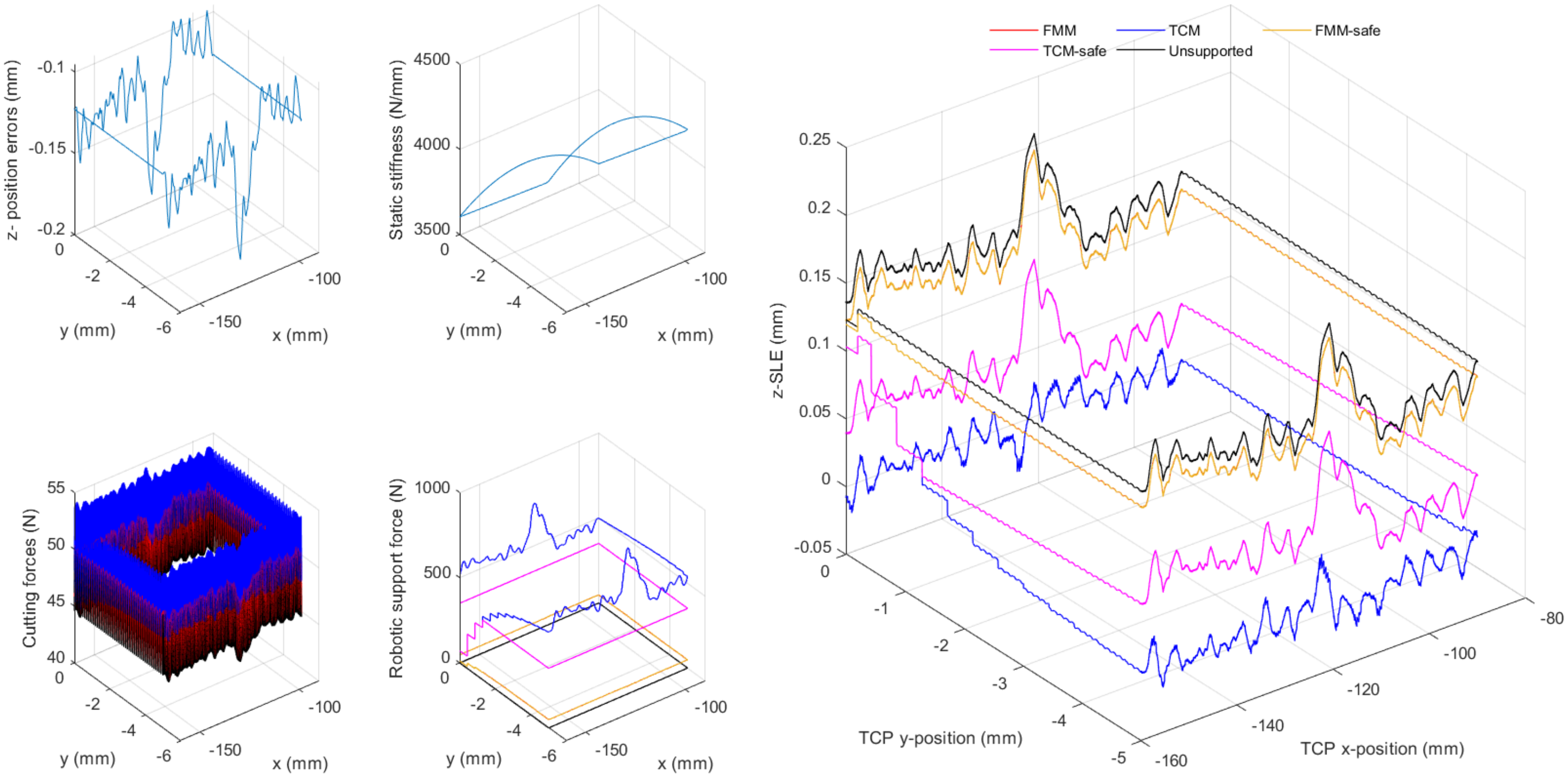

Figure 6.4 Simulation results with rectangular milling paths.

B.6 SIMULINK results for circular milling paths

The figure below shows the milling results for a circular milling path given changes in local workpiece static stiffness and position errors from the milling robot.

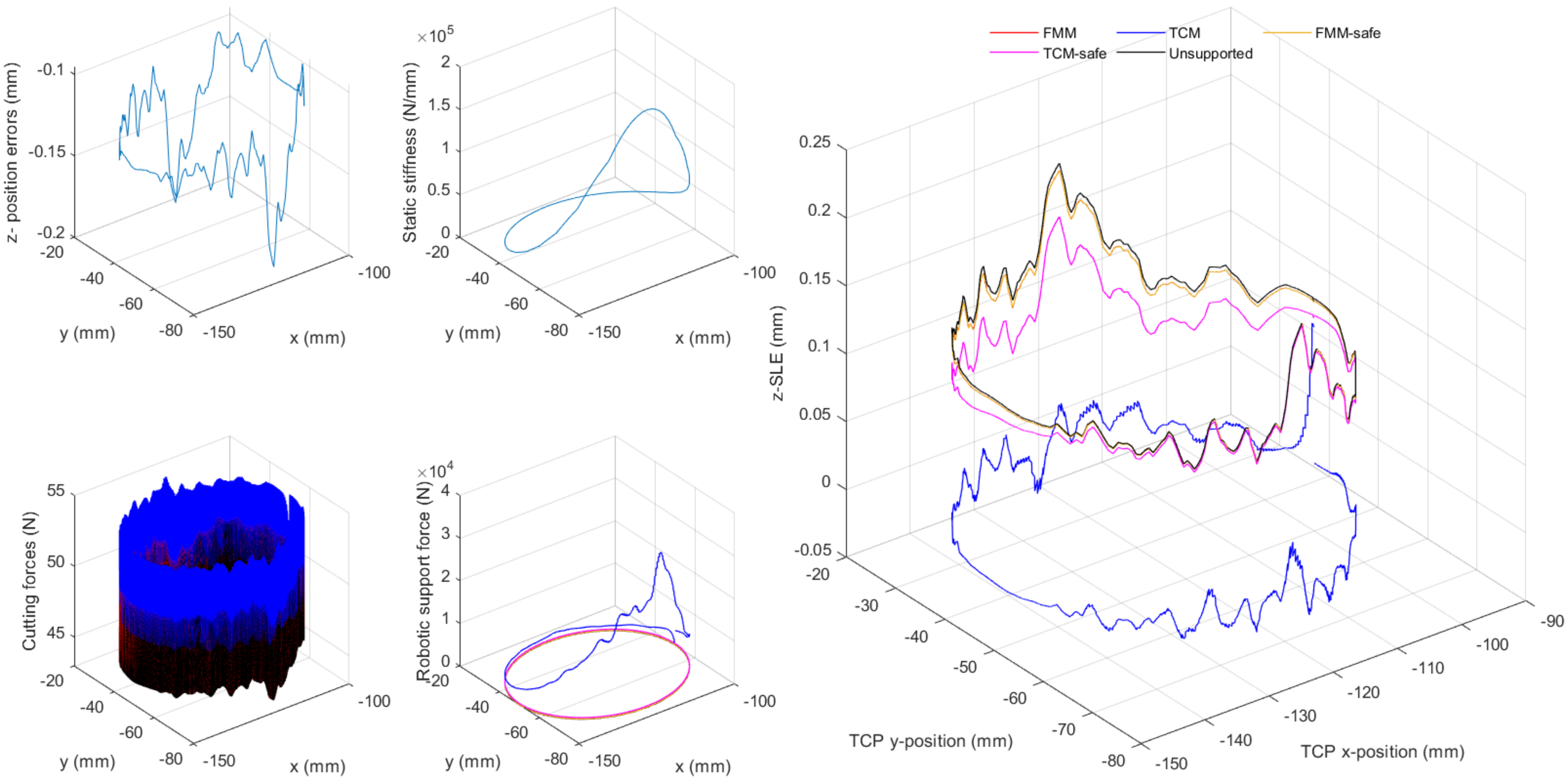

Figure 6.5 Simulation results with circular milling paths.

Appendix C

Experimental tests & benchmarking

C.1 Machine – robot collaboration setup - STAUBLI TX-90 robotic arm

Specifications	Details
Maximum reach (between axis 1 and 5)	900 mm
Load capacity at nominal speed	6kg
Maximum speed at load centre of gravity	10.42 m/s
Low speed in manual mode	0.25 m/s
Placing repeatability (ISO 9283)	± 0.03 mm

Table 6.1 STAUBLI TX-90 technical specifications.

C.2 Force sensor

Specifications	Axis	Details
Dimensions (mm)		25x35x30
Operating temperature (°)		-40 … 120
Calibrated measuring ranges (kN)	F_x; F_y	-0.5 … 0.5
	F_z	-3 … 3
Sensitivity (N/V)	F_x; F_y	49.78; 49.72
	F_z	300.07
Natural frequency (kHz)	$f_n(x)$; $f_n(y)$	5.6
	$f_n(z)$	20

Table 6.2 KISTLER 9317C load cell technical specifications.

C.3 End effectors used in machine-robot collaboration

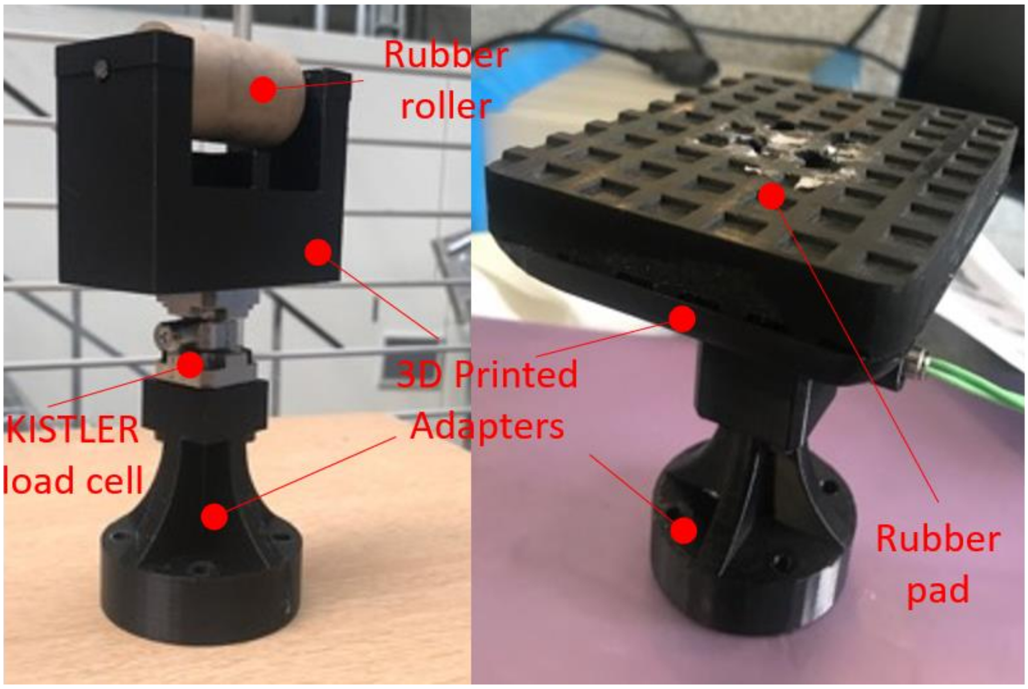

Figure 6.6 STAUBLI robot grippers – peripheral milling (left); pocket milling (right).

C.4 Force control PID discretisation

The transfer function of the PID force controller is given below.

$$G_{pid}(s) = K_p\left(1 + \frac{1}{T_i s} + T_d s\right)$$

Equation 6.1

To discretise the control algorithm, a z-transform is applied by using a zero holder

$$G_{pid}(z) = \mathcal{Z}\left\{\frac{1 - e^{-Ts}}{s} K_p\left(1 + \frac{1}{T_i s} + T_d s\right)\right\}$$

Equation 6.2

$$G_{pid}(z) = (1 - z^{-1})\mathcal{Z}\left\{\frac{1}{s}K_p\left(1 + \frac{1}{T_i s} + T_d s\right)\right\}$$

Equation 6.3

$$G_{pid}(z) = K_p + \frac{K_i}{1 - z^{-1}} + K_d(1 - z^{-1})$$

Equation 6.4

With $K_i = K_p \frac{\mathrm{T}}{T_i}$ and $K_d = K_p \frac{T_d}{T}$.

The discretisation formula is obtained by deriving the difference equation, as shown below.

$$\frac{Y_c(z)}{f_e(z)} = \frac{C(z)}{E(z)} = G_{pid}(z) = K_p + \frac{K_i}{1 - z^{-1}} + K_d(1 - z^{-1})$$

Equation 6.5

$$C(z)(1 - z^{-1}) = E(z)\left(K_p(1 - z^{-1}) + K_i + K_d(1 - 2z^{-1} + z^{-2})\right)$$

Equation 6.6

$$C[k] = C[k-1] + K_p(e[k] - e[k-1]) + K_i e[k] + K_d(e[k] - 2e[k-1] + e[k-2])$$

Equation 6.7

$$C[k] = C[k-1] + e[k]\big(K_p + K_i + K_d\big) - e[k-1]\big(K_p + 2K_d\big) + e[k-2](K_d)$$

Equation 6.8

Replacing C and E respectively by Y_c and f_e into Equation 6.8 (as shown in Equation 6.5) gives the discretisation formula

$$Y_c[k] = f_c[k-1] + K_p.\left\{f_e[k]\left(1 + \frac{T}{T_i} + \frac{T_d}{T}\right) - f_e[k-1]\left(1 + 2\frac{T_d}{T}\right) + f_e[k-2]\left(\frac{T_d}{T}\right)\right\}$$

Equation 6.9

C.5 FRF results

Direct transfer functions were measured in five different workpiece locations for no support, 120N support, 200N support force and 280N support force. The transfer functions at point 1 are shown below. Higher dynamic stiffness is seen for cases with support; there is a 95% decrease in amplitude from the unsupported workpiece to the one where 120N of robotic support force is applied. However, there is no significant influence of the change in support force on the FRF; the difference in amplitudes is relatively small.

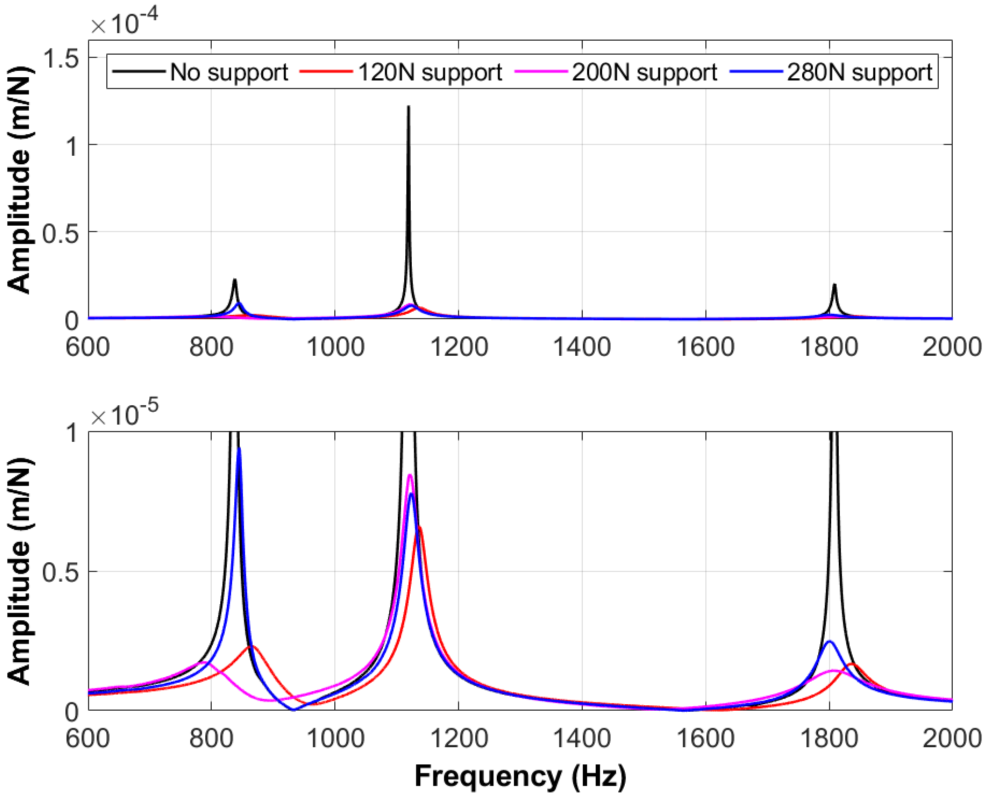

Figure 6.7 FRF comparison with different robotic support forces applied – general comparative graph (top); zoomed-in view on supported cases (bottom).

C.6 Experimental SLE results and analytical results

x-value	Unsupported	60N	120N	200N	280N
-10	0.1649069	0.1135051	0.0977367	0.0652858	0.023449
-30	0.1234753	0.0846318	0.0885497	0.0548542	0.0115187
-50	0.1102348	0.0658688	0.0684599	0.044998	0.000627
-70	0.0919221	0.0588343	0.0689697	0.0377213	0.0018861
-90	0.0825808	0.0511562	0.04772	0.0242539	-0.0005328
-110	0.0812049	0.0447044	0.042731	0.0157365	-0.0004218
-130	0.0912271	0.0523894	0.0485458	0.0204244	0.0030087
-150	0.0830402	0.0540968	0.0518402	0.0284665	0.0094473
-170	0.0970463	0.0639888	0.059737	0.0340375	0.0139928
-190	0.1130581	0.0628345	0.0604644	0.0341352	0.0172462
-210	0.1299116	0.0931301	0.0731342	0.0425563	0.0275406
-230	0.1590949	0.1176557	0.0998276	0.0704669	0.0258449

Table 6.3 Peripheral milling form error values.

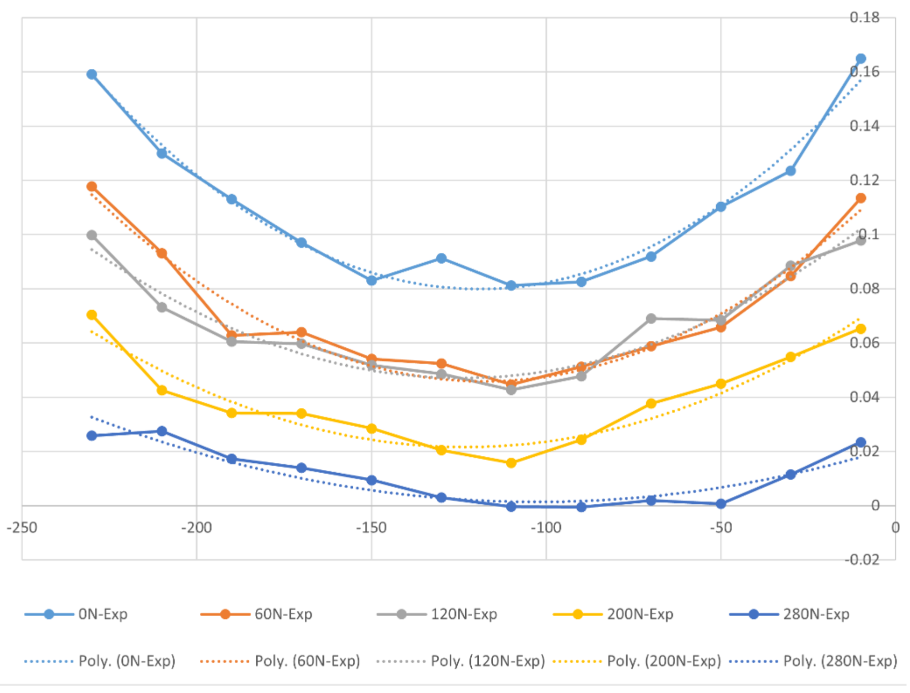

Figure 6.8 Parabolic fit of experimental values.

x-value	Unsupported	60N	120N	200N	280N
-10	0.157	0.109	0.102	0.069	0.018
-30	0.131	0.088	0.085	0.054	0.012
-50	0.111	0.071	0.070	0.042	0.007
-70	0.096	0.058	0.059	0.032	0.003
-90	0.085	0.050	0.052	0.026	0.002
-110	0.080	0.046	0.048	0.022	0.001
-130	0.081	0.047	0.047	0.022	0.003
-150	0.086	0.052	0.050	0.024	0.006
-170	0.096	0.061	0.056	0.030	0.010
-190	0.112	0.074	0.065	0.038	0.016
-210	0.133	0.092	0.078	0.050	0.024
-230	0.159	0.115	0.094	0.064	0.033

Table 6.4 Peripheral milling form error values (interpolated from parabolic fits).

x-value	Unsupported	60N	120N	200N	280N
-10	2975.43	3727.07	3397.47	3855.83	10421.66
-30	3555.74	4632.71	4104.77	4954.79	16167.73
-50	4211.75	5742.45	4934.80	6432.33	27782.65
-70	4885.85	6985.03	5834.08	8314.91	54406.26
-90	5465.67	8135.30	6670.57	10391.86	110972.20
-110	5804.02	8817.18	7238.05	11997.01	126794.61
-130	5791.24	8722.58	7345.02	12248.76	66636.68
-150	5431.80	7898.19	6950.45	10978.20	32925.93
-170	4840.89	6697.31	6197.88	8952.55	18525.34
-190	4165.06	5471.89	5303.44	6969.99	11650.46
-210	3513.00	4406.71	4434.41	5364.62	7940.83
-230	2938.86	3548.14	3673.73	4157.96	5738.10

Table 6.5 Analytical static stiffness values.

Appendix D

Research papers

D.1 Integration and demonstration of force controlled support in pocket milling [86]

Available online at www.sciencedirect.com

ScienceDirect

Procedia CIRP 101 (2021) 158–161

www.elsevier.com/locate/procedia

9th CIRP Conference on High Performance Cutting (HPC 2020)

Integration and demonstration of force controlled support in pocket milling

Patrick L. F. Kengne[a]*, Chao Sun[a], Simon Pope[b], Erdem Ozturk[a]

[a]AMRC with Boeing, The University of Sheffield, Sheffield S60 5TZ, UK
[b]Department of Automatic Controls and Systems Engineering, The University of Sheffield, Sheffield S1 3JD, UK

* Corresponding author. Tel.: +44 (0)772 928 0929. *E-mail address:* patrick.kengne@sheffield.ac.uk

Abstract

The pursuit of productivity and quality optimization in thin wall machining has given rise to a growing interest in robotic assisted milling. This is the interaction between robot, workpiece and machine tool, in which the robot is used to increase stiffness and damping of the structure during machining, via a controlled supporting force on the structure. In this research, the efficacy of the fixturing method is evaluated in pocket milling applications. Machining test results demonstrated decreased form error on the pocket floor.

Peer-review under responsibility of the scientific committee of the 9th CIRP Conference on High Performance Cutting.

Keywords: Integration; robot; milling.

1. Introduction

In aerospace industry, there is an increasing demand for lightweight structures. [1] As they generally contain thin floors and walls, they are prone to chatter vibrations during machining. [2] Predictive chatter mitigation techniques have been investigated, such as stability lobes [3]. They are used to eliminate chatter and improve productivity by determining and optimizing chatter-free spindle speeds and depths of cut.

To further improve productivity, additional fixturing solutions are applied [4], among which two methods have been investigated: fixed [5] and mobile supports [6]. Fei et al. developed a mobile damper attached to the spindle housing through an auxiliary device [6]. It was able to provide local damping and stiffness enhancement during the milling operation, as the damper follows the milling path. It yielded an increase in stability of the part. However, due to the design restrictions, the damper's applicability to different parts or process parameters was very restricted.

Ozturk et al, developed a moving and reconfigurable solution through the use of a robotic arm [7]. This fixture utilized a roller damper attached to the end effector of the robot, applying a support force to the back face of the workpiece. This resulted in the improvement of both stiffness and damping to counteract chatter vibrations, and static deflection to minimize form error.

Previous work was carried on the performance of robotic fixtures in peripheral milling [7-8]; however, a solution was not developed for pocket milling.

In this paper, a new end effector is designed for pocket milling and machining trials carried out to assess the performance of the robotic fixture in the machining of an 8-pocket workpiece. In section 2, the conceptual design and implementation of the force control measure is introduced. In section 3, a detailed presentation of workpiece, experimental setup and machining conditions is given. In section 4, a comparison of FRF and form error results is carried out with all trials. In section 5, a comprehensive summary of the findings is laid out and prospective developments are introduced.

2212-8271 © 2020 The Authors. Published by Elsevier B.V.

Peer-review under responsibility of the scientific committee of the 9th CIRP Conference on High Performance Cutting.
10.1016/j.procir.2021.05.151

2. Methodology

In this section the development and integration of the force control approach are presented in detail.

2.1. Hardware control design

A Kistler 9317C load cell was attached to the end effector of a Staubli Tx-90 robotic arm (see Fig. 1) and used to measure the supporting force F_m exerted by the fixture on the structure. Force data is acquired through a National Instruments Compaq DAQ-9133 chassis, a standalone DAQ (data acquisition device) programmed in a LabVIEW environment.

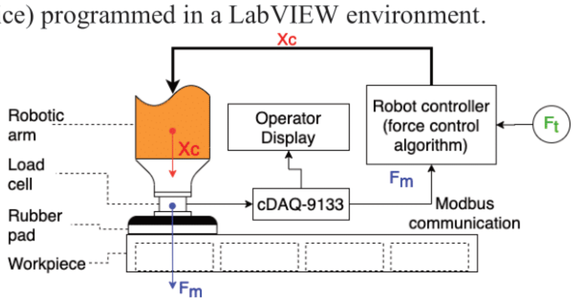

Fig. 1. Hardware control setup.

The data is then fed to the robot controller via Modbus, a serial communication protocol, where, upon input of the target force F_t, the robot displacement X_c is computed (via the force control algorithm) every 4ms. This output value enables the robot to act as an actuator, moving into and away from the workpiece, depending on the force readings. This is ensured through a motion instruction called "Alter Control", which makes the robot's motion path reactive to changes in measured force values. [9]

2.2. Software control implementation and tuning

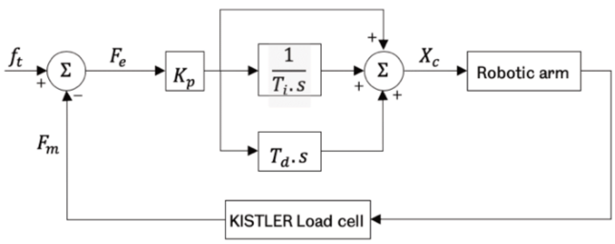

Fig. 2. Force (PID) control block diagram

Two control algorithms were investigated. The first one, called logic-based control, was implemented by setting a target force value and a fixed tolerance margin. The robot was programmed to retract and advance accordingly by a specific position increment when the force readings were out of the tolerance margin. Later on, external setup parameters, such as the robot's speed, the position increment, were fine-tuned; however, the lowest percentage error value achieved for a target force of 10N was 57%. The simplicity of the approach contributed to its instability; a more robust approach needed to be considered.

PID (Proportional-Integral-Derivative) was the second control algorithm implemented in this research, determining an error value F_e between the target force value F_t and the measured force F_m and minimizing this error by adjusting the system's control parameters, K_p, T_i and T_d, as shown in the block diagram in Fig. 2. [10]

The PID gain is as given in the equation below. The control value, otherwise known as the robot displacement (X_c), needed to minimize F_e is then computed in the robot motion code every 4ms.

$$G_{pid}(s) = \frac{X_c(s)}{F_e(s)} = K_p\left(1 + \frac{1}{T_i s} + T_d s\right) \quad (1)$$

2.3. Tuning and testing stage

The system's control parameters were pre-tuned using the Ziegler-Nichols tuning [10] and later on fine-tuned manually to achieve better control performance.

A rubber roller was attached at the end of the robotic arm to carry out tuning tests. [8] Two scenarios were investigated. In the first, the rubber roller acted as a fixed damper, supporting the structure only at one point; in the second one, the roller provided workpiece support as it travelled from one top end of the workpiece to the other.

For $K_p = 0.00021$, $T_i = 0.0004$ and $T_d = 50$, and a target force of 100N, the percentage errors were respectively about 3% and 10% with the fixed and moving dampers (see Fig. 3).

Further tests were undertaken by comparing the supporting force measured by the load cell as the rubber travels along the workpiece with and without force control. For a target force of 120N, the percentage error was reduced from 75% (without force control) to 2.6% (with force control), as shown in Fig. 4.

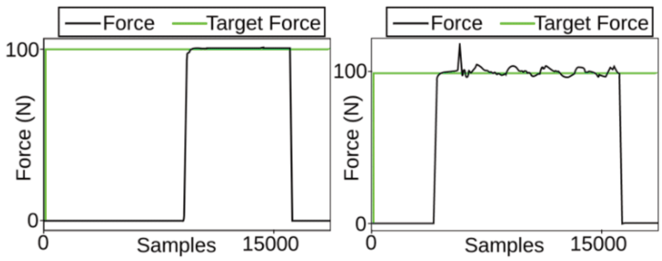

Fig. 3. Force control tuning tests: (left) fixed damper; (right) moving damper

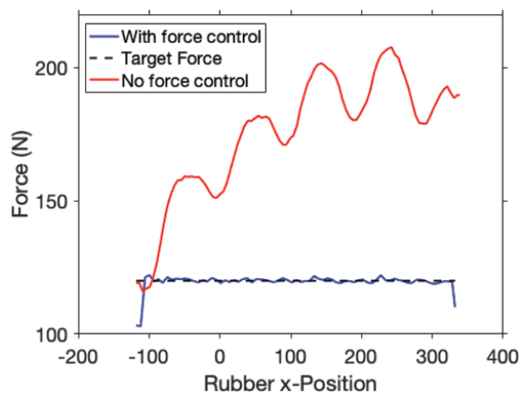

Fig. 4. Robotic performance of force control with a moving damper.

3. Experimental Setup

This section presents the machining conditions in this investigation.

3.1. Workpiece

An L-shaped aluminum part was designed, with 6 closed and 2 open pockets. In order to prevent asymmetric distortion, the pockets were machined by alternating from one side of the workpiece to the other; moreover, to ensure the maximum stiffness of the workpiece as the machining progresses, the upper part of the workpiece was first machined (Fig. 5). More information about the part is compiled in Table 1.

Table 1. Workpiece specifications

Properties	Description
Material	AL 7075
Dimensions	496x215x72mm
Pocket dimensions	122x88x30mm
Wall thickness (floor & side)	2mm

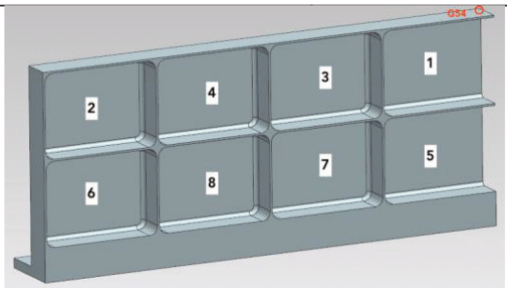

Fig. 5. CAD Model of machined part.

3.2. Test setup

The test setup consisted of a Staubli Tx-90 robotic arm installed on the rotary platform of a SORALUCE FX12000 machine. A rubber pad was mounted on the end effector of the robot to provide damping to the workpiece (see Fig. 6). The industrial robot was used to provide a localized and fixed support depending on the pocket machined. Moreover, it applied controlled support force of 60N at the back face of the aluminium workpiece during machining conditions (see Fig. 7). The force was kept constant through the control algorithm discussed earlier.

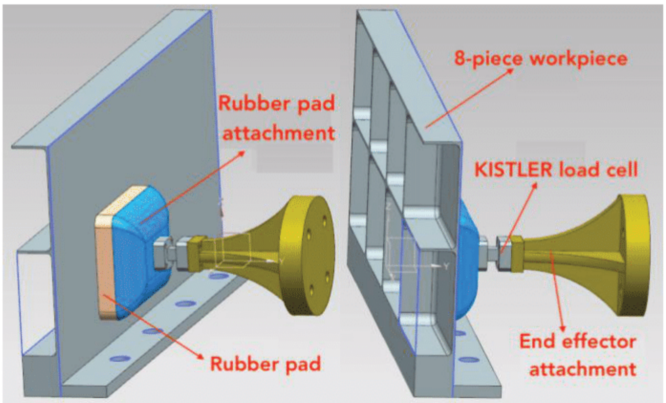

Fig. 6. (a) rubber pad; (b) load cell + robotic end effector attachment

Three workpieces were manufactured with different cutting conditions to assess the efficiency of the robotic fixture.

- Aggressive – unsupported (AU): the milling operation was carried in high productive cutting conditions without robotic support.
- Aggressive – Supported (AS): robotic support is provided during cutting in high productive conditions.
- Conservative – Unsupported (CU): part is machined using moderate cutting conditions without robotic assistance.

For all trials, the spindle speed was 4000rpm, and the stock allowance for finishing was 0.5mm (for floor) and 0.2mm (for walls). For roughing, the axial and radial depths were respectively 29.5mm and 2mm; from aggressive to conservative conditions, the feed per tooth was decreased from 3600 mm/min to 1800 mm/min. For finishing, the feed per tooth for both conditions was 900mm/min.

The cutting tool used was a solid carbide slot milling cutter with a cutting diameter of 16mm, a corner radius of 4mm, a cutting length of 32mm, and 3 teeth.

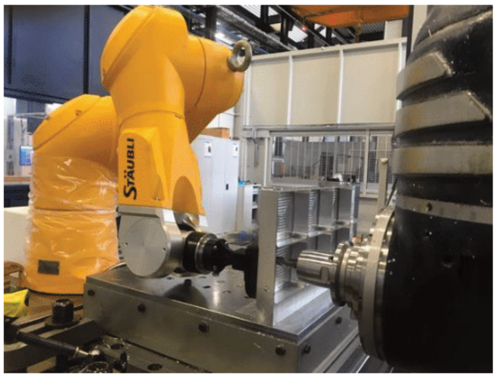

Fig. 7. Soraluce trial setup.

4. Results

This section showcases the comparison of FRF and form error results across all three workpieces.

4.1. Tap tests

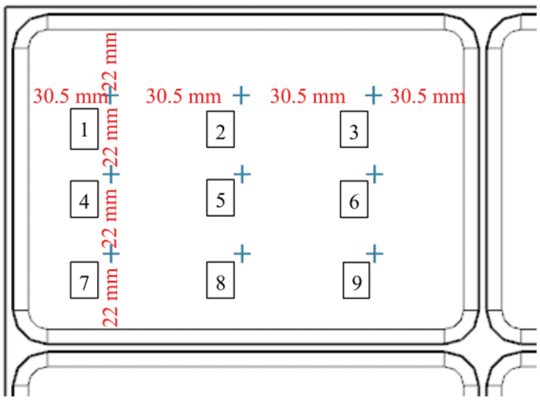

Fig. 8. Pocket floor probing points.

Direct transfer functions were measured for all three workpieces at 9 points on the floor of each pocket, as shown in Fig. 8. They were used to compare the workpiece stiffness with and without robotic support.

This is a resupply of March 2023 as the template used in the publication of the original article contained errors. The content of the article has remained unaffected.

Fig. 9 shows a considerable increase in the stiffness of the part in pocket 1 (point 5 of Fig. 8) with the robotic support; the same trend was observed with all other tap tests.

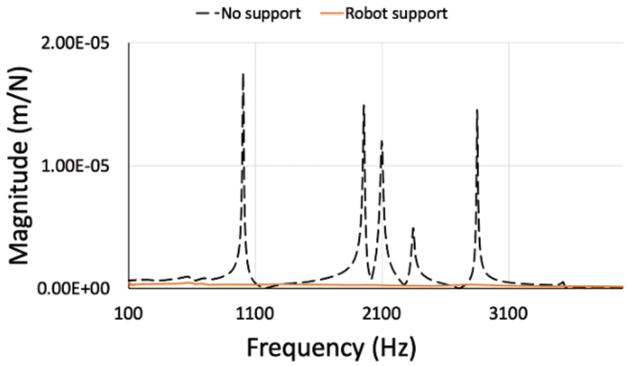

Fig. 9. Tap test results (Pocket 1, point 5).

4.2. Form error

For any given workpiece, surface quality was assessed for the bottom floor of each pocket. Form errors were measured at nine points using an on-machine probe; the probing locations are illustrated in Fig. 8.

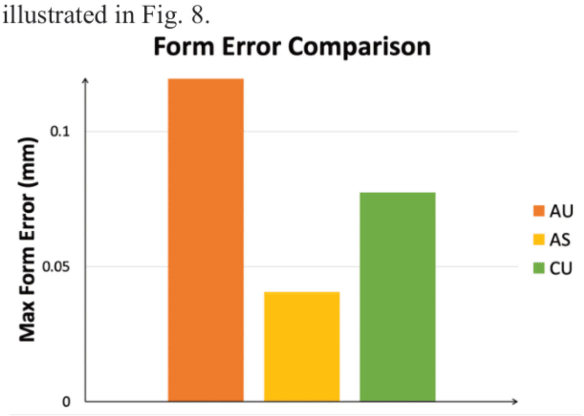

Fig. 10. Maximum form error values.

A comparative analysis of maximum form error values (of all 72 points per workpiece) across all three machined parts was made to assess the performance of the robotic fixture (Fig. 10); positive values indicate under-cutting. The integrated fixture yielded the best results, at about 40μm, as well as a 63% decrease in form error from the unsupported case; the form error achieved was also within tolerance (±0.1mm).

4.3. Productivity

Cycle time data was also obtained given the two sets of cutting conditions: aggressive and conservative (see Table 2). The table below shows a 37% increase in productivity with aggressive cutting parameters.

Table 2. Average cycle time data (per closed pocket)

Cutting conditions	Machining time (min)	Material removal rate (mm^3/min)
Aggressive	6.14	52,456
Conservative	9.75	33,033

5. Conclusion

The analysis of the data from the Soraluce trials showed an improvement in productivity in pocket milling with the help of the robotic mobile fixture. In more productive conditions, the robot yielded lower form error results than in unsupported and more conservative cutting conditions. This was due to the stiffness imparted to the structure by the robotic arm, as well as the damping (yielding positive results in FRF analysis) from the rubber pad.

Despite the good performance of the force-controlled support on the pocket floor's form error, the form error values on side walls were rather the highest with the robotic fixture upon complete probing inspection of the parts; this unusual observation is yet to be understood and requires further work.

Moreover, the PID control implemented had some limitations; the Modbus communication used between the load cell and the robot controller was asynchronous, hence decreasing the efficiency of the algorithm. Additionally, for a non-linear system such as our setup, the tuning process was very long and highly affected by external factors such as physical relocation of the robot and end effector. Further work needs to be carried out to find more robust control approaches.

Acknowledgements

The authors would like to acknowledge the funding provided by the European Commission under the Horizon 2020 Programme to the COROMA project under grant agreement no. 723853. Furthermore, they would like to acknowledge the contribution of partners, mainly Soraluce, IDEKO and Aciturri.

References

[1] Altintas Y, Weck M. Chatter Stability of Metal Cutting and Grinding. 2, s.l. : Elsevier, 1 1 2004, CIRP Annals, Vol. 53, pp. 619-642.
[2] Kolluru K, Axinte D. Novel ancillary device for minimising machining vibrations in thin wall assemblies; 2014. International Journal of Machine Tools and Manufacture, Vol. 85, pp. 79-86.
[3] Budak E, Altintas Y. Analytical Prediction of Chatter Stability in Milling—Part II: Application of the General Formulation to Common Milling Systems.1, s.l. : American Society of Mechanical Engineers, 1 3 1998, Journal of Dynamic Systems, Measurement, and Control, Vol. 120, p. 31.
[4] Aoyama T, Kakinuma Y. Development of Fixture Devices for Thin and Compliant Workpieces. 1, s.l. : Elsevier, 1 1 2005, CIRP Annals, Vol. 54, pp. 325-328.
[5] Kolluru K, Axinte D, Becker A. A solution for minimising vibrations in milling of thin walled casings by applying dampers to workpiece surface. 1, s.l. : CIRP, 2013, CIRP Annals - Manufacturing Technology, Vol. 62, pp. 415-418.
[6] Jixiong F, Bin L, Shuai Y, Mei D, Juliang X, Jin Z, Xiaofeng Z, Chunhui J, Tianyi S. Chatter mitigation using moving damper. s.l. : Elsevier Ltd, 2017, Journal of Sound and Vibration, Vol. 410, pp. 49-63.
[7] Ozturk E, Barrios A, Sun C, Rajabi S, Munoa J. Robotic assisted milling for increased productivity. CIRP Ann. 67 (2018) 427–430.
[8] Sun C, Kengne P, Barrios A, Ozturk E. Form Error Prediction in Robotic Assisted Milling, 17th CIRP Conference on Modeling of Machining Processes, 13-14 June 2019
[9] Staübli. VAL3 manual. 2017.
[10] Åström K.J., Hägglund T. PID controllers: theory, design, and tuning. ISA, 1995; pp. 59-70; 134-138.

D.2 Form error prediction in robotic assisted milling [76]

Available online at www.sciencedirect.com

ScienceDirect

Procedia CIRP 82 (2019) 491–496

www.elsevier.com/locate/procedia

17th CIRP Conference on Modelling of Machining Operations

Form Error Prediction in Robotic Assisted Milling

Chao Sun[a], Patrick L. F. Kengne[a], Asier Barrios[b], Sara Mata[b], Erdem Ozturk[a]*

[a] AMRC with Boeing, the University of Sheffield, Sheffield S60 5TZ, UK
[b] IK4 Ideko, Elgoibar, Spain

* Corresponding author. Tel.: +44 (0)114 222 6671 . *E-mail address:* e.ozturk@sheffield.ac.uk

Abstract

Robotic assisted milling is a process where a robot supports a workpiece while a machine tool cuts the workpiece. It can be used to suppress vibrations and minimize form errors in thin wall workpieces. In this paper, form error on a workpiece is simulated using a static force model, a frequency domain model and a hybrid model while a robot supports the workpiece from the other side. Machining results show that assistance of the robot has a considerable effect of the magnitude of form errors. Hence, support force should be carefully selected by simulation before machining. Finally, simulation results show that hybrid model gives the best fit among those three models.

Peer-review under responsibility of the scientific committee of The 17th CIRP Conference on Modelling of Machining Operations

Keywords: robotic assisted milling; form error; thin-wall machining.

1. Introduction

Light weight structures, also known as thin walled parts, are very commonly used in the aerospace sector. The machining times of these components are usually limited by chatter vibrations that occur due to low stiffness of the parts. Milling stability theory [1] can be used to eliminate chatter and increase productivity by optimizing machining parameters such as spindle speed and depth of cut. To further improve the productivity, dynamic response of the thin-wall structure needs to be improved.

To improve the dynamic response of the workpiece, fixturing of the part has been investigated. Two kinds of support methods, fixed support [2–4] and mobile support [5–7], are proposed. Compared to fixed support, the advantage of mobile support is that the support on the part will be very close to the cutting zone throughout the process as the support is following the motion of the milling tool. Mtorres machine tool company designed a special surface milling machine [5]. This machine has special apparatus support the component on the opposite side of machining. Fei et al. [6] developed an mobile support attached to the spindle housing of a machine tool. It showed that mobile support increased the stability of the process. Ozturk et al. proposed robotic assisted milling [7], where a robot provides mobile support while a machine tool performs milling operation, provides an flexible and reconfigurable solution.

The support force provided by mobile fixture will cause deflection of the part, which will influence the form error of the machined surface. To find proper magnitude of the support force, a form error model for machining process with mobile fixture need to be developed. For traditional machining process which do not have extra support force, the form error prediction model has been investigated in both time domain[8,9] and frequency domain[10]. However, a form error model has not been developed yet for a machining process with mobile fixture.

In this paper, three different form error prediction models for robotic assisted machining are proposed and compared. In Section 2, these three models are introduced in detail. In Section 3, machining tests results are compared with simulation results.

2212-8271 © 2019 The Authors. Published by Elsevier B.V.
Peer-review under responsibility of the scientific committee of The 17th CIRP Conference on Modelling of Machining Operations
10.1016/j.procir.2019.04.335

2. Form error modelling

In this section, different models to predict form errors are introduced. It begins with the model using static stiffness. Then the model using dynamic response is discussed. Finally, model combining both static stiffness and dynamic stiffness is proposed. It should be noted here that these models are for thin-wall parts and only the deflection of workpiece is considered.

2.1. Static deflection model

In this part, a form error model using static stiffness is presented. First, the cutting force calculation method is introduced. Then the equations to calculate the form error are presented.

The cutting tool can be discretized into M number of small disks along tool axis within the axial depth of cut a. As shown in Fig. 1, the form error in milling process is only influence by the cutting force in Y direction. The cutting force $F_{y,m}(\phi)$ for each disk in Y direction can be calculated by Equation (1), where K_{tc} is tangential cutting force coefficient, K_{rc} is radial cutting force coefficient, K_{te} is tangential edge force coefficient, K_{re} is radial edge force coefficient, f_t is the feedrate, $j = 1,2, \dots N$ is the flute index and ϕ is the instantaneous angle of immersion.

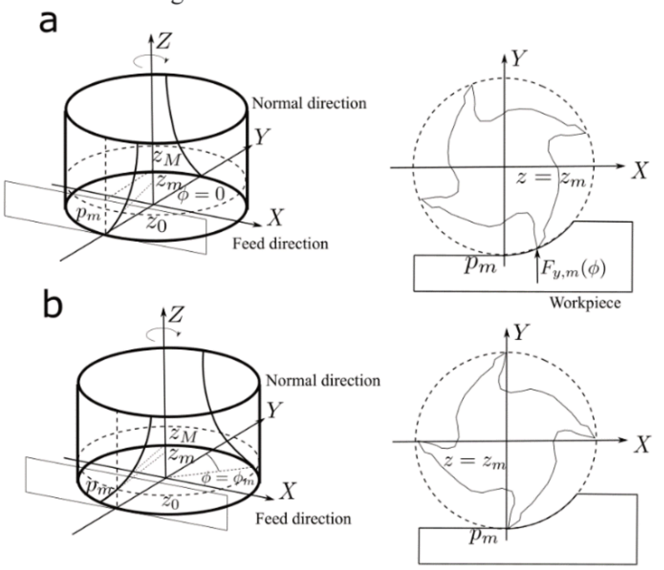

Fig. 1. Geometry of helical end mill. (a) $\phi = 0$; (b) $\phi = \phi_m$.

$$F_{y,m}(\phi) = \frac{a}{M}\sum_{j=1}^{N}\{f_t[K_{tc}\sin\phi_j - K_{rc}\cos\phi_j]\sin\phi_j + [K_{te}\sin\phi_j - K_{re}\cos\phi_j]\} \tag{1}$$

The total instantaneous cutting force in Y direction that sums the contribution of each disc can be calculated by Equation (2).

$$F_y(\phi) = \sum_{m=1}^{M} F_{y,m}(\phi) \tag{2}$$

As shown in Fig. 1, the flute pass the surface of workpiece at different instantaneous angle of immersion ϕ. ϕ_m for each disk can be calculated by Equation (3), in which β is the helix angle, R is the radius of cutter, z_m is the height of point p_m.

$$\phi_m = \frac{z_m \tan\beta}{R} \tag{3}$$

For each flute j, the instantaneous angle $\phi_{m,j}$ can be calculated by Equation (4), in which ϕ_p is the cutter pitch angle.

$$\phi_{m,j} = \phi_m + (j-1)\phi_p \tag{4}$$

Then the instantaneous cutting force in Y direction at which the flute pass point p_m can be calculated by Equation (2).

As shown in Fig. 2, in robotic assisted machining, the forces cause the deflection of the workpiece are composed of the cutting forces from the machining process and the support force from robot. Therefore, δ_m, the form error at point p_m, can be calculated by Equation (5). F_C is the cutting force on workpiece in surface normal direction, which is Y direction of cutting tool in Fig. 1. F_S is the support force and k is the static stiffness of workpiece. It should be noted that the positive result of δ_m means under cut, while the negative result of δ_m means over cut.

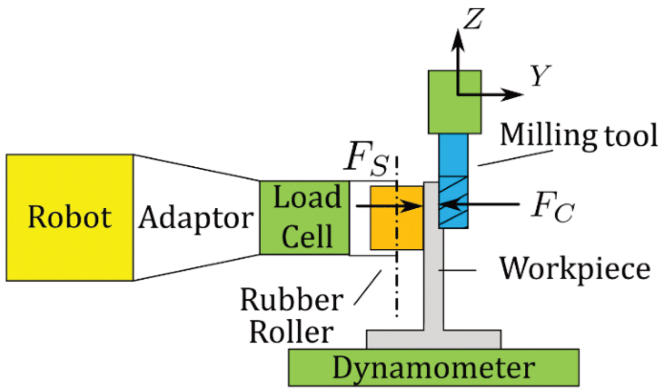

Fig. 2. Setup of robotic assisted machining.

$$\delta_m(t) = \frac{F_C - F_S}{k} = \frac{F_y[\phi(t_m)] - F_S}{k} \tag{5}$$

2.2. Frequency domain model

In this part, the frequency domain model is presented.

The force applied on workpiece in Y direction can be expressed in Equation (6), in which F_C is the cutting force and F_S is the support force (Fig. 2).

$$F_w(\phi) = F_C - F_S = -F_y(\phi) - F_S \quad (6)$$

It can be expressed in frequency domain using a Fourier series as presented in Equation (7).

$$F_w(\omega) = \mathcal{F}[F_w(t)] = \mathcal{F}\{F_w[\phi(t)]\} \quad (7)$$

Then the vibration of workpiece in frequency domain can be calculated using Equation (8), where $\Phi(\omega)$ is the frequency response function of workpiece.

$$\delta(\omega) = F_w(\omega)\Phi(\omega) \quad (8)$$

The vibration of workpiece in time domain $\delta(t)$ can be calculated through inverse Fourier transform of $\delta(\omega)$.
Finally, the form error at point p_m can be calculated by Equation (9), where t_m is the time when the flute pass the point p_m and ω_n is spindle speed in rad/s.

$$\delta_m = \delta(t_m) = \delta(\phi_m/\omega_n) \quad (9)$$

2.3. Hybrid model

In this part, a method using both static stiffness and dynamic frequency response is presented.

During robotic assisted machining process, the deflection is caused by both cutting forces and support force. The support force applies a static force, while the cutting forces apply dynamic forces. Therefore, the deflection from support force can be calculated using Equation (10).

$$\delta_{m,S} = \frac{F_S}{k} \quad (10)$$

The deflection caused by cutting force $\delta_{m,C}$ can still be calculated using Equation (7)~(9) by substituting the total force on workpiece $F_w[\phi(t)]$ with the cutting force $F_y[\phi(t)]$.

The total form error can be calculated as follows:

$$\delta_m = \delta_{m,S} + \delta_{m,C} \quad (11)$$

The differences among three models are shown in Fig. 3. In static model, the form error is calculated based on static stiffness. The influence of dynamic behavior of the workpiece is ignored. In frequency domain model, the force (F_w) applied on workpiece is firstly calculated by adding the support (F_S) to cutting forces (F_C). Then the form error is calculated with F_w and workpiece FRF from tap test. In hybrid model, the form errors caused by support force and cutting forces are calculated separately. Static stiffness from direct measurement, which is expected to be more accurate than static stiffness estimated from FRF from tap test, is utilized to calculate the form error from support force. The total form error is calculated from the sum of form errors from support force and cutting forces. It should be noted that FRF change due to material removal in cutting is not considered in this paper.

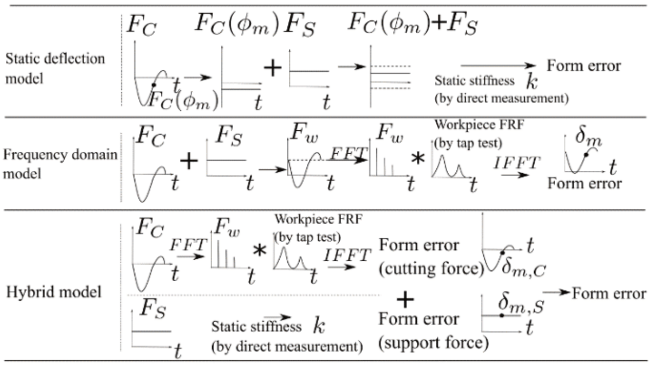

Fig. 3. Comparison of three models.

3. Experiment and simulation result

3.1. Test set-up

In the test set-up, a Staubli TX90 robot was installed to provide support force for machining process on a Starrag STC1250 5-axis milling machine. A rubber roller was assembled on to the end effector of the robot. A Kistler 9317C load cell was positioned between the adapters to be able to measure the support force F_S. The support force F_S is sent back to robot to control the support force. The milling tool (Sandvik R216.32-20025-AP20A H10F) was a 20 mm diameter carbide end mill with 2 flutes. The workpieces were T-profiles from Aluminium 6082-T6, of which height, thickness and length were 101.6, 9.5mm and 250mm, respectively. The workpieces were clamped to the Kistler 9255C dynamometer to measure forces on the workpiece (Fig. 4). Workpiece frame (X_W, Y_W, Z_W) and process frame (X, Y, Z) are shown in Fig. 4.

Cutting tests were performed with different support forces to demonstrate its effect on form errors. For each trial, a new T-profile workpiece was used. In these tests, down milling were used. Spindle speed and feed per tooth was 7000rpm and 0.1mm/tooth, respectively. 2mm radial depth of cut and 10mm axial depths of cut were used.

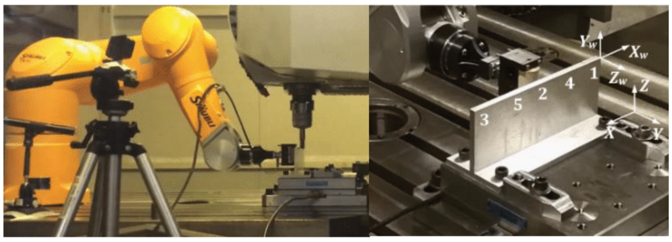

(a) (b)

Fig. 4. (a) Experimental set-up (b) measurement points.

3.2. FRF, stiffness and cutting force

Direct transfer functions were measured in five different locations by tap test for no support, 120N support and 200N support. Fig. 5 shows the result of G11, G22 and G44 with 120N support force. It shows that the transfer functions varies along the X_W axis. The transfer functions at point 1 with no support, 120N support and 200N support are shown in Fig. 6.

Higher dynamic stiffness was seen for cases with support. The change of support force doesn't show significant influence on FRF. Compared to the difference between the FRF result with support and that without support, the difference between the FRF results with 120N support and that with 200N support is relatively small.

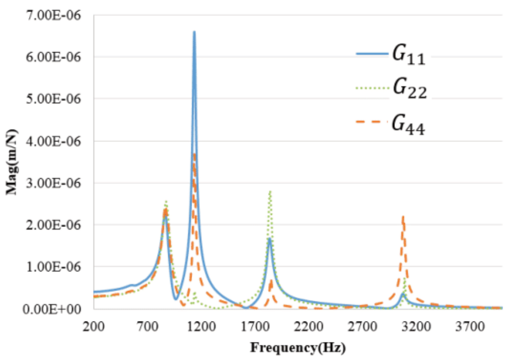

Fig. 5. Direct frequency response function G_{11}, G_{22}, G_{44} with 120N support force.

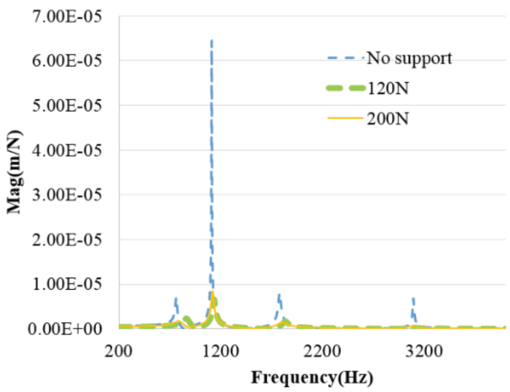

Fig. 6. Direct frequency response function G_{11}.

The static stiffness of workpiece were measured using laser displacement sensor and load cell (Table 1).

Table 1. Static stiffness results.

No.	Position in X_W *(mm)*	Stiffness *(N/mm)*
P1	-10	2500
P4	-67.5	3333
P2	-125	5000
P5	-182.5	3333
P3	-240	2500

The cutting force is first simulated for the simulation of form error. Acquired from cutting force coefficient test, the cutting force coefficient *Ktc* and *Krc* are 1168N/mm^2 and 632N/mm^2 respectively. The edge force coefficient *Kte* and *Kre* are 0.75N/mm and 0.27N/mm respectively. Fig. 7 shows the simulation and the measurement of cutting forces in *Zw* (*Y* direction of tool). The maximum cutting force from measurement is 467N and that from simulation is 430N. From the simulation, When the flute of the tool pass the points at Y_W=-6mm, the force in *Zw* (*Y* direction of tool) is 70N.

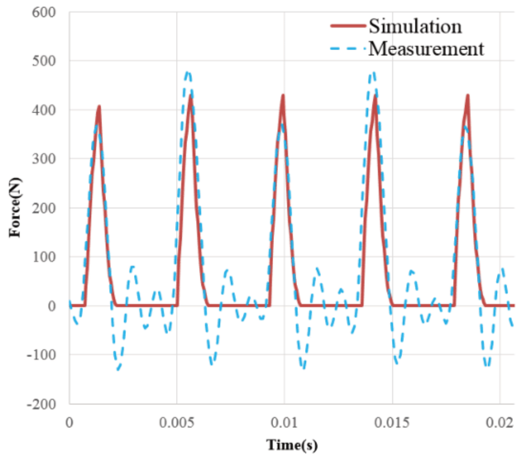

Fig. 7. Cutting force result for test with no support.

3.3. Form error

The form errors were measured using an on machine probe with 20 mm increments along the length of the workpiece between -10mm and -230mm along the workpiece coordinate *Xw* (Fig. 4). The probing points were 6 mm below the top face of the workpiece (*Yw*=-6mm). As shown in Fig. 8, support forces showed large influences on the form errors. Although the same support force is applied, the form error varies among different points because the FRF varies along the workpiece (Fig. 5).

In this case, the smallest form error is with 280N support. It should be noted that it is not necessarily that larger support force will lead to lower form error, as the form error with no support could be negative in some cases, for example, sometimes in up milling case.

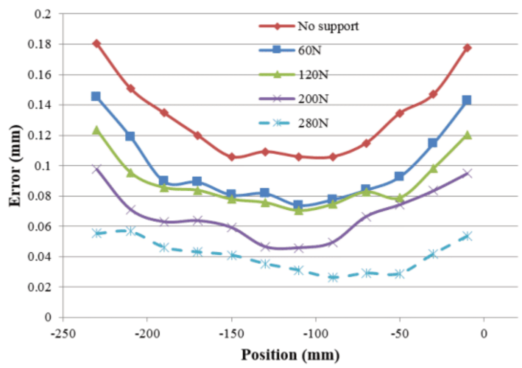

Fig. 8. Form errors results from measurement.

Simulation results using static model for no support, 120N support and 280N support are shown in Fig. 9. The results for no support test presented in Fig. 9 show that the static model underestimate the form error caused by cutting force. The maximum difference is 0.149mm. For 120N support and 280N, the curve shape of the simulation results are different from the measurement results.

Using the dynamic model, simulations are done from point 1 to point 5. Simulation results using dynamic model for no support, 120N support and 280N support are shown in Fig. 10. Fig. 10 shows that the maximum error for no support test is 0.038mm, which is a positive value. However, for 280N support force, the maximum error is -0.069mm. It can be seen that the errors of the simulation change from positive to negative with the increase of support force. The reason could be, in dynamic model, the static stiffness is estimated from FRF from tap test result, which may not be as accurate as direct measurement of static deflection. In contrast, static stiffness values listed in Table 1 are used in hybrid model.

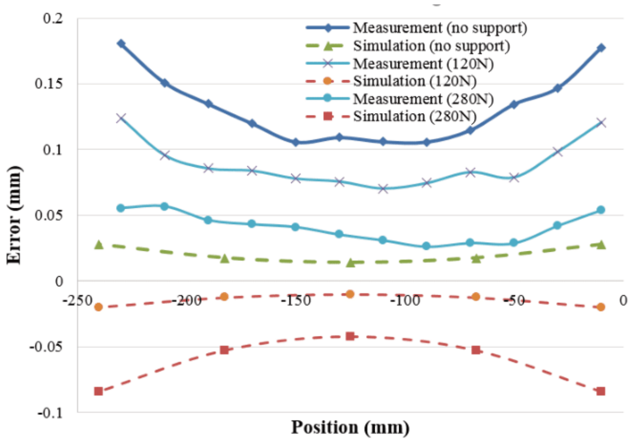

Fig. 9. Simulation using static deflection model and measurement results.

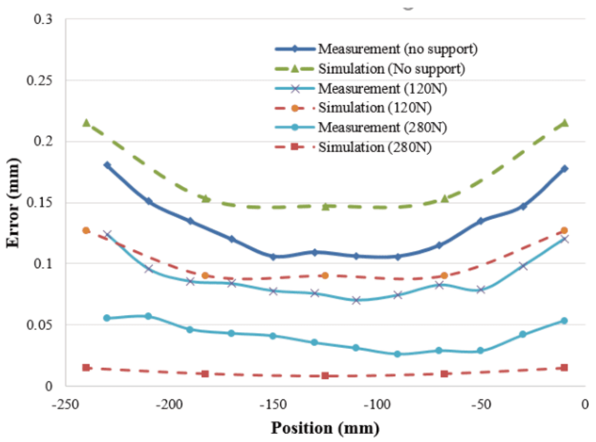

Fig. 10. Simulation using frequency domain model and measurement results.

For no support simulation, hybrid model and frequency domain model is the same. The simulation results for 120N support and 280N support are shown in Fig. 11. The simulation results show relatively consistent positive errors.

Table 2 compares the maximum error of each model. The static model shows the largest maximum error for all of the cases. The dynamic deflection model shows smallest maximum error for 120N case. However, the sign of the error changes when the support force increases in dynamics model.

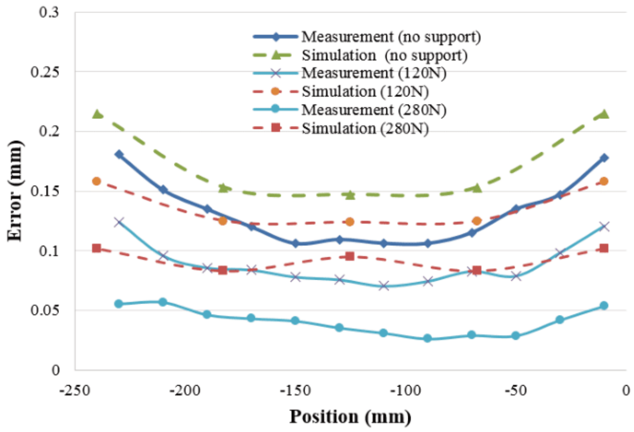

Fig. 11. Simulation using hybrid model and measurement results.

Table 2. Maximum simulation errors of each model.

	No support	120N support	280N support
Static deflection model	-0.149mm	-0.103mm	-0.137mm
Dynamic deflection model	0.038mm	0.015mm	-0.069mm
Hybrid model	0.038mm	0.049mm	0.06mm

The maximum error from hybrid model keeps positive, which is more reasonable. These consistent positive errors could come from cutter radius error, machine tool positioning error and measurement errors. In this test, the machine tool positioning accuracy is 0.005mm. The maximum radius error of the tool, including the runout, is 0.014mm. These two may introduce form errors. The probing tool itself has a high accuracy, which is around 0.001mm. However, as the probing is done on machine tool, the machine tool positioning accuracy will also bring in the measurement errors.

4. Conclusion

Three methods for calculating form errors for robotic assisted milling are developed in the paper. A few conclusions can be acquired from the results in this paper. Firstly, the support force in robotic assisted machining can change the form error. Therefore, form error should be simulated and support force should be carefully selected. Second, among all three methods, hybrid model shows more reasonable results. Compared to static model and frequency domain model, hybrid model gives relatively consistent differences with the measurement. Finally, measurement results show that the form errors are different at different points with constant support force on the workpiece. For example, the form errors on point 1 and point 2 show different values. This is because the dynamic and static stiffness are different at each point. Therefore, to achieve a constant form error on a workpiece, a profile of support forces should be calculated and applied at different positions on workpiece.

Acknowledgements

The authors would like to acknowledge the funding provided by the European Commission under the Horizon 2020 Programme to the COROMA project under grant agreement no. 723853. Companion information to the paper is available at the project's Zenodo repository under https://zenodo.org/communities/coroma-project.

References

[1] Y. Altintas, Manufacturing Automation, in: Cambridge University Press, 2012. doi:10.1017/CBO9780511843723.001.
[2] X.-J. Wan, Y. Zhang, A novel approach to fixture layout optimization on maximizing dynamic machinability, Int. J. Mach. Tools Manuf. 70 (2013) 32–44. doi:10.1016/j.ijmachtools.2013.03.007.
[3] K. Kolluru, D. Axinte, A. Becker, A solution for minimising vibrations in milling of thin walled casings by applying dampers to workpiece surface, CIRP Ann. 62 (2013) 415–418. doi:10.1016/j.cirp.2013.03.136.
[4] A. Matsubara, Y. Taniyama, J. Wang, D. Kono, Design of a support system with a pivot mechanism for suppressing vibrations in thin-wall milling, CIRP Ann. 66 (2017) 381–384. doi:10.1016/j.cirp.2017.04.055.
[5] Mtorres, Torres Surface Milling, (n.d.). https://goo.gl/Sd7bNP (accessed December 20, 2019).
[6] J. Fei, B. Lin, S. Yan, M. Ding, J. Xiao, J. Zhang, X. Zhang, C. Ji, T. Sui, Chatter mitigation using moving damper, J. Sound Vib. 410 (2017) 49–63. doi:10.1016/j.jsv.2017.08.033.
[7] E. Ozturk, A. Barrios, C. Sun, S. Rajabi, J. Munoa, Robotic assisted milling for increased productivity, CIRP Ann. 67 (2018) 427–430. doi:10.1016/j.cirp.2018.04.031.
[8] D. Montgomery, Y. Altintas, Mechanism of Cutting Force and Surface Generation in Dynamic Milling, J. Eng. Ind. 113 (1991) 160. doi:10.1115/1.2899673.
[9] T. Schmitz, J. Ziegert, Examination of surface location error due to phasing of cutter vibrations, Precis. Eng. 23 (1999) 51–62. doi:10.1016/S0141-6359(98)00025-7.
[10] T.L. Schmitz, B.P. Mann, Closed-form solutions for surface location error in milling, Int. J. Mach. Tools Manuf. 46 (2006) 1369–1377. doi:10.1016/j.ijmachtools.2005.10.007.

References

[1] L. Cen, S. N. Melkote, J. Castle, and H. Appelman, 'A Wireless Force-Sensing and Model-Based Approach for Enhancement of Machining Accuracy in Robotic Milling', *IEEE/ASME Transactions on Mechatronics*, vol. 21, no. 5, pp. 2227–2235, Oct. 2016, doi: 10.1109/TMECH.2016.2567319.

[2] Z. Pan and H. Zhang, 'Robotic machining from programming to process control: A complete solution by force control', *Industrial Robot*, vol. 35, no. 5, pp. 400–409, 2008, doi: 10.1108/01439910810893572/FULL/HTML.

[3] L. T. Tunc and D. Stoddart, 'Tool path pattern and feed direction selection in robotic milling for increased chatter-free material removal rate', *International Journal of Advanced Manufacturing Technology*, vol. 89, no. 9–12, pp. 2907–2918, Apr. 2017, doi: 10.1007/S00170-016-9896-2/METRICS.

[4] H. Celikag, 'On the dynamics of robotic machining', 2020.

[5] A. Klimchik, A. Pashkevich, D. Chablat, and G. Hovland, 'Compliance error compensation technique for parallel robots composed of non-perfect serial chains', *Robot Comput Integr Manuf*, vol. 29, no. 2, pp. 385–393, Apr. 2013, doi: 10.1016/J.RCIM.2012.09.008.

[6] V. Nguyen, J. Johnson, and S. Melkote, 'Active vibration suppression in robotic milling using optimal control', *Int J Mach Tools Manuf*, vol. 152, p. 103541, May 2020, doi: 10.1016/J.IJMACHTOOLS.2020.103541.

[7] S. Mejri, V. Gagnol, T. P. Le, L. Sabourin, P. Ray, and P. Paultre, 'Dynamic characterization of machining robot and stability analysis', *International Journal of Advanced Manufacturing Technology*, vol. 82, no. 1–4, pp. 351–359, Jan. 2016, doi: 10.1007/S00170-015-7336-3/METRICS.

[8] J. Li, B. Li, N. Y. Shen, H. Qian, and Z. M. Guo, 'Effect of the cutter path and the workpiece clamping position on the stability of the robotic milling system', *International Journal of Advanced Manufacturing Technology*, vol. 89, no. 9–12, pp. 2919–2933, Apr. 2017, doi: 10.1007/S00170-016-9759-X/METRICS.

[9] M. Ozsoy, N. D. Sims, and E. Ozturk, 'Robotically assisted active vibration control in milling: A feasibility study', *Mech Syst Signal Process*, vol. 177, p. 109152, Sep. 2022, doi: 10.1016/J.YMSSP.2022.109152.

[10] R. Torres, I. Elguea, J. Aginaga, X. Iriarte, N. Agirre, and I. Inziarte, 'Robotic assisted thin-wall machining with a collaborative robot', pp. 1505–1508, 2020.

[11] E. Ozturk, A. Barrios, C. Sun, S. Rajabi, and J. Munoa, 'Robotic assisted milling for increased productivity', *CIRP Annals*, vol. 67, no. 1, pp. 427–430, 2018, doi: 10.1016/j.cirp.2018.04.031.

[12] S. A. Tobias, *Machine tool vibration*. London: Blackie and Son Ltd., 1965. Accessed: Dec. 19, 2017. [Online]. Available: http://www.worldcat.org/title/machine-tool-vibration/oclc/939408898

[13] Y. Altintas and M. Weck, 'Chatter Stability of Metal Cutting and Grinding', *CIRP Annals*, vol. 53, no. 2, pp. 619–642, Jan. 2004, doi: 10.1016/S0007-8506(07)60032-8.

[14] J. DePree and C. Gesswein, 'Robotic machining white paper project', 2008.

[15] J. L. Xiao, S. L. Zhao, H. Guo, T. Huang, and B. Lin, 'Research on the collaborative machining method for dual-robot mirror milling', *International Journal of Advanced Manufacturing Technology*, vol. 105, no. 10, pp. 4071–4084, Dec. 2019, doi: 10.1007/S00170-018-2367-1/METRICS.

[16] A. Verl, A. Valente, S. Melkote, C. Brecher, E. Ozturk, and L. T. Tunc, 'Robots in machining', *CIRP Annals*, vol. 68, no. 2, pp. 799–822, Jan. 2019, doi: 10.1016/J.CIRP.2019.05.009.

[17] I. Iglesias, M. A. Sebastián, and J. E. Ares, 'Overview of the State of Robotic Machining: Current Situation and Future Potential', *Procedia Eng*, vol. 132, pp. 911–917, Jan. 2015, doi: 10.1016/J.PROENG.2015.12.577.

[18] U. Schneider *et al.*, 'Improving robotic machining accuracy through experimental error investigation and modular compensation', *International Journal of Advanced Manufacturing Technology*, vol. 85, no. 1–4, pp. 3–15, Jul. 2016, doi: 10.1007/S00170-014-6021-2/METRICS.

[19] P. L. Fenou Kengne, C. Sun, and D. Polson, 'Robotic force control for workpiece during machining', The University of Sheffield, 2018.

[20] S. Zhang, Q. Bi, Y. Ji, and Y. Wang, 'Real-time thickness compensation in mirror milling based on modified Smith predictor and disturbance observer', *Int J Mach Tools Manuf*, vol. 144, no. June, p. 103427, 2019, doi: 10.1016/j.ijmachtools.2019.103427.

[21] E. Appleton and D. J. Williams, 'Industrial Robot Applications', p. 240, 1987, Accessed: May 16, 2023. [Online]. Available: https://books.google.com/books/about/Industrial_Robot_Applications.html?id=d1j-CAAAQBAJ

[22] W. Ji and L. Wang, 'Industrial robotic machining: a review', *The International Journal of Advanced Manufacturing Technology 2019 103:1*, vol. 103, no. 1, pp. 1239–1255, Apr. 2019, doi: 10.1007/S00170-019-03403-Z.

[23] J. Padremenos, C. Doukas, P. Stavropoulos, and G. Chryssolouris, 'Machining With Robots: A Critical Review', in *7th International Conference on Digital Enterprise Technology*, Athens, Greece, 2011.

[24] Y. Altintas, 'Manufacturing Automation: Metal Cutting Mechanics, Machine Tool Vibrations, and CNC Design', *Manufacturing Automation*, Jan. 2012, doi: 10.1017/CBO9780511843723.

[25] S. H. Kim *et al.*, 'Robotic Machining: A Review of Recent Progress', *International Journal of Precision Engineering and Manufacturing*, vol. 10, pp. 1629–1642, 2019.

[26] E. Ozturk and E. Budak, 'Modeling of 5-axis milling processes', *Machining Science and Technology*, vol. 11, no. 3, pp. 287–311, Jul. 2007, doi: 10.1080/10910340701554808.

[27] B. Tao, X. W. Zhao, and H. Ding, 'Mobile-robotic machining for large complex components: A review study', *Sci China Technol Sci*, vol. 62, no. 8, pp. 1388–1400, Aug. 2019, doi: 10.1007/S11431-019-9510-1/METRICS.

[28] A. Grau, M. Indri, L. Lo Bello, and T. Sauter, 'Industrial robotics in factory automation: From the early stage to the Internet of Things', *Proceedings IECON*

2017 - 43rd Annual Conference of the IEEE Industrial Electronics Society, vol. 2017-January, pp. 6159–6164, Dec. 2017, doi: 10.1109/IECON.2017.8217070.

[29] H. Celikag, N. D. Sims, and E. Ozturk, 'Cartesian stiffness optimization for serial arm robots', *Procedia CIRP*, vol. 77, pp. 566–569, 2018, doi: 10.1016/J.PROCIR.2018.08.222.

[30] B. Tao, X. W. Zhao, and H. Ding, 'Mobile-robotic machining for large complex components: A REVIEW STUDY', *Sci China Technol Sci*, vol. 62, no. 8, pp. 1388–1400, Aug. 2019, doi: 10.1007/S11431-019-9510-1.

[31] A. Grau, M. Indri, L. Lo Bello, and T. Sauter, 'Industrial robotics in factory automation: from the early stage to the Internet of Things', *IECON 2017: 43rd IEEE Annual Conference of the IEEE Industrial Electronics Society: China National Convention Center, Beijing, China, 29, October-01 November, 2017: proceedings*, vol. 2017-January, pp. 6159–6164, Dec. 2018, doi: 10.1109/IECON.2017.8217070.

[32] A. Klimchik, A. Ambiehl, S. Garnier, B. Furet, and A. Pashkevich, 'Efficiency evaluation of robots in machining applications using industrial performance measure', *Robot Comput Integr Manuf*, vol. 48, pp. 12–29, 2017, Accessed: Oct. 03, 2023. [Online]. Available: https://www.academia.edu/33264522/Efficiency_evaluation_of_robots_in_machining_applications_using_industrial_performance_measure

[33] J. Jędrzejewski and W. Modrzycki, 'Intelligent Supervision of Thermal Deformations in High Precision Machine Tools', *Proceedings of the Thirty-Second International Matador Conference*, pp. 457–462, 1997, doi: 10.1007/978-1-349-14620-8_72.

[34] R. Ramesh, M. A. Mannan, and A. N. Poo, 'Error compensation in machine tools - a review. Part I: Geometric, cutting-force induced and fixture-dependent errors', *Int J Mach Tools Manuf*, vol. 40, no. 9, pp. 1235–1256, 2000, doi: 10.1016/S0890-6955(00)00009-2.

[35] J. Ni, 'CNC Machine Accuracy Enhancement Through Real-Time Error Compensation', *J Manuf Sci Eng*, vol. 119, no. 4B, pp. 717–725, Nov. 1997, doi: 10.1115/1.2836815.

[36] J. Bryan, 'International Status of Thermal Error Research (1990)', *CIRP Annals*, vol. 39, no. 2, pp. 645–656, Jan. 1990, doi: 10.1016/S0007-8506(07)63001-7.

[37] R. Venugopal, M. Barash, and M. C. Shaw, 'Thermal Effects on the Accuracy of Numerically Controlled Machine Tools', *CIRP Annals*, vol. 35, no. 1, pp. 255–258, Jan. 1986, doi: 10.1016/S0007-8506(07)61882-4.

[38] P. L. B. Oxley, *The Mechanics of Machining*. Ellis Horwood Limited, 1989.

[39] H. B. Lacerda and V. T. Lima, 'Evaluation of Cutting Forces and Prediction of Chatter Vibrations in Milling', vol. XXVI, no. 1, 2004, Accessed: Dec. 19, 2017. [Online]. Available: https://pdfs.semanticscholar.org/b04d/bb0c3a6fd00a63c304c0206fce4e1cf68906.pdf

[40] G. Boothroyd and G. Boothroyd, 'Temperatures in Orthogonal Metal Cutting', *Proceedings of the Institution of Mechanical Engineers*, vol. 177, no. 1, pp. 789–810, Jun. 1963, doi: 10.1243/PIME_PROC_1963_177_058_02.

[41] X. Li, E. M. Kopalinsky, and P. L. B. Oxley, 'A Numerical Method for Determining Temperature Distributions in Machining with Coolant: Part 2: Calculation Method and Results', *Proc Inst Mech Eng B J Eng Manuf*, vol. 209, no. 1, pp. 45–52, Feb. 1995, doi: 10.1243/PIME_PROC_1995_209_052_02.

[42] L. N. López De Lacalle and A. Lamikiz, 'Machine tools for high performance machining', *Machine Tools for High Performance Machining*, pp. 1–442, 2009, doi: 10.1007/978-1-84800-380-4/COVER.

[43] A. H. Slocum, *Precision Machine Design*. Prince-Hall, Inc, 1992.

[44] U. Heisel, F. Richter, and K. H. Wurst, 'Thermal Behaviour of Industrial Robots and Possibilities for Error Compensation', *CIRP Annals*, vol. 46, no. 1, pp. 283–286, Jan. 1997, doi: 10.1016/S0007-8506(07)60826-9.

[45] V. Robin, L. Sabourin, and G. Gogu, 'Optimization of a robotized cell with redundant architecture', *Robot Comput Integr Manuf*, vol. 27, no. 1, pp. 13–21, Feb. 2011, doi: 10.1016/J.RCIM.2010.06.010.

[46] S. H. Kim *et al.*, 'Robotic Machining: A Review of Recent Progress', *International Journal of Precision Engineering and Manufacturing*, vol. 20, no. 9, pp. 1629–1642, Sep. 2019, doi: 10.1007/S12541-019-00187-W.

[47] Y. T. Oh, 'Influence of the joint angular characteristics on the accuracy of industrial robots', *Industrial Robot: An International Journal*, vol. 38, no. 4, pp. 406–418, 2011, doi: 10.1108/01439911111132094/FULL/HTML.

[48] X. Yang, L. Wu, J. Li, and K. Chen, 'A minimal kinematic model for serial robot calibration using POE formula', *Robot Comput Integr Manuf*, vol. 30, no. 3, pp. 326–334, Jun. 2014, doi: 10.1016/J.RCIM.2013.11.002.

[49] Joon Hyun Jang, Soo Hyun Kim, and Yoon Keun Kwak, 'Calibration of geometric and non-geometric errors of an industrial robot', *Robotica*, vol. 19, no. 3, pp. 311–321, May 2001, doi: 10.1017/S0263574700002976.

[50] A. Nubiola and I. A. Bonev, 'Absolute calibration of an ABB IRB 1600 robot using a laser tracker', *Robot Comput Integr Manuf*, vol. 29, no. 1, pp. 236–245, Feb. 2013, doi: 10.1016/J.RCIM.2012.06.004.

[51] M. Cordes and W. Hintze, 'Offline simulation of path deviation due to joint compliance and hysteresis for robot machining', *International Journal of Advanced Manufacturing Technology*, vol. 90, no. 1–4, pp. 1075–1083, Apr. 2017, doi: 10.1007/S00170-016-9461-Z/METRICS.

[52] M. Ruderman, F. Hoffmann, and T. Bertram, 'Modeling and identification of elastic robot joints with hysteresis and backlash', *IEEE Transactions on Industrial Electronics*, vol. 56, no. 10, pp. 3840–3847, 2009, doi: 10.1109/TIE.2009.2015752.

[53] M. N. Nevmerzhitskiy, B. S. Notkin, A. V. Vara, and K. V. Zmeu, 'Friction Model of Industrial Robot Joint with Temperature Correction by Example of KUKA KR10', *Journal of Robotics*, vol. 2019, 2019, doi: 10.1155/2019/6931563.

[54] C. Gong, J. Yuan, and J. Ni, 'Nongeometric error identification and compensation for robotic system by inverse calibration', *Int J Mach Tools Manuf*, vol. 40, no. 14, pp. 2119–2137, 2000, doi: 10.1016/S0890-6955(00)00023-7.

[55] J. Zhou, H. N. Nguyen, and H. J. Kang, 'Simultaneous identification of joint compliance and kinematic parameters of industrial robots', *International Journal of Precision Engineering and Manufacturing*, vol. 15, no. 11, pp. 2257–2264, Nov. 2014, doi: 10.1007/S12541-014-0589-1/METRICS.

[56] I. Tyapin, K. B. Kaldestad, and G. Hovland, 'Off-line path correction of robotic face milling using static tool force and robot stiffness', *IEEE International Conference on Intelligent Robots and Systems*, vol. 2015-December, pp. 5506–5511, Dec. 2015, doi: 10.1109/IROS.2015.7354157.

[57] B. Siciliano and O. Khatib, *Handbook of Robotics*. Springer Berlin Heidelberg, 2008. doi: 10.1007/978-3-540-30301-5.

[58] P. S. Shiakolas, K. L. Conrad, and T. C. Yih, 'On the Accuracy, Repeatability, and Degree of Influence of Kinematics Parameters for Industrial Robots', *International Journal of Modelling and Simulation*, vol. 22, no. 4, pp. 245–254, 2002, doi: 10.1080/02286203.2002.11442246.

[59] C. Möller, H. C. Schmidt, N. H. Shah, and J. Wollnack, 'Enhanced Absolute Accuracy of an Industrial Milling Robot Using Stereo Camera System', *Procedia Technology*, vol. 26, pp. 389–398, Jan. 2016, doi: 10.1016/J.PROTCY.2016.08.050.

[60] J. F. Brethé, E. Vasselin, D. Lefebvre, and B. Dakyo, 'Determination of the repeatability of a Kuka robot using the stochastic ellipsoid approach', *Proc IEEE Int Conf Robot Autom*, vol. 2005, pp. 4339–4344, 2005, doi: 10.1109/ROBOT.2005.1570788.

[61] S. K. Mustafa, P. Y. Tao, G. Yang, and I. M. Chen, 'A geometrical approach for online error compensation of industrial manipulators', *IEEE/ASME International Conference on Advanced Intelligent Mechatronics, AIM*, pp. 738–743, 2010, doi: 10.1109/AIM.2010.5695784.

[62] P. Corke, *Robotics, Vision and Control*. in Springer Tracts in Advanced Robotics. Cham: Springer International Publishing, 2011. doi: 10.1007/978-3-319-54413-7.

[63] Y. Chen and F. Dong, 'Robot machining: Recent development and future research issues', *International Journal of Advanced Manufacturing Technology*, vol. 66, no. 9–12, pp. 1489–1497, Jun. 2013, doi: 10.1007/S00170-012-4433-4.

[64] S. Ratchev, S. Liu, and A. A. Becker, 'Error compensation strategy in milling flexible thin-wall parts', *J Mater Process Technol*, vol. 162–163, no. SPEC. ISS., pp. 673–681, 2005, doi: 10.1016/j.jmatprotec.2005.02.192.

[65] J. Tlusty and L. Spacek, 'Self-excited vibrations on machine tools (in Czech.)', *Prague: Nakl. CSAV*, 1954.

[66] K. Kolluru, D. Axinte, and A. Becker, 'A solution for minimising vibrations in milling of thin walled casings by applying dampers to workpiece surface', *CIRP Ann Manuf Technol*, vol. 62, no. 1, pp. 415–418, 2013, doi: 10.1016/j.cirp.2013.03.136.

[67] F. (Franz) Koenigsberger and J. Tlustý, *Machine tool structures*. Pergamon Press, 1967.

[68] E. Budak and Y. Altintas, 'Analytical Prediction of Chatter Stability in Milling—Part II: Application of the General Formulation to Common Milling Systems', *J Dyn Syst Meas Control*, vol. 120, no. 1, p. 31, Mar. 1998, doi: 10.1115/1.2801318.

[69] J. Tlusty and M. Polacek, 'The stability of machine tools against self-excited vibrations in machining', *International research in production engineering*, vol. 1, pp. 465--474, 1963, doi: 10.1016/j.procir.2014.03.068.

[70] B. P. Mann, K. A. Young, T. L. Schmitz, and D. N. Dilley, 'Simultaneous stability and surface location error predictions in milling', *Journal of Manufacturing Science and Engineering, Transactions of the ASME*, vol. 127, no. 3, pp. 446–453, 2005, doi: 10.1115/1.1948394.

[71] A. K. Kiss, D. Bachrathy, and G. Stepan, 'Cumulative Surface Location Error for Milling Processes Based on Tool-tip Frequency Response Function', *Procedia CIRP*, vol. 46, pp. 323–326, 2016, doi: 10.1016/j.procir.2016.04.015.

[72] A. K. Kiss, D. Bachrathy, and G. Stepan, 'Cumulative Surface Location Error for Milling Processes Based on Tool-tip Frequency Response Function', *Procedia CIRP*, vol. 46, pp. 323–326, Jan. 2016, doi: 10.1016/J.PROCIR.2016.04.015.

[73] Y. Chen and J. E. McInroy, 'Decoupled Control of Flexure-Jointed Hexapods Using Estimated Joint-Space Mass-Inertia Matrix', *IEEE Transactions on Control Systems Technology*, vol. 12, no. 3, pp. 413–421, 2004, doi: 10.1109/TCST.2004.824339.

[74] F. Leali, A. Vergnano, F. Pini, M. Pellicciari, and G. Berselli, 'A workcell calibration method for enhancing accuracy in robot machining of aerospace parts', *International Journal of Advanced Manufacturing Technology*, vol. 85, no. 1–4, pp. 47–55, Jul. 2016, doi: 10.1007/S00170-014-6025-Y/METRICS.

[75] K. McMullen, 'Industrial Robotics for Advanced Machining', MPhil thesis, University of Sheffield, Sheffield, 2022.

[76] C. Sun, P. L. F. Kengne, A. Barrios, S. Mata, and E. Ozturk, 'Form error prediction in robotic assisted milling', *Procedia CIRP*, vol. 82, pp. 491–496, 2019, doi: 10.1016/j.procir.2019.04.335.

[77] K. Kolluru and D. Axinte, 'Novel ancillary device for minimising machining vibrations in thin wall assemblies', *Int J Mach Tools Manuf*, vol. 85, pp. 79–86, 2014, doi: 10.1016/j.ijmachtools.2014.05.007.

[78] J. Fei *et al.*, 'Investigation of moving fixture on deformation suppression during milling process of thin-walled structures', *J Manuf Process*, vol. 32, pp. 403–411, 2018, doi: 10.1016/j.jmapro.2018.03.011.

[79] J. Fei *et al.*, 'Chatter mitigation using moving damper', *J Sound Vib*, vol. 410, pp. 49–63, 2017, doi: 10.1016/j.jsv.2017.08.033.

[80] L. Xu, D. Zhang, J. Xu, R. Wang, and Y. Sun, 'A stiffness matching-based deformation errors control strategy for dual-robot collaborative machining of thin-walled parts', *Robot Comput Integr Manuf*, vol. 88, p. 102726, Aug. 2024, doi: 10.1016/J.RCIM.2024.102726.

[81] L. Uriarte *et al.*, 'Machine tools for large parts', *CIRP Annals*, vol. 62, no. 2, pp. 731–750, Jan. 2013, doi: 10.1016/J.CIRP.2013.05.009.

[82] C. Dong, H. Liu, Q. Liu, T. Sun, T. Huang, and D. G. Chetwynd, 'An approach for type synthesis of overconstrained 1T2R parallel mechanisms', *Mechanisms and Machine Science*, vol. 50, pp. 274–281, 2018, doi: 10.1007/978-3-319-60867-9_31/COVER.

[83] R. Wang and Y. Sun, 'Chatter prediction for parallel mirror milling of thin-walled parts by dual-robot collaborative machining system', *Robot Comput Integr Manuf*, vol. 88, p. 102715, Aug. 2024, doi: 10.1016/J.RCIM.2024.102715.

[84] E. Shamoto, T. Mori, B. Sencer, N. Suzuki, and R. Hino, 'Suppression of regenerative chatter vibration in multiple milling utilizing speed difference method-Analysis of double-sided milling and its generalization to multiple milling operations', *Precis Eng*, vol. 37, no. 3, pp. 580–589, Jul. 2013, doi: 10.1016/J.PRECISIONENG.2013.01.003.

[85] R. Fu *et al.*, 'Double-sided milling of thin-walled parts by dual collaborative parallel kinematic machines', *J Mater Process Technol*, vol. 299, p. 117395, Jan. 2022, doi: 10.1016/J.JMATPROTEC.2021.117395.

[86] P. L. F. Kengne, C. Sun, S. Pope, and E. Ozturk, 'Integration and demonstration of force controlled support in pocket milling', *Procedia CIRP*, vol. 101, pp. 158–161, 2020, doi: 10.1016/j.procir.2021.05.151.

[87] J. L. Xiao, S. L. Zhao, H. Guo, T. Huang, and B. Lin, 'Research on the collaborative machining method for dual-robot mirror milling', *International Journal of Advanced Manufacturing Technology*, vol. 105, no. 10, pp. 4071–4084, 2019, doi: 10.1007/s00170-018-2367-1.

[88] K. Shimana, E. Kondo, D. Shigemori, S. Yamashita, Y. Kawano, and N. Kawagoishi, 'An Approach to Compensation of Machining Error Caused by Deflection of End Mill', *Procedia CIRP*, vol. 1, pp. 677–678, 2012, doi: 10.1016/j.procir.2012.05.024.

[89] J. Depree and C. Gesswein -Halcyon, 'Robotic Machining White Paper Project', 2008.

[90] E. Ozturk, O. Ozkirimli, T. Gibbons, M. Saibi, and S. Turner, 'Prediction of effect of helix angle on cutting force coefficients for design of new tools', *CIRP Annals*, vol. 65, no. 1, pp. 125–128, Jan. 2016, doi: 10.1016/J.CIRP.2016.04.042.

[91] 'Forms of milling'. Accessed: Oct. 16, 2020. [Online]. Available: http://www.uotechnology.edu.iq/dep-production/branch3_files/15luma.pdf

[92] A. H. Committee, 'Properties and Selection: Nonferrous Alloys and Special-Purpose Materials', *Properties and Selection: Nonferrous Alloys and Special-Purpose Materials*, Jan. 1990, doi: 10.31399/ASM.HB.V02.9781627081627.

[93] J. W. D. Callister, 'Materials Science and Engineering an Introduction. John Wiley & Sons Inc', 2013, Accessed: Jan. 23, 2025. [Online]. Available: https://books.google.com/books/about/Materials_Science_and_Engineering_An_Int.html?id=TmxbAgAAQBAJ

[94] 'MatWeb Material Property Data Sheet for Aluminium 6082-T6'. Accessed: Jan. 23, 2025. [Online]. Available: https://www.matweb.com/search/datasheetText.aspx?bassnum=MA6082T6

[95] I. J. Polmear, 'Light alloys: From traditional alloys to nanocrystals', *Light Alloys: From Traditional Alloys to Nanocrystals*, pp. 1–421, Dec. 2005, doi: 10.1016/B978-0-7506-6371-7.X5000-2.

[96] M. P. Groover, 'Fundamentals of Modern Manufacturing: Materials, Processes, and Systems', p. 520, 2006, Accessed: Jan. 23, 2025. [Online]. Available: https://www.wiley.com/en-gb/Fundamentals+of+Modern+Manufacturing%3A+Materials%2C+Processes%2C+and+Systems%2C+7th+Edition-p-9781119475217

[97] S. Kalpakjian, S. Schmid, and V. Sekar, 'Manufacturing engineering and technology in SI units', *Pearson Education Centre*, pp. 364–370, 2021, Accessed: Jan. 23, 2025. [Online]. Available: /content/one-dot-com/one-dot-com/se/en/Nordics-Higher-Education/subject-

catalogue/engineering/ManufacturingEngineering-and-Technology-7th-SI-Edition.html

[98] J. R. Davis, 'ASM speciality handbook: Aluminium and aluminium alloys', *Metallic Materials*, p. 700, 1996, Accessed: Jan. 23, 2025. [Online]. Available: https://books.google.com/books/about/Aluminum_and_Aluminum_Alloys.html?id=Lskj5k3PSIcC

[99] S. H. Avner, 'Introduction to Physical Metallurgy', p. 696, 1974.

[100] E. O. Ezugwu, J. Bonney, and Y. Yamane, 'An overview of the machinability of aeroengine alloys', *J Mater Process Technol*, vol. 134, no. 2, pp. 233–253, Mar. 2003, doi: 10.1016/S0924-0136(02)01042-7.

[101] 'ASM Handbook Volume 15: Casting', 2008, Accessed: Jan. 23, 2025. [Online]. Available: https://www.asminternational.org/results/-/journal_content/56/05115G/PUBLICATION/

[102] EP. DeGarmo, JT. Black, and RA. Kohser, 'Materials and processes in manufacturing, 9th ed', p. 1154, 2003.

[103] P. N. . Rao, 'Manufacturing technology. Volume 1, Foundry, forming and welding', p. 512, 2013, Accessed: Jan. 23, 2025. [Online]. Available: https://books.google.com/books/about/Manufacturing_Technology.html?id=fSHZAgAAQBAJ

[104] E. O. Ezugwu and Z. M. Wang, 'Titanium alloys and their machinability—a review', *J Mater Process Technol*, vol. 68, no. 3, pp. 262–274, Aug. 1997, doi: 10.1016/S0924-0136(96)00030-1.

[105] Erik. Oberg, F. D. . Jones, H. Lynedon. Horton, and H. H. . Ryffel, 'Machinery's handbook : a reference book for the mechanical engineer, designer, manufacturing engineer, draftsman, toolmaker, and machinist', p. 2511, 1988.

[106] G. Welsch, R. Boyer, and E. W. Collings, 'Materials properties handbook: Titanium alloys, 2nd ed', *ASM International: Materials Park, OH*, p. xxii 1176, 1998.

[107] C. Leyens and M. Peters, 'Titanium and titanium alloys : fundamentals and applications / ed. by C. Leyens and M. Peters', *Titanium and titanium alloys fundamentals and applications*, 2003.

[108] R. C. Reed, 'The Superalloys fundamentals and applications', *The Superalloys: Fundamentals and Applications*, vol. 9780521859042, pp. 1–372, Jan. 2006, doi: 10.1017/CBO9780511541285.

[109] 'Metals handbook. Volume 1 Properties and selection : irons, steels, and high-performance alloys', 1990.

[110] 'MatWeb Material Property Data Sheet for Stainless Steel 304'. Accessed: Jan. 23, 2025. [Online]. Available: https://www.matweb.com/search/datasheet.aspx?MatGUID=abc4415b0f8b490387e3c922237098da&ckck=1

[111] Donald. Peckner and I. M. . Bernstein, 'Handbook of stainless steels', p. 800, 1977.

[112] R. E. . Reed-Hill, 'Physical metallurgy principles', p. 920, 1973.

[113] ASM, 'ASM handbook Volume 2 - Properties and selection: Nonferrous alloys and special-purpose materials', *ASM Metals Handbook*, vol. 2, p. 1300, 1993, Accessed: Jan. 15, 2025. [Online]. Available: https://www.asminternational.org/results/-/journal_content/56/06182G/PUBLICATION/

[114] 'MatWeb Material Property Data Sheet for Ti6Al-4V'. Accessed: Jan. 23, 2025. [Online]. Available: https://asm.matweb.com/search/specificmaterial.asp?bassnum=mtp641

[115] H. Moradi, M. R. Movahhedy, and G. Vossoughi, 'Linear and Nonlinear Model of Cutting Forces in Peripheral Milling: A Comparison Between 2D and 3D Models', *ASME International Mechanical Engineering Congress and Exposition, Proceedings (IMECE)*, vol. 3, pp. 955–962, Apr. 2012, doi: 10.1115/IMECE2010-38641.

[116] A. Weremczuk, R. Rusinek, and J. Warminski, 'Bifurcation and stability analysis of a nonlinear milling process', *AIP Conf Proc*, vol. 1922, no. 1, p. 100008, Jan. 2018, doi: 10.1063/1.5019093/608609.

[117] G. Stepan, Z. Dombovari, and J. Muñoa, 'Identification of cutting force characteristics based on chatter experiments', *CIRP Annals*, vol. 60, no. 1, pp. 113–116, Jan. 2011, doi: 10.1016/J.CIRP.2011.03.100.

[118] M. A. Rubeo and T. L. Schmitz, 'Milling Force Modeling: A Comparison of Two Approaches', *Procedia Manuf*, vol. 5, pp. 90–105, 2016, doi: 10.1016/J.PROMFG.2016.08.010.

[119] D. Montgomery and Y. Altintas, 'Mechanism of cutting force and surface generation in dynamic milling', *Journal of Manufacturing Science and Engineering, Transactions of the ASME*, vol. 113, no. 2, pp. 160–168, 1991, doi: 10.1115/1.2899673.

[120] T. Schmitz and J. Ziegert, 'Examination of surface location error due to phasing of cutter vibrations', *Precis Eng*, vol. 23, no. 1, pp. 51–62, 1999, doi: 10.1016/S0141-6359(98)00025-7.

[121] T. L. Schmitz and B. P. Mann, 'Closed-form solutions for surface location error in milling', *Int J Mach Tools Manuf*, vol. 46, pp. 1369–1377, 2006, doi: 10.1016/j.ijmachtools.2005.10.007.

[122] J. J. Junz Wang and C. M. Zheng, 'An analytical force model with shearing and ploughing mechanisms for end milling', *Int J Mach Tools Manuf*, vol. 42, no. 7, pp. 761–771, May 2002, doi: 10.1016/S0890-6955(02)00019-6.

[123] B. Lin, L. Wang, Y. Guo, and J. Yao, 'Modeling of cutting forces in end milling based on oblique cutting analysis', *International Journal of Advanced Manufacturing Technology*, vol. 84, no. 1–4, pp. 727–736, Apr. 2016, doi: 10.1007/S00170-015-7724-8/METRICS.

[124] G. Li, D. Qu, W. W. Feng, B. Wang, and N. Li, 'Modeling and experimental study on the force of micro-milling titanium alloy based on tool runout',

International Journal of Advanced Manufacturing Technology, vol. 87, no. 1–4, pp. 1193–1202, Oct. 2016, doi: 10.1007/S00170-016-8473-Z/METRICS.

[125] X. Su, G. Wang, J. Yu, F. Jiang, J. Li, and Y. Rong, 'Predictive model of milling force for complex profile milling', *International Journal of Advanced Manufacturing Technology*, vol. 87, no. 5–8, pp. 1653–1662, Nov. 2016, doi: 10.1007/S00170-016-8589-1/METRICS.

[126] J. H. Ko and D. W. Cho, '3D ball-end milling force model using instantaneous cutting force coefficients', *J Manuf Sci Eng*, vol. 127, no. 1, pp. 1–12, 2005, doi: 10.1115/1.1826077.

[127] P. Lee and Y. Altintaş, 'Prediction of ball-end milling forces from orthogonal cutting data', *Int J Mach Tools Manuf*, vol. 36, no. 9, pp. 1059–1072, Sep. 1996, doi: 10.1016/0890-6955(95)00081-X.

[128] A. Sadredine, 'Surface Roughness Prediction of Thin-Walled Parts Impacted by Radial Depth of Cut Variations During Peripheral Milling Process', *FME Transactions*, vol. 51, no. 3, pp. 284–297, 2023, doi: 10.5937/FME2303284S.

[129] Y. Dun, L. Zhu, and S. Wang, 'Investigation on milling force of thin-walled workpiece considering dynamic characteristics of workpiece', *Journal of Mechanical Science and Technology*, vol. 33, no. 9, pp. 4061–4079, Sep. 2019, doi: 10.1007/S12206-019-0802-3/METRICS.

[130] H. Li and Y. C. Shin, 'A Comprehensive Dynamic End Milling Simulation Model', *J Manuf Sci Eng*, vol. 128, no. 1, pp. 86–95, Feb. 2006, doi: 10.1115/1.2035694.

[131] M. L. Campomanes and Y. Altintas, 'An Improved Time Domain Simulation for Dynamic Milling at Small Radial Immersions', *J Manuf Sci Eng*, vol. 125, no. 3, pp. 416–422, Aug. 2003, doi: 10.1115/1.1580852.

[132] K. Weinert, P. Kersting, T. Surmann, and D. Biermann, 'Modeling regenerative workpiece vibrations in five-axis milling', *Production Engineering*, vol. 2, no. 3, pp. 255–260, 2008, doi: 10.1007/S11740-008-0113-5.

[133] E. Budak and Y. Altintas, 'Modeling and avoidance of static form errors in peripheral milling of plates', *Int J Mach Tools Manuf*, vol. 35, no. 3, pp. 459–476, Mar. 1995, doi: 10.1016/0890-6955(94)P2628-S.

[134] J. S. Tsai and C. L. Liao, 'Finite-element modeling of static surface errors in the peripheral milling of thin-walled workpieces', *J Mater Process Technol*, vol. 94, no. 2, pp. 235–246, Sep. 1999, doi: 10.1016/S0924-0136(99)00109-0.

[135] M. Wan, W. Zhang, K. Qiu, T. Gao, and Y. Yang, 'Numerical prediction of static form errors in peripheral milling of thin-walled workpieces with irregular meshes', *J Manuf Sci Eng*, vol. 127, no. 1, pp. 13–22, 2005, doi: 10.1115/1.1828055.

[136] Y. G. Kang and Z. Q. Wang, 'Two efficient iterative algorithms for error prediction in peripheral milling of thin-walled workpieces considering the in-cutting chip', *Int J Mach Tools Manuf*, vol. 73, pp. 55–61, 2013, doi: 10.1016/J.IJMACHTOOLS.2013.06.001.

[137] Z. L. Li, O. Tuysuz, L. M. Zhu, and Y. Altintas, 'Surface form error prediction in five-axis flank milling of thin-walled parts', *Int J Mach Tools Manuf*, vol. 128, pp. 21–32, May 2018, doi: 10.1016/J.IJMACHTOOLS.2018.01.005.

[138] H. O. Bansal, R. Sharma, and P. R. Shreeraman, 'PID Controller Tuning Techniques: A Review', *Journal of Control Engineering and Technology*, vol. 2, no. 4, pp. 168–176, 2012, doi: 10.2/JQUERY-UI.MIN.JS.

[139] S. Skogestad and I. Postlethwaite, *Multivariable feedback control: analysis and design*, vol. 2. Wiley New York, 2007.

[140] 'PID Controller Tuning in Simulink - MATLAB & Simulink - MathWorks United Kingdom'. Accessed: Jan. 03, 2024. [Online]. Available: https://uk.mathworks.com/help/slcontrol/gs/automated-tuning-of-simulink-pid-controller-block.html

[141] P. Onawumi and C. Sun, 'Prediction of Dimensional Errors in Robotic Milling', Sheffield, Feb. 2022.

[142] 'Threaded Stud Ball Transfer Units - 81 & 91 Series'. Accessed: Feb. 04, 2025. [Online]. Available: https://www.omnitrack.com/ball-transfer-units/heavy-duty/81-91-series-threaded-stud/

[143] 'Rolling Resistance and Industrial Wheels'. Accessed: Jan. 08, 2025. [Online]. Available: https://www.hamiltoncaster.com/Blog/EntryId/222/Rolling-Resistance-and-Industrial-Wheels

[144] Q. Bo, H. Liu, M. Lian, Y. Wang, and K. Liu, 'The influence of supporting force on machining stability during mirror milling of thin-walled parts', doi: 10.1007/s00170-018-3113-4.

[145] D. Stöbener and B. Beekhuis, 'Application of an in situ measuring system for the compensation of wall thickness variations during turning of thin-walled rings', *CIRP Annals*, vol. 62, no. 1, pp. 511–514, Jan. 2013, doi: 10.1016/J.CIRP.2013.03.129.

[146] N. Huang, C. Yin, L. Liang, J. Hu, and S. Wu, 'Error compensation for machining of large thin-walled part with sculptured surface based on on-machine measurement', *International Journal of Advanced Manufacturing Technology*, vol. 96, no. 9–12, pp. 4345–4352, Jun. 2018, doi: 10.1007/S00170-018-1897-X/METRICS.

[147] H. B. Liu, Y. Q. Wang, Z. Y. Jia, and D. M. Guo, 'Integration strategy of on-machine measurement (OMM) and numerical control (NC) machining for the large thin-walled parts with surface correlative constraint', *International Journal of Advanced Manufacturing Technology*, vol. 80, no. 9–12, pp. 1721–1731, Oct. 2015, doi: 10.1007/S00170-015-7046-X/METRICS.

[148] M. Dijkman and G. Goch, 'Distortion compensation strategies in the production process of bearing rings', *Materwiss Werksttech*, vol. 40, no. 5–6, pp. 443–447, May 2009, doi: 10.1002/MAWE.200900474.

[149] A. Mahmud, 'Mechanical Pocket Milling of Thin Aluminum Panel with a Grasping and Machining End Effector', PhD Thesis, Université De Montreal, 2015.

[150] P. R. Murray and R. J. Dewhurst, 'A laser/EMAT system for thickness monitoring applications using shear and L-S mode-converted waves', *Meas Sci Technol*, vol. 12, no. 10, pp. 1651–1659, Oct. 2001, doi: 10.1088/0957-0233/12/10/305.

[151] F. Niese, A. Yashan, H. W.-9th E. C. on NDT, undefined Berlin, and undefined 2006, 'Wall thickness measurement sensor for pipeline inspection using EMAT technology in combination with pulsed eddy current and MFL', *9th European Conference on NDT*, vol. 18, no. Berlin, pp. 45–52, 2006, Accessed: Jan. 10, 2024. [Online]. Available: https://citeseerx.ist.psu.edu/document?repid=rep1&type=pdf&doi=9ae3e2fac230dc8fb90d5405bd50139193f1f552

[152] R. Panczuk and P. Y. Foissac, 'Process and a device for the machining of panels', US7682112B2, 2010 Accessed: Jan. 10, 2024. [Online]. Available: https://patents.google.com/patent/US7682112B2/en

[153] R. Viitala, G. Gruber, B. Hemming, T. Widmaier, K. Tammi, and P. Kuosmanen, 'Device and method for measuring thickness variation of large roller element bearing rings', *Precis Eng*, vol. 55, pp. 59–69, 2018, Accessed: Jan. 10, 2024. [Online]. Available: https://www.sciencedirect.com/science/article/pii/S0141635918303210

[154] C. Spínola, M. J. M. Vázquez, A. G. Bohorquez, J. M. Bonelo, and J. Vizoso, 'Calibration of thickness measurement instruments based on twin laser sensors. Isolines bilinear look up tables', *Conference Record - IEEE Instrumentation and Measurement Technology Conference*, vol. 2, pp. 1079–1083, Jan. 2001, doi: 10.1109/imtc.2001.928246.